AD-A007 451

GROUND MOTION MODELS AND COMPUTER TECHNIQUES

T. David Riney, et al

Systems, Science and Software

Prepared for:

Defense Nuclear Agency
Advanced Research Projects Agency

April 1972

DISTRIBUTED BY:

NTIS

National Technical Information Service
U. S. DEPARTMENT OF COMMERCE

100117 D-C

(1)

DNA 2915Z
APRIL 1972
3SR-1071

AD A007451

GROUND MOTION MODELS AND COMPUTER TECHNIQUES

FORMAL REPORT

T. D. RINEY
J. K. DIENES
G. A. FRAZIER
S. K. GARG
J. W. KIRSCH
D. H. BROWNELL
A. J. GOOD

PRICES SUBJECT TO CHANGE

Prepared for
Headquarters, Defense Nuclear Agency
Washington, D.C. 20305

SYSTEMS, SCIENCE AND SOFTWARE
LA JOLLA, CALIFORNIA 92037

Contract No. DASA 01-69-C-0159(P00003)

261

DNA 2915Z
APRIL 1972
3SR-1071

SYSTEMS, SCIENCE AND SOFTWARE

P. O. BOX 1620, LA JOLLA, CALIFORNIA 92037, TELEPHONE (714) 453-0060

GROUND MOTION MODELS AND COMPUTER TECHNIQUES

FORMAL REPORT

This work was supported by the Defense Nuclear Agency
under NWER Subtask ZL438-01

T. D. RINEY
J. K. DIENES
G. A. FRAZIER
S. K. GARG
J. W. KIRSCH
D. H. BROWNELL
A. J. GOOD

Prepared for
Headquarters, Defense Nuclear Agency
Washington, D.C. 20305
Contract No. DASA 01-69-C-0159(P00003)
Program Code Number OF10, ARPA Order No. 1438

FOREWORD

This formal technical report entitled "Ground Motion Predictive Techniques for Porous Geologic Media," is submitted by Systems, Science and Software (S^3) to the Advanced Research Projects Agency (ARPA) and to the Defense Nuclear Agency (DNA). The report presents the results of the third phase of a continuing effort to develop reliable material models and computer techniques for predicting the motion of inhomogeneous and porous geologic media. This work, in support of the PRIME ARGUS and MILITARY GEOPHYSICS programs, was accomplished under Contract No. DASA 01-69-C-0159(P00003), which was funded by ARPA and monitored by DNA. Dr. Stanley Ruby was the ARPA Program Manager and Mr. Clifton B. McFarland was the DNA Project Scientist.

Dr. T. David Riney was the S^3 Project Manager for the study. The technical results presented in this report represent the work of a number of S^3 staff members in addition to the authors. It is appropriate to list here the contributors to technical Sections II through V.

Section II:	J. W. Kirsch, A. J. Good, G. D. Anderson
Section III:	J. K. Dienes, G. D. Anderson, K. G. Hamilton
Section IV:	S. K. Garg, D. H. Brownell, R. J. Archuleta
Section V:	G. A. Frazier, S. K. Garg

Dr. M. H. Rice participated as a consultant on this project.

CONTENTS

Contents (continued)

Contents (continued)

ABSTRACT

The work reported consists of three task areas: (a) development of constitutive models and computer methods for calculating stress wave effects in geologic media in the vicinity of a buried energy source, (b) verification of the computer models and their application to examine the sensitivity of ground motion predictions to the material parameters assumed in the constitutive models, and (c) development of methods for calculating the perturbation of residual tectonic stress-strain distributions induced by changing the pore water pressure. A general computer subroutine (TAMEOS) is described which generates thermodynamic equations of state of porous wet media for use with a table look-up procedure in standard ground motion codes. TAMEOS has been applied to NTS tuff and is used in the SKIPPER code for a series of spherical calculations in which the crushup strength and volume fractions of the rock-water-void mixture were varied. Four constitutive models and associated subroutines have been incorporated into SKIPPER for improved ground motion calculations for rocks with high shear strength. The cap model is generalized to treat the full range of pressure and strain encountered in underground tests. Generalized Mohr-Coulomb models include one without work hardening, one with isotropic work hardening, and one with kinematic work hardening. Model sensitivity calculations for granite are presented for the four SKIPPER options. Detailed comparison of calculations with field measurements are presented for the kinematic work hardening and cap models. A thermodynamic formulation of the Theory of Interacting Continua (TINC) is presented as well as the numerical procedure used in the new POROUS code for treating spherical ground motion problems

in the TINC framework. Limited calculations using the new code are presented for partially saturated tuff. Linearized TINC equations are developed for describing the interaction of a pore fluid with a rock matrix as the fluid is driven through the geologic mass under a hydraulic gradient. The 2-D finite element computer code (FRI) for treating these geohydrological processes is described. Test calculations for the rock-fluid interactions in the vicinity of a fluid injection well are presented.

I. INTRODUCTION

Adequate material response models and associated computational techniques are required if ground motion predictions are to be made with confidence. One is concerned with a signal which has attenuated from stress levels in the source vicinity, which may be megabars, to stresses at large distances, which are small compared to strengths of earth media.

In this transition region between the hydrodynamic source and the distant elastic region, the material response models should consider such complex nonlinear physical processes as dynamic void compaction, heterogeneity, pore water pressure and diffusion, yield and fracture phenomena, dilatancy, water and rock interactions, material phase changes, and dependence of strength parameters on the thermodynamic state. This report describes improved techniques for predicting ground motion that have been developed in the current study. The general approach followed here, as in earlier work described in 3SR-267 and 3SR-648,* is to construct material models of increasing sophistication from available material properties data and to develop the required numerical methods to evaluate stress wave phenomena as each additional effect is introduced into the model.

In addition to the development and application of improved techniques for predicting ground motion, the report also describes work directed toward understanding earthquake triggering mechanisms. A computer model is being developed to calculate the quasi-static perturbation in a residual tectonic stress-strain distribution as a pressurized fluid penetrates through a geologic medium under a hydraulic gradient. The objective is to analyze the effect of siting

*Here and throughout this document, 3SR-267 and 3SR-648 refer to the reports [Refs. 1 and 2, respectively] describing earlier phases of this contract.

a reservoir or a deep waste disposal well in the vicinity of a pre-existing fault zone.

A typical geologic medium consists of a rock or soil matrix containing cracks or pores that may be partially filled with water. Even if the matrix material is unchanged, the porosity and the water content will vary with depth and with surface distance and the stress propagation characteristics of the medium will vary accordingly. For teleseismic calculations it is impossible to know the porosities and degrees of saturation at inaccessible nuclear test sites. Even when local geological conditions and the water table location have been established by field logging tests, as would be possible in evaluating the vulnerability of underground structures, it is economically impractical to perform laboratory material properties tests on all the porosities and degrees of saturation that occur. Consequently, it is desirable to construct the material models in such a fashion that the response of the medium can be predicted as these quantities are varied.

From the outset of the present study, therefore, the geologic medium has been considered to be composite and a description of its wave propagation characteristics has been sought in terms of the behavior of the isolated rock matrix and water components. Reference to the detailed microstructure of the composite is avoided, however, since the models are to be used in continuum type computer codes in which the phenomena of interest are on a much larger geometrical scale. Consequently, the Theory of Interacting Continua (TINC) was adopted to provide a framework general enough to allow explicit treatment of pore pressure effects and relative motion between the rock and water components. Computer codes usually employed for ground motion calculations, however, treat a geologic medium as a single continuum so that each incremental volume of the medium has associated single

values of pressure, velocity, etc. Since practical calculations are currently performed using such codes, material response models have also been developed to be compatible with application in single continuum codes by adding the homogenizing assumption of no relative motion between the rock and water.

In 3SR-267 and 3SR-648 the modeling effort centered on a representative tuff at the Nevada Test Site (NTS tuff) to be specific, but the basic methods are applicable to other porous geologic media with relatively small shear strengths. For example, one of the homogenized composite equation of state models has also been used to predict the behavior of clay shale media at the MIDDLE GUST test site.[3] In this report the model development has also specifically treated Cedar City tonalite, a representative geologic media with a large shear strength.

Section II describes an homogenized equation of state for NTS tuff for the pressure range of 1 mbar down to a few bars. A computer routine has been developed which calculates the isotropic thermodynamic states of rock-water-void mixtures, including a description of irreversible collapse of the air-filled pores (void volume). These states are tabulated and may be utilized in conjunction with a table look-up procedure as a subroutine in standard ground motion codes. Primary inputs to the TAMEOS subroutine (for Tabular Arrays Of Mixtures Equation Of State) are the homogenized model to be utilized (e.g., one of the PTEQ, PEQ or P*EQ models described in 3SR-648),* equations of state of the isolated rock and water components, and initial volume fractions of rock, water and air-filled pores. For cases in which experimental data are unavailable, a simple crushup model is employed requiring the crushup pressure, sound speed, and elastic crush limit, as the only additional inputs to be

---

*At the time of writing TAMEOS has been used only with tables generated with the PEQ model, but may be readily used with other pressure-equilibrium models.

specified. If experimental data are available, the crushup curve can be directly incorporated into the TAMEOS subroutine.

The TAMEOS subroutine has been incorporated into the single continuum SKIPPER code and a series of spherical calculations made using the PEQ model for a representative tuff with varied degrees of water saturation of the pore space. An 8-kT nuclear source is simulated by a $\gamma = 1.4$ gas in a cavity of initial radius of 3.72 m in these material property sensitivity calculations. (In Appendix B the results of several spherical calculations for a 1000-lb high explosive energy source of interest to the NTS underground test program are also presented.)

Section III describes the basic theory and the associated series of subroutines that have been incorporated into SKIPPER for improved ground motion calculations for high-shear-strength igneous rocks. Constitutive laws more general than the Mohr-Coulomb model used in much of the earlier work are introduced. In each case, an associated flow rule is assumed in developing the flow law and the influence of finite deformation is properly treated in the kinematic relations. Major emphasis was on the work to generalize, program and test the Weidlinger cap model (for Cedar City tonalite[4]) in order to arrive at a constitutive equation that covers the full range of pressure and strain encountered in nuclear shots. Generalized Mohr-Coulomb constitutive equations were also incorporated into SKIPPER as options, including one without work hardening, one with isotropic work hardening, and one with kinematic work hardening.

These four modes of the SKIPPER code were exercised in a series of material model sensitivity calculations for a spherical configuration . These parameter studies for Cedar City tonalite are all for the same simulated 8-kT nuclear source used in the tuff calculations. Effects of the strength

parameters on cavity size, stress attenuation and displacement are examined. Most of the work described in Section III, however, concerns comparison of the Hardhat and Piledriver ground motion measurements with SKIPPER calculations using the generalized cap model and the kinematic work hardening model. It is shown that the latter model predicts ground motion in much better agreement with field measurements than is possible when the cap model is employed.

A modification of the TINC formulation to more realistically treat the deviatoric stresses in the rock matrix, and its extension to account for thermodynamic effects, is presented in Section IV. The 1-D computer code POROUS for computing stress wave effects has been completely rewritten to account for the more comprehensive TINC model. The code now treats spherical as well as planar configurations whereas the initial version for solving the TINC equations within the mechanical formulation treated only plane waves (see 3SR-267 and 3SR-648]. Limited calculations using this new POROUS code for partially saturated NTS tuff are presented.

The mechanical interaction of a pore fluid with a saturated rock matrix as the fluid is driven through the geologic mass surrounding a fluid injection well has been modeled within the linearized TINC equations. The formulation, presented in Section V, couples the deformation and diffusion fields of interest to the problem. In order to solve the associated set of linearized quasi-static equations, retaining all of the potentially important interaction terms, a finite-element method of solution was selected. Available 2-D finite element computer codes for treating the separate elastic and diffusive processes were modified and combined into a single code for treating the coupled processes. This 2-D fluid-rock interaction code (FRI) is described in Section V along with some test calculations.

In Section VI, the status of the work is summarized and suggestions are made for the direction of the effort during the next contract period.

It seems appropriate here to record a number of technical publications that have appeared in the open literature describing aspects of the work reported in 3SR-267 and 3SR-648. Gurtman, Kirsch and Hastings[5] presented an analytical equation of state for compressed states of water. Morland[6] described the initial version of the TINC formulation for fluid saturated materials. Garg[7] presented numerical results describing wave propagation effects using the mechanical TINC formulation. Garg and Kirsch[8] showed that the TINC framework is general enough to include various homogenized composite equations of state (e.g., PTEQ, PEQ, and P*EQ) as special cases. Morland[9] presented a finite deformation plasticity theory with isotropic work hardening. Additional results of the earlier phases of the work have also been described in a number of oral presentations at technical symposia.

II. HOMOGENIZED TREATMENT OF POROUS WET TUFF

2.1 INTRODUCTION

One of the most important problem areas in the development of ground motion codes is the treatment of hydrodynamic rock/water mixtures. It has been demonstrated in 3SR-648 that one may derive various mixture equations of state on the basis of a number of "equilibrium" conditions achieved behind a shock wave. A unique set of shock states is specified only when a constraint is prescribed for the (shock) partitioning of internal energy between the rock and the water. Such a set of states can be obtained if the pressure and temperature of the constituents are equal (PTEQ). If there is insufficient time for thermal equilibration, but the components are homogenized to the point that they are in pressure equilibrium, other shock state specifications may be made, such as in the PEQ and P*EQ models discussed in 3SR-648. The latter formulations are of great importance, since all laboratory (and most field) experiments designed to measure ground motion parameters fall within the regime of thermal nonequilibrium.

Should analytic expressions for the rock and water components' equations of state be available, it is clear from the preceding study (3SR-648) that an analytic formulation of the geologic composite does not result for the mixture models commonly utilized. The situation is further complicated by the presence of voids in the mixture. Hence, it should be recognized that the simplification associated with modeling the effects of partial water saturation by deriving a single hydrodynamic equation of state of the mixture, will generally require tabular arrays of mixture states that must be utilized in place of an analytic expression.

In the following section we describe a new computational tool, called Tabular Arrays of Mixture Equations of State, TAMEOS. This routine calculates homogenized mixture states and stores them in a tabular array. The table is stored in the computer and individual states are retrieved by a rapid table look-up routine. In its simplest form, the table consists of a rectangular array of specific volumes (V) and specific internal energies (E) and the corresponding pressure (p). To treat irreversible pore crushup for a partially saturated rock-water-void mixture a fourth variable (α) must be introduced to monitor the current stage of the crushup process. In the work to be described here, the homogenized treatment of the porous wet mixtures has first been specialized to the PEQ model under the disconnected pores postulate (see 3SR-648). All of the air-filled porosity (void space) is presumed to be distributed within the rock under this postulate. The porous rock and water components are then considered to be in pressure equilibrium; the two components are assumed to shock to the same states as if isolated and to isentropically release without any heat transfer between them. This formulation was selected for first treatment because of its relative simplicity. (Other pressure equilibrium formulations could be tabulated in a similar manner. It is planned to treat the P*EQ and PTEQ models described in 3SR-648.)

For this model α is defined in terms of the rock-water-void volume fractions as follows*

$$\alpha = \frac{n^{(1)} + n^{(3)}}{n^{(1)}} \qquad (2.1)$$

*Alternatively, the crushup parameter could be defined in terms of the distention ratio for the mixture

$$\alpha_M = \frac{n^{(1)} + n^{(2)} + n^{(3)}}{n^{(1)} + n^{(2)}}$$

where

$n^{(1)}$ = rock matrix material volume fraction

$n^{(3)}$ = void volume fraction (air-filled porosity).

($n^{(2)}$ represents the water volume fraction, $n^{(1)} + n^{(2)} + n^{(3)} = 1$) Mixture states must be calculated for each $\alpha > 1$. Hence, this irreversible crushup regime requires a three-dimensional table (V, E, and α) to specify p.

As in the case of a porous, single component media, a suitable expression for $\alpha(p,V)$ is required to utilize the tabular array of states in the incompletely crushed regime. In the interest of generality, the crush curve may be specifically prescribed if enough experimental data were available. However, for calculational purposes, a specific form of crush curve for the rock component has been developed for TAMEOS which incorporates the key aspects of the physics of such processes, and requires a minimum of parameter specifications (crush strength, sound speed in poreless material, elastic crush regime limit).

The mixture states have been computed for six mixtures of tuff and water. The water equation of state in 3SR-648 has been supplemented to include the high pressure regime ($p > 200$ kbar). A new poreless tuff equation of state has been developed especially for use at shock pressures as high as a megabar. SKIPPER calculations were made to check out the TAMEOS routines and, subsequently, a parametric study was conducted to ascertain the effects of varying water and void (air-filled) volume content on the ground motion resulting from 8-kT underground nuclear explosions. The volume fractions of tuff matrix material considered were 0.95 and 0.8. Three degrees of water saturation were considered for

each; all pores empty, half the pores filled with water (half saturated), and all pores filled with water (fully saturated). Quantitative comparisons of these computer calculations are presented which graphically illustrate the effect of water saturation during the first 20 msecs after the detonation. Major variations were observed in the stress time histories and peak stress levels. Decreasing water content (and therefore higher air-filled void content) leads to dramatically lower stress levels, delayed wave arrival times, and smaller radial displacements.

2.2 PRESSURE-EQUILIBRIUM MIXTURES

2.2.1 Void-Free Mixtures

Equations of state utilized in ground motion codes usually are written in the form

$$p = p(V,E) \tag{2.2}$$

Typically, the condition of pressure equilibrium between the constituents is assumed, i.e.,

$$P_i\left(V_i, E_i\right) = P_j\left(V_j, E_j\right) \tag{2.3}$$

where the i,j subscripts refer to the ith and jth component. Under this condition, a hydrodynamic pressure, $p = P_i$, can be assigned to the mixture. Hence, overall characterization of the mixture is obtained by taking

$$p = P(V,E) = P_i\left(V_i, E_i\right) = \ldots \tag{2.4}$$

where

$$V = \sum_{i=1}^{k} M_i V_i \tag{2.5}$$

$$E = \sum_{i=1}^{k} M_i E_i \tag{2.6}$$

and M_i is the mass fraction of the ith constituent.

Obviously, this system of equations, (2.4) through (2.6), is not determinate. Given a k component mixture, and a set of values of V and E, there are $k+1$ equations for $2k$ unknowns (V_i, E_i). Thus, $k-1$ additional equations are required to fully specify the mixture state.

In some problems of interest, there may be enough time for the constituents to thermally equilibrate (see 3SR-648 for a simplified analysis of this effect). Under this condition, one can close the algebraic loop by requiring the temperature of each constituent to be equal,

$$T_i = T_j = \ldots \tag{2.7}$$

Of course, one must also specify the caloric equations of state of the constituents;

$$E_i = E_i(V_i, T_i) \tag{2.8}$$

The pressure-thermal equilibrium blending recipe (PTEQ) given by Eqs. (2.4) through (2.8) can be solved with iterative computer routines for the simultaneous solution of the set of algebraic equations. Generally, these take considerable computer time and in hydrodynamic calculations, the PTEQ formulation can most efficiently be utilized by generating a tabular array of V, E states. These are used in place of an equation of state with a rapid table look-up routine.

Thermal non-equilibrium mixtures are, conceptually, more difficult to model. The PTEQ formulation can be treated as a homogeneous material whose states are uniquely defined. When constituent materials are allowed to be at different temperatures within the same control volume, the mixture model no longer represents a truly homogeneous material (in the thermodynamic sense).

The PEQ and P*EQ models, introduced in 3SR-648 and 3SR-297, are based on hypotheses concerning the material interactions under shock loading. The mixture Hugoniot is derived on the basis of these assumptions. Subsequent release states are calculated by taking pressure-equilibrium

mixtures of the release adiabats associated with the shock states of each constituent.

In the PEQ formulation, each constituent is assumed to (shock) compress to a state on the Hugoniot of the pure material. Similarly, upon release from a shock state, each mixture component releases along the isentropic path of the pure material. Hence the shock and release states are computed by using the shock pressure, p_H, as a parameter. Each value of p_H implies specific values of V_i, E_i. These are then utilized in Eq. (2.5), (2.6) to calculate V, E of the PEQ mix. Since these values satisfy the Hugoniot relations, they imply that certain interactions will occur which result in these Hugoniot states.

Off-Hugoniot states are obtained by calculating the components' release isentropes from a given shock pressure and imposing pressure equilibrium. Thus, the interactions that occurred under the irreversible shock-loading process are frozen upon release and each constituent expands isentropically.

One may take a different tack, however, and specify that interactions occur which result in a mixture Hugoniot that differs from the PEQ version. One such formulation is the P*EQ model introduced in 3SR-648. It is based on the assumption that the entropy of the water component is determined by a double-shock process and remains at that level behind the leading portion of the shock wave. The double-shock results from the impedance mismatch between the rock and water.

As noted in 3SR-648, these P*EQ sets of water and tuff states are different than the individual Hugoniots of each constituent that are used in the PEQ model. This is

to be expected since the interaction model prescribes lower values of water entropy at a given particle velocity than is predicted for pure water. Once these sets of shock states are known, isentropes of each component passing through a given shock pressure may be put into pressure equilibrium to construct the mixture release adiabat (as in the PEQ model). It is evident that the PEQ and P*EQ models are very similar in concept. They differ only in how the shock interactions are modeled. Consequently, the mechanics of filling a tabular array of states is exactly the same for either mixture model.

2.2.2 Mixtures with Voids

Accurate predictions of the response of naturally-occurring geologic materials can be made only if the effects of the presence of air-filled voids (pores, cracks, etc.) are taken into account. In the case of shock wave propagation in these materials, porosity effects are manifest in two regimes: pressure levels high enough so that material is fully crushed and the lower pressure states wherein the voids are not completely removed. In both regimes, shock wave propagation is retarded due to the extra energy required to crush the material. The extra shock heating due to porosity results in Hugoniot curves which are displaced to the right of the poreless material Hugoniot in the p-V plane (see Fig. 2.1). In the present analysis, the mass contribution due to the compressed air has been ignored, so the excess shock heating is presumed to be immediately available to the rock/water mixture.

The fully crushed regime is readily adapted to the homogeneous mixture models discussed in the preceding section. All that is required is the specification of a different set of constitutive relations to partition the internal energy behind the shock wave. In PTEQ, this requirement is still

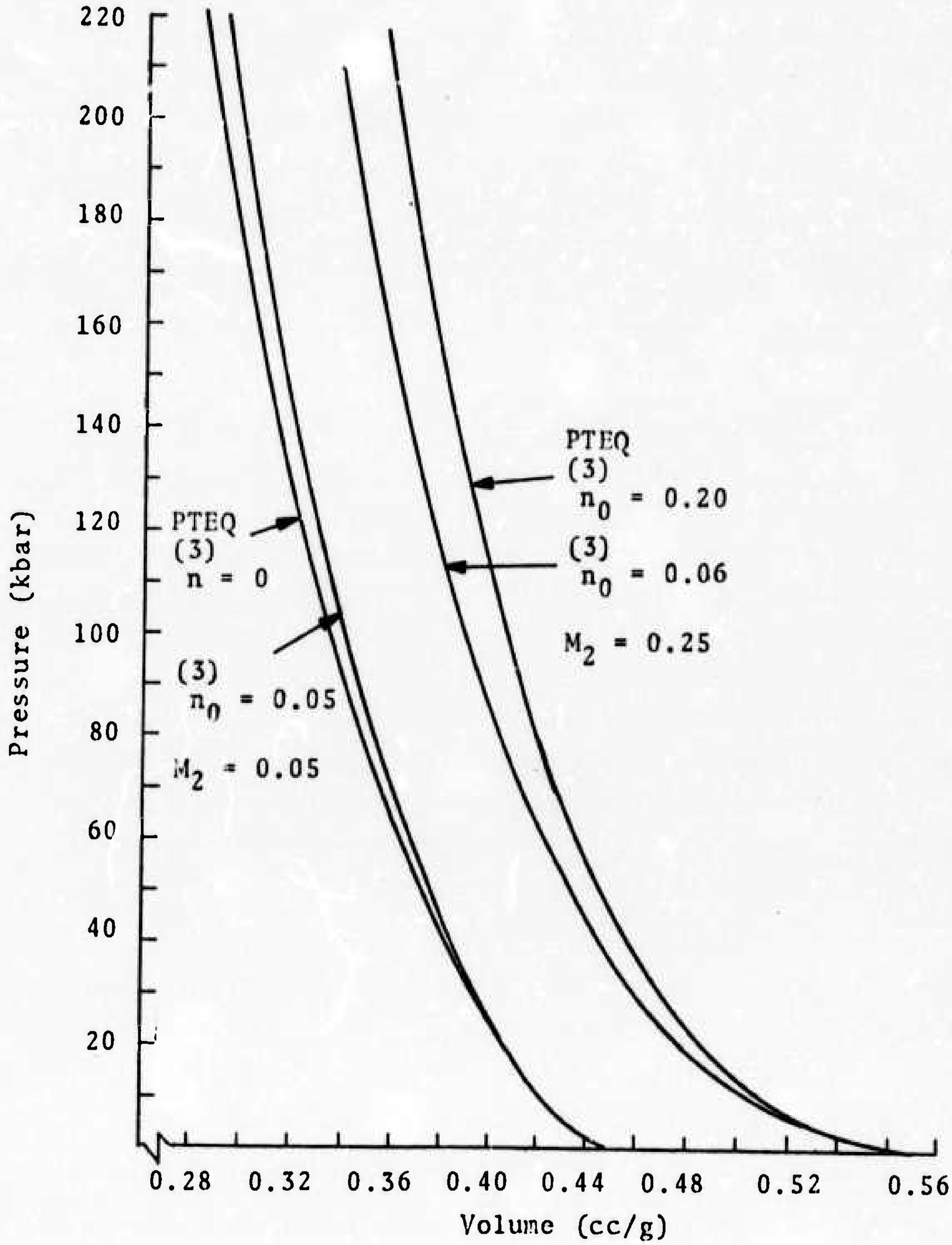

Fig. 2.1--"Shifting" of the Hugoniots in the p-V plane due to the extra shock heating associated with initial air-filled porosity for two PTEQ NTS tuff/water mixtures. (The NTS tuff equation of state is given in 3SR-648.)

taken care of by the assumption of thermal equilibrium. An alternative model is the initially porous version of the PEQ model (PEQP) introduced in 3SR-648. It maintains that the volume fraction of voids in each of the constituents is equal to the void volume fraction of the mixture. Hugoniots for the completely crushed constituents can be calculated from their equations of state. From there on, the mixture equation of state calculational procedure is identical to that outlined for the PEQ model.*

The energy partition is directly determined by the percentage of original void volume that is assigned to the water and tuff matrix components. Consequently, a multitude of PEQP-type mixtures exist, each based on different sharing of the void volume fraction. The disconnected pores postulate is utilized as the basic mixture model in this report. It assumes that all voids (air-filled pores) are contained in the rock matrix and that the bulk pressure in the distended tuff is in equilibrium with the effective pressure of the water. The special advantage of this formulation is that a minimum of experimental information is required to characterize the incompletely crushed regime.

There is ample evidence that porous geologic materials do not actually lose all of their porosity until sufficiently high compressions are achieved [e.g., Refs. 10 through 12]. the partially saturated rock matrix also may exhibit precursor effects which do not appear at higher degrees of water

*The derivation of mixture equations of state for initially porous materials can also be approached from different vantage points such as that used in developing P*EQ for tuff/water mixtures. In this instance, the water is presumed to undergo two major shock waves as the crush wave propagates through the material. For example, the leading shock develops from the initial wave and the secondary shock results when the voids are closed. In 3SR-648, such a model (P*EQP) was introduced to account for these multiple shock interactions.

saturation.[13] Hence, to account for this behavior, the crushing of the partially saturated rock/water composite should include an elastic, reversible process at low stress levels, followed by a regime wherein plastic, irreversible deformation occurs as the matrix collapses. These are complex processes which are not well understood.

A useful model has been suggested for metallic foams by Herrmann[14] that simplifies discussion of the problem. The distension parameter, α, is assumed to be a function of stress level,

$$\alpha = \alpha(p) \tag{2.9}$$

and the hydrodynamic stress is computed from the equation of state of the matrix material, with the modification that the effective specific volume, V/α, be utilized in place of V, i.e.,

$$p = P\left(\frac{V}{\alpha}, E\right) \tag{2.10}$$

Of course, $\alpha(p)$ is not generally known. It is only a convenient functional representation that ignores any internal energy effects. Herrmann discusses some general forms of $\alpha(p)$ which have been employed to analyze the incomplete crush regime of some porous metals. Qualitatively, these are sketched in Fig. 2.2. The critical parameters in such a model are the pressure at which all pores are (irreversibly) removed, p_c, the pressure limit to the elastic, reversible regime, p_e, and the slope of $\alpha(p)$ at $p = 0$.*

---

* $\alpha'(p)$ at $p = 0$ is related to the ratio of the sound speed in the porous material to that in the condensed rock matrix (see Appendix A).

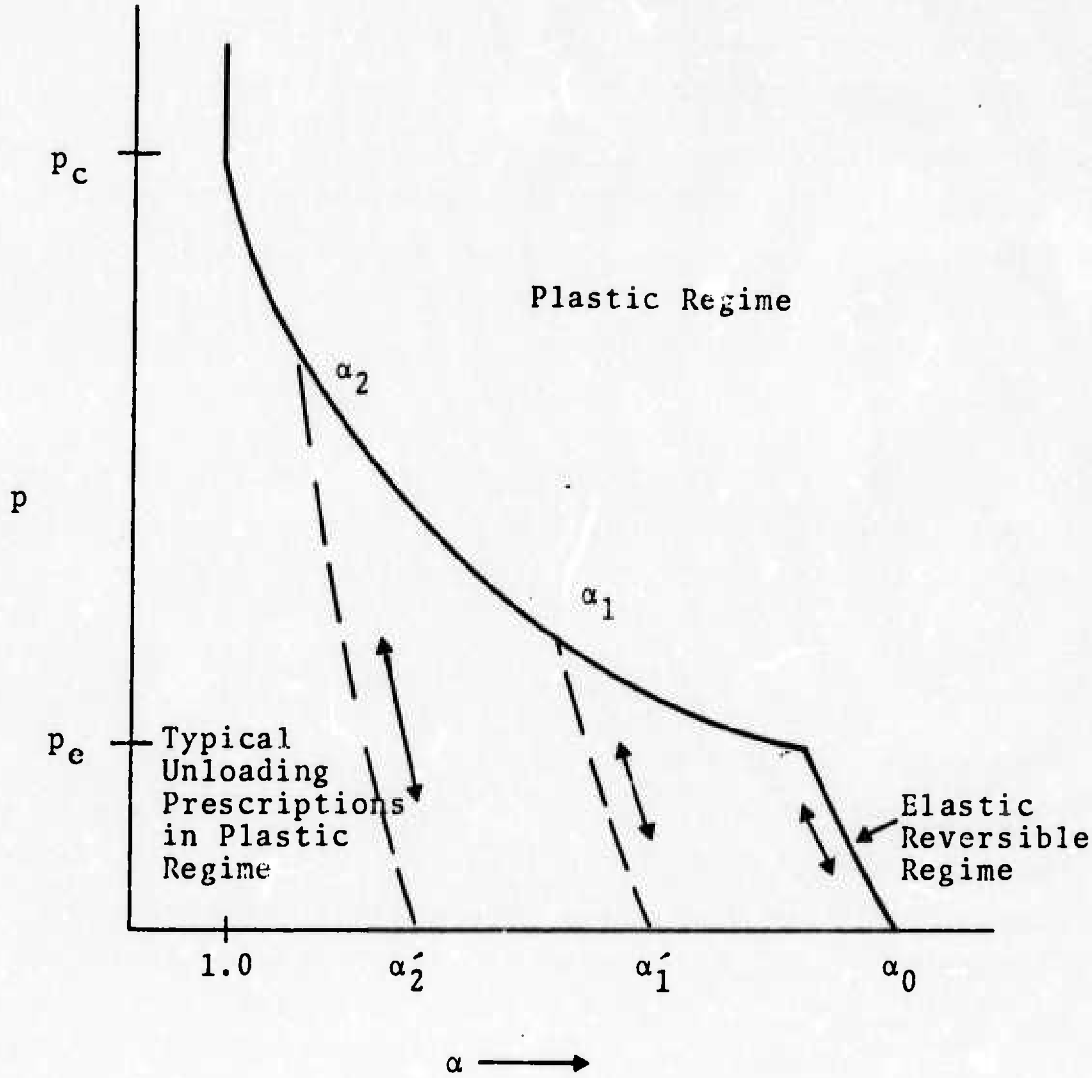

Fig. 2.2--Schematic of Herrmann's model for the distension ratio, $\alpha(p)$. Note that above the elastic limit, release from a plastic crush state occurs along a prescribed (reversible) release path which could result in some void recovery ($\alpha_2' > \alpha_2$). Release in the elastic regime is confined to the loading curve.

A review of the tuff crush-up data then available was reported in 3SR-648. A "universal" crush curve for tuffs was derived that could "fit" the available crush data when adjusted for grain density variations from specimen to specimen. However, the error band in this universal crush law law was quite large. Hence, if experimental crush curves are available for a given tuff (or other rock matrix) they should certainly be utilized.

The S^3 universal fit to crush data was functionally represented by $\alpha(\rho)$ instead of Herrmann's $\alpha(p)$ formulation (where ρ is the density). The concept of a crush density was easier to apply to the data, since the crush pressure varied considerably for the different tuffs. However the framework created by invoking the disconnected pores postulate makes it especially convenient to utilize an $\alpha(p)$ formulation so as to facilitate the derivation of pressure equilibrium rock/water/void mixtures. Hence, during the past year a generalized $\alpha(p)$ crush curve formulation has been developed for the rock matrix which yields similar results to the universal description and can be "tuned" to fit available experimental information.

2.2.3 S^3 Mixture Crush Model (Disconnected Pores)

The basic formulation of the pressure equilibrium mixture with porosity in one component (rock) is redefined in terms of equating the bulk pressure of the porous rock matrix to the pressure in the water. As pointed out in 3SR-648, the bulk pressure in an isotropic porous rock component can be defined as

$$p = \frac{1}{\alpha} p \left(\frac{V_1}{\alpha} , E_1 \right) \tag{2.11}$$

where the subscript 1 denotes the poreless rock component.

That is, the bulk stress exerted on a gage is predicted to be less than the effective pressure assumed in Herrmann's formulation, Eq. (2.10). Carroll and Holt[15] recommend Eq. (2.11) in preference to (2.10) for the case that the pores are so small that one may consider the rock to be homogeneous. Another argument for this modification can be made on the grounds that the sound speeds predicted by Eq. (2.11) are physically more meaningful (see discussion in Appendix A).

The algebraic formulation of the disconnected pores mixture model is given by

$$p = \frac{1}{\alpha} P_1\left(\frac{V_1}{\alpha}, E_1\right) = P_2\left(V_2, E_2\right) = P(V,E) \tag{2.12}$$

where

$$V = M_1V_1 + M_2V_2 \tag{2.13}$$

$$E = M E + M V \tag{2.14}$$

α = distention ratio of rock, some function of the hydrostatic pressure (2.15)

and the subscripts 1 and 2 denote the poreless rock and water constituents respectively.

It is evident from Eq. (2.11) that a prescription of α is all that is required to completley formulate the porous mixture equation of state. This simplification ignores any modifications to α due to variations in moisture content or porosity. (However, α may be considered as an input function and any prescription can be used to calculate the states of a mixture.)

In lieu of experimental data for a particular site, a simple set of expressions have been developed for the crushing of the porous rock constituent. The plastic crush regime has been modeled by a quadratic expression:

$$\alpha = 1 + (\alpha_e - 1)\left(1 - \frac{p - p_e}{p_c - p_e}\right)^2 \tag{2.16}$$

where

α_e = distension ratio at limit of elastic region

p_e = pressure at upper limit of elastic region

p_c = pressure at which voids are completely removed.

The quadratic is the simplest formulation which has $\alpha = 1$ and $d\alpha/dp = 0$ at $p = p_c$. Thus, all that is required is a specification of the crush pressure and the match points for the elastic region (see Fig. 2.3).

Release from any point in this region occurs with α fixed to the minimum value achieved during loading. Hence, to derive the mixture equation of state, the release states are computed for values of α in the vicinity of the Hugoniot points in the $\alpha > 1$ regime (see discussion in Section 2.3). It should be noted that $\alpha(p)$ is dependent on the direction of the process, and is not a simple, analytic function of pressure. This creates the need for a three-dimensional table in this regime, so that with α specified, valid mixture states can be located without confusion. The possible overlap of release states in the p-V plane is readily taken into account by this method.

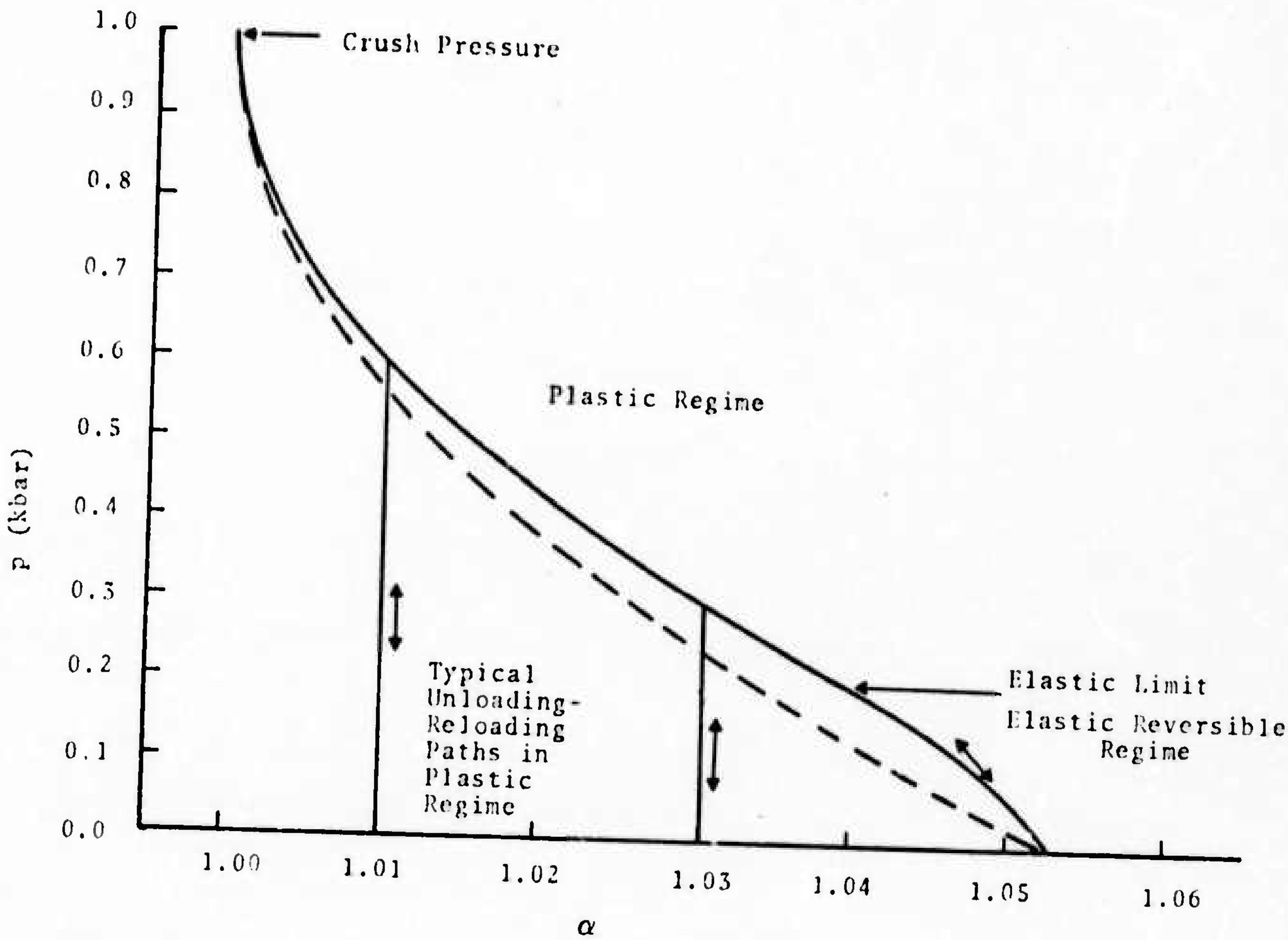

Fig. 2.3--Example of p-α crush curve for a sample of 5% porosity. All pores are completely closed at 1 kbar. Note the smooth transition across the elastic limit (p_e = 0.2 kbar). The dashed curve represents the crush curve without an elastic regime (p_e = 0). The initial slope in the elastic regime was chosen to produce an initial bulk modulus of 20 kbar for the porous mixture (compared to 83.3 kbar for the rock material and 8.9 kbar for the completely plastic curve.

Elastic regimes may not exist for all mixtures and plastic crushing may begin at $p = 0$. In this case, $p_e = 0$, $\alpha_e = \alpha_0$ (the initial porosity), and Eq. (2.16) reduces to

$$\alpha_0 = 1 + \left(\alpha_0 - 1\right)\left(1 - \frac{p}{p_c}\right)^2 \tag{2.17}$$

However, stress wave measurements in porous samples[13] have indicated the presence of some sort of precursor phenomena. It is not clear that one can characterize this as an elastic response or a strain rate effect. Recognizing the potential need for a model of the elastic regime, to be evaluated in other parametric studies, a formulation has been included in the TAMEOS routine.

The elastic regime in the S^3 model is limited by a peak elastic stress level (as shown in Fig. 2.3). Below this value, loading and unloading takes place along the same $\alpha(p)$ curve.

An exponential expression for $\alpha(p)$ in the elastic regime was selected because it afforded the widest choice of parameters to match to sound speed and bulk modulus data while retaining the feature that $\left(\frac{d\alpha}{dp}\right)_{p=0} > \left(\frac{d}{dp}\right)_{p=p_e}$. The distention ratio is given by

$$\alpha = \alpha_0 + \frac{(\alpha - \alpha_e)}{(e^n - 1)}\left(1 - e^{n\,p/p_e}\right) \tag{2.18}$$

$$e^n = \frac{1}{1 - n\kappa} \tag{2.19}$$

where

$$\kappa = \frac{(\alpha - \alpha_e)}{2(\alpha_e - 1)}\left(\frac{p_c}{p_e} - 1\right) < 1 \tag{2.20}$$

This expression is smoothly patched (continuous first derivative) to the plastic form for $\alpha(p)$ at $p = p_e$.

The transcendental relation, Eq. (2.19), determines the acceptable sets of values for α_e and p_e. Should sound speed and bulk modulus data be available for the porous rock matrix, an additional constraint is put on the values of α_e and p_e. As shown in Appendix A, the two elastic crush parameters, α_e and p_e, are related to the sound speed in the matrix at $p = 0$,

$$c^2 = \frac{c_0^2}{\left[1 - \frac{(d\alpha/dp)_0}{\alpha_0^2} K_0\right]} \qquad (2.21)$$

where K_0, is the bulk modulus, c_0 is the sound speed of the poreless material, and $(d\alpha/dp)_0$ is the slope of the crush curve at zero pressure. This slope determines the degree to which sound waves are slowed in porous materials. In a stiff matrix, $d\alpha/dp = 0$, $c = c_0$. The relationship between the sound speed in the porous matrix, and the elastic parameters is obtained by differentiating Eq. (2.18) and substituting into (2.21) to arrive at

$$c^2 = \frac{c_0^2}{\left[1 + \frac{\alpha_e - 1}{p_c - p_e} \cdot \frac{2}{e^n} \frac{K_0}{\alpha^2}\right]} \qquad (2.22)$$

2.3 TABULAR ARRAYS OF MIXTURE EQUATIONS OF STATE

A computer routine has been written to generate tabular arrays of thermodynamic states of rock-water mixtures. The flow chart for this numerical process is given in Fig. 2.4. Briefly, let us consider first how a table is constructed for a saturated rock-water mixture. For given equations of state of the two materials, the PEQ mixture states are determined by the volume fractions of each constituent. Additionally, a set of pressure points in the range of interest and the desired mesh fineness for V and E must be specified. The table generating program then computes the mixture release isentropes from states on the Hugoniot curve. Based on these isentropes, the program calculates p-V-E states for values of V and E which are suitable for the table look-up routine incorporated in TAMEOS. The resulting set of pressure points, along with the information on the V and E meshes, comprises the table for the specified (non-porous) mixture in the given range of pressures. Other states in this region are then computed in TAMEOS by interpolation.

If gas-filled pores are present in a given mixture ($\alpha = \alpha_0 > 1$), then a separate p-V-E table is constructed for each α at specified mesh intervals in the range $[1, \alpha_0]$ For each α there is a unique pressure point on the porous rock Hugoniot given by the solution to

$$E - E_0 = \left[\frac{1}{\alpha} P_1\left(\frac{V_1}{\alpha}, E_1\right) + \frac{1}{\alpha} P_1\left(\frac{V_{10}}{\alpha_0}, E_{10}\right)\right]\left(\frac{V_0 - V}{2}\right) \qquad (2.23)$$

where

$$p = P\left(V_1, E_1\right) \text{, equation of state for poreless rock} \qquad (2.24)$$

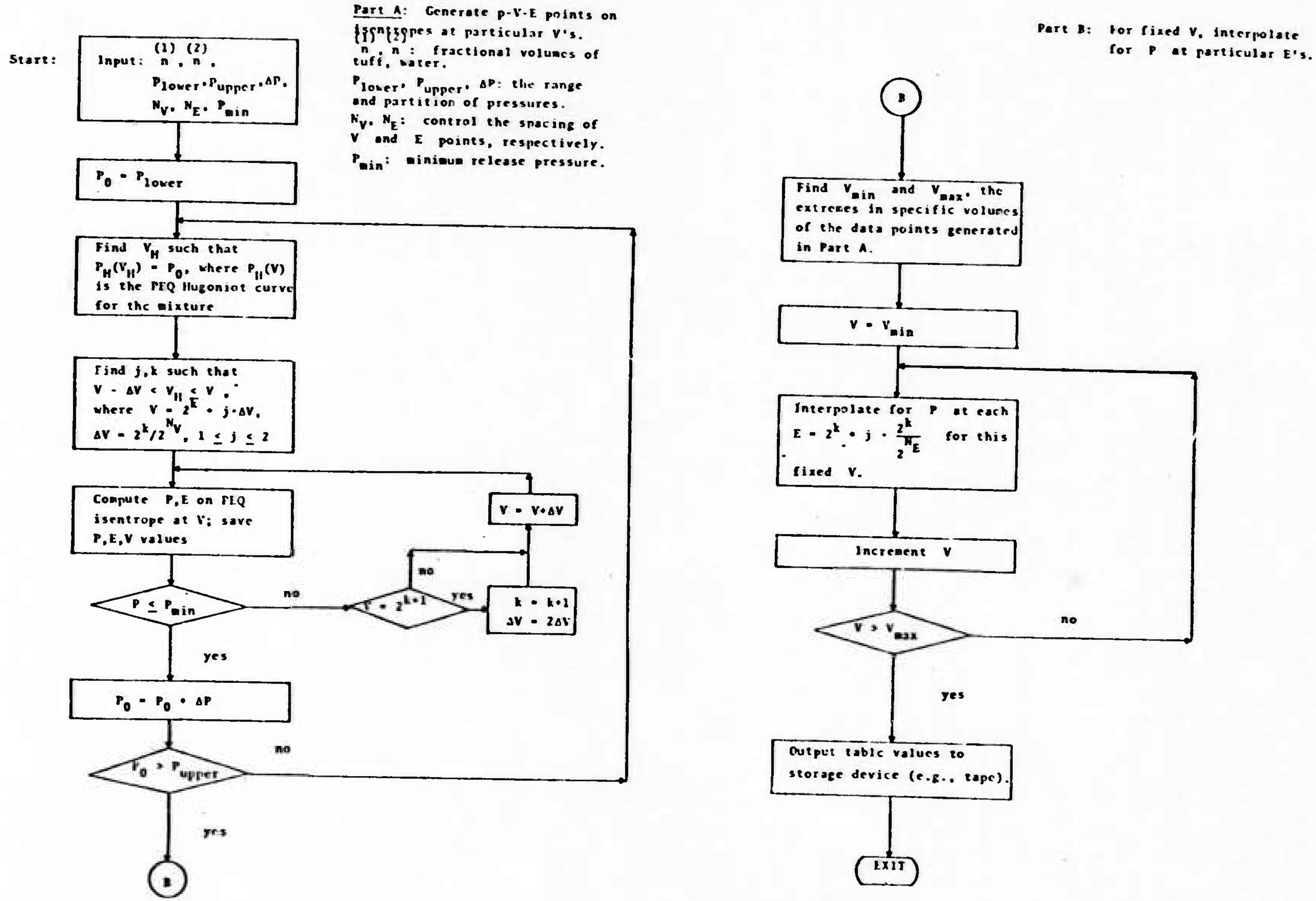

Fig. 2.4--Flow diagram of table generating portion of TAMEOS.

and

$$\left\{\begin{array}{l}\alpha = \alpha(p),\ p < p_c \\ \\ \alpha = 1,\ p \geq p_c\end{array}\right\} \qquad (2.25)$$

There is only one isentrope through the Hugoniot at this point, and to allow room for interpolation in the table, other isentropes are chosen by slightly shifting the specific volume to either side of the Hugoniot point and using the same pressure. A table of p-V-E states is then obtained for each α. To obtain the pressure at a given state α-V-E, the two tables corresponding to the bracketing values of α are used to compute a pair of pressures which are then used to interpolate for p at the given α.

In most situations, the desired pressure range encompasses both porous and compacted material states. Separate tables must then be constructed for the two regions, the value of α determines which of the tables to use.

Table Look-Up

The pressures which comprise a table correspond to values of V, E, and α chosen so that no time consuming search is needed when performing an interpolation at a given state. Briefly, the scheme consists of picking values for the independent variables (V, E, and α) of the form $2^k + j \cdot 2^k/2^n$, where k may be any integer, n any non-negative integer, and $0 \leq j < 2^n$. By varying n one can control the spacing of the grid; k and j determine not only the values but also the indexing of the independent variables. Full advantage is then taken of the binary representation of numbers in the computer to expedite the index calculation as well as the actual interpolation for p. The result is an extremely fast interpolation with a minimal amount of arithmetic.

Application of TAMEOS for Porous Mixtures

In calculations employing TAMEOS a simplification has been introduced for the crush curve, $\alpha(p)$. Experience has demonstrated that to avoid lengthy, time consuming iterations for α in the implicit equation, $\alpha = \alpha\left(\frac{1}{\alpha} P_1\left(\frac{V_1}{\alpha}, E_1\right)\right)$, one may reformulate $\alpha(p)$ as a (fitted) function of V_{mix}, along the Hugoniot, i.e.,

$$\left[\alpha(p)\right]_H = \alpha\left(p_H(V_H)\right) \equiv \alpha_R\left(V_{mix}\right) \tag{2.26}$$

This reformulation actually simplifies the calculation a great deal; given a state (V_{mix}, E_{mix}), the value of α can be quickly determined and TAMEOS furnishes the (interpolated) pressure for p_{mix} at $(\alpha, V_{mix}, E_{mix})$. Of course, checks are required to determine whether a cell is being loaded or undergoing a release process so that α may be computed correctly.

2.4 CHECK OUT CALCULATIONS WITH TAMEOS

A variety of calculations were conducted to verify the projected three-place accuracy of the TAMEOS routine and to gain experience in its application to typical ground motion calculations. In this regard, the retrieval time for a value for p, given E and V, was determined to be comparable to that of typical analytic expressions for equations of state. It is difficult to quantify this difference but it appears that TAMEOS can be utilized as quickly as any single component media equation of state. Of course, storage of the tabular array is required.

2.4.1 Equations of State of Constituents--Water and Tuff

The water equation of state utilized to derive rock/water mixtures equations of state is composed of the original, analytic expressions reported in 3SR-648 and a tabular representation for states with entropies greater than 3.3×10^7 ergs/g °K (corresponding to shock pressures higher than 200 kbar). The tabular portion, compiled by Bjork,[16] is valid up to 10 Mbar in the vicinity of the Hugoniot and treats expansions into the gas phase. In the present calculations, the bulk of the mixture states were of peak pressures below 200 kbar, so that the water equation of state in 3SR-648 describes most of the water states involved in this series.

A new equation of state for poreless tuff has been derived which is based on the Hugoniot curves for saturated Rainier Mesa tuff reported by Shipman, et al.[17] Points on the dry, poreless tuff Hugoniot were obtained from this data by assuming that the tuff is in pressure equilibrium with the water and that the water states are the same as those postulated for the pure water constituent. (Hence, these tuff states are those which satisfy the PEQ mixture

model.) At each pressure,

$$V_{HM}(p) = M_T\ V_{HT}(p) + M_W\ V_{HW}(p) \tag{2.27}$$

where $V_{HM}(p)$ is the specific volume of the saturated mixture at pressure p on the Hugoniot. $V_{HT}(p)$ and $V_{HW}(p)$ are the specific volumes of the tuff and water constituents at the same shock pressure.

It was determined that the NTS tuff representation used in 3SR-648 was not adequate at these higher shock pressures. A series of shock velocity-particle velocity points were computed on the basis of new tuff Hugoniot points extracted from high pressure data. These values did not lie on a straight line but could be fit within the experimental accuracy to the form

$$U = a + bu + du^2 \tag{2.28}$$

where U and u are the shock and particle velocities. This expression implies a pressure-density Hugoniot given by[18,19]

$$p_H(V) = \left(\rho_0 \bar{\eta}\ \bar{\lambda}/2\bar{\mu}\right)\left[1 - \left(1 - 4\bar{\mu}a^2/\bar{\lambda}^2\right)^{1/2}\right] \quad \bar{\eta}b < 1 \tag{2.29}$$

$$p_H(V) = \left(\rho_0 \bar{\eta}\ \bar{\lambda}/2\bar{\mu}\right)\left[1 + \left(1 - 4\bar{\mu}a^2/\bar{\lambda}^2\right)^{1/2}\right] \quad \bar{\eta}b > 1 \tag{2.30}$$

where $\bar{\eta} = \left(1 - V/V_0\right)$ and

$$\bar{\mu} = d^2\bar{\eta}^4 \tag{2.31}$$

$$\bar{\lambda} = (1-b\bar{\eta})^2 - 2ad\bar{\eta}^2 \tag{2.32}$$

The two branches of the Hugoniot curve are discussed fully in Ref. 18 and 19. The coefficients in Eq. (2.28) for dry compacted Rainier Mesa tuff are $a = 3.50$ mm/μsec, $b = 0.7047$, and $c = 0.1005$ (mm/μsec)$^{-1}$. Since in compression $b\bar{\eta} < 1$ the Hugoniot for this tuff will always be represented by Eq. (2.27)

The Hugoniot curves are used as the basis of a p-V-E equation of state for poreless tuff similar to that adapted by Butkovich,[20] i.e., a Mie-Gruneisen equation of state with the Gruneisen ratio proportional to specific volume. This is written

$$p = G_0\rho_0 E + p_H(V)\left[1 - \frac{G_0\rho_0}{2}\left(V_0 - V\right)\right] \tag{2.33}$$

where $G_0\rho_0$ is the product of the Gruneisen ratio and density at normal conditions. It was determined that

$$G_0\rho_0 = 0.732 \text{ g/cm}^3 \tag{2.34}$$

provided the best fit to release data. The solid, grain density, ρ_0, was assumed to be 2.22 g/cm³.

2.4.2 Check-out Calculations--Planar SKIPPER

As a test case, the initial volume fractions were selected to simulate a partially saturated tuff/water mixture;

$n_0^{(1)} = 0.70$, tuff

$n_0^{(2)} = 0.23$, water

$n_0^{(3)} = 0.07$, void.

The initial distension ratio in the tuff, α, is 1.1 and crush pressure was set at p_c = 5 kbar. It was assumed that the mixture had no strength and an elastic crush regime was not included $\alpha_e = \alpha_0$, p_e = 0, so that α is given by Eq. (2.17)

Figure 2.5 is a plot of the pressure-volume states calculated with the planar SKIPPER code for a step-pulse of p_H = 4 kbar followed by a release wave. The curves in Fig. 2.5 represent theoretical PEQ Hugoniot and release curves. For the crushup wave, the computed p-V-states are indicated by the squares, and the release states are represented by circles. The loading p-V states calculated in SKIPPER are seen to lie close to the PEQ Hugoniot. Release states follow an α = constant locus of states as evidenced by the calculated points for the 4-kbar release wave.

Figure 2.6 shows a similar calculation for a 145-kbar step pulse (complete crushing). It is evident that the low pressure $(p < p_c)$ crushing occurs very close to the PEQ Hugoniot p-V trace, while the higher pressure loading p-V states lie to the right of the Hugoniot as a consequence of the extra internal energy contributed by the q-term. The q-term insures that loading is along the Rayleigh line in order that the shock heat at p_H is correct. The computed release states are indeed seen to be in excellent agreement with the theoretical PEQ release adiabat.

2.4.3 Check-out Calculations--Spherical SKIPPER

The parametric study to investigate porosity effects on wave propagation in tuff was conducted with the spherical SKIPPER code. These calculations are discussed in detail in the next section. As a check on the accuracy of TAMEOS, a table for 20% porous dry tuff $\left(n^{(1)} = 0.80,\ n^{(2)} = 0.00,\ n^{(3)} = 0.20\right)$ was generated and utilized in an identical calculation to that made with the analytical equation of state.

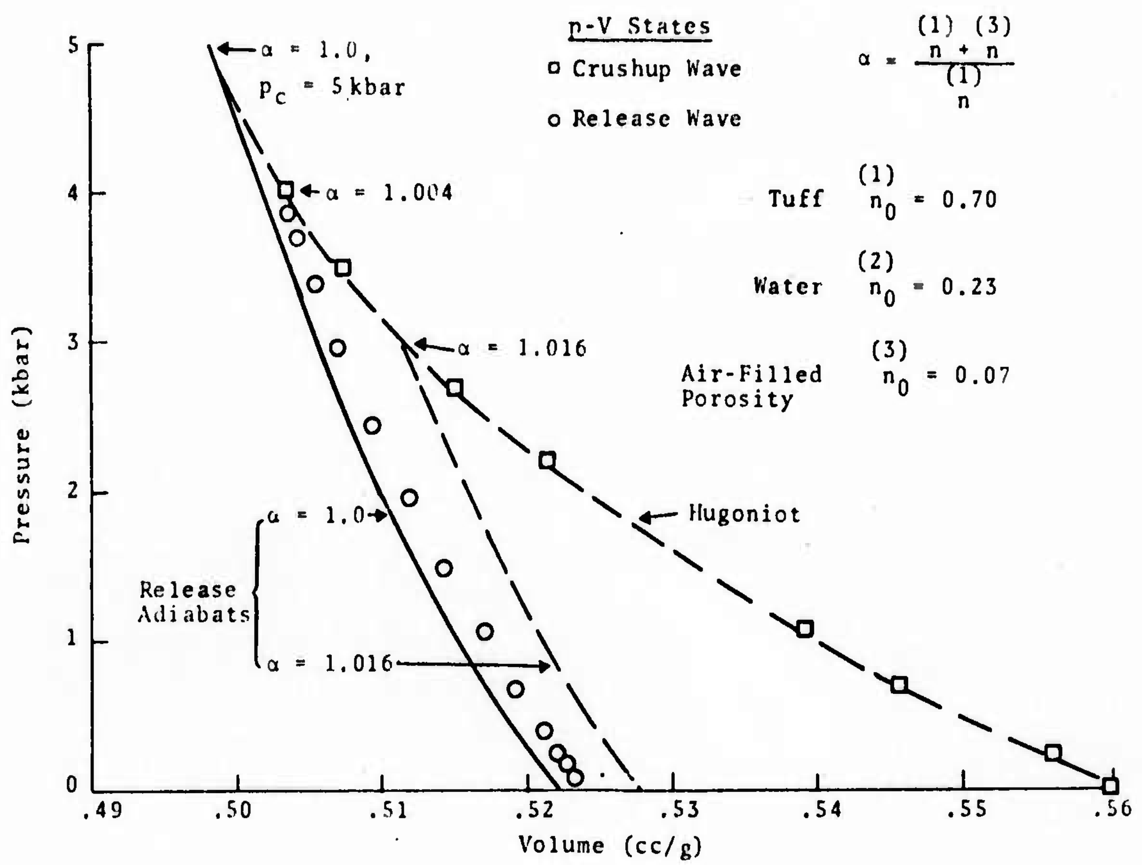

Fig. 2.5--Pressure-volume states taken from a (planar) SKIPPER code check-out calculation using the TAMEOS routine in the plastic crush regime. In this example a tuff/water mixture table was generated and used in place of an analytic equation of state.

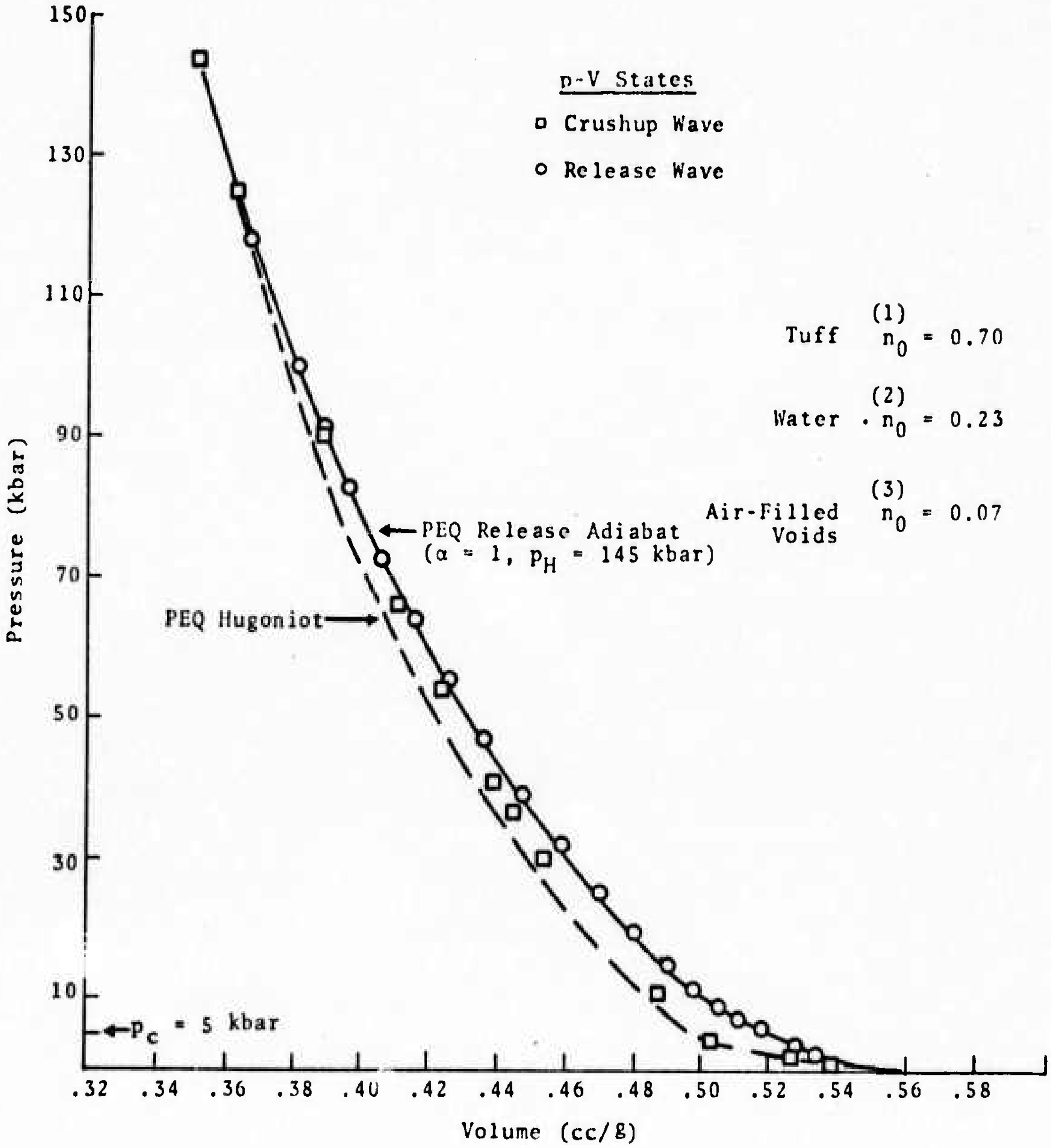

Fig. 2.6--Pressure-volume states taken from a (planar) SKIPPER code check-out calculation using TAMEOS in the completely crushed region ($p > p_c$). The shock state computed with TAMEOS was accurate to three places in this example.

(The crushup parameters were also the same.) Figure 2.7 is a comparison of the stress wave profile computed with the analytic and tabular equations of state after 500 cycles. The two results are almost identical and well within the projected three-place accuracy of the table.

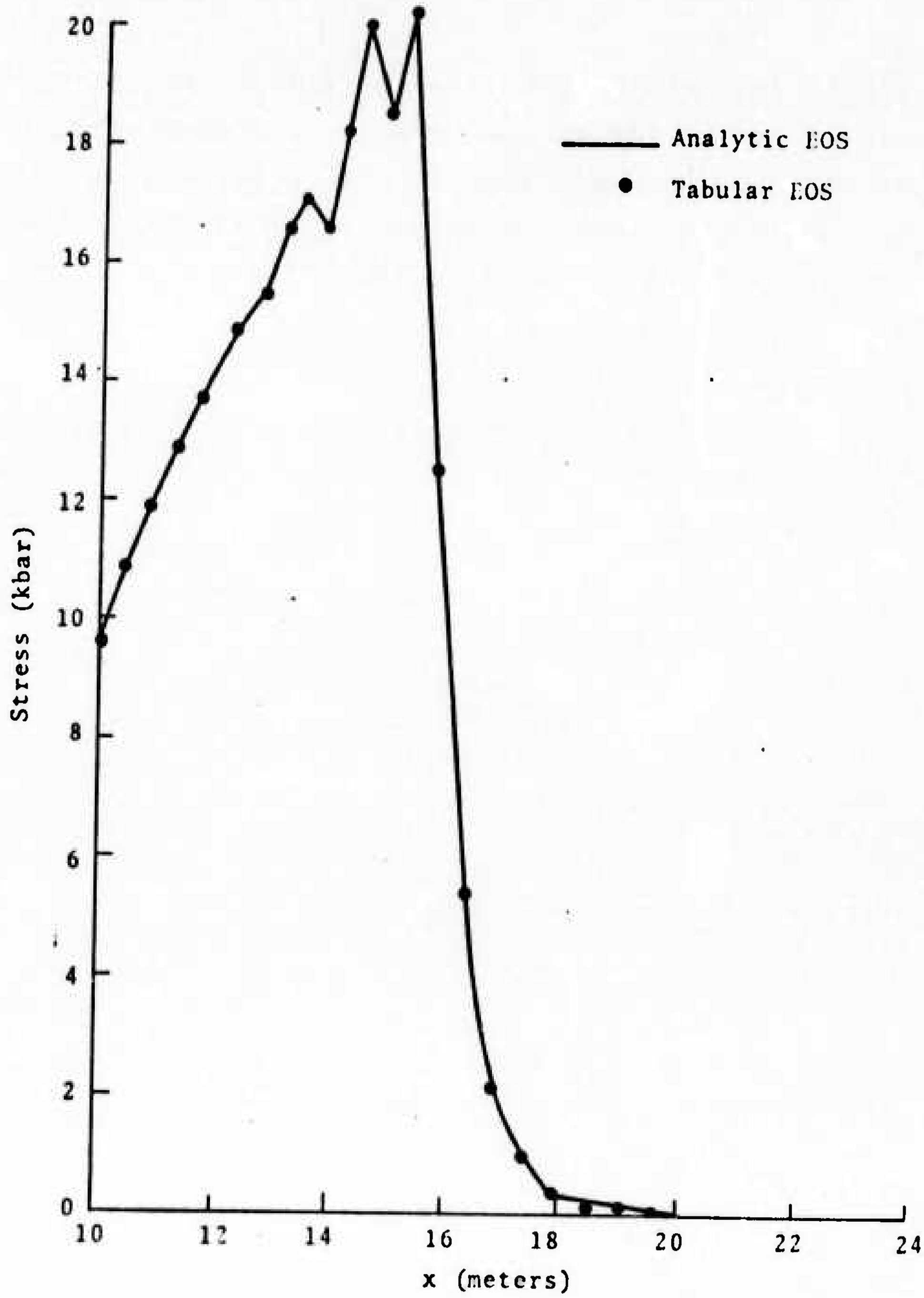

Fig. 2.7--Comparison of the radial stress profiles calculated with the analytic tuff equation of state (Eq. 2.33) and the tabular array of states for a 20% porous tuff media with no water present in the pores. The time is 3.45 msec after simulated detonation of an 8-kT source as computed with the SKIPPER code.

2.5 PARAMETRIC STUDIES OF TUFF/WATER MIXTURES

A series of spherically symmetric one-dimensional shock wave propagation problems in tuff/water mixtures were conducted using the S^3 SKIPPER Lagrangian finite difference code. These calculations were made to evaluate the effects of partial and full saturation of the tuff matrix on the ground motion associated with an underground detonation of 8 kT yield. They also demonstrate the utility of the TAMEOS routine in studies of this kind.

For this series, the spherical SKIPPER grid was divided into 400 zones with a maximum radius of 497.7 m. Thickness of the first zone was 50 cm. The calculations were carried out to times of 24 msec. In this time period, the peak stress varied from an initial value of 621 kbar down to less than 1 kbar.

Two choices for total pore volume fraction $\left(\text{i.e., } n^{(2)} + n^{(3)}\right)$ were evaluated, one with a total porosity of 20 percent and the other with a total porosity of 5 percent. Water content was varied so that the air-filled voids accounted for 100%, 50%, and 0% of the total pore volume. The mixture equations of state were derived from the tuff and water equations of state described in Section 2.4.1. TAMEOS was utilized to compute, store, and retrieve the mixture states.

The plastic crush pressure was set at p_c = 20 kbar. Elastic crushing was not considered ($\alpha_e = \alpha_0$, $p_e = 0$). The deviatoric response of the mixtures was modeled by the simple von Mises condition with a constant shear yield strength of Y_0 = 1.0 kbar and a rigidity modulus set at μ = 45 kbar:

$$S_1^2 + S_2^2 + S_3^2 \leq \frac{2}{3} Y_0^2 \qquad (2.35)$$

where $\sigma_i = -p + S_i$ expresses the total principal stress in terms of the pressure and deviatoric stress.

2.5.1 Source

The energy source in these tuff/water calculations consists of a spherical cavity which contains a gas obeying the ideal gas equation of state

$$E = \frac{pV}{\gamma - 1} \tag{2.36}$$

A value of $\gamma = 1.4$, corresponding to diatomic gas, was utilized.

Initially, the radius of the cavity is 3.72 meters and the internal energy of the gas is 33.5×10^{19} ergs/g, an amount of energy equivalent to the yield of 8 kT of high explosive. The flow within the cavity is not calculated. Rather, it is assumed that the pressure within the gas, and thus the stress acting on the cavity wall, is uniform during each time step in the calculation. Moreover, the gas is assumed to undergo an isentropic expansion (or compression) i.e.,

$$p(t) = p_0 \left(\frac{R_0}{R(t)} \right)^{3\gamma} \tag{2.37}$$

where $p(t)$ and $R(t)$ are the cavity pressure and radius, respectively. The initial value of 3.72 m for R_0 was selected because it approximately represents the volume of rock vaporized by an energy release of 8-kT of explosive. Initial pressure, p_0, was 621 kbar.

2.5.2 Peak Radial Stress

The variation of peak radial stress with distance from the cavity center is shown plotted for the 5% porous tuff calculations in Fig. 2.8. The 20% porosity cases are given in Fig. 2.9.

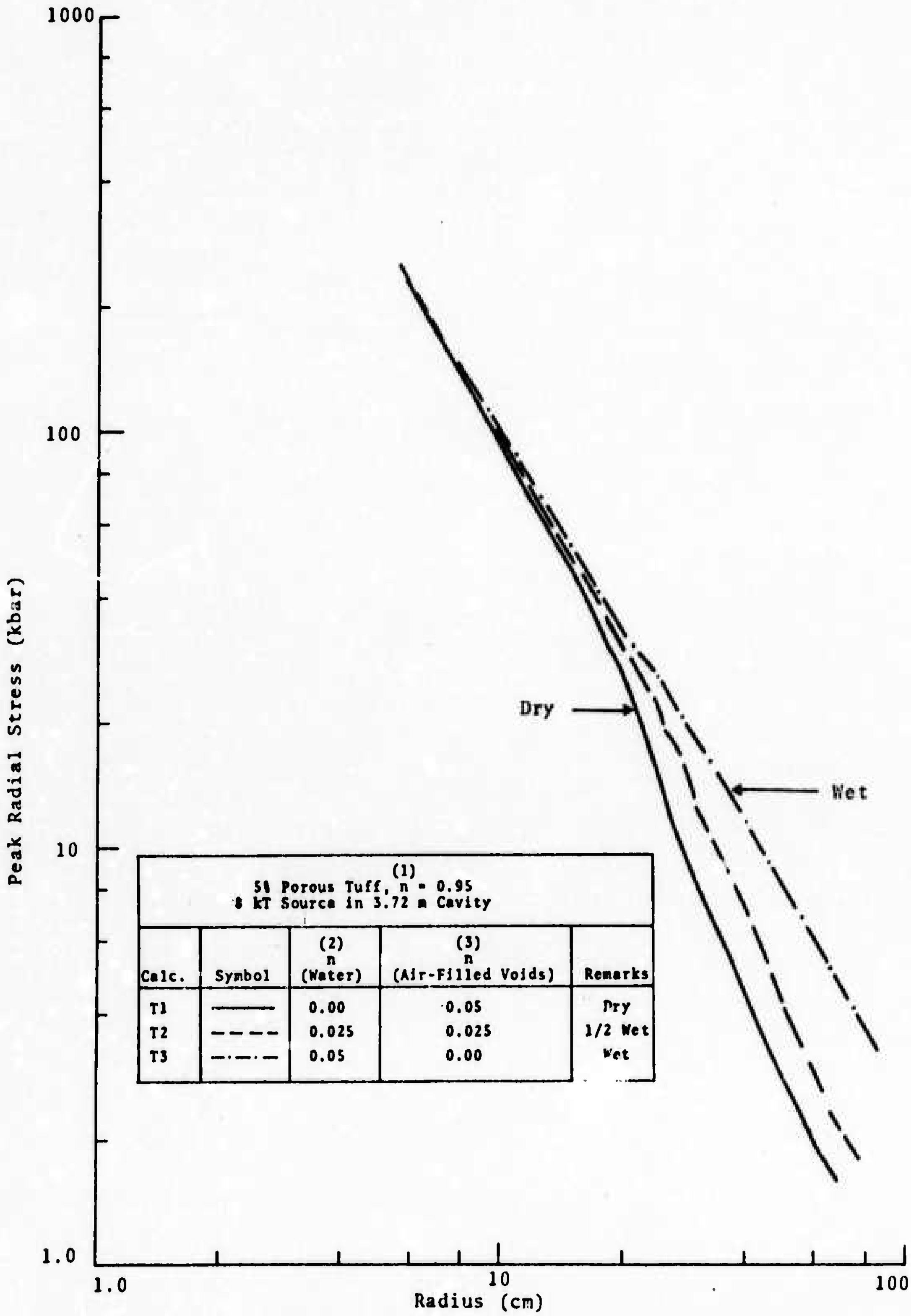

Fig. 2.8--Peak radial stress decay vs distance from source (8 kT) for 5% porous tuff, three degrees of water saturation.

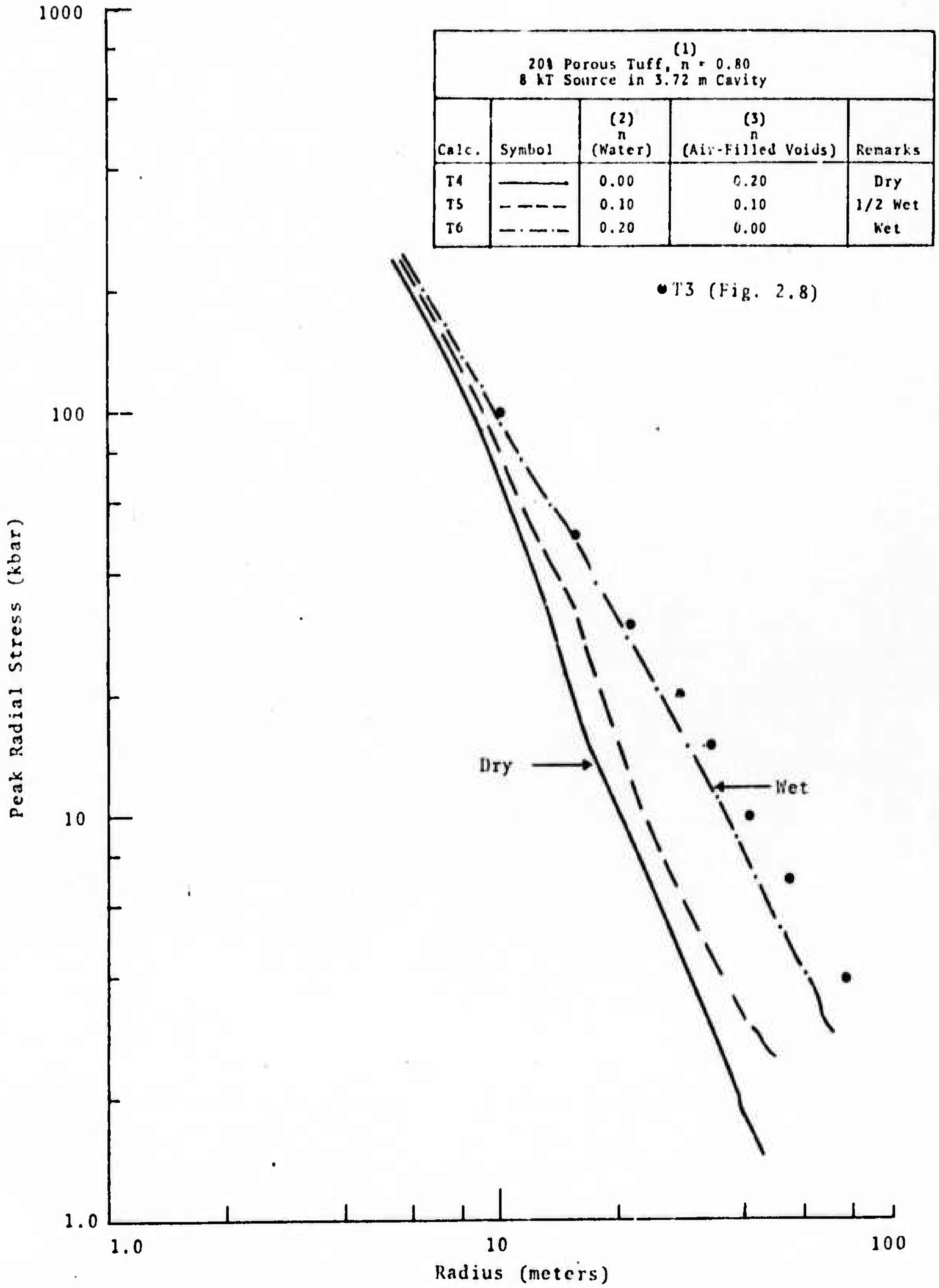

Fig. 2.9--Peak radial stress decay with distance from source (8 kT) for 20% porous tuff, three degrees of water saturation. Also shown are points for fully saturated 5% porous tuff (from Fig. 2.8).

At close-in radii, the partially and fully saturated matrices undergo slightly higher stress levels than the dry matrices. As the initial wave propagates out to larger radii, and the stress falls below $p_c = 20$ kbar, the partially saturated matrix peak stress levels are closer to those of the dry porous matrix than to those in the saturated material.

Most significant, peak stresses in the fully saturated mixtures are very close to one another despite the big difference in porosity. Note that values from the peak stress curve for the fully saturated, 5% porous tuff have been plotted in Fig. 2.9, and are very close to the 20%, fully saturated case.

It is clear from these results that porosity effects are most pronounced when the degree of water saturation is reduced. The radial stress wave is more retarded by the energy absorption associated with the air-filled voids than with the presence of water. In the 20% porous tuff, this results in about a 25-kbar reduction in the peak stress for the dry matrix within 8 meters of the cavity center. At larger distances, the partially saturated and dry matrices exhibit stress levels relatively far below the fully saturated material. (Roughly speaking, the peak stress is reduced by about 70 percent between 30 and 10 kbar.)

One may conclude, therefore, that the volume fraction of air-filled pores is the most influential parameter on the peak stress levels. The half-saturated media responds half-way between that of the saturated and dry media at high stress levels, $p > p_c$, but veers closer to that of the dry material at the lower stress levels.

2.5.3 Cavity Growth

The cavity radius as a function of time in each calculation is presented in Figs. 2.10 and 2.11. In this time period, the cavities grew monotonically. For each of the two tuff

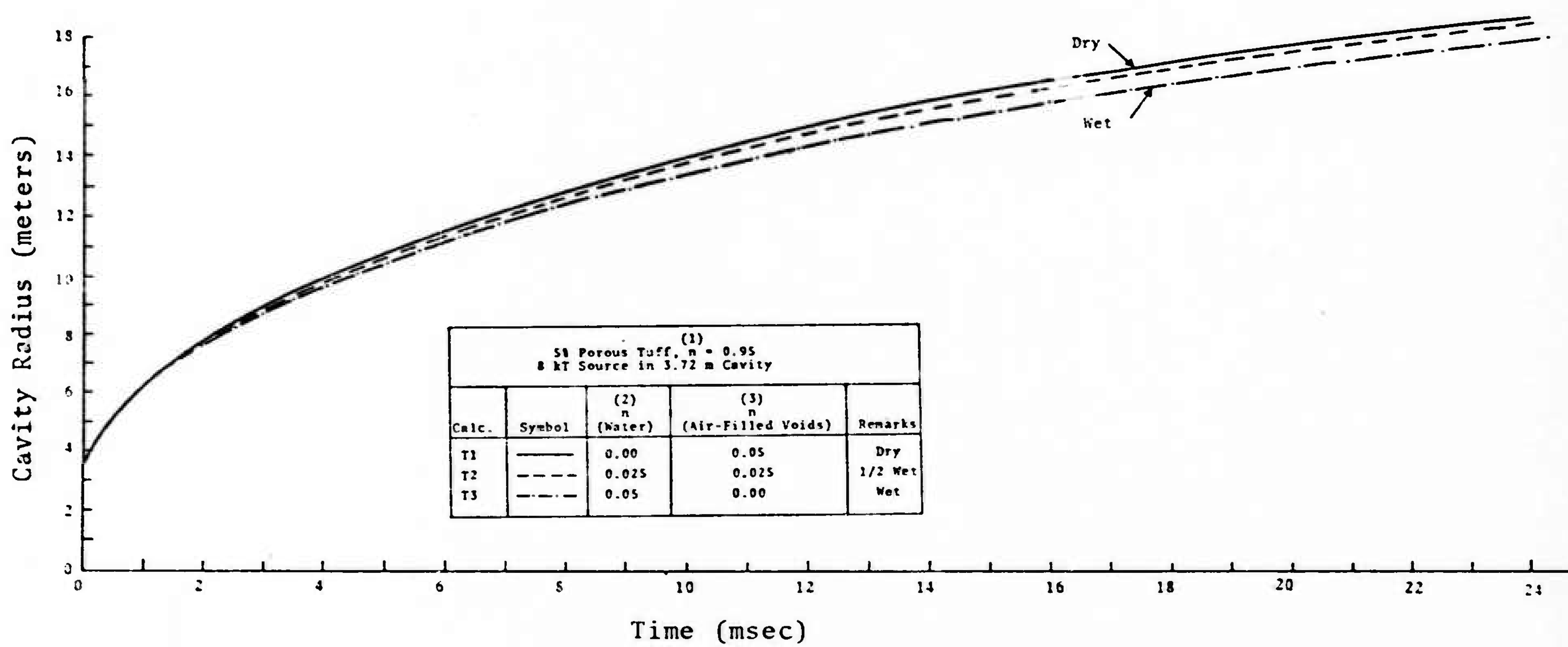

Fig. 2.10--Cavity radius as a function of time following an 8-kT explosion in 5% porous tuff. Three degrees of water saturation of 5% porous tuff are considered. The cavity radius is originally 3.72 m.

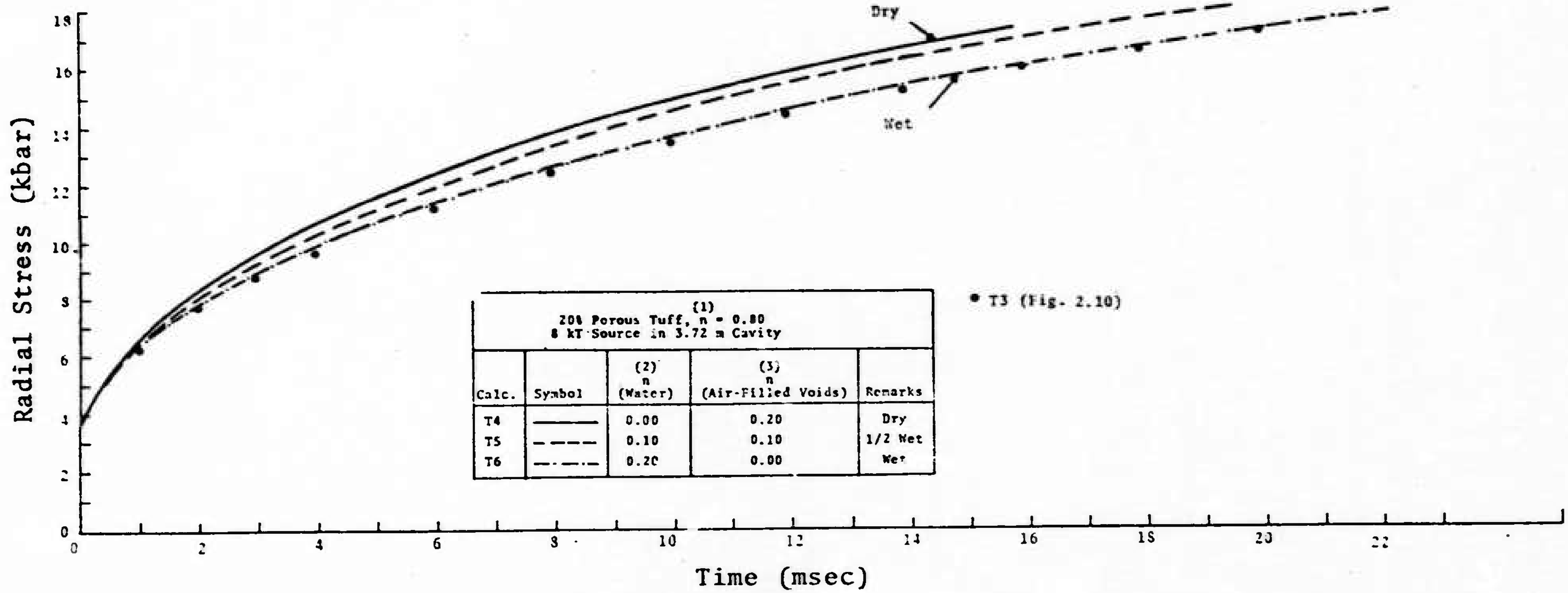

Fig. 2.11--Cavity radius as a function of time following an 8-kT explosion in 20% porous tuff. Three degrees of water saturation are considered. The fully saturated, 5% porous tuff cavity is also plotted (taken from Fig. 2.10).

porosity values, cavity growth was maximum for the completely dry matrix and minimum for the saturated tuff. Approximately 5 percent bigger cavity radius was produced in the 5% porous tuff (Fig. 2.10), while a 10% larger cavity (radii) were observed for the 20% porous tuff matrices (Fig. 2.11).

These results are to be expected since the higher percentage of air-filled voids leads to greater crushing of the matrix at the high stress levels. One could anticipate a non-linear relation between relative cavity wall displacement and porosity due to spherical geometry effects.

Once again it may be observed that the single most important parameter is $\overset{(3)}{n}$, the volume fraction of air-filled voids. The cavity radius for the saturated 5% porous tuff media is plotted for comparison to the 20% porous result in Fig. 2.11. There is very little difference between these two curves and it is insignificant in comparison to the effect due to increases in the void content of the media.

2.5.4 Stress vs Time Profile at R = 40 m

It is at radial distances much greater than the cavity radius that the largest relative differences occur in the stress-time histories of the various matrices. Fig. 2.12 is a plot of radial stress as a function of time at the 40-m station for the 5% porous tuff matrix. The stress levels at this location were below the crush pressure of p = 20 kbar, hence the crush process is incomplete in all cases.

The stress wave in the fully saturated mixture travels quicker and reaches the 40 m location 0.7 msec prior to the crush wave associated with the two matrices with voids. Apparently, the low degree of porosity leads to insignificant differences in shock arrival time for the latter two examples.

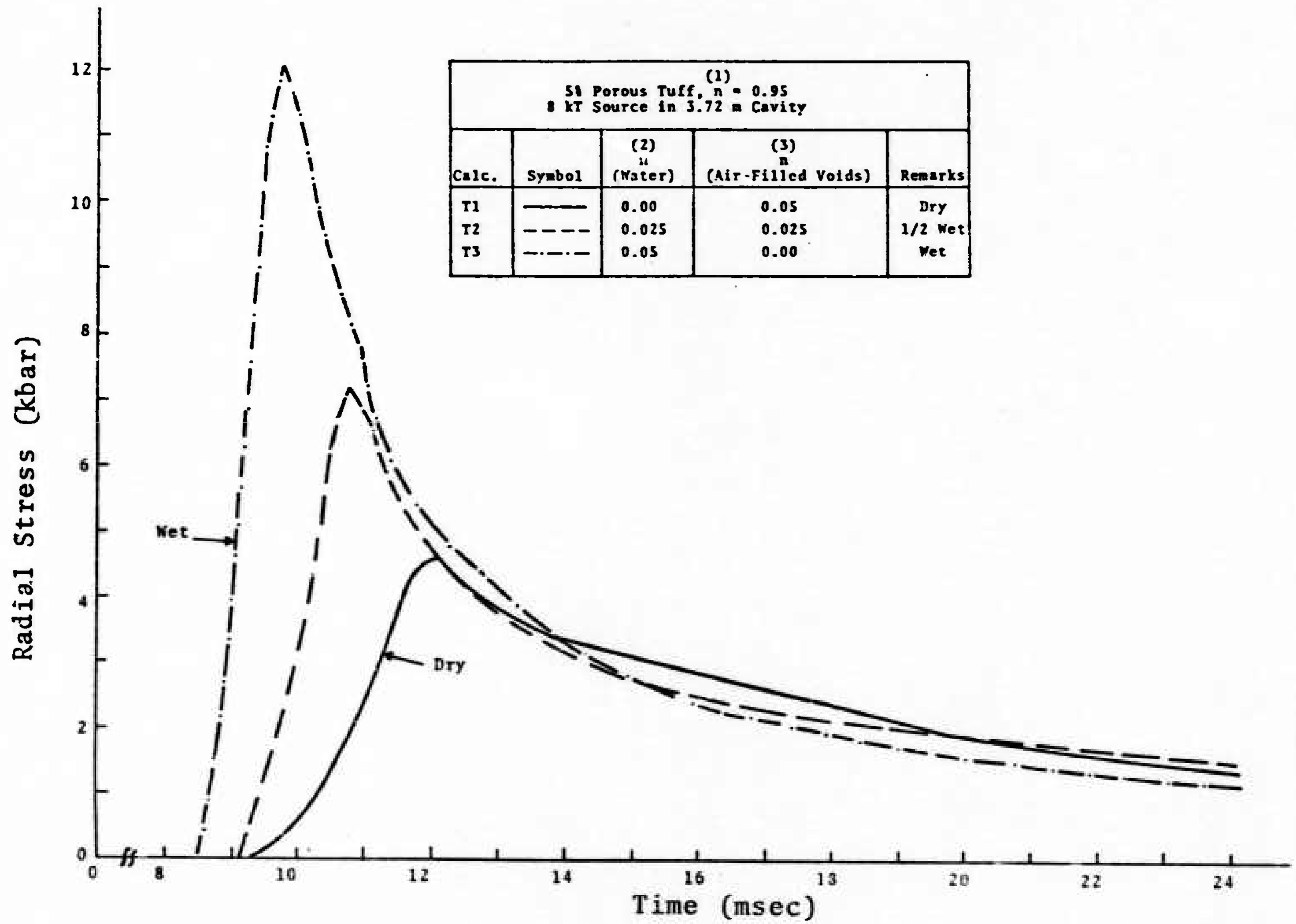

Fig. 2.12--Radial stress time histories in zone originally at R = 40 m for 5% porous tuff; three degrees of water saturation.

Clearly, the effects of increased void content are evident in the reduced peak stress and slower rise times of the stress wave. Interestingly, after the first 4 msec following wave arrival in the saturated media, it is difficult to discern significant differences in the stress levels of the three different matrices.

In Fig. 2.13 is the analogous stress time history plot for the higher porosity tuff matrix calculations. The effects noted for the 5% porous case are more evident for a 20% porosity. The wave is more effectively attenuated by the matrices with voids, especially the totally dry case. Once again, beyond a certain time (19 msec), it is difficult to differentiate between the three media during the unloading process.

From these results, it appears that radial stress attenuation and rise times to the peak during the loading process are extremely sensitive to the volume fraction of gas-filled pores. The shape of the release curve from the peak stress, however, is quite insensitive. It should also be noted that the fully saturated media exhibit similar stress-time histories (see Fig. 2.13). Air-filled porosity accounts for the major differences in the shape of the stress-time profiles.

2.5.5 Ground Motion of Media at R = 40 m

The attenuated stress waves associated with less saturated media lead to much smaller radial displacements. This is portrayed in the radial displacement curves in Figs. 2.14 and 2.15. Note that the two saturated materials exhibit almost identical displacement histories (see Fig. 2.15). This corroborates the main conclusion that differences in water content do not radically affect ground motion characteristics when the tuff is fully saturated. Air-filled

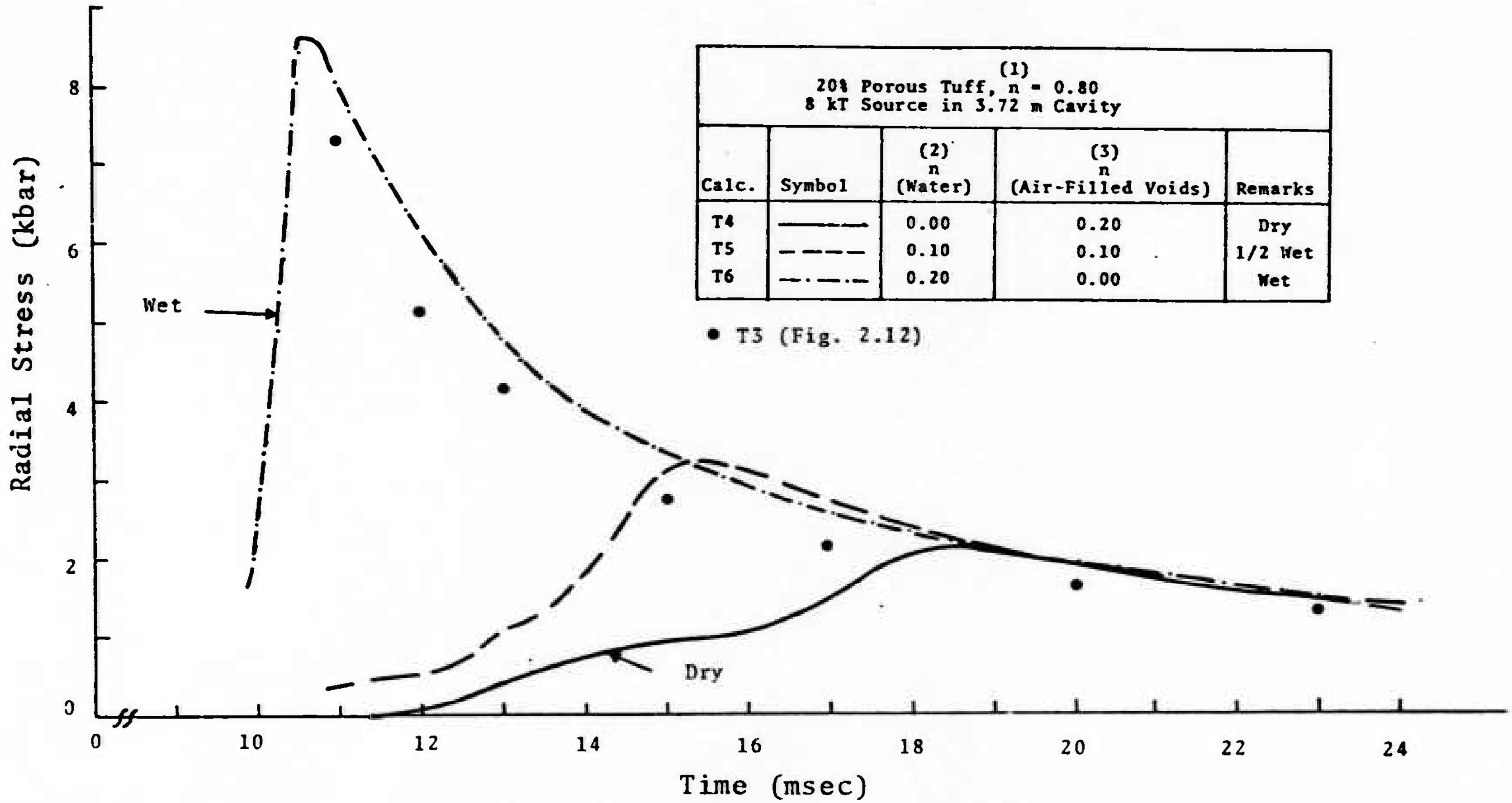

Fig. 2.13--Radial stress time histories in zone originally at R = 40 m for 20% porous tuff; three degrees of water saturation. (Also shown are stress-time points for fully saturated, 5% porous tuff.)

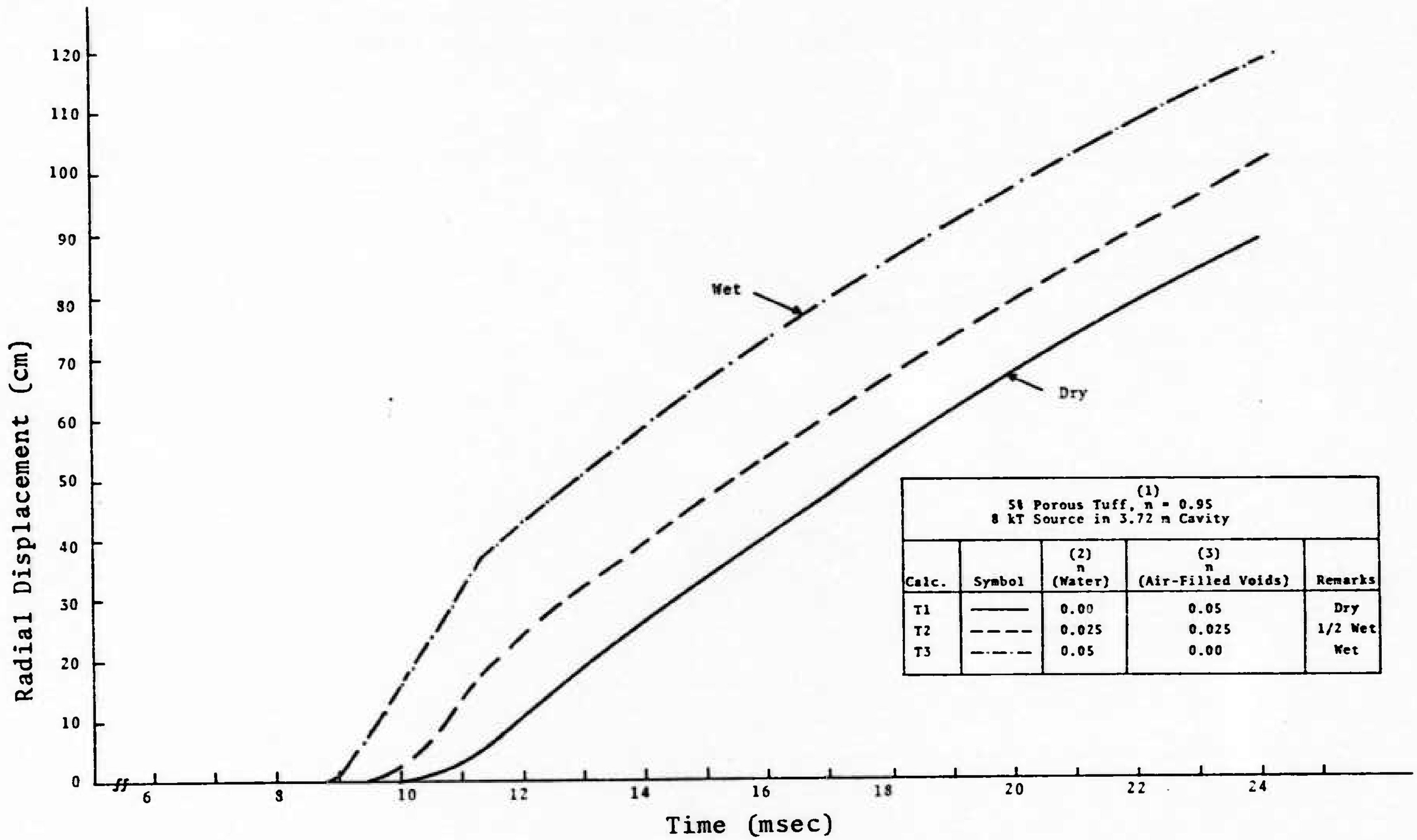

Fig. 2.14--Radial displacement of zone originally located at R = 40 m for 5% porous tuff; three degrees of water saturation.

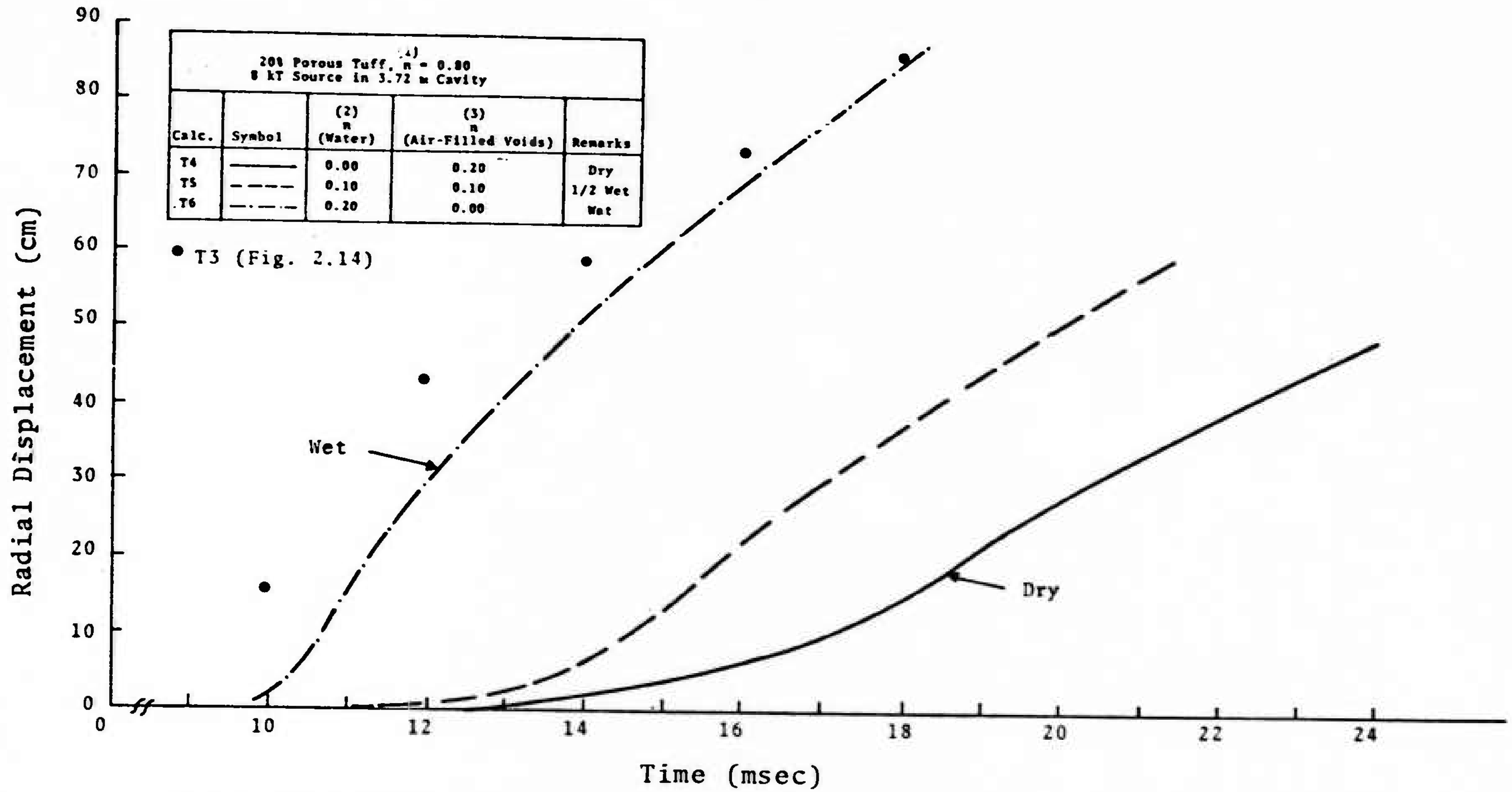

Fig. 2.15--Radial displacement of zone originally located at R = 40m for 20% porous tuff; three degrees of water saturation. Also shown are displacements for fully saturated 15% porous mixture (from Fig. 2.14).

porosity, however, does dramatically alter the stress wave propagation characteristics of tuff and should be carefully modeled in ground motion calculations. In Appendix B the effect of air-filled porosity is studied for a high-explosive energy source buried in tuff. This effect has also been recently studied by Bjork[21] and Anderson.[22,23]

III. IMPROVED PREDICTIVE METHODS FOR GRANITE

3.1 INTRODUCTION

A single constitutive theory that combines the high pressure equation of state for rock with a flow law which is valid at low pressures and high strains is described in this section. It has led to a computational scheme suitable for calculating spherical explosion phenomena in both the near and far field. The theoretical background for this development, described in detail in a topical report by Dienes,[24] is summarized in Sections 3.2 and 3.4. Section 3.2 presents a theory of finite strain suitable for describing large distortions of porous materials. Section 3.3 lists the equations of motion. Section 3.4 includes several alternative models for determining the flow stress in rock masses, and a description of the high pressure equation of state used. Also included is an approach to estimating strain rate and temperature effects. The important considerations made in incorporating the theory into the SKIPPER code are described in Section 3.5. Available ground motion measurements for underground shots in granite are reviewed in Section 3.6. The results of several calculations are presented and then compared with the underground shot data in Section 3.7. By adjustment of the flow stress it was found possible to calculate a cavity of the correct size and, for one of the flow models studied, the resulting displacement histories are in good agreement with measurements. Specifically, the kinematic hardening rule, which models anisotropic hardening, leads to a realistic calculation of shot data. The "cap" model, which assumes isotropic hardening, results in a computed behavior which does not exhibit the observed overshoot in displacement, and shows too rapid an attenuation of the shock. Kinematic hardening results in lower hysteresis and slower

relief waves than isotropic hardening, and these effects appear to be sufficient to bring the calculated results into better agreement with measurements. In Section 3.8 the results of seven calculations are presented to illustrate the sensitivity of ground motion to granite material parameters and plasticity models. Finally, Section 3.9 discusses the state of the research to date and its relation to other approaches.

3.2 FINITE DEFORMATION THEORY

Definitions of strain can be obtained in a variety of ways. For small deformations, they are generally equivalent, but there may be substantial differences at large distortions, and it is important in explosion work to select a definition which will lead to credible solutions for arbitrarily large motions. Such a definition is obtained if rate of strain is defined as the symmetric part of the velocity gradient, which in tensor notation is expressed as

$$D_{ij} = \frac{1}{2}\left(u_{i,j} + u_{j,i}\right) \tag{3.1}$$

where u_i denotes the ith component of the velocity vector and $u_{i,j}$ its spatial derivative with respect to the coordinate x_j. An equivalent definition involves representing the velocity gradient as the sum of symmetric and antisymmetric parts,

$$u_{i,j} = D_{ij} + W_{ij} \tag{3.2}$$

where W_{ij} is the spin tensor. Its components have the same magnitude as those of the vorticity vector. The tensor, $\underset{\sim}{D}$, whose components are D_{ij} has also been termed the rate of deformation tensor[25] and the stretching.[26]

In spherical symmetry, the case of current interest, the velocity gradient can be written

$$\underset{\sim}{D} = \begin{pmatrix} \frac{\partial v}{\partial r} & 0 & 0 \\ 0 & \frac{v}{r} & 0 \\ 0 & 0 & \frac{v}{r} \end{pmatrix} \tag{3.3}$$

where v is the radial velocity. To obtain explicit expressions for the strain, we may adopt the Lagrangian description of the deformation, thereby following particle paths. Then the previous equation reduces to

$$D_{11} = \frac{\partial \dot{r}}{\partial r}, \qquad D_{22} = \frac{\dot{r}}{r}, \tag{3.4}$$

where $r(r_0,t)$ is the radius of a particle initially at r_0. If the definition of strain for spherically symmetric flow is taken to be

$$\varepsilon_{11} = \ell n \frac{\partial r}{\partial r_0}, \qquad \varepsilon_{22} = \ell n \frac{r}{r_0} \tag{3.5}$$

it can be readily shown that the relation

$$\dot{\varepsilon}_{ij} = D_{ij} \tag{3.6}$$

between strain rate and the stretching is satisfied. This equation is not satisfied in alternative treatments of finite deformation plasticity. For example, in the approach followed by Clifton[27] the principal strains $\bar{\varepsilon}_i$ are defined by

$$\bar{\varepsilon}_i = \bar{U}_i - 1$$

where the $\bar{U}_i$ are the principal values of the stretch tensor. In view of the kinematic identity

$$\underset{\sim}{D} = \frac{1}{2} \underset{\sim}{R}\left(\dot{\underset{\sim}{U}}\, \underset{\sim}{U}^{-1} + \underset{\sim}{U}^{-1}\, \dot{\underset{\sim}{U}}\right)\underset{\sim}{R}^T \tag{3.7}$$

given by Truesdell in Ref. 26, the linear definition of strain given above is not consistent with Eq. (3.7). [In flows without rotation, the rotation matrix $\underset{\sim}{R}$ reduces to the identity matrix. This is, of course, the case for the spherical flows of interest here.]

Although in spherical flows materials may undergo large shears, there is no rotation of the elements. This makes it possible to separate the deformation into an elastic and a plastic part in a simple way. In view of the symmetry, the stretch tensor has the simple written form

$$\underset{\sim}{U} = \begin{pmatrix} \lambda_1 & 0 & 0 \\ 0 & \lambda_2 & 0 \\ 0 & 0 & \lambda_2 \end{pmatrix} \tag{3.8}$$

In Ref. 24 it is shown that

$$\lambda_1 = \frac{\partial r}{\partial r_0} , \qquad \lambda_2 = \lambda_3 = \frac{r}{r_0} . \tag{3.9}$$

As is common in plasticity, it is assumed that the strain can be represented as the sum of an elastic and a plastic part

$$\bar{\varepsilon}_i = \bar{\varepsilon}_i^e + \bar{\varepsilon}_i^p . \tag{3.10}$$

Expressing the elastic and plastic parts of the strain as logarithms of the corresponding stretches,

$$\bar{\varepsilon}_i^e = \ell n \, \lambda_i^e \tag{3.11}$$

$$\bar{\varepsilon}_i^p = \ell n \, \lambda_i^p \tag{3.12}$$

we find

$$\lambda_i = \lambda_i^e \, \lambda_i^p . \tag{3.13}$$

It is shown in Ref. 24 that the rate of change of compression, $\dot{\theta}$, can be expressed in the form

$$\dot{\theta} = \dot{\rho}/\rho = -\left(\dot{\bar{\varepsilon}}_1 + \dot{\bar{\varepsilon}}_2 + \dot{\bar{\varepsilon}}_3\right) . \tag{3.14}$$

Consequently, the compression can be expressed as the sum of an elastic and a plastic part, as are the individual strains, so that

$$\theta^e = -\ln\left(\lambda_1^e \lambda_2^e \lambda_3^e\right) , \tag{3.15}$$

$$\theta^p = -\ln\left(\lambda_1^p \lambda_2^p \lambda_3^p\right) . \tag{3.16}$$

The plastic part of the deformation of a compact material does not normally involve a volume change. Here we will consider the matrix of a porous material as compact, and as a result the plastic part of the compression can be interpreted as the change in void volume. The void fraction is defined as the volume of voids per unit volume of material, and can be expressed in terms of the plastic stretches by

$$f = \frac{V - V^e}{V} = 1 - \frac{\rho_0}{\rho_0^m \lambda_1^p \lambda_2^p \lambda_3^p} \tag{3.17}$$

where ρ_0 is the initial density of the porous material and ρ_0^m is the initial density of the matrix portion of the porous material.

3.3 EQUATIONS OF MOTION

For the case of point symmetry, which is appropriate for spherical explosions, the equations of motion are well known. They are given, for example, by Wilkins[28] or in Ref. 24 . The equation of mass conservation discussed in the previous section is equivalent to the rate form

$$\frac{\dot{\rho}}{\rho} = \frac{2v}{r} + \frac{\partial v}{\partial r} \tag{3.18}$$

given by Wilkins in which v is the radial velocity. The momentum equation is

$$\rho\dot{v} = \frac{\partial \sigma}{\partial r} + 2\,\frac{\sigma_r - \sigma_\theta}{r} \tag{3.19}$$

and the energy equation is

$$\rho\dot{E} = \sigma_r \frac{\partial v}{\partial r} + 2\sigma_\theta \frac{v}{r} \tag{3.20}$$

which is equivalent to the first law of thermodynamics.

3.4 CONSTITUTIVE EQUATIONS FOR STRAIN HARDENING MATERIALS

In spite of much experience with geologic materials, the formulation of a general theory suitable for determining the response of rock or soil to an arbitrary load has received intensive study only recently. The problem is more complex than for metals, in which plastic flow takes place at nearly constant shear stress. In rocks and soils the shear strength varies dramatically with mean stress, and the presence of voids, cracks, faults and pore water further complicates the material description. The approach taken in this research was to modify plasticity theory to account for these complications as they are required. In many respects the theory is conceptually more elaborate than is customary in rock mechanics. The reason for this is that finite strain and high energy effects are accounted for, as well as compaction and dilatancy. These effects are believed to be of great importance in calculating the consequences of underground nuclear explosions.

The approach to deriving a sufficiently general constitutive relation to account for all these effects draws on the thermodynamic equation of state for the high pressure behavior and on rock mechanics for the response at low pressure. Several theories for the hardening behavior of rocks were studied as alternative approaches. These theories have in common that they provide an equation for the yield surface which depends on the history of the deformation. In all cases the flow law of von Mises was used in connection with the equation for the yield surface to arrive at a constitutive relation. This relation is completed by using the constraint on the stresses that they must lie either on the yield surface or in its interior.

3.4.1 Equation of State

In the condensed region it is assumed that the equation of state has a form similar to that given by Allen[29] for geologic materials, which expresses the pressure as

$$p = F(E,\rho) = GE\rho + f(\rho) \qquad (3.21)$$

where ρ designates the matrix density, E designates the specific internal energy and

$$G = a + \frac{b}{\frac{E}{E_0 \eta^2} + 1} , \qquad \eta = \frac{\rho}{\rho_0} . \qquad (3.22)$$

In Allen's model, which emphasizes the fit to high pressure data

$$f(\rho) = A\mu + B\mu^2 , \qquad \mu = \frac{\rho}{\rho_0} - 1 \qquad (3.23)$$

To match the low pressure behavior, where porosity introduces a softening effect, Sandler and DiMaggio[30] use a variable bulk modulus

$$A = A_0 \left(1 - a_0 e^{\beta_0 J_1}\right) . \qquad (3.24)$$

This relation can be put into equivalent form specifying the pressure as a function of compression if we observe that $J_1 = -3p$ and $A = \frac{dp}{d\mu}$. Then a straightforward integration leads to

$$p = \frac{1}{3\beta_0} \ln \left(a_0 + \left(1 - a_0\right) e^{3\beta_0 A_0 \mu}\right) . \qquad (3.25)$$

An equation for $f(\rho)$ which fits both the low and high pressure behavior is given by

$$f(\rho) = \frac{1}{3\beta_0} \ln\left(a_0 + \left(1-a_0\right)e^{3\beta_0 A_0 \theta}\right) + B\theta^2 \, . \qquad (3.26)$$

Here, θ, the matrix compression, is given by Eq. (3.15), the superscript being temporarily dropped. The last term, which is quadratic in θ, should be dropped for underdense states since it would lead to unrealistic behavior. In this equation, the logarithmic compression, θ, rather than the linear compression, μ, is now used to allow a treatment compatible with finite deformation theory.

3.4.2 Hardening Models for Rock Behavior

In the theory of plasticity it is assumed that a definite surface exists in stress space with the property that the stresses must lie either on the surface itself or in its interior. For states of stress represented by points inside the yield surface, the material is described by the theory of elasticity, or possibly a generalization which involves non-linear elastic and thermo-elastic effects. For states of stress on the yield surface, the flow is governed by a flow law which constrains the stress to lie on the yield surface if the elastic theory would take the stress outside. The flow law of von Mises

$$D^{p}_{ij} = \lambda \frac{\partial f}{\partial \sigma_{ij}} \qquad (3.27)$$

leads to a unique solution in most cases, with λ being an undetermined multiplier which is specified by the constraint

that

$$g(\sigma_{ij}) = 0 \tag{3.28}$$

When the function specifying the constraint is not equivalent to the function f appearing in the flow rule, the flow rule is said to be non-associated, but only the case where $f = g$ was investigated in the current study.

The increase in shear strength at large strains that is observed in most materials can be modeled by letting the strength depend on the plastic work, the second invariant of plastic strain, or possibly one of the other parameters characterizing the distortion. If it is assumed that the flow does not depend on the third stress invariant, the yield surface has the hydrostat as an axis of symmetry. Models have been proposed in which the third invariant plays a role, such as the one discussed by Cherry[31] for rocks and Freudenthal[32] for metals, but in this report the emphasis is on yield surfaces symmetric about a straight axis. Three cases are treated in the discussions that follow. In the first, isotropic work hardening, the yield surface is a cone which expands isotropically as a function of the plastic work done. In the second, the "cap" model, a portion of the yield surface is conical, but it is completed by an elliptical cap. The conical portion is fixed, but the cap is free to move, though only in such a way that the flow stresses increase in magnitude. Finally, a kinematic hardening model is described in which the conical yield surface is free to translate in stress space but not to deform. These models are conceptually illustrated in Fig. 3.1.

The stress tensor, $\underset{\sim}{\sigma}$, is given by its component σ_{ij}, and it is often convenient to write the governing equations in terms of the components rather than the stress tensor itself.

- Isotropic Strain Hardening
- Yield Surface with Movable Cap
- Kinematic Hardening

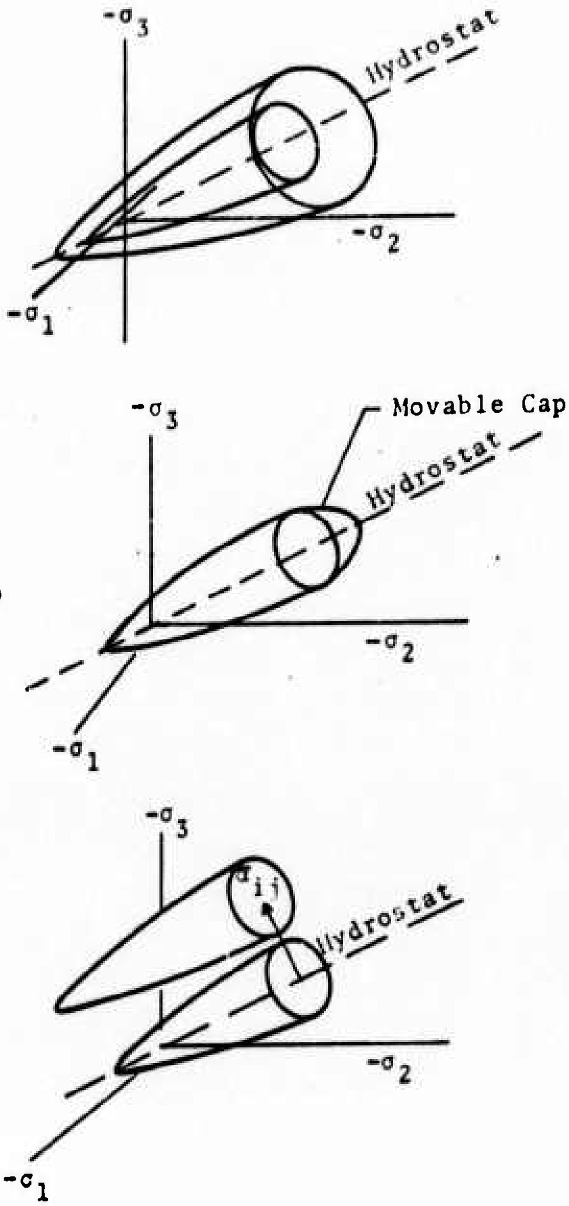

Fig. 3.1 Hardening models.

Defining the deviatoric stress by

$$s_{ij} = \sigma_{ij} - J_1 \delta_{ij}/3 \tag{3.29}$$

where

$$J_1 = \sigma_{ii} \tag{3.30}$$

is the first stress invariant, and the deviator strain by

$$e_{ij} = \varepsilon_{ij} - \varepsilon_{kk} \delta_{ij}/3 , \tag{3.31}$$

Hooke's law for shear deformation is expressed as

$$\dot{s}_{ij} = 2 \mu \dot{e}^{e}_{ij} \tag{3.32}$$

where μ is the shear modulus of the material.

When the shear stress attains a critical value the flow becomes inelastic and is then governed by a constitutive law of the form

$$\dot{\varepsilon}^{p}_{ij} = a \delta_{ij} + b\sigma_{ij} + c\sigma_{ik} \sigma_{kj} \tag{3.33}$$

where a, b, and c are usually taken to be functions of the stress invariants only. Higher order terms are not necessary, since they can be expressed in terms of the lower order terms, according to the Cayley-Hamilton theorem. The flow law is further restricted if we adopt the form

$$\dot{\varepsilon}^{p}_{ij} = \lambda \frac{\partial f}{\partial \sigma_{ij}} . \tag{3.34}$$

In the theory of metal plasticity it is assumed that $\dot{\varepsilon}^{p}_{ii} = 0$, a condition that we shall call isochoric plasticity, but in an investigation of the stability of soil masses by Drucker and Prager[33] this constraint was lifted. In their analysis

the yield surface was given by

$$f = \sqrt{J_2} - g(J_1) = 0 \qquad (3.35)$$

where

$$J_2 = \frac{1}{2} s_{ij} s_{ij} \qquad (3.36)$$

is the second invariant, and the Mohr-Coulomb flow condition

$$g(J_1) = Y - \alpha J_1 \qquad (3.37)$$

was adopted, with Y the yield stress in simple shear. Substitution of the expression given above for f leads to the constitutive equation

$$\dot{\varepsilon}^p_{ij} = \lambda\left(\frac{s_{ij}}{2g} - g'\delta_{ij}\right) \quad . \qquad (3.38)$$

With this result, the rate of change of specific volume is given by

$$\dot{\varepsilon}^p_{ii} = -3\lambda g'. \qquad (3.39)$$

In the case of a Mohr-Coulomb material

$$g' = -\alpha \qquad (3.40)$$

where α is a positive constant, and

$$\dot{\varepsilon}^p_{ii} = 3\lambda\alpha \ . \qquad (3.41)$$

It can be shown that λ is always positive, and, consequently, the flow always exhibits dilatancy in this case. The dilatancy is generally greater than observed in tests, and in reality

flows in which compaction occurs are also observed. This apparently led Drucker[34] to suggest that the yield surface should be completed by a spherical cap, for in that case g' can have either sign. At high pressures, the sign of g' is positive and compaction is indicated. At low pressure, g' is negative, implying dilatant behavior. This is the basis for assuming that porous material behavior can be described by the methods of plasticity theory.

Sandler and DiMaggio examined in detail the behavior of granite observed by Swanson,[35] and proposed an analytic model which is consistent with measurements. The model is recapitulated here, since it represents one of the more promising approaches to modeling granite, and it can be conveniently generalized. The yield surface is represented in two parts, a fixed "failure surface" given by

$$g = Y_c + \left(Y_1 - Y_c\right)e^{\beta_1 J_1} \qquad (3.42)$$

and a variable cap described by an ellipse tangent to the failure surface. These are illustrated in Fig. 3.2, which shows the yield surface in a "reduced stress space". In this space the horizontal axis represents distance along the hydrostat and the vertical axis represents the radius of the yield surface. The ellipse tangent to the failure surface at $J_1 = J_{1F}$ is given by

$$g_c^2 + \left(\frac{J - J_c}{R}\right)^2 = Q \qquad (3.43)$$

where J_c specifies the center of the ellipse, R denotes the ratio of major to minor axes and $\sqrt{Q}$ is the length of the semi-minor axis. The condition that the cap and failure

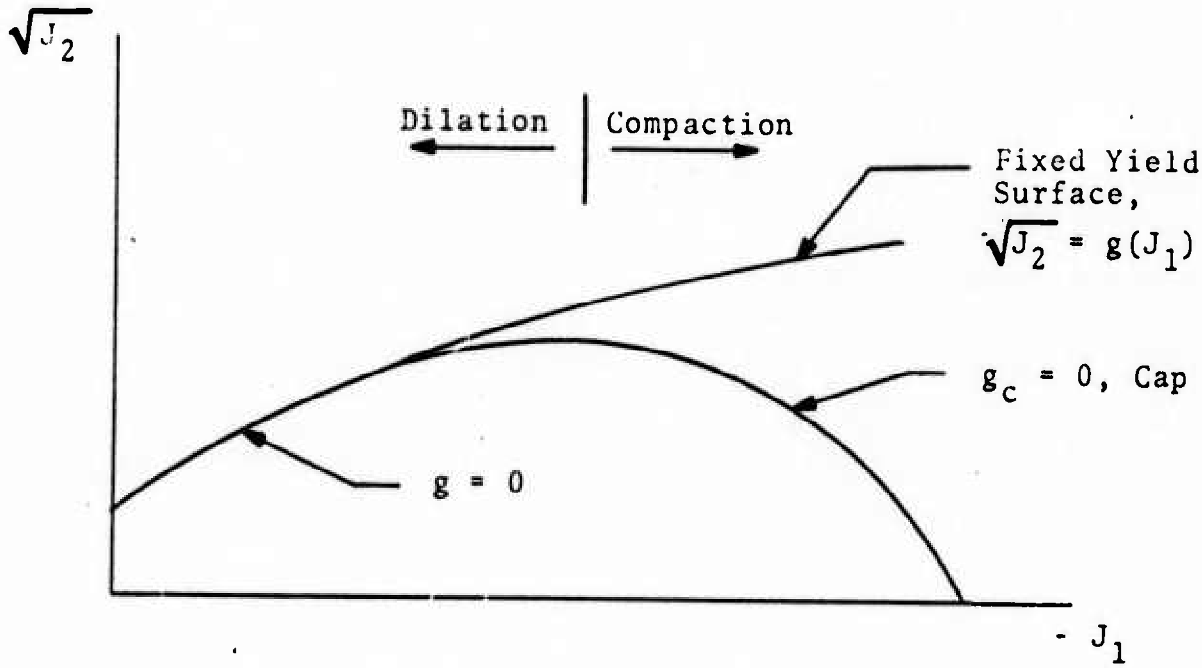

Fig. 3.2--Sketch of yield surface with a movable cap in a "reduced space space".

surface be tangent at their intersection determine J_c and Q:

$$J_c = J_{1F} - R^2 g_F g_F' \tag{3.44}$$

$$Q = g_F^2\left(1 + R^2 g_F'^2\right) \tag{3.45}$$

where

$$g_F = g\left(J_{1F}\right) = Y_0\left(1 - a_1 e^{\beta_1 J_{1F}}\right) , \tag{3.46}$$

and

$$g_F' = \left.\frac{\partial g}{\partial J_1}\right|_{J_{1F}} = -a_1 \beta_1 Y_0 e^{\beta_1 J_{1F}} , \tag{3.47}$$

and J_{1F} is the value of J_1 at the point of tangency. It was determined by Sandler and DiMaggio that a good fit to the data can be obtained by defining a hardening parameter, κ, by

$$\dot{\kappa} = \left(g - g_c\right)\sqrt{\dot{\varepsilon}^p_{ij}\dot{\varepsilon}^p_{ij}} \tag{3.48}$$

and letting the abscissa of the contact point move according to the law

$$J_{1F} = -W\kappa . \tag{3.49}$$

For the shape parameter they assumed a fit of the form

$$R = R_0 e^{\beta_2 W\kappa} . \tag{3.50}$$

The numerical values of Sandler and DiMaggio for Cedar City Tonalite are tabulated below. (The published value of β_0 is apparently a factor of ten too large due to an error in transcription.) We have modified the model for $\beta_2\kappa > 0.5$, since the cap lies outside the failure surface when κ takes on large values and would lead to negative hardening. More specifically, for $\beta_2\kappa > 0.5$, the value of R is held at its maximum value, R $\sqrt{e}$. In Fig. 3.3, the caps are shown for unmodified values of the Sandler and DiMaggio fit, and in Fig. 3.4 the result of limiting the maximum value of R as discussed above is shown.

TABLE 3.1

NUMERICAL VALUES OF CAP MODEL PARAMETERS FOR CEDAR CITY TONALITE GIVEN BY SANDLER AND DIMAGGIO [Ref. 30]

Y_0	152 ksi
a_1	0.953
R_0	4.0
W	450
β_0	0.002 ksi^{-1}
β_1	0.0029 ksi^{-1}
β_2	0.05 ksi^{-1}
μ	3300 ksi
A_0	7500 ksi
a_0	0.7

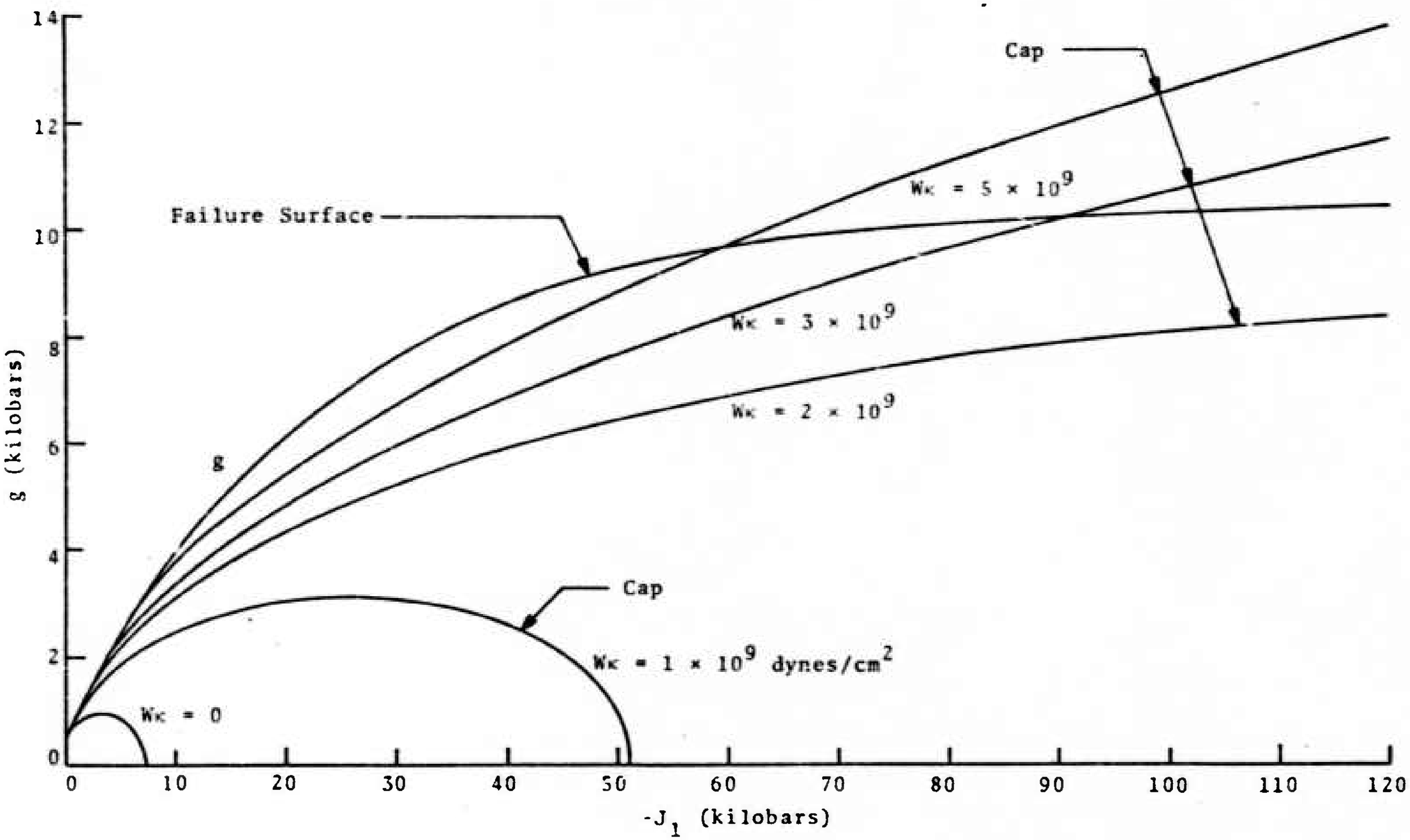

Fig. 3.3--Cap and failure surface for the unmodified cap model at high stress levels.

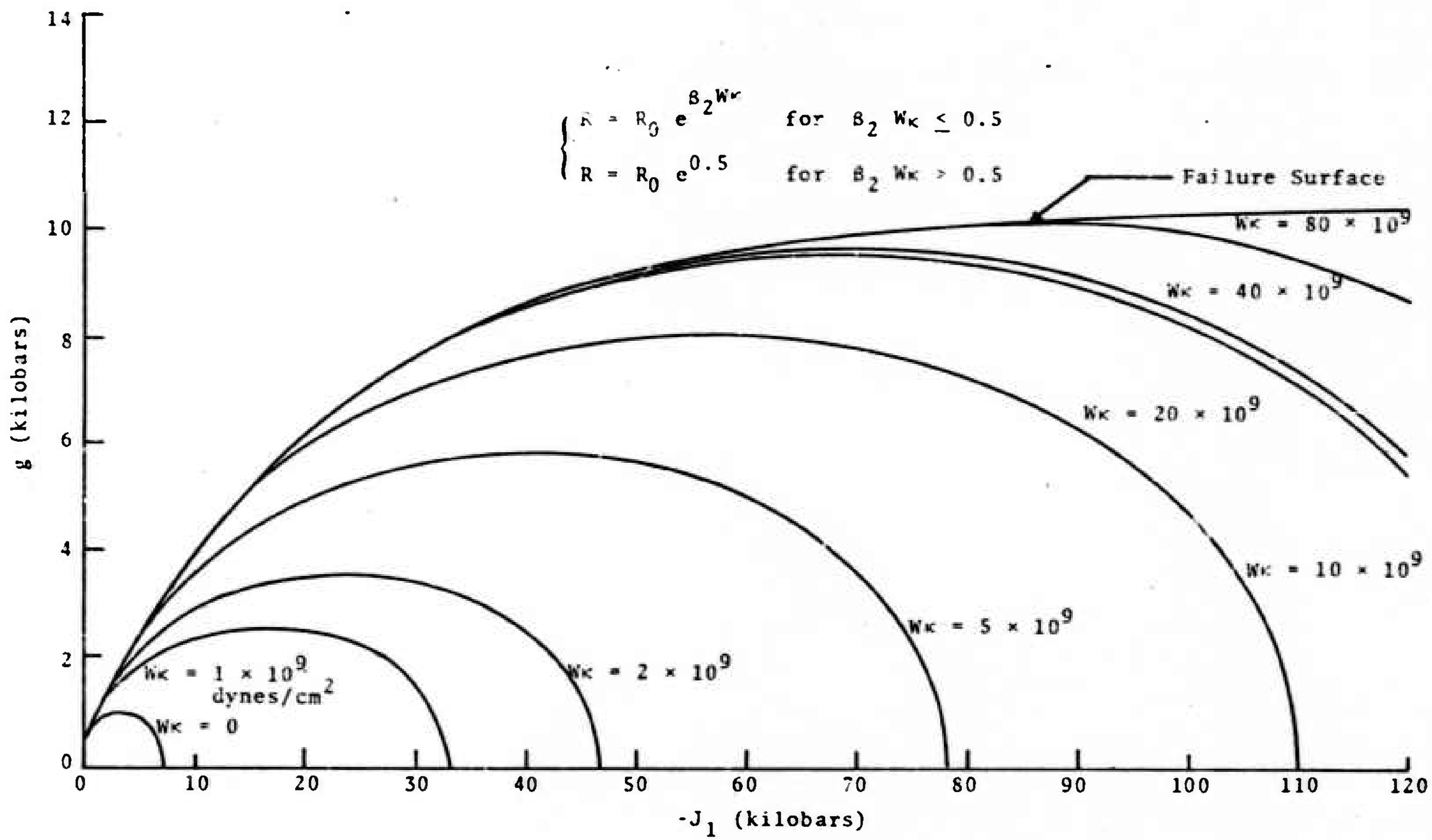

Fig. 3.4--Cap and failure surface for the modified cap model at high stress levels.

3.4.3 Flow Law for Materials with Hardening

To put the constitutive equation in a form suitable for numerical solution, it is necessary to solve for the stress rates explicitly in terms of the current stress and the strain rate, for these are the quantities available in the computational scheme. This is accomplished by writing the elastic strain rate as the sum of a deviatoric and an isotropic part

$$\dot{\varepsilon}^e_{ij} = \dot{e}^e_{ij} - \dot{\theta}^e \delta_{ij}/3 . \tag{3.51}$$

The elastic shear strain is given by Hooke's law in rate form

$$\dot{e}^e_{ij} = \dot{s}_{ij}/2\mu \tag{3.52}$$

and the matrix volume change by

$$\dot{\theta}^e = \frac{\partial h}{\partial J_1} \dot{J}_1 + \frac{\partial h}{\partial E} \dot{E} \tag{3.53}$$

where the function $\theta^e = h(J_1, E)$ represents the equation of state of the matrix material in a form in which the compression is given as a function of J_1, and the specific internal energy, E. The total strain rate

$$\dot{\varepsilon}_{ij} = \dot{\varepsilon}^e_{ij} + \dot{\varepsilon}^p_{ij} \tag{3.54}$$

can then be written

$$\dot{\varepsilon}_{ij} = \frac{\dot{\sigma}_{ij}}{2\mu} + \lambda \frac{\sigma_{ij}}{2g} - \left(T\dot{J}_1 + \lambda\overline{Q} + \frac{1}{3} h_E \dot{E}\right)\delta_{ij} \tag{3.55}$$

where

$$T = \frac{1}{6\mu} + \frac{1}{3}\frac{\partial h}{\partial J_1} \tag{3.56}$$

and

$$\overline{Q} = g' + \frac{J_1}{6g} . \tag{3.57}$$

To complete the solution it is assumed that λ can be written in the form

$$\lambda = \lambda_1 + \Lambda\dot{J}_1 \tag{3.58}$$

with λ_1 and Λ not explicitly dependent on the stress rates. Then the constitutive equation can be expressed

$$\dot{\sigma}_{ij} - Z\,\dot{\sigma}_{kk} = A_{ij} \tag{3.59}$$

where

$$A_{ij} = 2\mu\left\{\dot{\varepsilon}_{ij} - \lambda_1\frac{\sigma_{ij}}{2g} + \left(\lambda_1\,\overline{Q} + \frac{1}{3}\frac{\partial h}{\partial E}\,\dot{E}\right)\delta_{ij}\right\} \tag{3.60}$$

and

$$Z_{ij} = 2\mu\left\{(T + \Lambda Q)\,\delta_{ij} - \frac{\Lambda}{2g}\,\sigma_{ij}\right\} \tag{3.61}$$

The solution of Eq. (3.59) for the strain rates is straightforward, following the usual method for linear simultaneous equations. For spherical explosions, the solution is particularly simple, since $\sigma_{22} = \sigma_{33}$; and can be written,

$$\dot{\sigma}_{11} = \frac{A_{11} - 2R}{D} \tag{3.62}$$

$$\dot{\sigma}_{22} = \frac{A_{22} + R}{D} \tag{3.63}$$

where

$$R = Z_{22} A_{11} - Z_{11} A_{22} \tag{3.64}$$

and

$$D = 1 - Z_{11} - 2Z_{22} \ . \tag{3.65}$$

To complete the analysis, it is necessary to obtain expressions for λ_1 and Λ. This is done by combining the results of the preceeding analysis with the equation for the yield surface, as shown in the sections that follow.

3.4.4 Calculation of the Multiplier

The flow law given by Eq. (3.34) leaves an undetermined multiplier, λ. In the derivation of the flow law based on maximizing the rate of plastic work given by Hill [36] and due to von Mises, this λ appears as the Lagrangian multiplier that is inevitably introduced in extremum problems involving a constraint. The determination of λ requires that the constraint be satisfied, and involves differentiating the constraint equation and comparing with an appropriate scalar equation obtained from the flow law. An explicit expression for λ having the form $\lambda_1 + \Lambda\dot{J}_1$ was obtained in each of the four cases examined. In the first, the constraint is satisfied in the absence of hardening. The remaining three cases involve hardening models, and are simple work hardening, the "cap" model and kinematic hardening.

3.4.4.1 Multiplier for Materials Without Hardening

To obtain an expression for the multiplier, λ, the relation obtained by differentiating the yield condition, $f = 0$, with respect to time,

$$\dot{J}_2 = 2gg' \dot{J}_1 \tag{3.66}$$

is combined with a reduced form of the flow law obtained by multiplying Eq. (3.55) by σ_{ij}, resulting in the expression

$$\lambda = \frac{\left(\rho + \frac{J_1}{3}\frac{\partial h}{\partial E}\right)\dot{E} - \left(\frac{gg'}{\mu} - \frac{1}{3}\frac{\partial h}{\partial J_1} J_1\right)\dot{J}_1}{g - g' J_1} \tag{3.67}$$

which has the form $\lambda_1 + \Lambda \dot{J}_1$ previously assumed.

3.4.4.2 Multiplier for Materials with Isotropic Hardening

If the yield surface is assumed to expand isotropically as a function of the work, W^p, done against the plastic stresses, it is possible to represent the hardening of materials in a simple fashion. It is appropriate to note here that the unloading behavior is not well represented for many materials with this model, since the Bauschinger effect is not accounted for. Another limitation is that for materials whose strength depends significantly on the mean stress, this model exhibits too much dilatancy, but it has the advantage of being simple to deal with. The plastic work is determined by

$$\rho \dot{W}^p = \sigma_{ij} \dot{\varepsilon}^p_{ij} \tag{3.68}$$

and the yield surface has the equation

$$\sqrt{J_2} = g\left(J_1, W^p\right) . \tag{3.69}$$

Differentiating this relation leads to

$$\frac{\dot{J}_2}{2g} = \frac{\partial g}{\partial J_1} \dot{J}_1 + \frac{\partial g}{\partial W^p} \dot{W}^p \tag{3.70}$$

and from Eq. (3.38), we can show that

$$\rho \dot{W}^p = \lambda\left(g - \frac{\partial g}{\partial J_1} J_1\right). \tag{3.71}$$

The rate of plastic work can be eliminated from these equations, and after some straightforward algebraic manipulations a form for λ

$$\lambda = \frac{\left(\rho + \frac{J_1}{3}\frac{\partial h}{\partial E}\right)\dot{E} + \left(\frac{J_1}{3}\frac{\partial h}{\partial J_1} - \frac{g}{\mu}\frac{\partial g}{\partial J_1}\right)\dot{J}_1}{\left(1 + \frac{g}{\rho\mu}\frac{\partial g}{\partial W^p}\right)\left(g - \frac{\partial g}{\partial J_1} J_1\right)} \tag{3.72}$$

of the required type is obtained.

3.4.4.3 Multiplier for the Granite Cap Model

The yield surface for granite formulated by Sandler and DiMaggio involves both a fixed portion and a variable cap. The latter is represented by a family of ellipses that varies with the hardening parameter, κ, given by Eq. (3.48). When the stress lies on the fixed portion of the yield surface the analysis for flow without hardening discussed in Section 3.4.4.1 applies. On the cap, the stresses satisfy the equation

$$J_2 = g_c^2\,(J_1,\kappa) \tag{3.73}$$

where g_c is given by Eq. (3.43). It is easily shown that the plastic flow law of Eq. (3.27) leads to

$$\sqrt{\dot{\varepsilon}^p_{ij}\,\dot{\varepsilon}^p_{ij}} = \lambda\left(\frac{1}{2} + 3\left(\frac{\partial g_c}{\partial J_1}\right)^2\right)^{1/2} . \tag{3.74}$$

To determine λ the flow equation is operated on with σ_{ij}, the time derivative of Eq. (3.73) is taken and $\dot{\kappa}$ is eliminated from the resulting equations, leading to the result,

$$\lambda = \frac{\left(\rho + \frac{J_1}{3}\frac{\partial h}{\partial E}\right)\dot{E} + \left(\frac{J_1}{3}\frac{\partial h}{\partial J_1} - \frac{g_c}{\mu}\frac{\partial g_c}{\partial J_1}\right)\dot{J}_1}{\left[g_c - \frac{\partial g_c}{\partial J_1} + \frac{g_c}{\mu}\frac{\partial g_c}{\partial \kappa}(g-g_c)\right]\sqrt{\frac{1}{2} + 3\left(\frac{\partial g_c}{\partial J_1}\right)^2}} . \tag{3.75}$$

3.4.4.4 Multiplier for Kinematic Work Hardening

Prager's original rule[37] for the description of inelastic behavior assumed that the yield surface translates in stress space without change of shape as plastic deformation proceeds. This generalizes the bilinear hysteresis model sometimes assumed in representing plastic deformation when the state of stress is one-dimensional. In the current version of the model it is assumed that the translation of the yield surface is normal to its axis of symmetry. It is conceptually useful to visualize the surface as given by a vector in the three-dimensional space of principal stresses. In doing this, we may retain the double subscript notation, though in principal axes only the diagonal terms are non-zero. A point on the axis of symmetry of the yield surface is represented by

$$\alpha_{ij} = \bar{\alpha}_{ij} + \frac{1}{3} J_1 \delta_{ij} \tag{3.76}$$

where the term $\bar{\alpha}_{ij}$ represents the displacement of the axis and the second term represents the distance along the axis. The total stress is given by

$$\sigma_{ij} = \bar{s}_{ij} + \bar{\alpha}_{ij} + \frac{1}{3} J_1 \delta_{ij} \tag{3.77}$$

with $\bar{s}_{ij}$ representing the distance in stress space from the axis of symmetry of the yield surface to the stress point. The yield surface is specified by

$$f = \sqrt{J_2} - g(J_1) = 0 \tag{3.78}$$

where

$$J_2 = \frac{1}{2} \bar{s}_{ij} \bar{s}_{ij} = 0 \tag{3.79}$$

The crucial physical assumption is that $\bar{\alpha}_{ij}$ is linearly related to the plastic strain rate by

$$\dot{\bar{\alpha}}_{ij} = b \dot{e}^p_{ij} \tag{3.80}$$

where b is a hardening parameter and $\dot{e}^p_{ij}$ is the deviatoric plastic strain rate. Since $\dot{e}^p_{ij}$ is a deviator, $\dot{\bar{\alpha}}_{ii} = 0$, implying that the translation of the yield surface takes place normal to its axis of symmetry. To evaluate λ the flow law, Eq. (3.55), is operated on with $\bar{s}_{ij}$, and after straightforward manipulations we are lead to the result

$$\lambda = \frac{\sigma_{ij} \dot{\varepsilon}_{ij} - \frac{J}{3} \dot{\varepsilon}_{ii} - b\left(\varepsilon^p_{ij} - \frac{1}{3} \varepsilon^p_{kk} \delta_{ij}\right) \dot{\varepsilon}_{ij} - \frac{g\dot{J}_1}{\mu} \frac{\partial g}{\partial J_1}}{\left(1 + \frac{b}{2\mu}\right)\left(g + \frac{b}{2g} e^p_{ij} \left(\sigma_{ij} - b e^p_{ij}\right)\right)} \tag{3.81}$$

3.4.5 Temperature and Strain Rate Effects

The magnitude of the flow stress depends on both the state of stress and the history of the motion, as discussed in the preceding section. In addition it depends on temperature and strain rate. The justification for treating

temperature and strain effects together lies in the physical basis for the strain rate effect, which is simply that when the energy of a group of atoms exceeds the activation energy, some slip takes place through a rearrangement of atoms. The application of this Arrhenius activation energy concept is discussed by Handin[38] and Serdengecti and Boozer[39] for rocks and applied in detail to metal deformation by Zhurkov and Sanfirova[40] and more recently by Samanta.[41] A complete justification for the factor on theoretical grounds for either rocks or metals has, unfortunately, not been established, but Samanta discusses formulas of the type

$$\dot{\varepsilon} = \nu e^{\frac{v\sigma - \Delta H}{kT}} \tag{3.82}$$

with v the "activation volume" and ΔH the "activation enthalpy" with the parameters depending on the flow. If we identify the "flow stress," σ, with the yield stress of the earlier sections, then an expression for the yield stress in terms of temperature, strain rate and two material constants is obtained

$$Y/Y_0 = 1 + \alpha T \ln E_2'/\nu \tag{3.83}$$

in which E_2' is the second invariant of the deviatoric strain rate tensor. The substitution of $\sqrt{E_2'}$ for $\dot{\varepsilon}$ generalizes the one-dimensional approximation to multi-dimensional flows, and the constants, α, ν and Y_0 have to be obtained by experiments, theoretical arguments, or estimates based on experience with other materials. Some guidance is obtained from the fact that ν is of the order of magnitude of the atomic vibration frequency for simple materials, such as aluminum, and $\alpha = k/\Delta H$ is determined for simple materials by the empirical result that the activation enthalpy is very nearly the sublimation energy. This is the case for the materials investigated by Zhurkov and

Sanfirova and by Samanta. The situation is more complex for geologic materials than for metals and alloys but an understanding of some of the simpler examples is helpful. Strain rate effects are important in calculating the effects of underground nuclear explosions for two reasons. First, in the near field the temperature is high because of shock heating and lowers the strength. Second, the time scale of material motion is generally much longer for nuclear blasts than for laboratory tests. Consequently it seems important to estimate, at least roughly, the magnitude of strain rate effects and, in the absence of specific data for the case of interest, it is necessary to use an approximate relationship. In the granite calculations a value of α of 0.5×10^{-4} was used. This is probably somewhat high, but it was selected to minimize the effect of strength near the cavity at a very early time in the development of our techniques. Experiments to determine a realistic value of α would be desirable.

To use the correction factor $1 + \alpha T \ln \sqrt{E_2'}/\nu$ it is necessary to determine the temperature in the course of the calculation. To simplify the calculation, the effect of the deviatoric stresses on heating is ignored, and only the thermodynamic variables pressure and internal energy are accounted for. This is a good approximation where the temperature is high and its influence is significant. Where the influence of the deviatoric stresses is important the temperature is low, and it is not essential to make an accurate estimate of its deviation from normal.

A differential equation for temperature can be obtained by thermodynamic considerations. For any internal energy $E(V,T)$

$$dE = C_V dT + \left(\frac{\partial E}{\partial V}\right)_T dV \,. \qquad (3.84)$$

Combining with the thermodynamic identity

$$\left(\frac{\partial E}{\partial V}\right)_T = T\left(\frac{\partial p}{\partial T}\right)_V - p \tag{3.85}$$

it follows that

$$C_V dT = dE - \left(T\left(\frac{\partial p}{\partial T}\right)_V - p\right) dV \; . \tag{3.86}$$

A convenient expression for dT can be obtained by using the thermodynamic identity

$$\left(\frac{\partial p}{\partial T}\right)_V = \left(\frac{\partial p}{\partial E}\right)_V \left(\frac{\partial E}{\partial T}\right)_V \tag{3.87}$$

and the definition

$$\Gamma = V\left(\frac{\partial p}{\partial E}\right)_V \tag{3.88}$$

of Gruneisen's ratio, resulting in the expression

$$dT = \frac{dE}{C_V} + \left(\frac{p}{C_V} - \frac{T\Gamma}{V}\right) dV \tag{3.89}$$

which is used to update the temperature.

For the form of the equation of state given by Eqs. (3.21) and (3.22) we find

$$\Gamma = a + \frac{b}{\left(\frac{E}{E_0 \eta^2} + 1\right)^2} \; . \tag{3.90}$$

The differentials required in Eq. (3.89) are given in terms

of calculated quantities and the time step, dt, by

$$dE = \left[\left(\sigma_{11} - q\right)\dot{\varepsilon}_{11} + 2\left(\sigma_{22} - q\right)\dot{\varepsilon}_{22}\right] dt/\rho \qquad (3.91)$$

$$dV = \left(\sigma_{11} + 2\sigma_{22}\right) dt/\rho \qquad (3.92)$$

where q represents a viscous stress (artificial viscosity). These equations, together with the previous equation for dT, are continuously used in the computer program to update temperature.

3.5 SET-UP OF SPHERICAL EXPLOSION CALCULATIONS IN GRANITE

A number of calculations were carried out to determine how well the theoretical framework described in the previous sections predicts the observed motion of granite. A yield of 1 kT was selected for these runs, and in comparing with nuclear shot data the yield is scaled down to 1 kT by the standard "cube-root" scaling law. The initial cavity radius has been varied, but in the calculations cited here, it was held at 1.5 meters, which gives a volume that is realistic for medium yield shots.

The source was represented by a polytropic gas law with an index $\gamma = 4/3$. This value was selected as being representative since it is exact for pure radiation, which governs for very high yields at early times,and also for a tri-atomic gas without internal degrees of freedom. Since the cavity contains large amounts of water and silicon dioxide, it was felt that the real values might not vary significantly from 4/3. Studies by Allen and Duff[42] and Wagner and Louie[43] have indicated that the results are not highly sensitive to the value of γ, but a precise calculation should allow for ionization and other non-ideal features of the cavity gases.

A source calculation may involve either the expansion of thin spherical shells of gas, or it may assume that the shells mix as the result of turbulence. If the mixing is thorough, it is a good approximation to represent the source as a uniform sphere expanding adiabatically, and this is the approximation adopted in the current study. In view of the difficulty of studying mixing in a transient flow theoretically, a description of the source behavior will probably require an experimental approach. The discussions by Butkovitch[20,44] indicate that the water content of the rock significantly affects the results, but the emphasis in these calculations was on the effect of rock strength, and water content was not accounted for.

The zoning for the 1-kT problems is illustrated in Fig. 3.5. The computer program was formulated to allow 1000 zones, but only 350 were required for these calculations. The first zone is 50 cm in thickness, and the thickness was increased by 1 percent per zone. The total radius accounted for in the calculational grid is

$$r_{max} = r_0 + \Delta r_0 \frac{a^N - 1}{a - 1} \tag{3.93}$$

where a is the thickness ratio, r_0 is the initial radius of the source region, Δr_0 is the width of the first zone, and N is the number of zones. This radius is 1563 meters for the indicated zoning.

The SKIPPER program uses the standard, Lagrangian approach to the calculation of spherical motions described by Wilkins.[28] In addition to the stresses resisting the motion described in the preceding sections, an artificial viscosity is included in the program which incorporates both linear and quadratic terms. Details are given in the RIP report by Fisher, Cecil and Lane[45] (the SKIPPER code originated from the RIP code). It was found in the course of the current study that an improvement in the behavior at the shock front can be obtained by eliminating only the quadratic term in the artificial viscosity

$$q = \left(C_Q \, \Delta u^2 - C_L c \Delta u\right)\rho \tag{3.94}$$

where Δu is the velocity change across a zone, c is the sound speed and ρ is an average density, when the material is expanding. In the usual approach, both terms are dropped when material is expanding, but this leads to an excessively non-uniform treatment. A comparison of the two methods is illustrated in Fig. 3.6, which shows that a mild instability

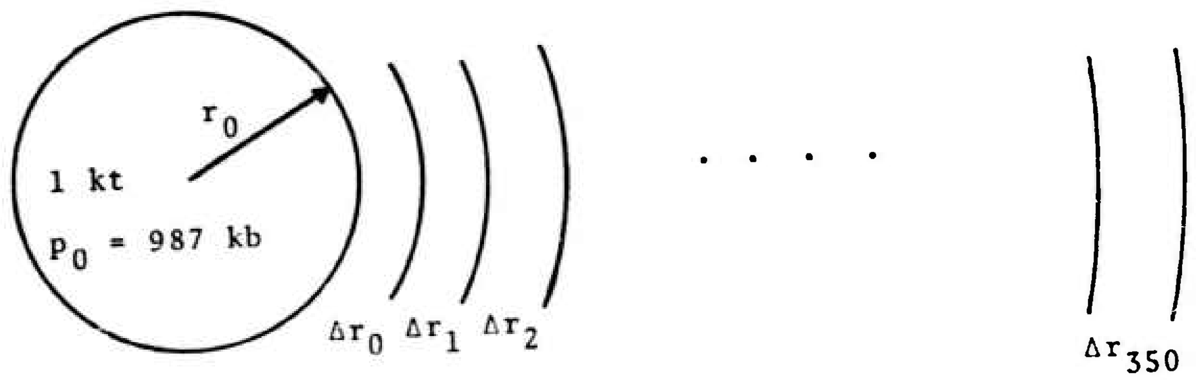

r_0 = 1.50 meters

Δr_0 = 0.50 meters

r_{350} = 1562 meters

Δr_{350} = 16 meters

$$p = (\gamma - 1)\left(\frac{r_0}{r}\right)^{3\gamma} \frac{E_0}{\frac{4}{3}\pi r_0^3}\text{, Source Pressure}$$

Fig. 3.5--Initial conditions and zoning.

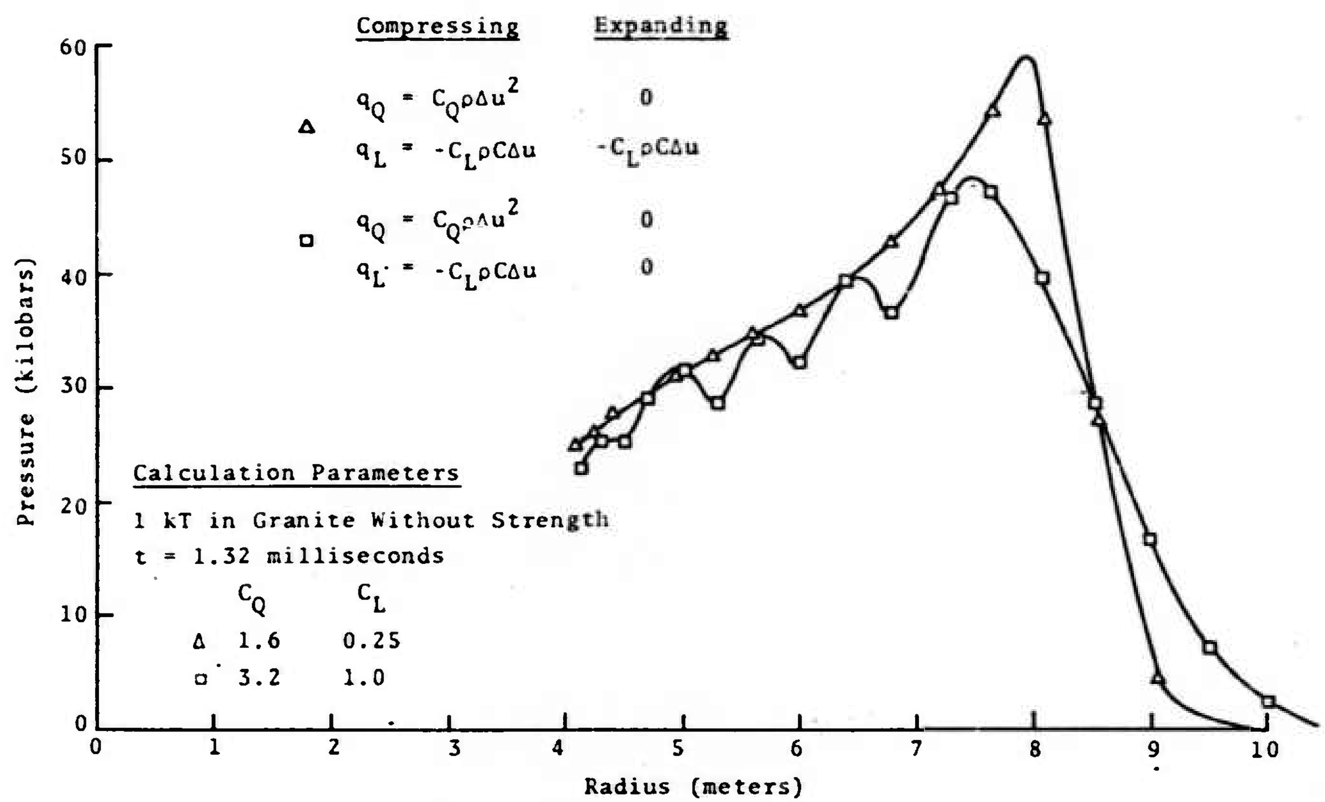

Fig. 3.6--Comparison of pressure profiles for two treatments of artififial viscosity [$q = q_Q + q_L$].

in the calculation that occurs for relatively large values of artificial viscosity (C_Q = 3.2, C_L = 1.0) disappears when the linear term is retained in the expansion region, even though the viscosity was lowered at the same time.

3.6 UNDERGROUND SHOT DATA

Before entering into a discussion of the calculated results, it seems appropriate to discuss some of the data taken from the Hardhat, Shoal and Piledriver shots, since these data are the basis for evaluating the validity of the calculations. This is especially true since there is a long history of calculations of underground shots with highly variable degrees of success. In analyzing the shot data it is observed that the cavity volume per kiloton of yield is remarkably consistent between shots. The data are summarized in Table 3.2. The consistency of the volume per unit yield

TABLE 3.2
CRATER RADIUS AND CRATER VOLUME PER TON
FOR THREE GRANITE SHOTS

Shot	Yield, Kilotons	Cavity Radius, Meters	Reference	Cavity Volume Per Unit Yield, Cubic Meters Per Ton
Hardhat	5.0	19.2	46	5.80
Shoal	12.5	25.6	46	5.69
Piledriver	61.	44.5	47	6.03

far exceeds the credibility of the individual measurements. Though both yield and cavity volume vary by nearly 20%, depending on the author and type of measurement, the average

cavity volume per unit yield is 5.7 cubic meters per ton with a variation of only 4 percent. For a 1-kT shot, the radius would be 11.1 meters.

Perret in his discussion of Piledriver[47] and Werth and Herbst in their discussion of Hardhat[48] have pointed out that the late-time displacement can be estimated from an elementary analysis based on the argument that the mass of material inside the sphere with radius R before the shot must equal the mass inside the sphere of radius $R+\delta$ after the shot, where δ is the displacement,provided the the material does not undergo significant compaction or bulking. It is reasonable for the granite shots cited here to assume that the initial cavity volume is negligible. The mass equation then takes the form

$$\frac{4}{3}\pi(R+\delta)^3 - \frac{4}{3}\pi R_C^3 = \frac{4}{3}\pi R^3 \tag{3.95}$$

which reduces, for $\delta << R$, to

$$\delta = R_C^3/3R^2 \tag{3.96}$$

where R_C is the cavity radius. For the Piledriver shot this leads to a value of 1.04 ft for the permanent displacement at a radius of 1000 ft. The fit by Borg[49] to 26 data points results in a displacement of 0.86 feet at this radius, a discrepancy of about 20%, consistent with the uncertainty in displacement, cavity radius and yield. The need for a reliable yardstick such as this in correlating theory and shot data is vital, since individual measurements may vary by a factor of five from the mean value. Many of the measurements of displacement cited by Borg, vary by a factor of ten from one another. Since these authors of granite shot studies agree on the validity of the above displacement formula, it seems to provide a good benchmark for testing the validity

of calculations. In view of the uncertainty in measurements, it is felt that caution should be exercised in searching for a correlation of individual measurements and calculations, such as velocity history at a fixed station.

Displacement history may be one of the more reliable indicators. Since it is an integrated quantity, it washes out some spurious details, and the final value can be estimated from the formula given above. This eliminates the possible effect of slow drift in the traces due to long term electrical effects.

The dynamic overshoot at displacement is very large. The peak displacement is compared with the final value in Table 3.3, and an overshoot of 350% is apparently typical.

TABLE 3.3

DISPLACEMENT OVERSHOOT FOR THREE GRANITE MEASUREMENTS

	Piledriver Station 1 (668 ft)	Piledriver Station 2 (1543 ft)	Hardhat (457 m)
Peak Displacement, d_{max}	65 in.	15.5 in.	3.8 cm
Final Displacement, d_∞	13 in.	9 in. (5.2 in.)*	1.19 cm
Overshoot ($100\ d_{max}/d_\infty$)	400%	172% (300%)*	320%

It is of considerable interest to explain this overshoot quantitatively by theoretical methods, but the constitutive equations previously used were not able to model the overshoot and late-time displacement in a straightforward fashion It will be shown that the kinematic hardening model does succeed in providing a reasonable theoretical description of the overshoot.

*The 9-in. figure given is questionable, and the alternative value, (5.2 in.) based on Borg's fit, is also tabulated for comparison.

3.7 COMPARISON OF CALCULATIONS AND FIELD DATA

Three calculations are described in this section which bear on the problem of how best to model granite. Two of these involve the same material constants, where applicable, and were designed to compare the "cap" and the kinematic hardening models. In these cases the strength (4.0 kbar, reference value) was chosen so that the "cap" model calculation would result in a cavity of roughly the right volume. Details of these calculations are supplied in the three sections that follow. The reference value for strength, Y_{00}, is the strength in the formula

$$Y_0 = Y_{00}\left(1 + \alpha T \ln\sqrt{E_2'}/\nu\right)$$

and represents the strength at $T = 0$ and $J_1 = -\infty$.

3.7.1 Cap Model Calculation

From previous studies[50] and test runs it was known that the parameters given in the original Sandler and DiMaggio fit to Cedar City Tonalite would lead to an unrealistically small value of cavity radius. With the premise in mind that the cavity radius should come out near to 11.1 meters for a one-kiloton shot, as discussed in Section 3.6, the yield strength was adjusted to give a realistic cavity volume. A set of parameters that accomplishes this is listed in Table 3.4.

In the table is also included a value for the dilatational wave speed,

$$C_d = \sqrt{(K + 4\mu/3)/\rho}\ , \quad K = A_0(1-a_0)\ . \tag{3.97}$$

The value of a_0 was adjusted so that this wave speed would be consistent with the 4.8 km/sec value for Hardhat granite at zero pressure published by Werth and Herbst.[48]

TABLE 3.4

PARAMETERS FOR CAP MODEL CALCULATION

Parameter	Value Given in Ref. [30], English Units	Value Given in Ref. [30], Metric Units	Value Used in Current Calculation
ρ_0	--	--	2.68 g/cc
a	--	--	0.5
b	--	--	1.3
E_a	--	--	$.16 \times 10^{12}$ ergs/g
A_0	7500	517 kbar	517 kbar
$A_0(1-a_0)$	0.255×10^6 psi	155 kbar	316 kbar
B	--	--	180 kbar
a_0	0.7	0.7	0.389
β_0	0.002 ksi^{-1}	0.029 $kbar^{-1}$	0.029 $kbar^{-1}$
Y_0	152 ksi	10.45 kbar	4.00 kbar
a_1	0.953	0.953	0.948
β_1	0.0029 ksi^{-1}	0.042 $kbar^{-1}$	0.042 $kbar^{-1}$
R_0	4.0	4.0	4.0
W	450	450	450
β_2	0.05	0.724 $kbar^{-1}$	0.724 $kbar^{-1}$
μ	3300 ksi	0.228 mbar	0.228 mbar
C_d	12,600 ft/sec	4.131 km/sec	4.80 km/sec
α	--	--	0.5×10^{-4} deg^{-1}

For the choice of parameters listed, the calculated crater radius is 10.5 meters. This is close enough to the 11.1-meter figure of Section 3.6, which was based on shot data, to justify a detailed comparison of other measurements with calculations. The main observation resulting from the comparison was that the cap model results in a displacement history which exhibits virtually no overshoot, whereas the test data indicates values of overshoot exceeding 300%. The detailed results of the calculations are deferred to Section 3.7.3 in which a comparison with both the data and the kinematic hardening model is discussed.

3.7.2 Kinematic Hardening

The kinematic hardening model discussed in Section 3.4.4.4 was used as the basis for a one-kiloton calculation with the same mechanical parameters as those used in the preceding discussion, except that the cap behavior was not accounted for. Hardening due to cap motion was replaced by translating the axis of symmetry of the yield surface according to Eq. (3.76) with displacement given by

$$\bar{\alpha}_{ij} = b e^{p}_{ij} \tag{3.98}$$

the value for b was 100 kilobars. A slope of 100 kbar is shown in Fig. 3.7; which is taken from Ref.35 to illustrate granite behavior. The cavity radius and displacement showed substantial overshoot in the calculation, and the final cavity radius was smaller than with the cap model of hardening. It was estimated that a reduction in the reference strength from 4 to 1.68 kbar would increase the cavity radius to 11.1 m. The result of these calculations are included in Figs. 3.8 through 3.13.

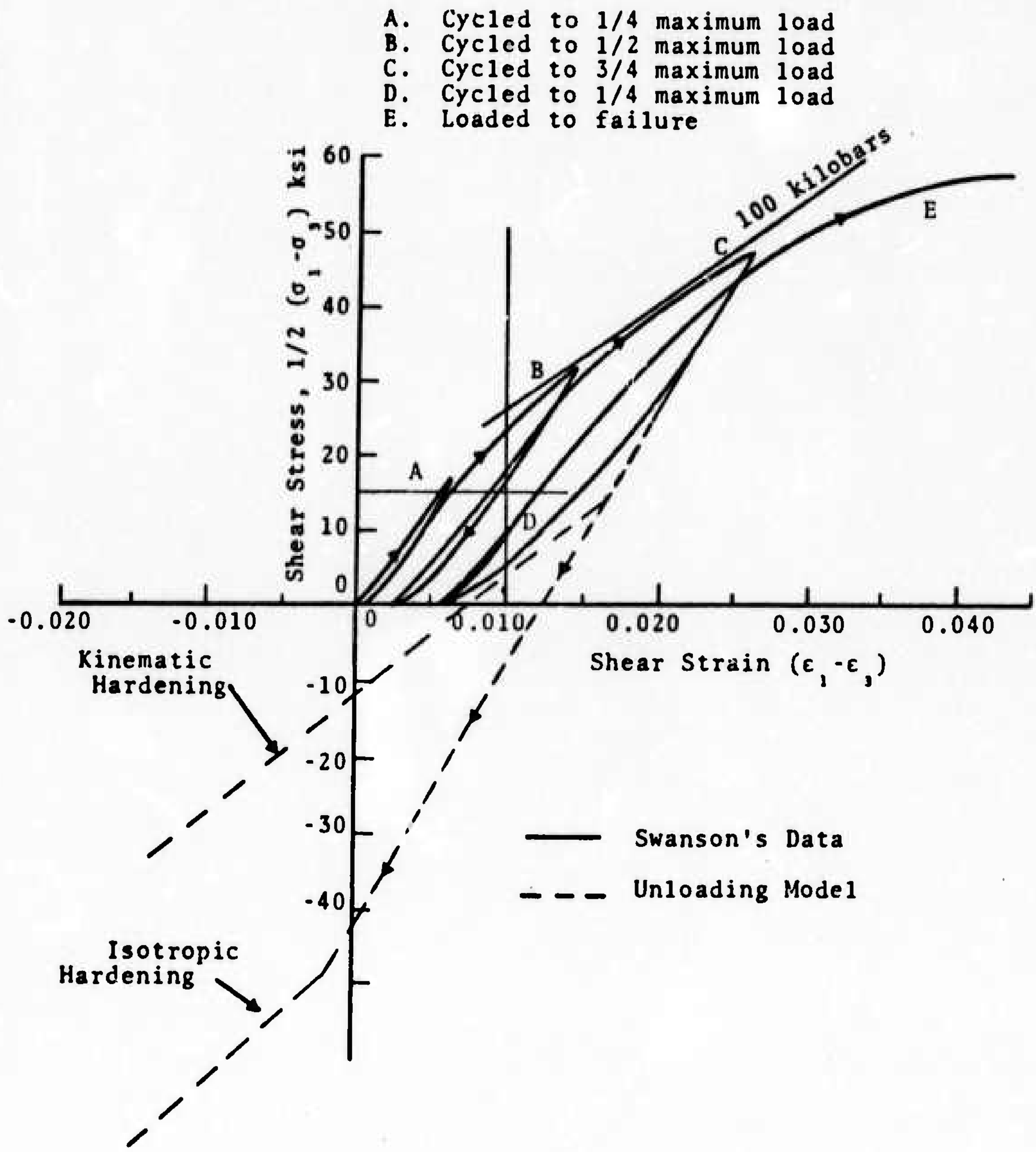

Fig. 3.7--Illustration of a stress-strain relation taken from Ref.35, showing the Bauschinger effect in Cedar City tonalite, and the theoretical model for pure shear.

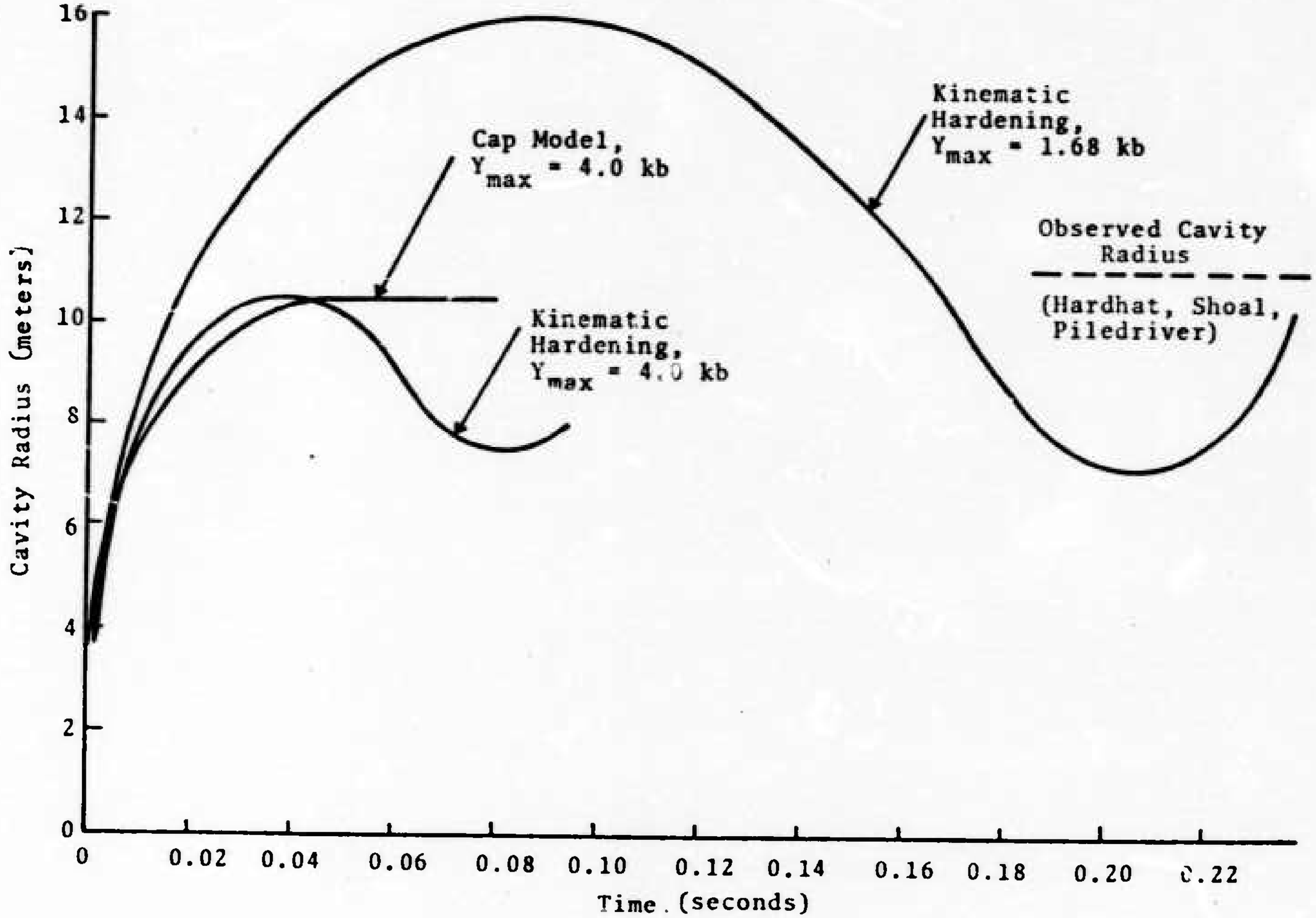

Fig. 3.8--Comparison of three calculations with observed cavity size.

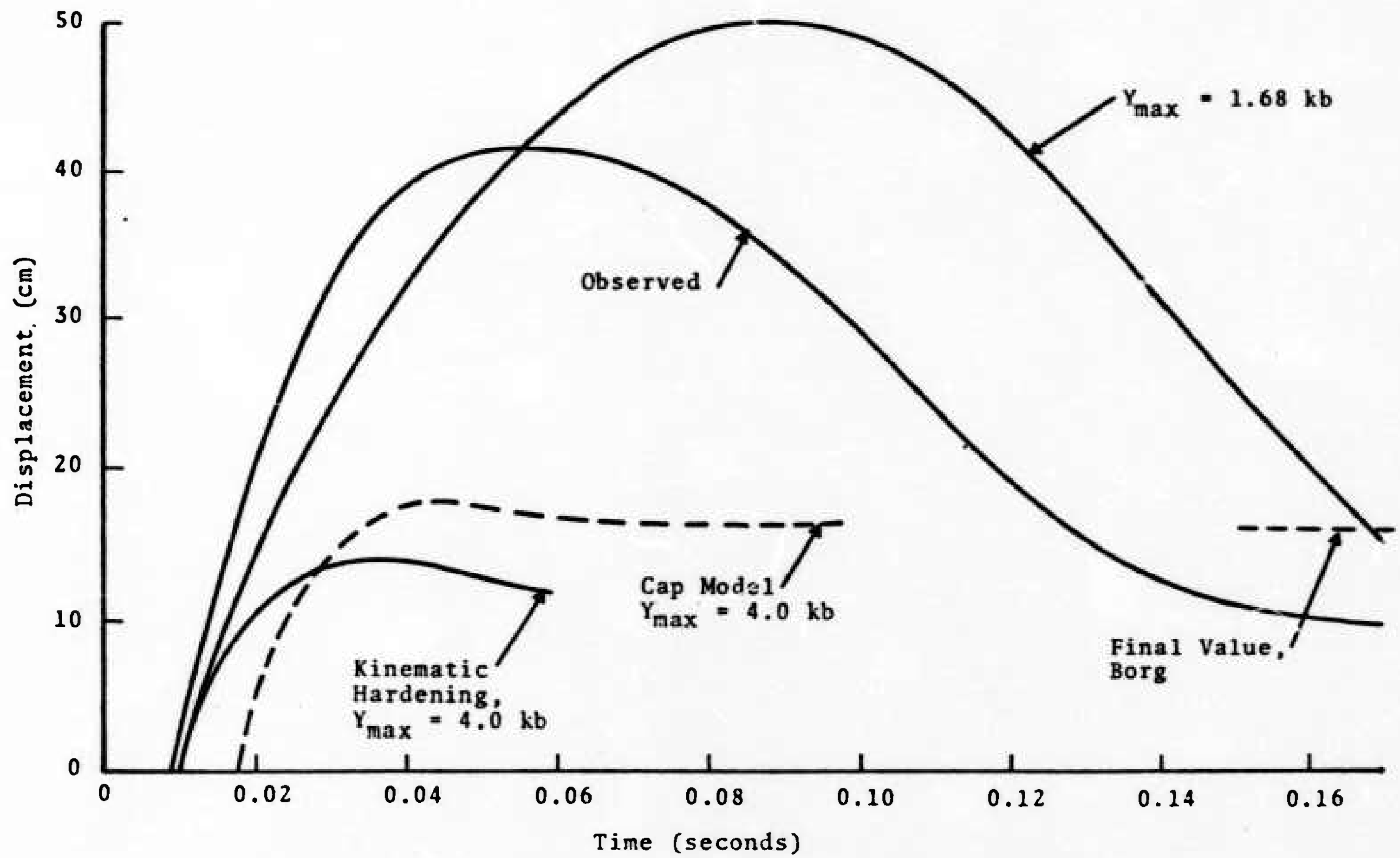

Fig. 3.9--Displacements at 51.9 m at Station 1 of Piledriver, scaled to 1-kT yield, based on data of Ref. 47.

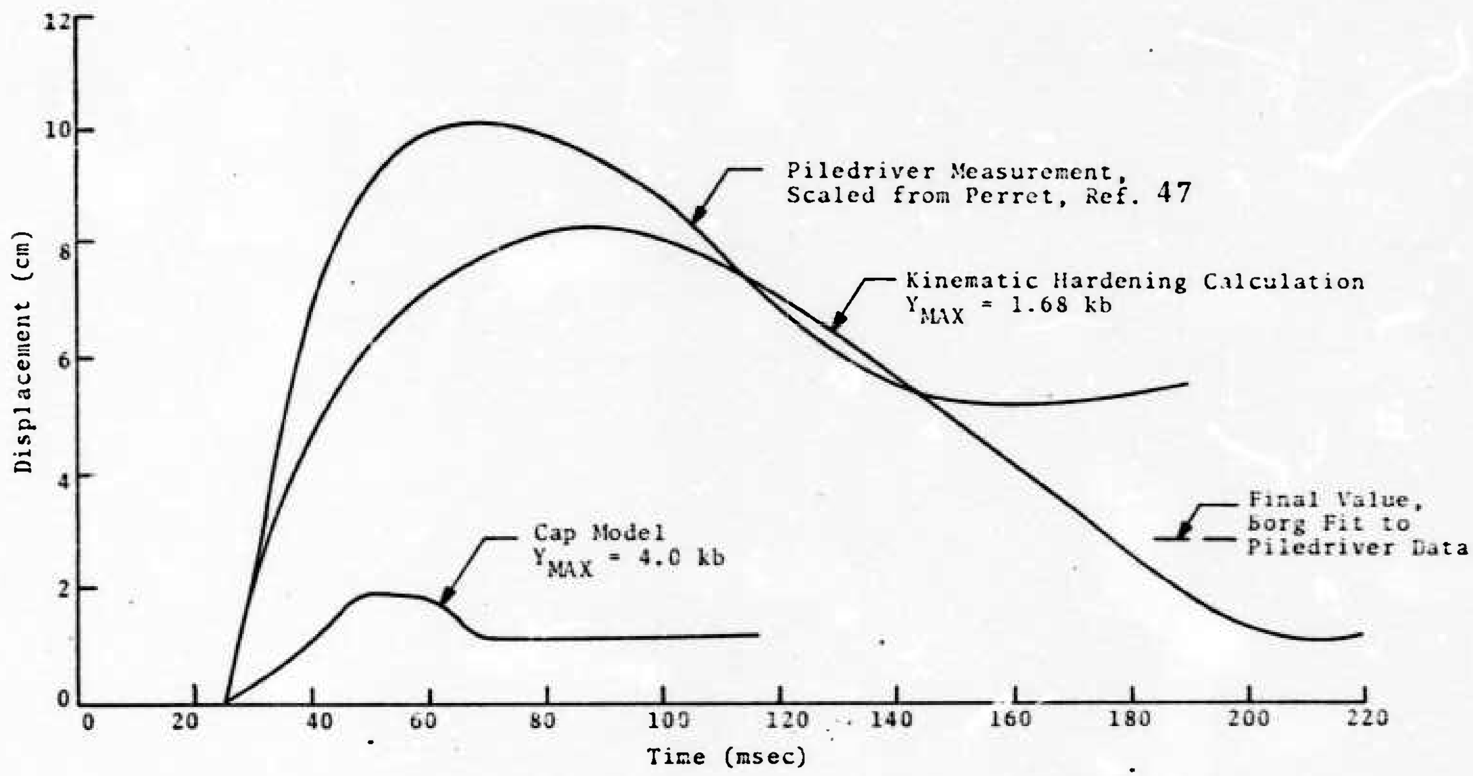

Fig. 3.10--Displacement at 120 m for a yield of 1 kT and comparison with measurement at Station 2 in Piledriver, based on data of Ref. 47

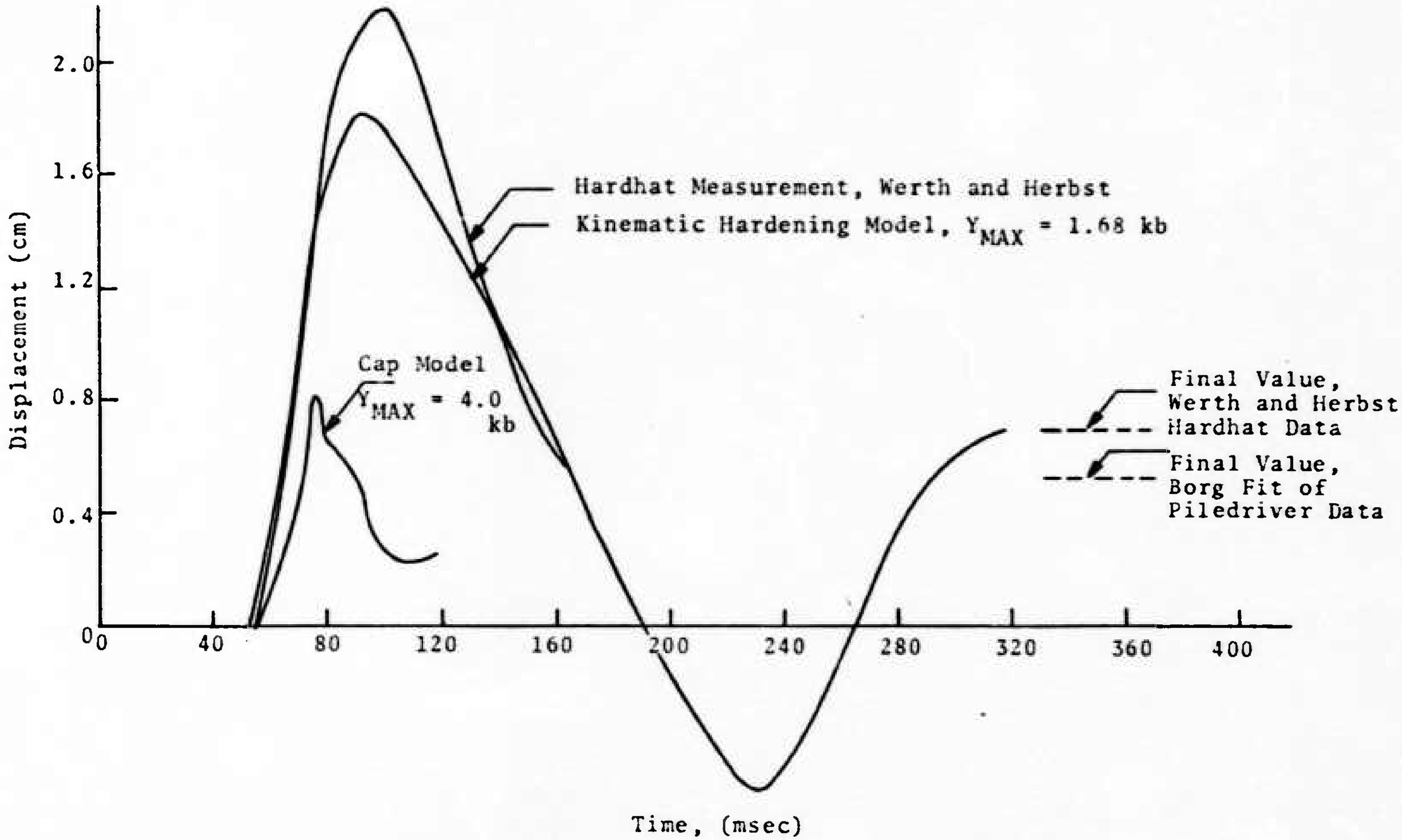

Fig. 3.11--Displacement at 267 m from a 1-kT source (scales to 457 m from Hardhat source--location of measurement 3VR), based on data of Ref. 48

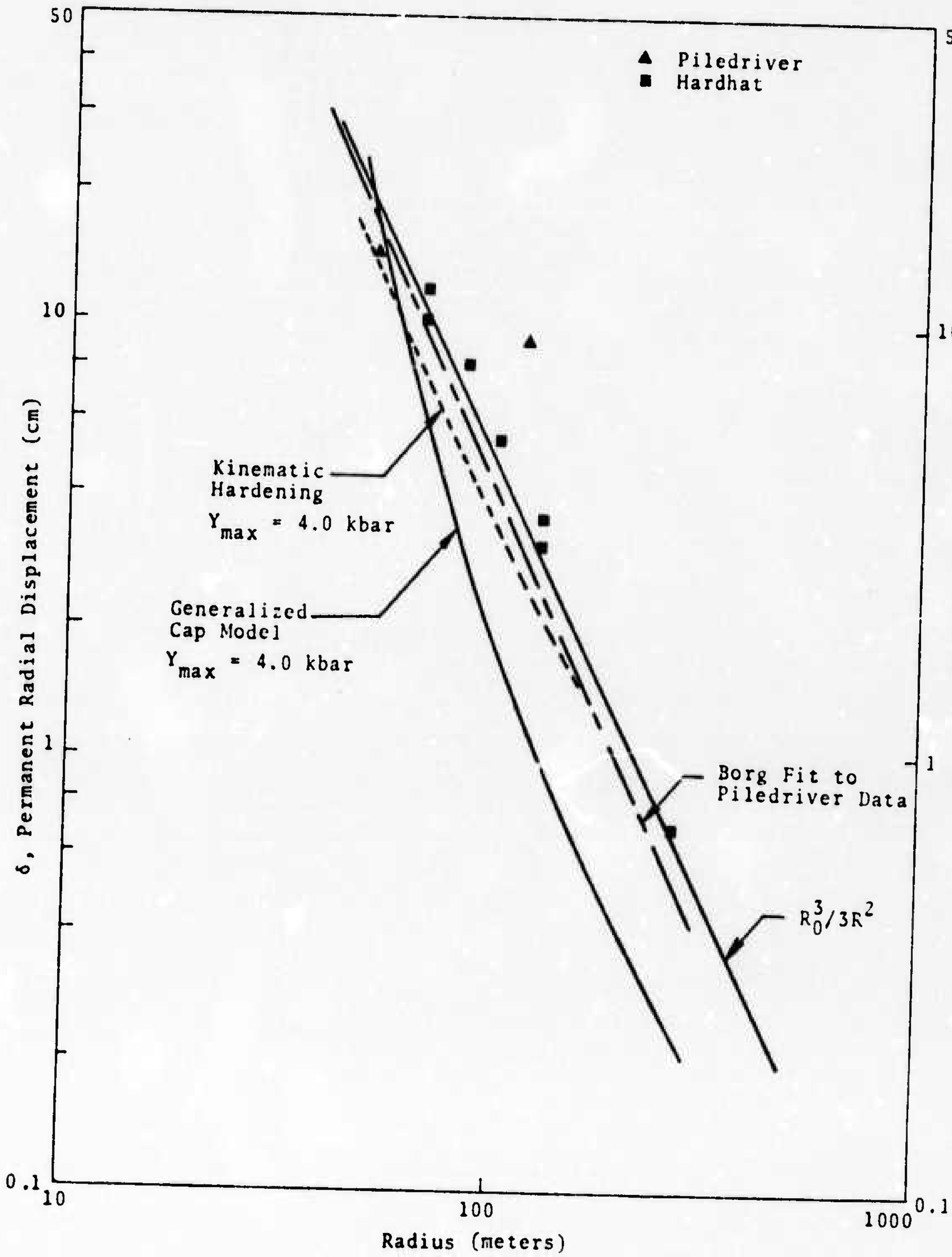

Fig. 3.12--Comparison of theoretical displacements with field results for a 1-kT explosion in granite.

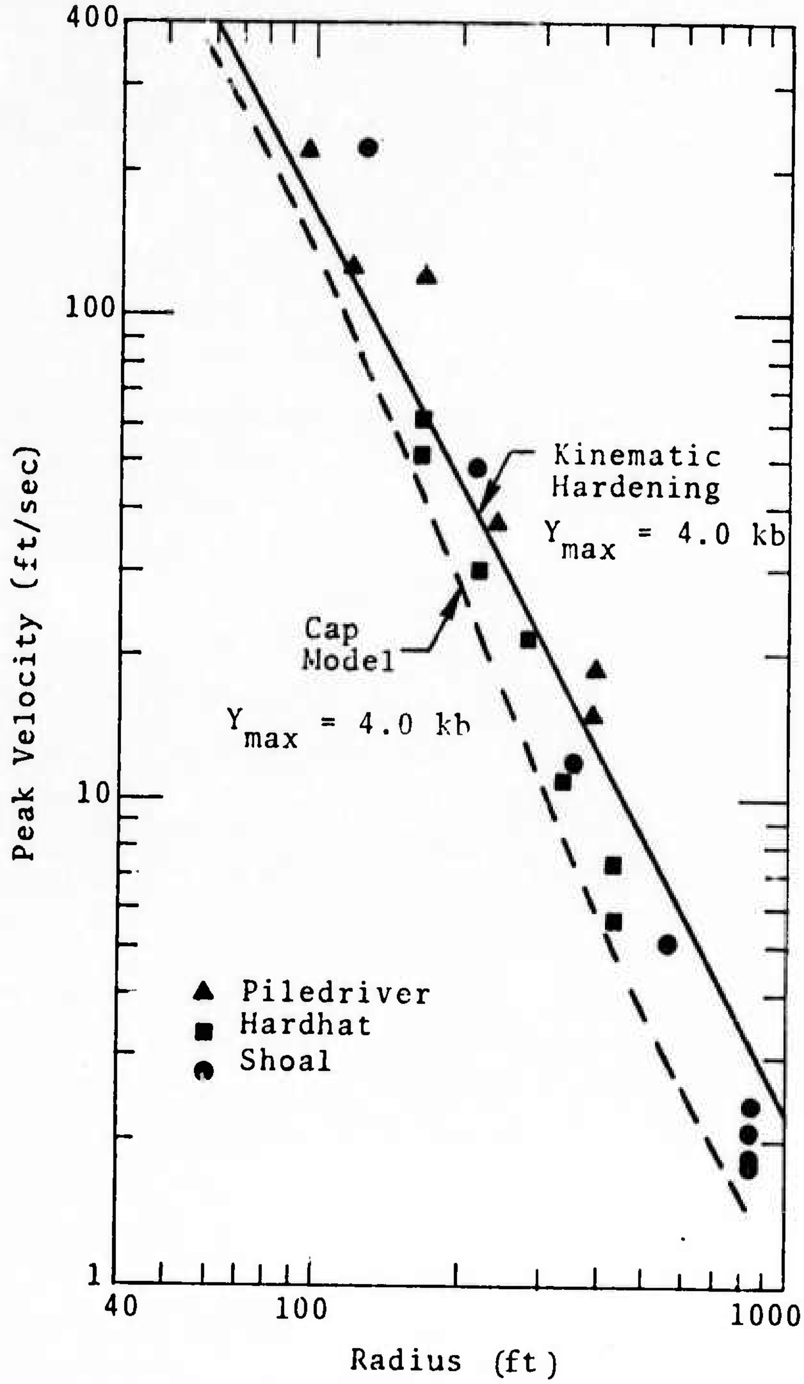

Fig. 3.13--Comparison of observed and calculated peak velocities for a 1-kT explosion in granite.

3.7.3 Comparisons of Calculations

The cap model can be adjusted to give a realistic value of crater size by lowering the value of flow stress from the laboratory value of 10.56 kbar to 2.6 kbar at normal strain rates. The maximum, or reference, flow stress is 4.0 kbar, but the 2.6 kbar value is cited for comparison, since this is the value of Y_0 that would be obtained at normal conditions using the strain-rate relation of Eq. (3.83). (A justification for this is that large masses of rock can be expected to include large cracks and hence a lower mean strength, than laboratory samples. In addition, the presence of water *in situ* can be expected to lower the strength significantly.) The time history of crater radius using the cap model, with adjusted strength is shown in Fig. 3.8. The final value of crater radius is 10.5 m, whereas the best estimate based on averaging Piledriver, Hardhat and Shoal data is 11.1 m. In view of the many uncertainties, it did not seem appropriate to improve this agreement by adjusting parameters. In the same figure the history of cavity radius is shown for kinematic hardening. The strength is unchanged from the cap model value, but the radius is somewhat lowered, and a significant amount of overshoot takes place. To get a computed cavity radius that agrees with the shot data, the reference strength for the kinematic hardening calculation was lowered to 1.68 kbar. It can be seen in the figure that the amount of overshoot was significantly increased as a result of this change. Unfortunately, as a result of the way the problem was set up (the number of zones was limited to 350), it was not possible to continue the calculation until the oscillation died out. It seems probable, however, that the final value of cavity radius would be near the observed size.

Comparisons with measured displacements are shown in Figs. 3.9, 3.10, and 3.11. The first two correspond to the

668- and 1543-foot stations for Piledriver. The displacement histories given by Perret were scaled to 1 kT, assuming a yield of 61 kT and the cube root scaling law to get the traces called "observed". The third comparison with a measured displacement history is based on the displacement trace reported by Werth and Herbst. In the first comparison, at a scaled radius of 51.9 m, the "cap" model curve approaches the value based on the Borg fit, 16 cm, with very little overshoot, the peak amplitude being 18 cm. The observed peak displacement, scaled, is 41.5 cm. Inspection of the figure shows that the kinematic hardening model results in a more realistic behavior. The peak overshoot is 50 cm, for Y_0 = 1.68 kbar, and the timing is generally like that observed. At a radius of 120 m the conclusions are similar. The cap model results in a peak displacement of 1.90 cm where the measured peak is 10.1 cm, and it occurs considerably later. The kinematic hardening model gives a peak of 8.3 cm and the timing is also roughly similar to that observed. In interpreting these results, it should be borne in mind that there is considerable variation in measurement between different instruments at the same station. The difference between the kinematic hardening calculation and the observed displacement is not greater than the difference between records from a velocity pick-up and an accelerometer at this station.

The displacement reported by Werth and Herbst, scaled to 1 kT, has a peak value of 2.18 cm where the cap model gives a peak value of 0.82 cm, and the peak occurs somewhat early. The kinematic hardening model gives a peak value of 1.8 cm which occurs only slightly earlier than the observed peak value.

The permanent displacement data is summarized in Fig. 3.12, with the experimental points being reduced to 1 kT by cube root scaling, as before. The values for Hardhat

and Piledriver displacement are taken from Perret's report, except for the last Hardhat point, which is taken from Werth and Herbst. The experimental data points generally correlate well with Borg's fit and with the theoretical value, $R_0^3/3R^2$, except for one Piledriver point which is questionable. The "cap" model predicts more attenuation than is observed, whereas the kinematic hardening model gives very nearly the correct slope. Only the kinematic hardening calculation for the reference strength of 4.0 kbar is plotted, since the displacement had not reached a steady state in the second kinematic hardening calculation.

Peak velocity data are compared in Fig. 3.13, which is taken from Perret's report and compares data from Piledriver, Hardhat and Shoal, scaled to 1 kiloton. Superimposed on the data are the results of a cap model and a kinematic hardening model calculation, both for the 4.0 kbar reference strength. The cap model calculation lies consistently below the measurements, whereas the kinematic hardening model is in general agreement with the measurements. The slope of the kinematic hardening calculation seems to be a little lower than the indicated slope of the measured peak velocities. Unfortunately, peak values of velocity for the kinematic hardening model with reference strength of 1.68 kbar are not available because the printing frequency in setting up the calculation was too low.

3.8 PARAMETRIC STUDIES OF GRANITE

A series of spherically symmetric one-dimensional shock wave propagation problems in granite was run using the SKIPPER finite difference code. The purpose of these calculations was to evaluate the effects on ground motion of varying certain material properties. To run problems in which all parameters occurring in the constitutive relations are varied in a controlled manner so that the effect of each on wave propagation could be evaluated would be a very lengthy task. Inasmuch as the greatest uncertainty in material response models for media affected by an explosion in the ground is for stresses in the region below ten kilobars, variations of strength parameters were investigated. Thermodynamic parameters, which would be more important in the very high pressure regime, were held constant. Ideally, it would have been desirable to carry the problems to the point at which the peak stress levels had attenuated to the level of seismic signals and motion had essentially ceased. This was done in the calculations for comparison with field data (Section 3.7), but was not feasible for the parameter studies. The problems were run to times of about 20 msec and stresses had attenuated to the order of one kilobar. These calculations were sufficient to show the effect of varying certain strength parameters on peak stress attenuation cavity growth, pulse shape and particle displacement. The strength parameters were chosen in a range that is representative of what one might expect to find in granite.

The source in all but one of the calculations reported in this section is the same as used for the material parameter study for tuff reported in Section II. It consists of a spherical cavity in the material which contains a gas obeying a pressure-volume-energy (p,V,E) equation of state

given by

$$E = \frac{pV}{\gamma - 1} \tag{3.99}$$

The value $\gamma = 1.4$ was used. Initially the radius of the cavity is 3.72 meters and the internal energy of the gas is 33.5×10^{19} ergs, an amount of energy equivalent to the yield of 8 kT of high explosive. The flow within the cavity gas is not calculated. The pressure within the gas, and thus the stress acting on the cavity wall, is taken to be uniform during each time step in the calculation and is given by

$$p(t) = p_0 \left(\frac{R_0}{R(t)}\right)^{3\gamma}, \qquad p_0 = 621 \text{ kbar} \tag{3.100}$$

where $p(t)$ and $R(t)$ are the cavity pressure and radius respecitvely at time t. The initial value of 3.72 m for the cavity was chosen on the basis that it approximately represents the volume of rock vaporized by an energy release of 8 kT of explosive. In one problem the cavity radius was increased to 8 m to give an order of magnitude increase in the volume in which the 8 kT was deposited.

The p-V-E equation of state used for the rock material was the blend between the high pressure and low pressure forms described in Section 3.4.1. The required material constants used are those listed below:

$$\rho_0 = 2.68 \text{ g/cc}$$

$$a = 0.5$$

$$b = 1.3$$

$$E_0 = 1.6 \times 10^{11} \text{ ergs/g}$$

$$A_\alpha = 518 \text{ kbar}$$

$$B = 180 \text{ kbar}$$

$$a_0 = 0.409$$

$$\beta_0 = 0.029 \text{ kbar}^{-1}$$

$$E_m = 1.8 \times 10^{10} \text{ ergs/g}$$

Except for a small change in a_0 and A_0 these are the same values used for granite in Section 3.7 (Table 3.4).

A principal stress component σ_i is given by

$$\sigma_i = -p + S_i \tag{3.101}$$

where S_i is the associated principal deviatoric stress. In the calculations reported in this section, three models were used to limit the deviatoric terms and treat the strength of the rock material. These three models are:

(a) Simple von Mises

$$S_1^2 + S_2^2 + S_3^2 \leq \frac{2}{3} Y_0^2 \left(1 - \frac{E}{E_m}\right) \tag{3.102}$$

where Y_0 is a constant yield strength.

(b) Mohr-Coulomb

$$S_1^2 + S_2^2 + S_3^2 \leq \frac{2}{3} Y^2(p) \left(1 - \frac{E}{E_m}\right) \tag{3.103}$$

where $Y(p)$ is a yield strength which is dependent upon the hydrostatic pressure. In the present work the form of $Y(p)$ is taken to be the exponential form

$$Y(p) = Y_0 - \left(Y_0 - Y_1\right) e^{-3\beta_1 p} \tag{3.104}$$

where Y_0, Y_1, and β_1 are constants.

For all cases the rigidity modulus was held constant at μ = 228 kbars. The factor $(1 - E/E_m)$ multiplying the Y's represents a thermal softening term. When the internal energy E reaches the melt energy, E_m, the strength vanishes and the material can no longer support any deviatoric stresses.

(c) <u>Capped Yield Surface</u>

The yield surface has the exponential form given by Eq. (3.104). However, it is capped by an ellipse which is tangent to the exponential yield surface at their point of intersection. The elliptical cap moves in the Y-p plane* according to the amount of plastic work hardening that occurs. The point of intersection of the yield surface and the cap, the ratio of the major and minor axes of the elliptical cap, and the center of the ellipse are functions of a work hardening parameter. The computation of the work hardening parameter, κ, is described in Section 3.4.2. The yield surface and cap are shown in Fig. 3.4.

---

*Some confusion can arise between the p-Y plane and the J_1 vs $\sqrt{J_2}$ plane where J_1 is the first stress total invariant and J_2 is the second deviatoric stress invariant. Here the following definitions are used:

$$p \equiv -\frac{1}{3}\left(\sigma_1 + \sigma_2 + \sigma_3\right)$$

$$\frac{2}{3} Y^2 \equiv S_1^2 + S_2^2 + S_3^2$$

$$J_1 \equiv \sigma_1 + \sigma_2 + \sigma_3$$

$$J_2 \equiv \frac{1}{2}\left(S_1^2 + S_2^2 + S_3^2\right)$$

Thus, $J_1 = -3p$ and $\sqrt{J_2} = \frac{Y}{\sqrt{3}}$

After several short test runs to assure that the constitutive relations described above were functioning satisfactorily in the SKIPPER code, a total of seven production runs, calculations on granite were carried out to times in excess of 20 milliseconds. A description of the plasticity models for these runs is summarized in Table 3.5 and the calculational results are presented in Figs. 3.14 through 3.25.

The asymptotic value approached by the shear yield strength in the Mohr-Coulomb model in Run G1 is the same as the constant shear strength in the von Mises model in Run G2. The Mohr-Coulomb model produces a larger cavity (Fig. 3.14), more rapid attenuation of the peak stress for $R > 60$ m (Figs. 3.16, 3.18, 3.20) and greater radial displacement (Figs. 3.22, 3.24). For the von Mises model, tensile hoop stresses and tensile radial stresses occur (Fig. 3.20).

Runs G1 and G4 both employ the Mohr-Coulomb model, but the asymptotic shear strength in Run G4 is only half that in Run G1. The smaller shear strength produces a larger cavity (Fig. 3.15), less rapid attenuation for $R > 50$ m (Figs. 3.17, 3.19, 3.21) and greater radial displacement (Figs. 3.23, 3.25).

The effect of introducing a material fracture by setting tensile stresses to zero that occur in the von Mises model is illustrated by comparing Runs G2 and G3. This failure criterion causes a larger cavity (Fig. 3.14), more rapid attenuation of the peak stress once the unloading wave from the fractured region at the tail of the pulse catches up with the wave front (Figs. 3.16, 3.18, 3.20), and, apparently, a larger final radial displacement (Figs. 3.22, 3.24). The displacement histories also have different shapes since the imposition of the failure criterion inhibits rebound (Fig. 3.24).

TABLE 3.5

GRANITE PARAMETER STUDY RUNS

Run No.	Strength Model	Strength Parameters	Comments
G1	Mohr-Coulomb High Strength	Y_0 = 6.928 kbar Y_1 = 0.358 kbar β_1 = 0.042 $kbar^{-1}$	Reference calculation for other runs.
G2	Von Mises Without Failure	Y_0 = 6.928 kbar	Yield strength same as asymptotic value in Run G1. Tensile hoop stresses develop after about 11.3 msec.
G3	Von Mises With Failure	Y_0 = 6.928 kbar	Identical to Run G2 except tensile failure criterion introduced. No tensile stresses allowed. If tensile stress develops, it is set equal to zero and stress deviators readjusted.
G4	Mohr-Coulomb Low Strength	Y = 3.464 kbar Y_1 = 0.358 kbar β_1 = 0.042 $kbar^{-1}$	Identical to Run G1 except asymptotic value of Y(p) is one half that of Run G1.
G5	Capped Surface Low Strength	Cap Parameters R_0 = 4.0 β_2 = 0.724 × 10^{-9}	Same yield surface as in Run G4. Elliptical cap and associated flow rule added.
G6	Mohr-Coulomb Large Cavity	Same as Run G4	Identical to Run G4 except energy deposited gas in 8-m radius cavity instead of 3.72-m radius cavity.
G7	Mohr-Coulomb High Bulk Modulus	Same as Run G4 except a_0 = 0	Here Eq. (3.23) reduced to $f(\rho) = A\mu$ Low pressure bulk modulus is greater than in Run G4.

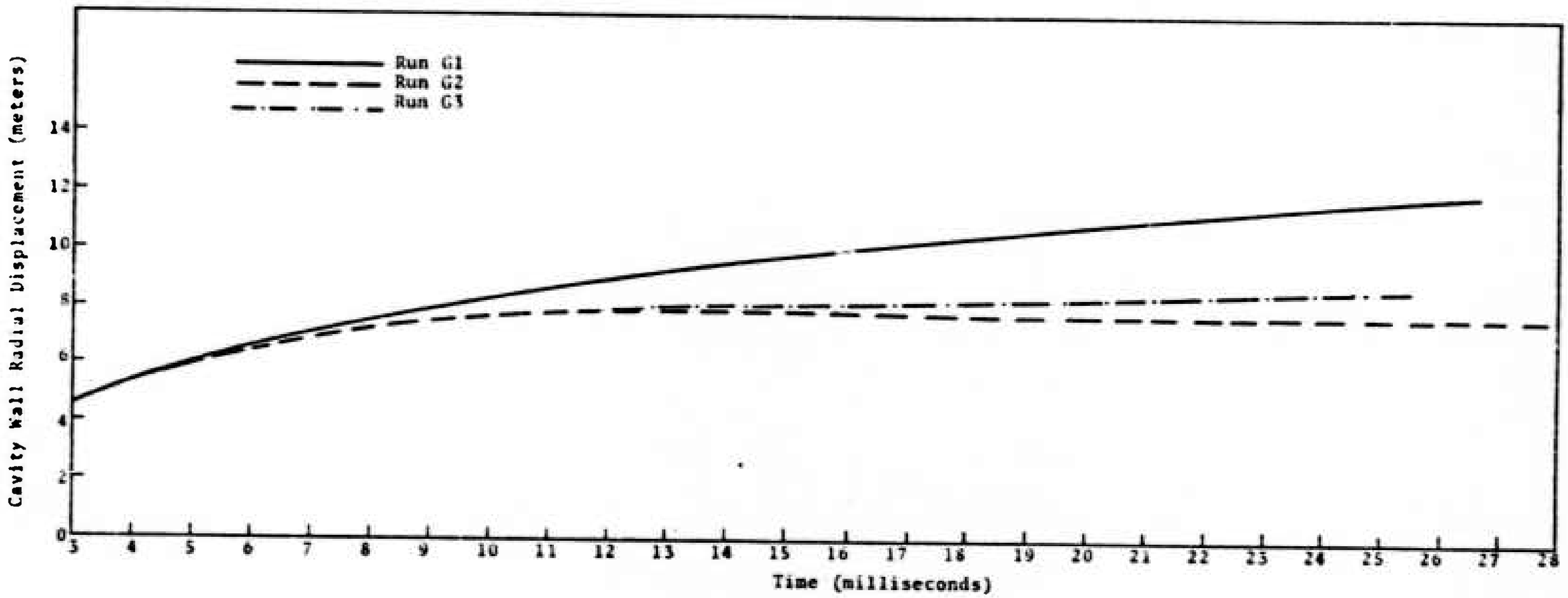

Fig. 3.14--Cavity wall displacement-time histories for Run G1 (Mohr-Coulomb, high strength), Run G2 (von Mises, without failure), and Run G3 (von Mises, with failure).

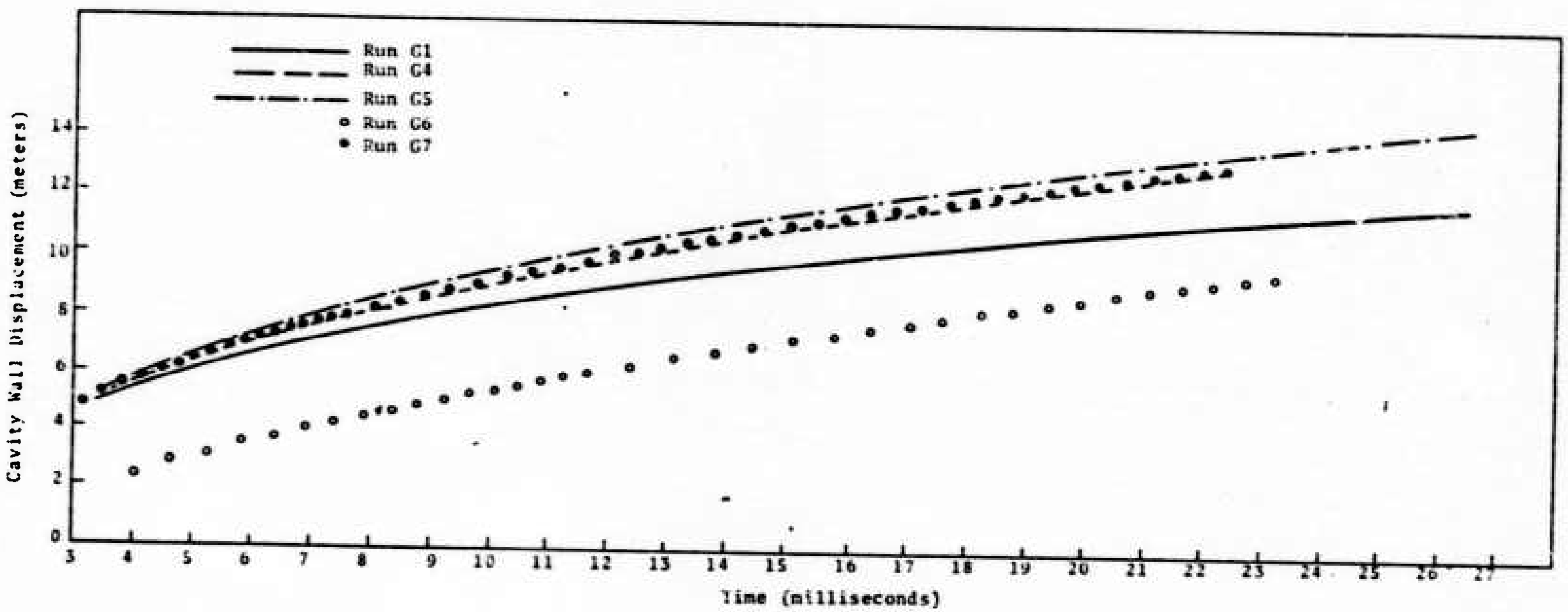

Fig. 3.15--Cavity wall displacement-time histories for Run G1 (Mohr-Coulomb, high strength), Run G4 (Mohr-Coulomb, low strength), Run G5 (capped surface, low strength), Run G6 (Mohr-Coulomb, large cavity), and Run G7 (Mohr-Coulomb, high bulk modulus).

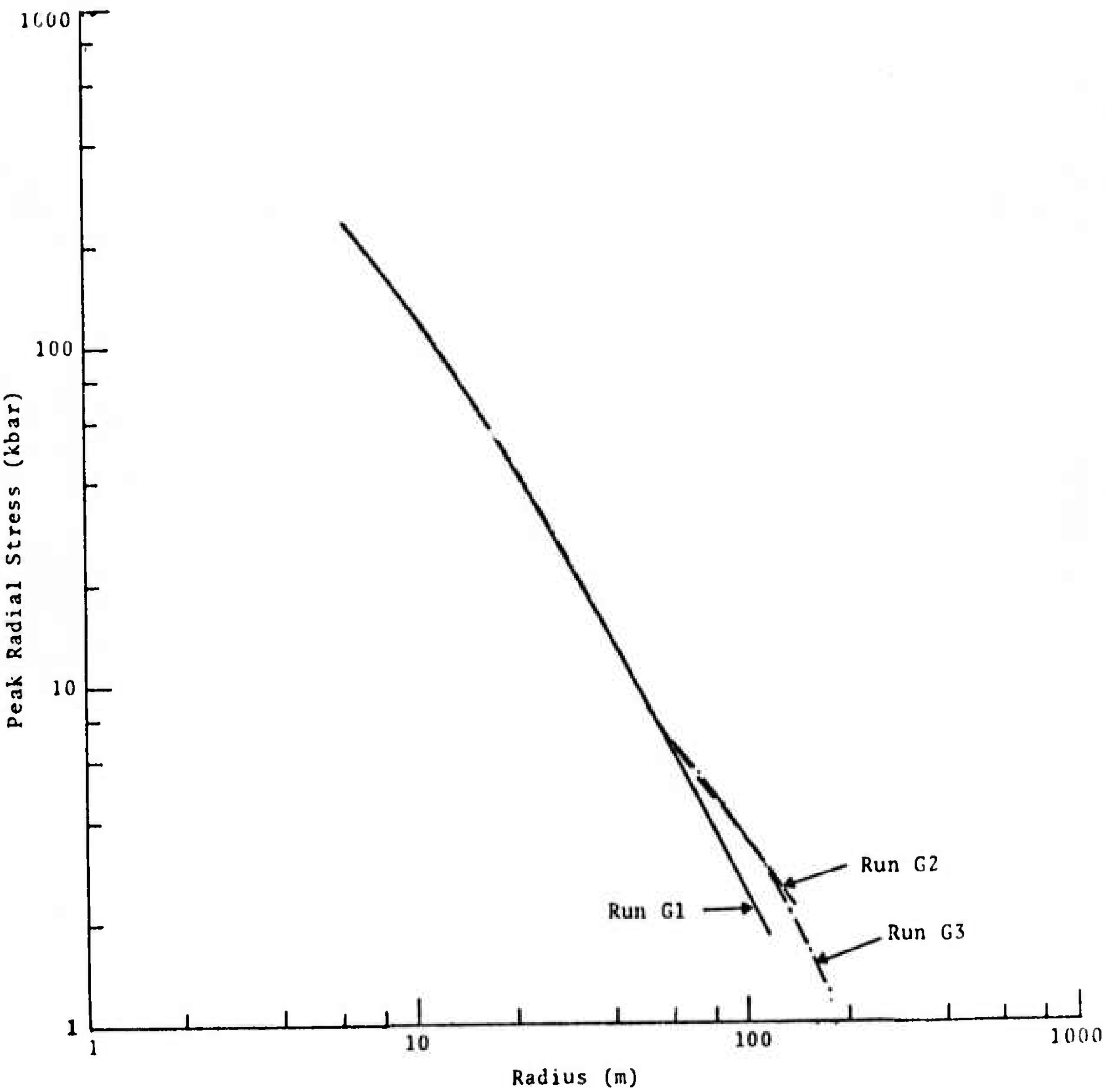

Fig. 3.16--Peak radial stress vs distance from source for Run G1 (Mohr-Coulomb, high strength), Run G2 (von Mises, without failure) and Run G3 (von Mises, with failure).

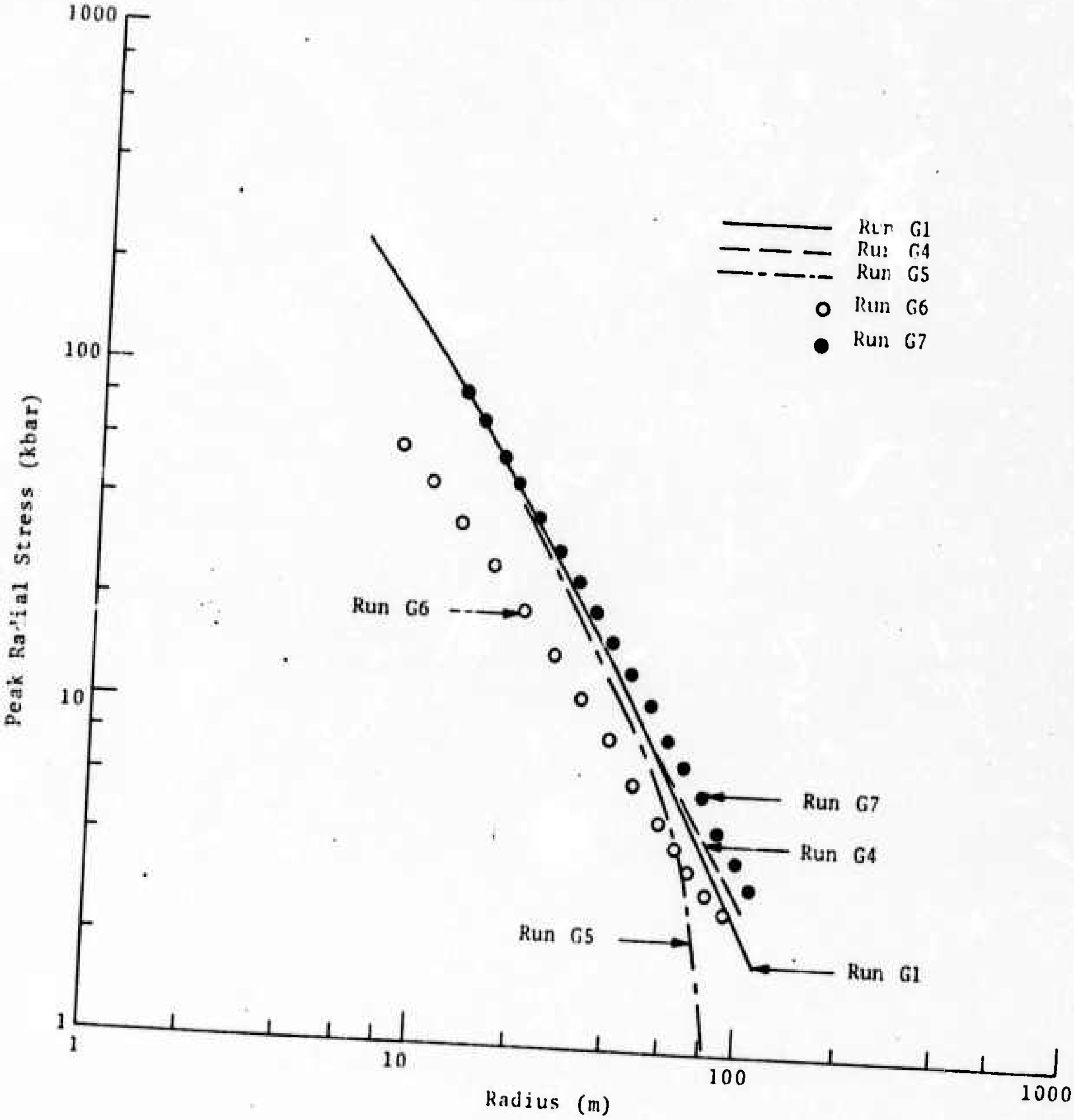

Fig. 3.17--Peak radial stress vs distance from source for Run G1 (Mohr-Coulomb, high strength), Run G4 (Mohr-Coulomb, low strength), Run G5 (capped surface, low strength), Run G6 (Mohr-Coulomb, large cavity) and Run G7 (Mohr-Coulomb, high bulk modulus).

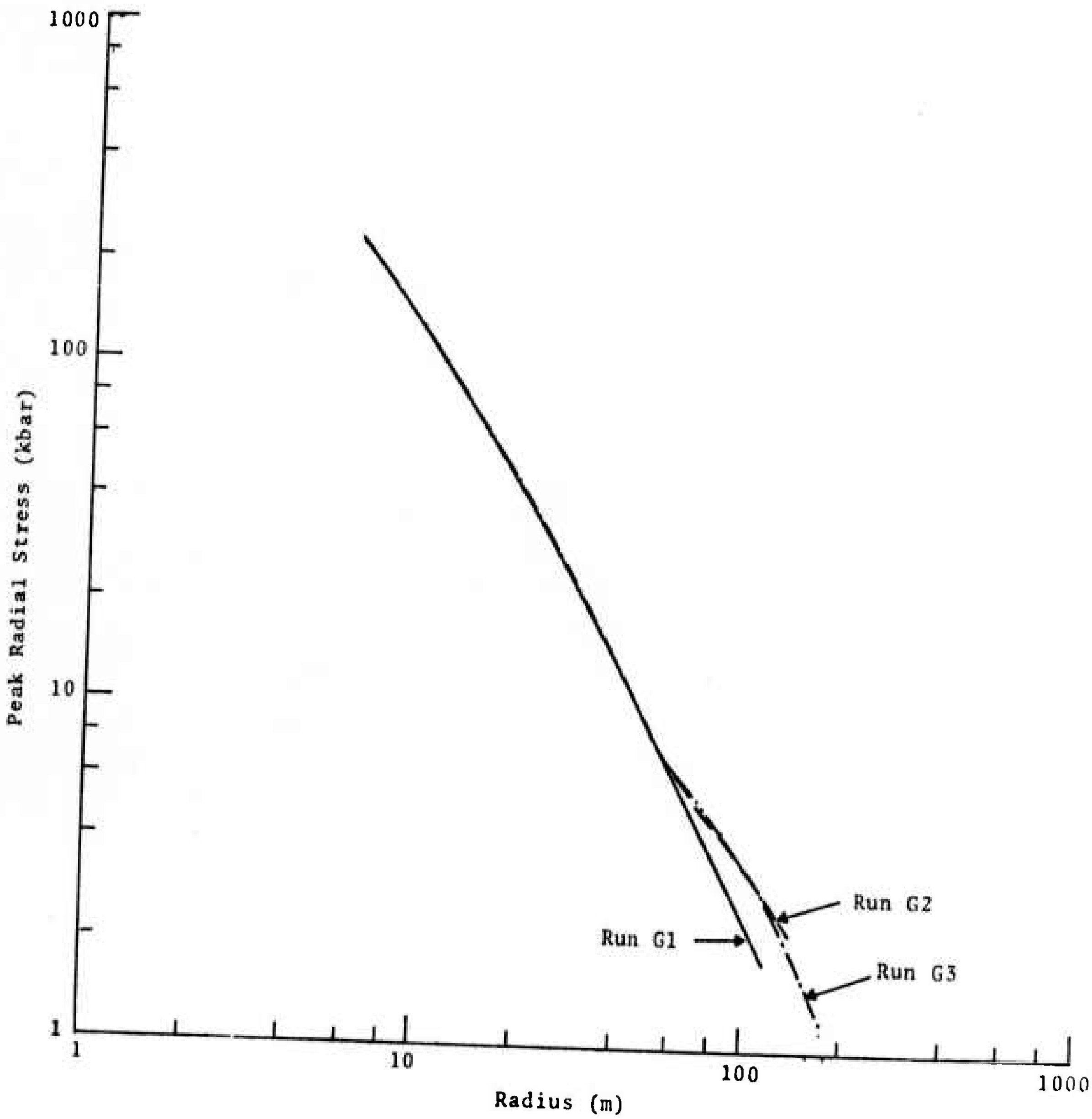

Fig. 3.16--Peak radial stress vs distance from source for Run G1 (Mohr-Coulomb, high strength), Run G2 (von Mises, without failure) and Run G3 (von Mises, with failure).

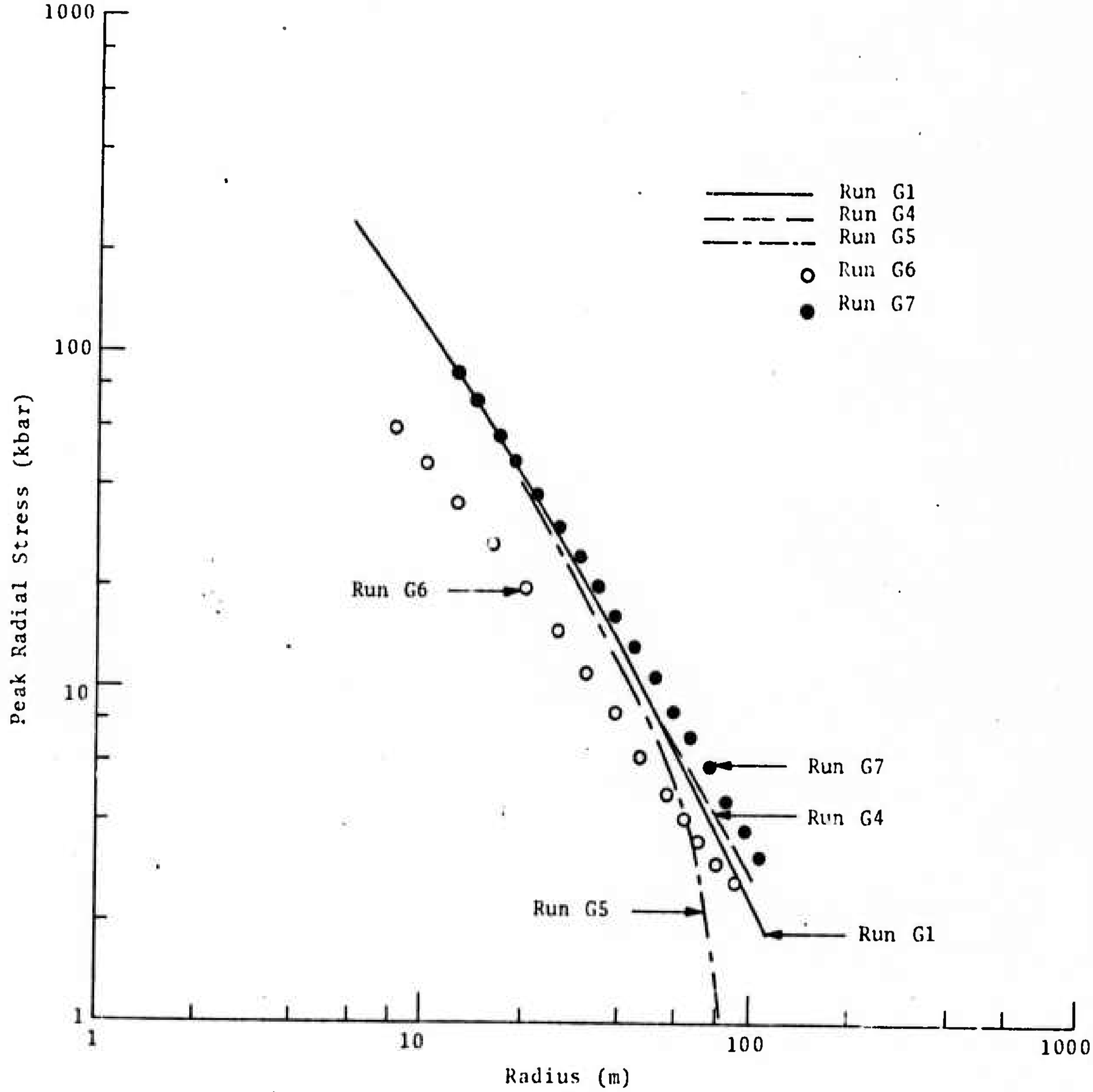

Fig. 3.17--Peak radial stress vs distance from source for Run G1 (Mohr-Coulomb, high strength), Run G4 (Mohr-Coulomb, low strength), Run G5 (capped surface, low strength), Run G6 (Mohr-Coulomb, large cavity) and Run G7 (Mohr-Coulomb, high bulk modulus).

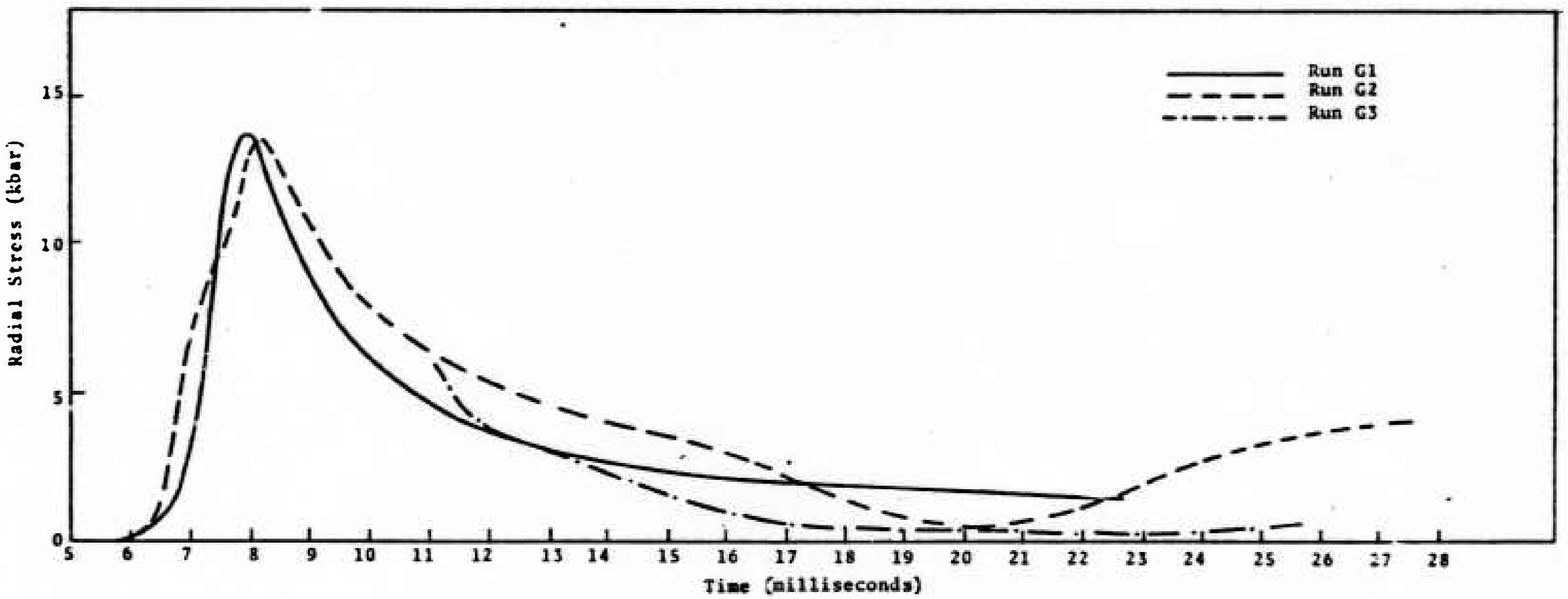

Fig. 3.18--Radial stress-time histories of particle initially 40.11 m from center of source for Run G1 (Mohr-Coulomb, high strength), Run G2 (von Mises, without failure) and Run G3 (von Mises, with failure).

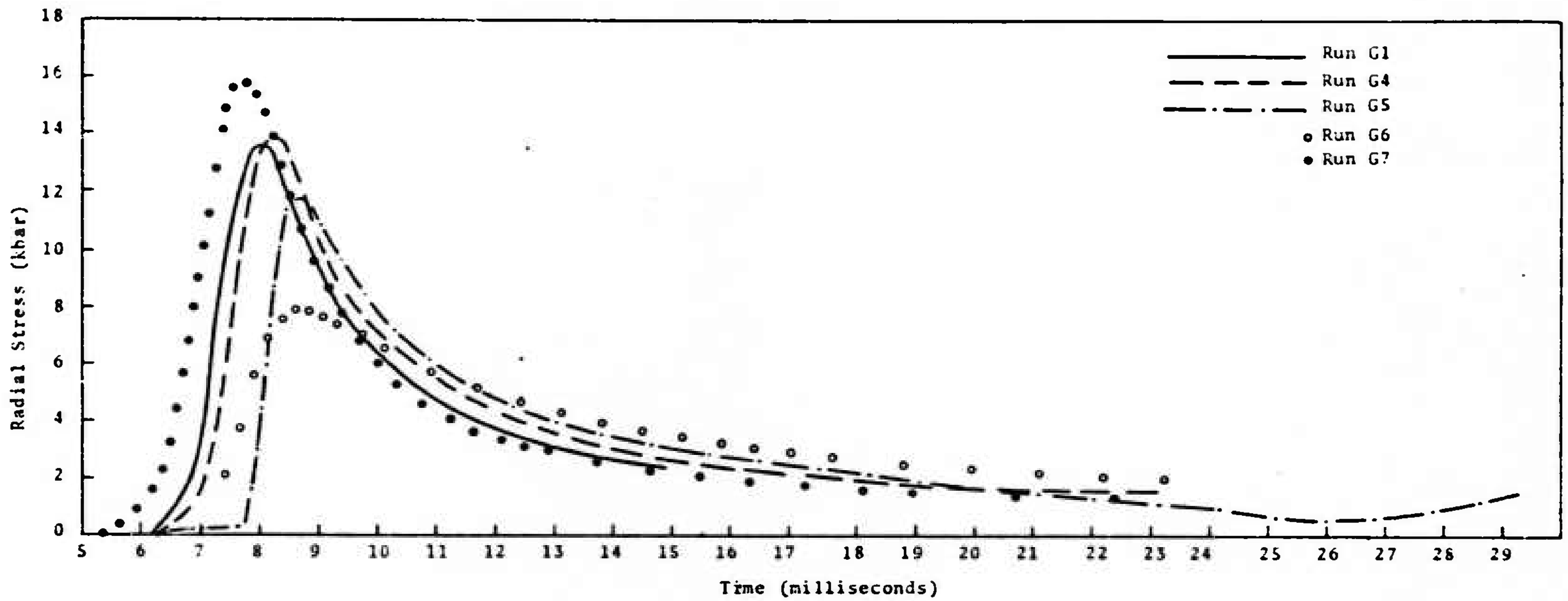

Fig. 3.19--Radial stress-time histories of particle initially 40.11 m from center of source for Run G1 (Mohr-Coulomb, high strength), Run G4 (Mohr-Coulomb, low strength), Run G5 (capped surface, low strength), Run G6 (Mohr-Coulomb, large cavity), and Run G7 (Mohr-Coulomb, high bulk modulus).

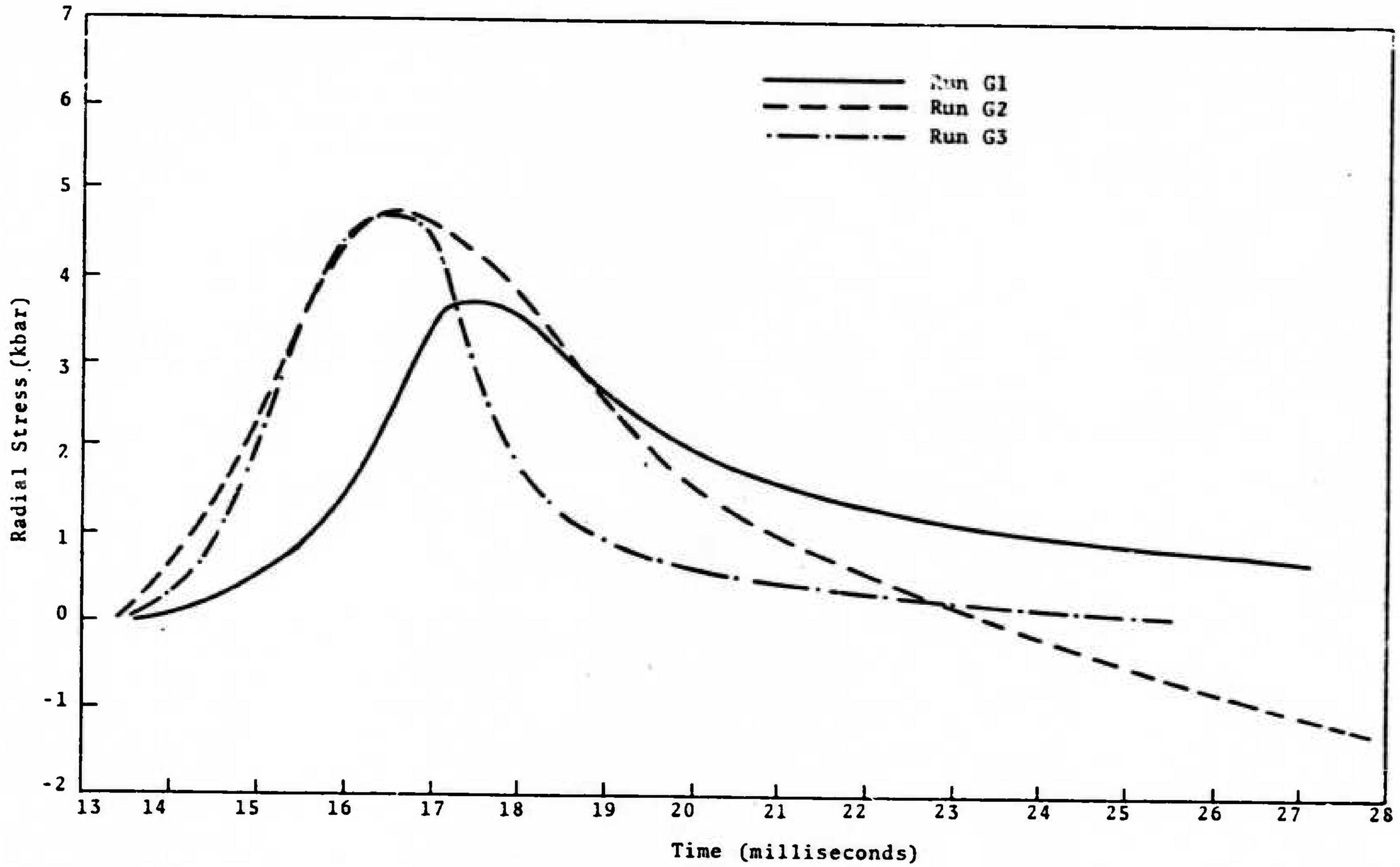

Fig. 3.20--Radial stress-time histories of particle initially 80.54 m from center of source for Run G1 (Mohr-Coulomb, high strength), Run G2 (von Mises, without failure), and Run G3 (von Mises, with failure).

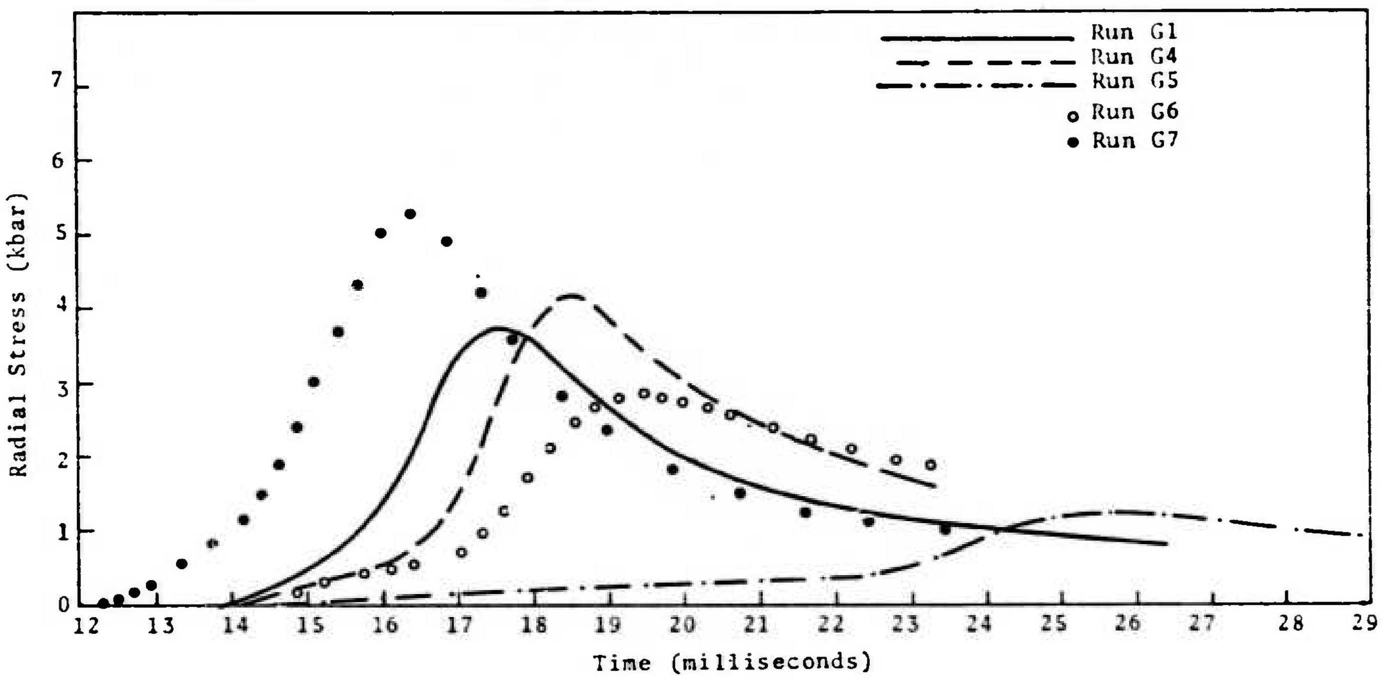

Fig. 3.21--Radial stress-time histories of particle initially 80.54 m from center of source for Run G1 (Mohr-Coulomb, low strength), Run G4 (Mohr-Coulomb, low strength), Run G5 (capped surface, low strength), Run G6 (Mohr-Coulomb, large cavity), and Run G7 (Mohr-Coulomb, high bulk modulus).

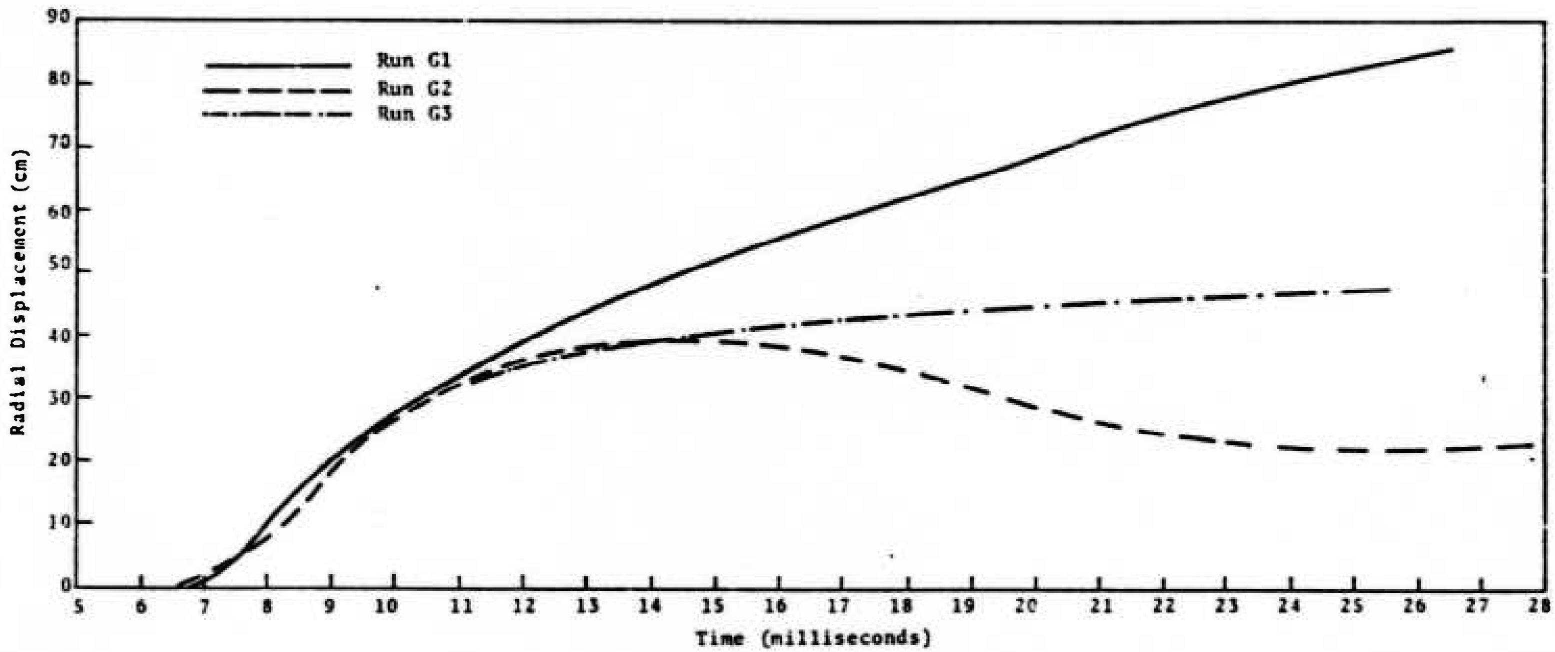

Fig. 3.22--Radial displacement-time histories of particle initially 40.11 m from center of source for Run G1 (Mohr-Coulomb, high strength), Run G2 (von Mises, without failure), and Run G3 (von Mises, with failure).

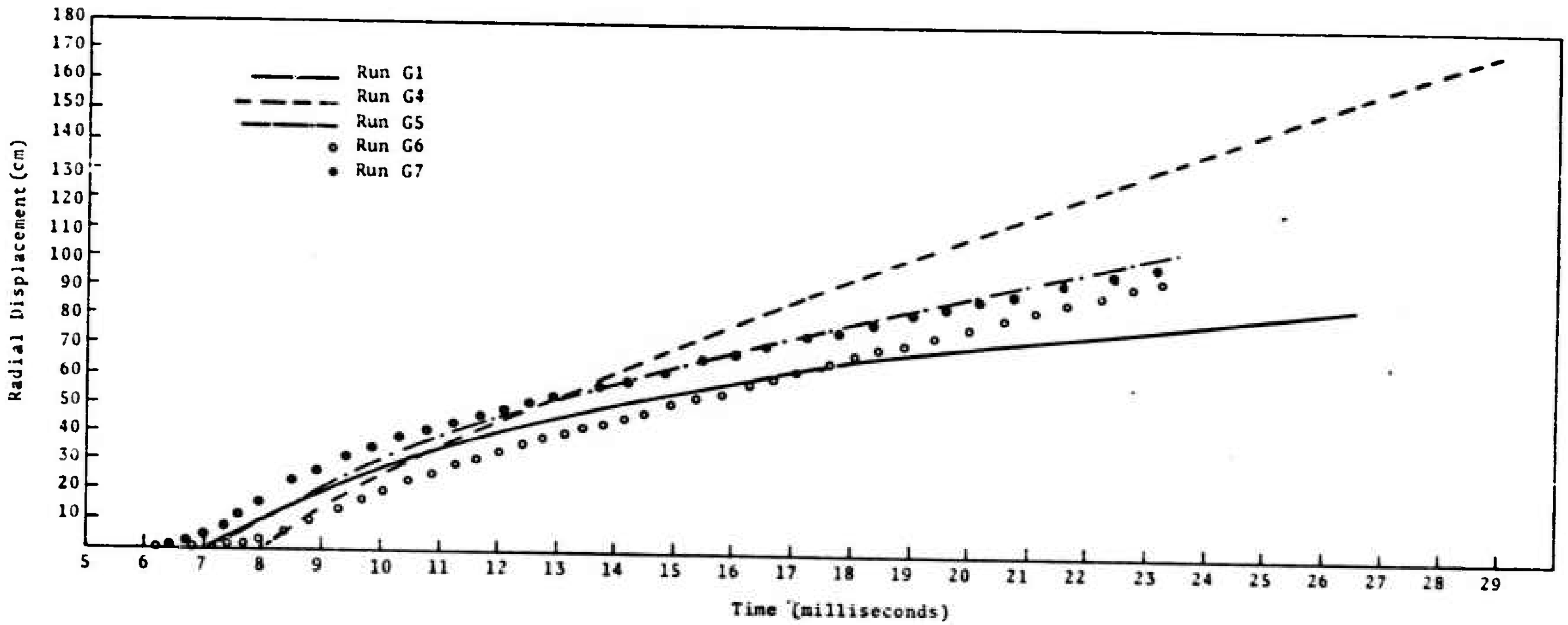

Fig. 3.23--Radial displacement-time histories of particle initially 40.11 m from center of source for Run G1 (Mohr-Coulomb, low strength), Run G4 (Mohr-Coulomb, low strength), Run G5 (capped surface, low strength), Run G6 (Mohr-Coulomb, large cavity), and Run G7 (Mohr-Coulomb, high bulk modulus).

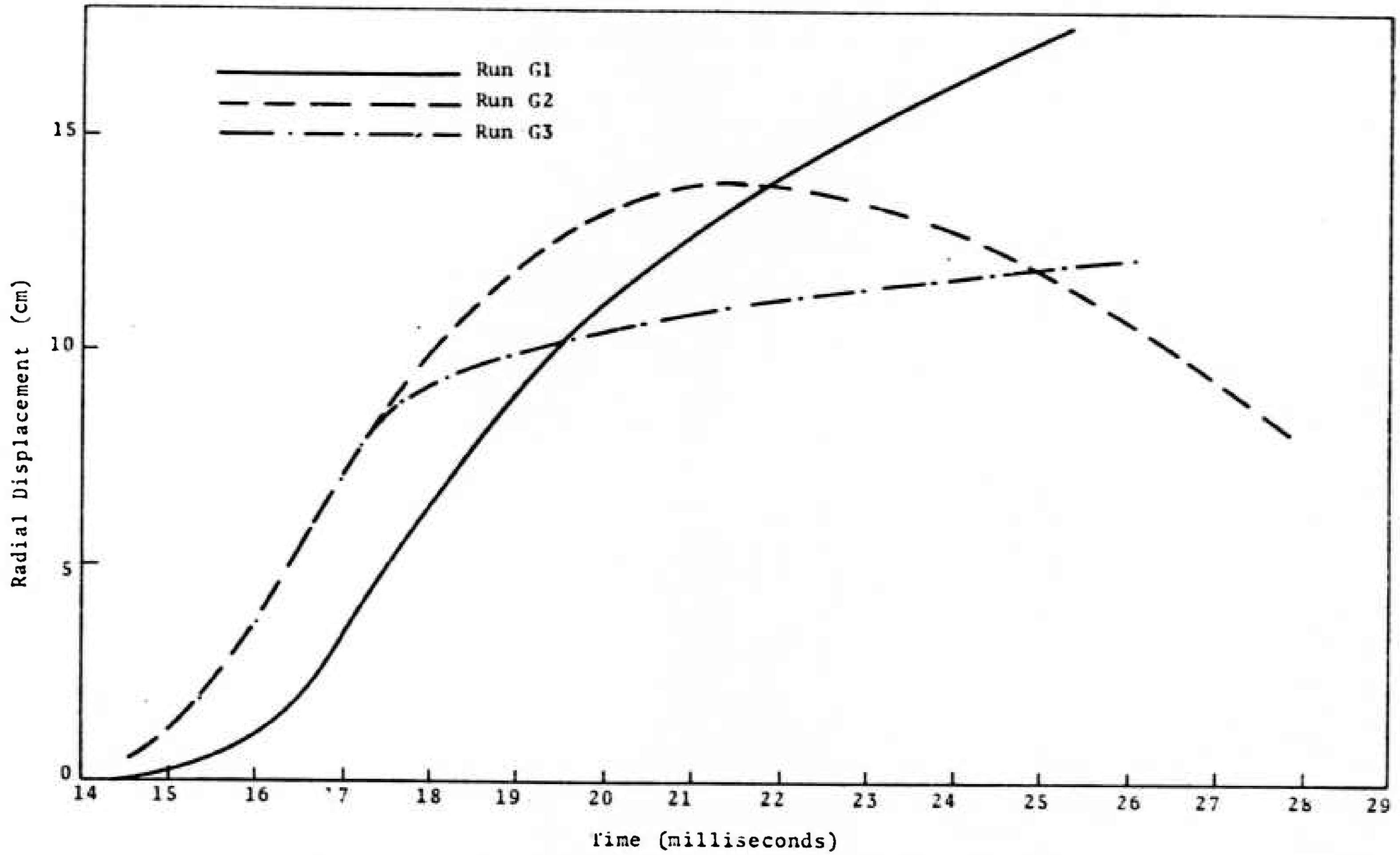

Fig. 3.24--Radial displacement-time histories of particle initially 80.54 m from center of source for Run G1 (Mohr-Coulomb, High Strength), Run G2 (von Mises, without failure), and Run G3 (von Mises, with failure).

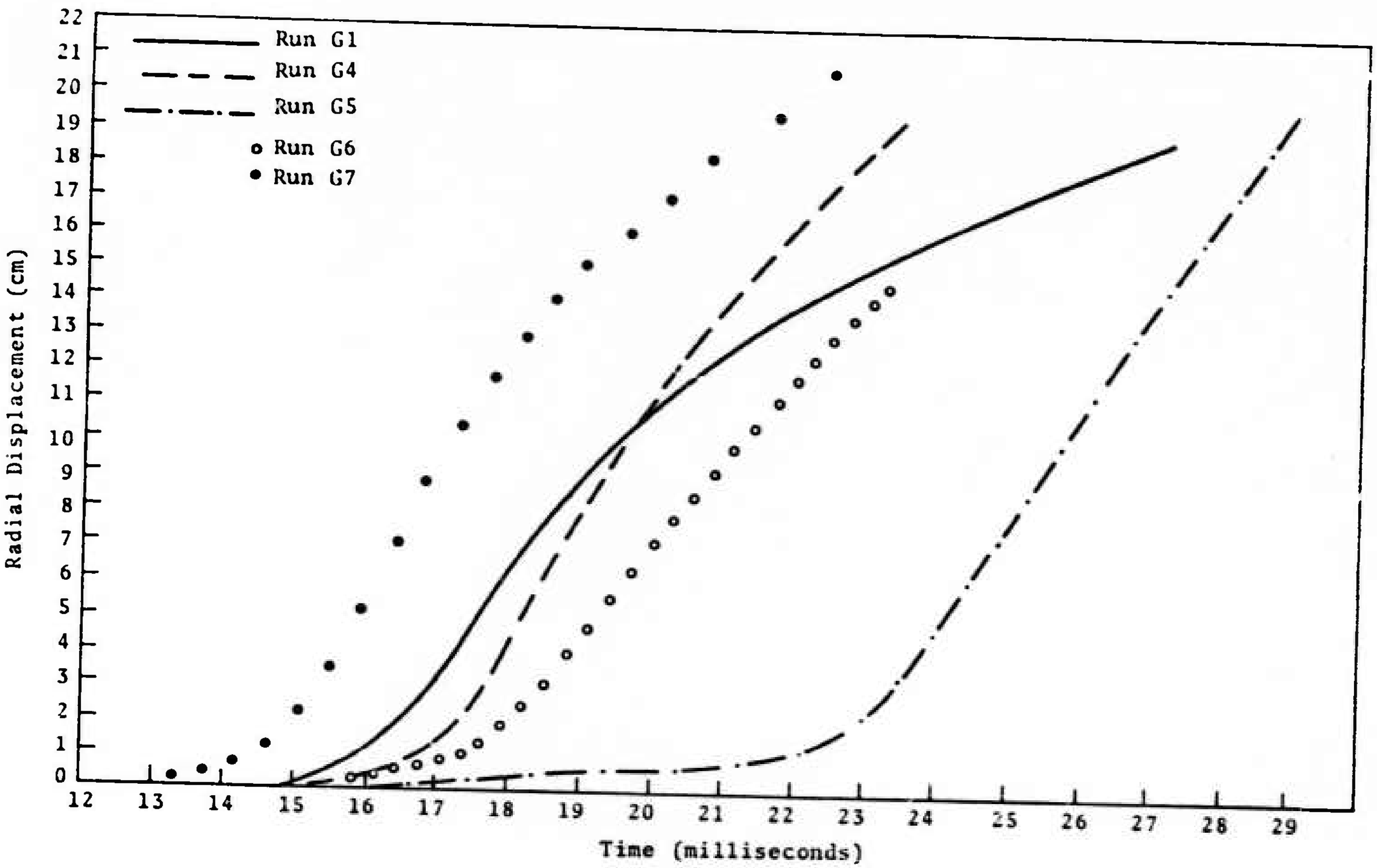

Fig. 3.25--Radial displacement-time histories of particle initially 80.54 m from center of source for Run G1 (Mohr-Coulomb, low strength), Run G4 (Mohr-Coulomb, low strength), Run G5 (capped surface, low strength), Run G6 (Mohr-Coulomb, large cavity), and Run G7 (Mohr-Coulomb, high bulk modulus).

The effect of putting a cap on the Mohr-Coulomb elliptical yield surface and introducing an associated flow rule is demonstrated by comparing Runs G4 with Run G5. The cap model in Run G5 produces a slightly larger cavity size (Fig. 3.15), much faster wave attenuation for $R > 30$ m (Figs. 3.17, 3.19, 3.21), and apparently, smaller radial displacements (Figs. 3.23, 3.25). The great difference in attenuation arises from the treatment of void collapse inherent in the cap plasticity model, but not in the Mohr-Coulomb model as treated in Run G4. The porosity effect could be introduced in the p-V-E equation of state within the Mohr-Coulomb model (or the von Mises model) and a result closer to that obtained by the cap model would be obtained.

Run G6 uses the identical Mohr-Coulomb model used by Run G4, but the cavity in which the 8-kT energy is initially deposited is increased by an order of magnitude so that the initial pressure in the gas is reduced from 1.54 mbar to 60 kbars. All ground motion quantities are drastically reduced, at least for $R < 100$ m. The gas pressure is too near the value of the shear strength of the granite for the results to be insensitive to the choice of the cavity radius.

Run G7 uses the same Mohr-Coulomb model as Run G4 except the bulk modulus is kept constant at the value derived from shock wave data rather than permitted to vary continously with pressure according to Eq. (3.24). The effectively higher bulk modulus produces almost an identical cavity size (Fig. 3.15), but causes decreased wave attenuation and higher wave speed at large distances (Figs. 3.7, 3.19, 3.21). At $R = 40.11$ m, it produces a smaller radial displacement (Fig. 3.23), but apparently a larger radial displacement at distance $R = 80.54$ m from the source.

3.9 DISCUSSION OF RESULTS

In formulating the constitutive equations, particular attention was given to the definition of strain and strain rate. The current definitions lead to constitutive equations consistent with those used by Wilkins and in common use in a variety of spherical, Lagrangian codes. This is accomplished by defining the principal strains as the logarithms of the principle stretches, and equating the strain rate tensor with the symmetric part of the velocity gradient. Other approaches considered lead to mathematical and physical difficulties.

In particular, Morland[51] expresses the constitutive equation through an equation of the form

$$\dot{\underset{\sim}{U}}^{p} = a\underset{\sim}{I} + b\underset{\sim}{\sigma} + c\underset{\sim}{\sigma}^{2} \tag{3.105}$$

where U^p is the plastic part of the right stretch tensor. If the principal strain is defined as the logarithm of the principal stretch, a constitutive equation of this form is awkward since it contains the stretch explicitly. Furthermore, the condition of incompressibility

$$\frac{\dot{\lambda}_1}{\lambda_1} + \frac{\dot{\lambda}_2}{\lambda_2} + \frac{\dot{\lambda}_3}{\lambda_3} = 0 \tag{3.106}$$

becomes difficult to enforce in a calculational scheme. By comparison, a constitutive equation of the form

$$\underset{\sim}{D}^{p} = a\underset{\sim}{I} + b\underset{\sim}{\sigma} \tag{3.107}$$

which involves the stretching, $\underset{\sim}{D}$, where

$$\underset{\sim}{D} = \frac{1}{2}\underset{\sim}{R}\left(\dot{\underset{\sim}{U}}\,\underset{\sim}{U}^{-1} + \underset{\sim}{U}^{-1}\,\dot{\underset{\sim}{U}}\right)\underset{\sim}{R}^{T} \tag{3.108}$$

is very convenient, since the separation of strain rates

$$\underset{\sim}{D} = \underset{\sim}{D}^p + \underset{\sim}{D}^e \tag{3.109}$$

follows trivially from the condition for separation of strains, $\varepsilon_{ij} = \varepsilon^e_{ij} + \varepsilon^p_{ij}$. Furthermore, the condition of incompressibility of plastic strains

$$D^p = \frac{\dot{\lambda}^p_1}{\lambda^p_1} + \frac{\dot{\lambda}^p_2}{\lambda^p_2} + \frac{\dot{\lambda}^p_3}{\lambda^p_3} = 0 \tag{3.110}$$

can be enforced by putting

$$a = -b \; tr(\underset{\sim}{\sigma}) \; , \tag{3.111}$$

which makes the plastic strain rate proportional to the deviatoric stress.

In the approach taken by Clifton the principal elastic strains are defined by

$$\varepsilon^e_i = \lambda^e_i - 1 \tag{3.112}$$

and the plastic strain by

$$\varepsilon^p_i = \lambda^p_i - 1 \tag{3.113}$$

and the plastic and elastic stretches are related by

$$\lambda^e_i \, \lambda^p_i = \lambda_i \; , \quad \text{not summed on } i \; . \tag{3.114}$$

As in Morland's approach, it is not a simple matter to enforce plastic incompressibility on the equations formulated in this manner, and the constitutive equations that

would result are quite complicated in their dependence on stretch and strain.

To recapitulate, it was found that a considerable simplification to the constitutive equations for finite deformation plasticity could be obtained by defining the principal strains as the logarithms of the principle stretches. The strain rate tensor becomes identical with the velocity gradient, a result not always obtained with previously suggested formulations.

The constitutive equation is obtained by setting the strain rate tensor proportional to the gradient of the plastic potential. The right stretch tensor is written as the product of an elastic and a plastic part.

$$U = U^e \, U^p \tag{3.115}$$

and no restriction is placed upon the plastic volume. Consequently, there is a plastic change in volume, and it is identified with the change in pore volume. The change in volume can be either an increase or a decrease, depending on the constitutive equation and the history of the deformation. Thus, the kinematics allows for either bulking or compaction.

The computer program and the analysis were formulated in such a way as to allow a choice of either no hardening, isotropic hardening as expansion of the yield surface, hardening by displacement of an elliptical cap, or kinematic hardening. Recent studies by Allen, et al.[50] at S³ and by Maxwell, et al.[52] at Physics International have indicated that the overshoot using the cap model is less than observed and this conclusion is consistent with the current results. A study by McKay and Godfrey[53] indicates that in the "tombstone" studies the attenuation of the calculated pulse is more rapid than observed. Both of these deficiencies in the

theoretical results can be explained by the absence of a Bauschinger effect in the isotropic hardening models. By accounting for the Bauschinger effect, the velocity of rarefaction waves is reduced and the unloading takes place more slowly. The velocity pulse at a fixed station is also stretched out over a longer time. This is generally what is required to bring the reported calculations into better agreement with measurements.

Although a parameter study using various plasticity models was conducted, Section 3.8, our major emphasis has been on trying to establish whether the currently used theories are consistent with measurements. In view of the disappointing correlation reported in the references of the preceding paragraphs, it seemed worthwhile to make an overall examination of the existing data and the material model. It was concluded that permanent displacement seems to be the most reliable measurement, and good correlations were generally found between measurements and the simple formula, $\delta = R_0^3/3R^2$. One Piledriver displacement is a notable exception. This displacement lies a factor of three above the "best fit" by Borg. Its reliability is, however, questionable simply in view of the substantial difference between the velocity and integrated acceleration measurements at the 1543-ft station, reported by Perret. (Though the two measurements agree quite well at early times, they diverge after 0.3 sec real time, or 76 msec in the scaled plot of Fig. 3.10. The accelerometer trace would lead to final values of displacement well below the best estimates given by Borg, and, in fact, would ultimately have the wrong sign since the duration of the negative velocity phase is indefinitely long.)

The peak velocity and final displacement predicted by the "cap" model are too low. This can be interpreted as a consequence of the excessively high rate of unloading when

the Bauschinger effect is not accounted for. A more realistic attenuation is predicted with the kinematic hardening model.

There remain a number of specific investigations which should be carried through to explain the existing discrepancies between calculation and measurement. Of particular concern is the reduction in flow stress by a factor of six that is required to bring calculations into agreement with shot data. The existence of large cracks and pore water are probably responsible for this discrepancy. It would be desirable to get quantitative information on this question, and on the relative importance of pore water and size effect on strength.

The effect of material dilatancy has not been examined in enough detail. Dilatancy was considered at one time to be one of the main effects causing discrepancy between calculation and shot data. The effect may be important, but as a result of the current study, it is believed that dilatancy should be considered in conjunction with a model that accounts for the Bauschinger effect.

The lithostatic pressure in the far-field causes the cavity to rebound. In addition, it significantly influences the strength. We have not accounted for either of these depth effects in the current calculation.

Finally, we note that a reasonable model for gross fracture due to excessive strain or tensile stress should be added to the simulation. The treatment of fracture should reflect the finite time required for cracks to propagate, and for the material to lose its competence. Such a model has not yet been incorporated into the computer programs commonly used to calculate underground nuclear explosions, but it is felt that the delay in fracturing and the residual strength would significantly influence the late behavior. Without a

gradual failure model, the material would tend to form isolated shells in the calculation, whereas in practice some competence is retained almost everywhere.

IV. THEORY OF INTERACTING CONTINUA

4.1 INTRODUCTION

Shock wave propagation in composite materials (e.g., fiber reinforced composites, water saturated rocks) is of interest to many areas of science and engineering. Composite materials display certain effects (e.g., geometric wave dispersion, internal dissipation) which cannot be adequately modeled within the usual restrictions of a homogeneous, isotropic media. The material properties of the various constituents, geometrical arrangement and the porosity (or void content) all affect the thermo-mechanical response of the composite. Thus, it is necessary to develop an analytical model, based on the microstructure of the composite which will enable one to evaluate the thermo-mechanical behavior of the material under various static and dynamic loading conditions. However, the variability in material properties and the difficulty of characterizing interfaces make a purely microscopic approach somewhat unattractive. A practical analytical model should provide an average description of the constituents rather than a detailed thermo-mechanical description at each material interface at each instant of time. The theory of interacting continua (TINC) provides a means for proceeding directly to the desired macroscopic level.

In 3SR-267[1] and 3SR-648,[2], this theory was introduced to provide a framework for describing the behavior of a geologic (dry and partially saturated tuff) material in terms of the isolated behavior of the constituents. The major emphasis therein was placed on developing a mechanical theory appropriate for planar stress wave propagation. This model was incorporated into the planar POROUS code. Additionally, Hugoniot relations were derived for a binary mixture in

Preceding page blank

3SR-648. During the past year, the prime objective has been to develop a thermodynamical theory suitable for wave propagation studies in planar or spherical geometry. After outlining the conservation relations in Section 4.2, we discuss the various interaction terms in Section 4.3. The constitutive relations are given in Section 4.4. The incorporation of the thermodynamical theory into a completely new version of POROUS treating both 1-D planar and spherical configurations is discussed in Section 4.5. Finally, in Section 4.6, we discuss some material parameter calculations using this code. Only limited calculations have been made since the new POROUS code is still in its final development stage at the time this report is being written.

4.2 GENERAL CONSERVATION LAWS

In TINC, it is assumed that every small volume of the composite body is occupied by particles of each constituent $\overset{(\alpha)}{s}$ (α = 1, 2, ... r). Furthermore, each constituent $\overset{(\alpha)}{s}$ has a velocity field $\overset{(\alpha)}{\underline{v}}(\underline{x},t)$ through the composite where $\underline{x}$ denotes the position vector in space (with reference to a fixed Newtonian frame) and t denotes time. The mass of constituent $\overset{(\alpha)}{s}$ per unit volume of composite is called its partial density $\overset{(\alpha)}{\rho}(\underline{x},t)$ and the total mass per unit volume of composite $\rho(\underline{x},t)$ is given by:

$$\rho = \sum_{\alpha=1}^{r} \overset{(\alpha)}{\rho} \tag{4.1}$$

Similarly, the total stress tensor $\underset{\sim}{\sigma}$ associated with a unit area of the composite can be decomposed into partial stresses $\overset{(\alpha)}{\underset{\sim}{\sigma}}$ associated with each component $\overset{(\alpha)}{s}$

$$\underset{\sim}{\sigma} = \sum_{\alpha=1}^{r} \overset{(\alpha)}{\underset{\sim}{\sigma}} \tag{4.2}$$

(For a physical explanation of the various terms occurring herein, reference is made to a paper by Garg.[7])

General relations expressing conservation of mass, momentum and energy may be written for each $\overset{(\alpha)}{s}$ (3SR-267 and 3SR-648). We will now assume that: (1) external body forces are absent, (2) there is no heat transfer to the external world, (3) no mass transfer occurs between the constituents due to chemical interactions, and (4) partial stress tensors $\overset{(\alpha)}{\sigma}_{ij}$ are symmetric. With these assumptions, the conservation relations become:

Continuity:

$$\int_V \left[\frac{\overset{(\alpha)}{D}\,\overset{(\alpha)}{\rho}}{Dt} + \overset{(\alpha)}{\rho}\,\mathrm{div}\,\overset{(\alpha)}{\underline{v}} \right] dV$$

$$= \int_V \frac{\partial \overset{(\alpha)}{\rho}}{\partial t}\, dV + \int_S \overset{(\alpha)}{\rho}\,\overset{(\alpha)}{v}_j\, n_j\, dS = 0 \qquad (4.3)$$

Momentum:

$$\int_V \overset{(\alpha)}{\rho}\, \frac{\overset{(\alpha)}{D}\,\overset{(\alpha)}{v}_i}{Dt}\, dV$$

$$= \int_V \frac{\partial}{\partial t}\left(\overset{(\alpha)}{\rho}\,\overset{(\alpha)}{v}_i\right) dV + \int_S \overset{(\alpha)}{\rho}\,\overset{(\alpha)}{v}_i\,\overset{(\alpha)}{v}_j\, n_j\, dS$$

$$= \int_S \overset{(\alpha)}{\sigma}_{ij}\, n_j\, dS + \int_V \rho\,\overset{(\alpha)}{\beta}_i\, dV \qquad (4.4)$$

Energy:

$$\int_V \overset{(\alpha)}{\rho}\, \frac{\overset{(\alpha)}{D}}{Dt}\left[\overset{(\alpha)}{E} + \frac{1}{2}\,\overset{(\alpha)}{v}_j\,\overset{(\alpha)}{v}_j\right] dV$$

$$= \int_V \frac{\partial}{\partial t}\left[\overset{(\alpha)}{\rho}\left(\overset{(\alpha)}{E} + \frac{1}{2}\,\overset{(\alpha)}{v}_j\,\overset{(\alpha)}{v}_j\right)\right] dV$$

$$+ \int_S \overset{(\alpha)}{\rho}\left[\overset{(\alpha)}{E} + \frac{1}{2}\,\overset{(\alpha)}{v}_j\,\overset{(\alpha)}{v}_j\right]\overset{(\alpha)}{v}_i\, n_i\, dS$$

$$= \int_S \overset{(\alpha)}{\sigma}_{ij} \overset{(\alpha)}{v}_i n_j \, dS - \int_S \overset{(\alpha)}{q}_j n_j \, dS$$

$$+ \int_V \left\{ \overset{(\alpha)}{\rho} \, \overset{(\alpha)}{\underline{\beta}} \cdot \underline{v} + \rho \overset{(\alpha)}{\psi} \right\} dV \qquad (4.5)$$

where

$$\overset{(\alpha)}{D}/Dt = \partial/\partial t + \overset{(\alpha)}{\underline{v}} \cdot \text{grad}$$

$\overset{(\alpha)}{\underline{v}}$ = velocity of material $\overset{(\alpha)}{s}$

$\overset{(\alpha)}{\rho}$ = partial density of $\overset{(\alpha)}{s}$

$\overset{(\alpha)}{\sigma}_{ij}$ = partial stress tensor for $\overset{(\alpha)}{s}$

$\rho \overset{(\alpha)}{\underline{\beta}}$ = momentum supply to $\overset{(\alpha)}{s}$ per unit mass of composite due to interaction forces

$\overset{(\alpha)}{E}$ = specific internal energy of $\overset{(\alpha)}{s}$

$\rho \overset{(\alpha)}{\psi}$ = energy supply to $\overset{(\alpha)}{s}$ per unit mass of composite due to interaction with the remaining α-1 constituents

$\underline{n}$ = normal to the surface S

$\overset{(\alpha)}{\underline{q}}$ = heat flux vector into $\overset{(\alpha)}{s}$ from the remaining α-1 constituents

The requirements that the total momentum and energy contributions of the internal material interaction forces be zero may be written as

$$\sum_{\alpha=1}^{r} \overset{(\alpha)}{\rho} \overset{(\alpha)}{\underset{\sim}{\beta}} = 0 \tag{4.6}$$

$$\sum_{\alpha=1}^{r} \left[\left(\overset{(\alpha)}{\underline{\beta}} \cdot \overset{(\alpha)}{\underline{v}} + \overset{(\alpha)}{\psi} \right) - \operatorname{div} \overset{(\alpha)}{\underline{q}} \right] = 0 \tag{4.7}$$

The balance equation for internal energy, $\overset{(\alpha)}{E}$, may be obtained by combining Eqs. (4.3), (4.4), and (4.5).

$$\int_V \overset{(\alpha)}{\rho} \frac{\overset{(\alpha)}{D}}{Dt} \left(\overset{(\alpha)}{E} \right) dV = \int_V \frac{\partial}{\partial t} \left(\overset{(\alpha)}{\rho} \overset{(\alpha)}{E} \right) dV + \int_S \overset{(\alpha)}{\rho} \overset{(\alpha)}{E} \overset{(\alpha)}{v}_i n_i \, dS$$

$$= \int_V \overset{(\alpha)}{\sigma}_{ij} \overset{(\alpha)}{v}_{i,j} \, dV - \int_S \overset{(\alpha)}{q}_j n_j \, dS$$

$$+ \int_V \overset{(\alpha)}{\rho} \overset{(\alpha)}{\psi} \, dV \, . \tag{4.8}$$

In writing down the above conservation relations in the TINC framework, no reference is made to the actual mean area, $\overset{(\alpha)}{m}$, and mean volume, $\overset{(\alpha)}{n}$, occupied by $\overset{(\alpha)}{s}$ per unit cross-sectional area and volume of the composite. If the interaction terms and constitutive relations for the composite are to be expressed in terms of the behavior of the isolated constituents, reference must be made to the actual constituents. In 3SR-267, effective densities, $\overset{(\alpha)}{\rho}{}^{e}$, and effective stress tensors, $\overset{(\alpha)}{\underset{\sim}{\sigma}}{}^{e}$, were defined in terms of partial densities

and partial stress tensors by the scaled relations:

$$\overset{(\alpha)}{\rho} = \overset{(\alpha)}{n}\,\overset{(\alpha)}{\rho}{}^{e} \tag{4.9a}$$

$$\overset{(\alpha)}{\underset{\sim}{\sigma}} = \overset{(\alpha)}{m}\,\overset{(\alpha)}{\underset{\sim}{\sigma}}{}^{e} \tag{4.9b}$$

where

$$\sum_{\alpha=1}^{r} \overset{(\alpha)}{n} = \sum_{\alpha=1}^{r} \overset{(\alpha)}{m} = 1 \tag{4.9c}$$

If the composite is isotropic so that each plane through the medium intersects the same area fraction of $\overset{(\alpha)}{s}$, the area and the volume fractions are the same for each $\overset{(\alpha)}{s}$.

$$\overset{(\alpha)}{m} = \overset{(\alpha)}{n} \tag{4.10}$$

In this case a single scaling function occurs in the relations (4.9).

In the following discussion $\alpha = 1, 2, 3$ will be used to designate rock (poreless), water and voids, respectively. The interaction terms in the next section are derived for the case when $\overset{(3)}{n} \equiv 0$, i.e., a fully saturated porous solid. The applicability of these terms to the unsaturated case is discussed in Section 4.4.

4.3 INTERACTION TERMS

For sake of convenience, we will restrict the discussion in this section to plane wave propagation in the x-direction. The interaction terms derived herein are, however, also applicable to spherical wave propagation. For planar wave propagation, the conservation relations (4.3), (4.4) and (4.8) may be written in the differential form as:

$$\frac{\partial \overset{(\alpha)}{\rho}}{\partial t} + \overset{(\alpha)}{v} \frac{\partial \overset{(\alpha)}{\rho}}{\partial x} + \overset{(\alpha)}{\rho} \frac{\partial \overset{(\alpha)}{v}}{\partial x} = 0 \tag{4.11}$$

$$\overset{(\alpha)}{\rho}\left(\frac{\partial \overset{(\alpha)}{v}}{\partial t} + \overset{(\alpha)}{v} \frac{\partial \overset{(\alpha)}{v}}{\partial x}\right) = \rho \overset{(\alpha)}{\beta} + \frac{\partial \overset{(\alpha)}{\sigma}_x}{\partial x} \tag{4.12}$$

$$\overset{(\alpha)}{\rho}\left(\frac{\partial \overset{(\alpha)}{E}}{\partial t} + \overset{(\alpha)}{v} \frac{\partial \overset{(\alpha)}{E}}{\partial x}\right) = \overset{(\alpha)}{\sigma}_x \frac{\partial \overset{(\alpha)}{v}}{\partial x} + \rho \overset{(\alpha)}{\psi} \tag{4.13}$$

In writing Eq. (4.13), we assumed no heat transfer between constituents,

$$\overset{(\alpha)}{q} \equiv 0 \tag{4.14}$$

Our primary interest is in mixtures in which the second component is a fluid.

$$\overset{(2)}{\sigma}_{ij} = -\overset{(2)}{p}\, \delta_{ij} \tag{4.15a}$$

$$\overset{(2)}{p} = \overset{(2)}{n}\, \overset{(2)}{p}{}^{e} \tag{4.15b}$$

Rewriting Eq. (4.6), we obtain

$$\rho \overset{(1)}{\beta} = -\rho \overset{(2)}{\beta} = \rho\beta \tag{4.16}$$

The interaction term, $\rho\beta$, contains both dilatational and diffusive parts

$$\rho\beta = \rho\beta_d + \rho_0\eta \qquad (4.17)$$

To derive an expression for $\rho\beta$, we consider the ordinary momentum equation for fluid flow with friction through a variable area tube,

$$\overset{(2)}{m}\,\overset{(2)}{\rho}{}^{e}\left(\frac{\partial \overset{(2)}{v}}{\partial t} + \overset{(2)}{v}\,\frac{\partial \overset{(2)}{v}}{\partial x}\right) = -\rho_0\eta + \overset{(\alpha)}{m}\,\frac{\partial \overset{(2)}{p}{}^{e}}{\partial x} \qquad (4.18)$$

where $-\rho_0\eta$ denotes the drag experienced by the fluid as it flows through the rock. Combining Eqs. (4.9), (4.10), (4.12), (4.16), (4.17) and (4.18), we obtain:

$$\rho\beta = -\overset{(2)}{p}{}^{e}\,\frac{\partial \overset{(2)}{n}}{\partial x} + \rho_0\eta \qquad (4.19)$$

Note that Eq. (4.19) holds only as long as (4.10) is true.

We will now assume that the diffusive force $\rho_0\eta$ depends on the two velocity fields in the following manner:

$$\rho_0\eta = \rho_0 d\left(\overset{(2)}{v} - \overset{(1)}{v}\right) \qquad (4.20)$$

where d has the dimension of the reciprocal of time. Note that d is related to Darcy's law (3SR-648)

$$\rho_0 d = \frac{\overset{(2)}{n}{}^{2}\,\mu}{k} \qquad (4.21)$$

where μ and k denote the kinematic viscosity of the fluid and the permeability of the rock, respectively. For water, μ is equal to 0.01002 g/sec-cm. For tuff, k is in the range 50-10,000 μdarcies (1 darcy = $0.987\ 10^{-8}$ cm^2).

It appears worthwhile to note here that (1/d) is a measure of the momentum relaxation time, i.e., the time required to exchange momentum between the two materials. In numerical computations, this fact can be very important in deciding the allowable time steps. Ideally, the time step should be an order of magnitude less than the momentum relaxation time, 1/d.

4.3.1 Interaction Energy Term: $\rho \overset{(\alpha)}{\psi}$

Provided there is no heat flow between the constituents $\left(\overset{(\alpha)}{q} \equiv 0\right)$, the requirement that the energy contributions of the interaction forces be zero may be written as

$$\rho\beta\left(\overset{(1)}{v} - \overset{(2)}{v}\right) + \rho\left(\overset{(1)}{\psi} + \overset{(2)}{\psi}\right) = 0 \tag{4.22}$$

The internal energy balance relation for $\overset{(2)}{s}$ can be rewritten as:

$$\overset{(2)}{\rho} \frac{\overset{(2)}{D}}{Dt} \overset{(2)}{E} = -\overset{(2)}{p} \frac{\partial \overset{(2)}{v}}{\partial x} + \rho \overset{(2)}{\psi} \tag{4.23}$$

The interaction energy term, $\rho \overset{(2)}{\psi}$, contains both dilatational, $\rho \overset{(2)}{\psi}_d$, and diffusive, $\rho \overset{(2)}{\psi}_s$, contributions

$$\rho \overset{(2)}{\psi} = \rho \overset{(2)}{\psi}_d + \rho \overset{(2)}{\psi}_s \tag{4.24}$$

Also, we have

$$\overset{(2)}{E}{}^e \equiv \overset{(2)}{E} \tag{4.25}$$

To derive an expression for $\rho \overset{(2)}{\psi}$, we consider the usual internal

balance equation for fluid flow with friction

$$\overset{(2)}{n}\,\overset{(2)}{\rho}{}^{e}\,\frac{\overset{(2)}{D}}{Dt}\,\overset{(2)}{E} = -\overset{(2)}{n}\,\overset{(2)}{p}{}^{e}\,\operatorname{div}\overset{(2)}{\underline{v}}{}^{e} + \rho\,\overset{(2)}{\psi}_{s} \tag{4.26}$$

where $\rho\,\overset{(2)}{\psi}_{s}$ denotes the diffusive energy contribution to the fluid as it passes through the rock.

Now, we have from mass conservation:

$$\operatorname{div}\overset{(2)}{\underline{v}}{}^{e} = \frac{-\overset{(2)}{D}\,\overset{(2)}{\rho}{}^{e}}{Dt} \Big/ \overset{(2)}{\rho}{}^{e}$$

$$= \frac{-\overset{(2)}{D}\,\overset{(2)}{\rho}}{Dt} \Big/ \overset{(2)}{\rho} + \frac{1}{\overset{(2)}{n}}\,\frac{\overset{(2)}{D}\,\overset{(2)}{n}}{Dt}$$

$$= \operatorname{div}\overset{(2)}{\underline{v}} + \frac{1}{\overset{(2)}{n}}\,\frac{\overset{(2)}{D}\,\overset{(2)}{n}}{Dt}$$

$$= \frac{\partial\overset{(2)}{v}}{\partial x} + \frac{1}{\overset{(2)}{n}}\,\frac{\overset{(2)}{D}\,\overset{(2)}{n}}{Dt} \tag{4.27}$$

Substituting from Eq. (4.27) into Eq. (4.26) and utilizing Eqs. (4.22) and (4.24), we obtain

$$\rho\,\overset{(2)}{\psi}_{d} = -\overset{(2)}{p}{}^{e}\left\{\frac{\partial\overset{(2)}{n}}{\partial t} + \overset{(2)}{v}\,\frac{\partial\overset{(2)}{n}}{\partial x}\right\} \tag{4.28}$$

The requirement that the energy contribution of the internal interaction forces be zero yields

$$-\overset{(2)}{p}{}^{e}\left[\frac{\partial\overset{(2)}{n}}{\partial t} + \frac{\partial\overset{(2)}{n}}{\partial x}\,\overset{(1)}{v}\right] + \rho\,\overset{(1)}{\psi} + \rho_{0}\eta\left(\overset{(1)}{v} - \overset{(2)}{v}\right) + \rho\,\overset{(2)}{\psi}_{s} = 0 \tag{4.29}$$

The internal energy contribution $\rho\overset{(1)}{\psi}$ can be split up into two parts, $\rho\overset{(1)}{\psi}_d$ and $\rho\overset{(1)}{\psi}_s$.

$$\rho\overset{(1)}{\psi} = \rho\overset{(1)}{\psi}_d + \rho\overset{(1)}{\psi}_s \tag{4.30}$$

We have thus two equations, (4.29) and (4.30), with four unknowns, $\rho\overset{(1)}{\psi}_d$, $\rho\overset{(2)}{\psi}_d$, $\rho\overset{(1)}{\psi}_s$, $\rho\overset{(2)}{\psi}_s$. It will now be assumed that the dilatation and diffusive contributions must be separately equal to zero, i.e.,

$$\rho\overset{(1)}{\psi}_d = \overset{(2)}{p}{}^e \left[\frac{\partial \overset{(2)}{n}}{\partial t} + \overset{(1)}{v}\,\frac{\partial \overset{(2)}{n}}{\partial x}\right] \tag{4.31}$$

$$\rho\overset{(1)}{\psi}_s + \rho\overset{(2)}{\psi}_s = \rho_0 \eta \left(\overset{(2)}{v} - \overset{(1)}{v}\right) \tag{4.32}$$

This assumption is exact for inviscid $\left(\rho\overset{(1)}{\psi}_s \equiv \rho\overset{(2)}{\psi}_s \equiv \rho_0\eta \equiv 0\right)$ and incompressible materials $\left(\overset{(2)}{n} \equiv \text{constant}\right)$. However, in the general case, it has to be regarded as a constitutive assumption.

We still require another constitutive assumption to separately evaluate $\overset{(1)}{\psi}_s$ and $\overset{(2)}{\psi}_s$. Since diffusion is a dissipative process, the following inequalities follow:

$$\rho\overset{(1)}{\psi}_s \geq 0 \qquad \rho\overset{(2)}{\psi}_s \geq 0 \tag{4.33}$$

We now assume that $\rho\overset{(1)}{\psi}_s$ is zero. Then

$$\rho\overset{(2)}{\psi}_s = \rho_0\eta\left(\overset{(2)}{v} - \overset{(1)}{v}\right) \geq 0 \tag{4.34}$$

The last assumption states that the fluid receives all the diffusive energy contribution, and is justified by the fact that the thermal conductivity of the rock is usually much less than that of the fluid [see also Ref. 54].

A more general procedure for evaluating the various interaction terms is outlined in the Appendix.

4.3.2 Relation to Earlier Work

In previous work (3SR-648), it was assumed that

$$\rho \psi^{(\alpha)} = -\rho\beta v^{(\alpha)} \tag{4.35}$$

If one now assumes that the present splitting of $\rho \psi^{(\alpha)}$ into dilatation and diffusive components is valid, then it follows from Eq. (4.35)

$$\rho \psi_s^{(1)} = -\rho_0 \eta v^{(1)} \tag{4.36}$$

$$\rho \psi_s^{(2)} = -\rho_0 \eta v^{(2)} \tag{4.37}$$

It is easily seem that Eqs. (4.36) and (4.37) cannot possibly satisfy inequalities (4.33). Hence, it is concluded that Eqs. (4.36) and (4.37) are invalid. It may also be verified that for the steady case, present expressions for $\rho \psi_d^{(1)}$ and $\rho \psi_d^{(2)}$ reduce to the Eq. (4.35). The present expressions for $\rho \psi_s^{(1)}$ and $\rho \psi_s^{(2)}$ are identical with Eqs. (4.36) and (4.37) for $v^{(1)} \equiv v^{(2)}$, $\rho_0 \eta \equiv 0$ and $v^{(1)} \equiv 0$. Thus, we observe that the Hugoniot analysis of 3SR-648 remains valid except in the case when $v^{(1)} \neq v^{(2)}$ and $\rho_0 \eta \neq 0$. The results of 3SR-648 may be modified in a straightforward manner to include this case as well. We will not, however, pursue this question any further here.

The derivation of interaction terms for spherical flow is similar to the planar case. In fact, Eqs. (4.19), (4.28) and (4.34) are directly applicable to the spherical case with x replaced by the spherical space variable r.

4.4 CONSTITUTIVE RELATIONS

In 3SR-648 mechanical constitutive relations were presented for a partially saturated rock under the assumption of disconnected voids (voids contained in rock matrix and separated from saturated pores). The major effort this last year has been directed towards (1) improving the deviatoric stress-strain relations for the rock, (2) including thermal effects into constitutive laws, and (3) developing a suitable thermal crushup model. This work is discussed more fully in the following subsections.

4.4.1 Improved Formulation for Deviatoric Stresses

In the previous TINC work, the following constitutive relations were employed for the rock component $\overset{(1)}{s}$ in the elastic regime:

$$\overset{(1)}{\sigma}_i = -\overset{(1)}{p} + \overset{(1)}{S}_i \tag{4.38a}$$

$$\overset{(1)}{p} = \overset{(1)}{n}\, P_1\left(\frac{\overset{(1)}{n}}{\overset{(1)}{n}_0}\,\lambda\right) \tag{4.38b}$$

$$\overset{(1)}{S}_i - \overset{(1)}{S}_j = 2\,\overset{(1)}{n}\,\mu_1\left\{\left(\frac{\overset{(1)}{n}}{\overset{(1)}{n}_0}\right)^{1/3}\left(\lambda_i - \lambda_j\right)\right\} \tag{4.38c}$$

Here $\overset{(1)}{\sigma}_i$, $\overset{(1)}{p}$ and $\overset{(1)}{S}_i$ denote, respectively, the partial stress, the partial pressure and the partial deviatoric stresses. λ_i's are the partial principal stretches; λ is the partial Jacobian of deformation; $\overset{(1)}{n}$ is the volume fraction of $\overset{(1)}{s}$. Functional P_1 determines the pressure response

of the poreless rock; μ_1 is the shear modulus of the poreless rock.

For a dry rock, partial quantities correspond to the quantities actually measured in a laboratory. Thus, for example, λ and $\overset{(1)}{\lambda_i}$ are related to the bulk volumetric strain, θ, and the bulk principal strains ε_i's through the relations:

$$\lambda = 1 + \theta$$

$$\lambda_i = 1 + \varepsilon_i \tag{4.39}$$

$$\theta = \varepsilon_i + \varepsilon_2 + \varepsilon_3$$

We now assume that for the dry rock in the regime of small deformations, $\overset{(1)}{n}$ depends only upon the volumetric strain,

$$\overset{(1)}{n} = \overset{(1)}{n}_0 \left(1 + a_1\theta + a_2\theta^2 + \ldots\right) \tag{4.40}$$

where a_1, a_2, ... are constants. Substituting from Eqs. (4.39) and (4.40) into Eq. (4.38) and neglecting terms of $O(\theta^2)$, there follows:

$$\overset{(1)}{p} = - \overset{(1)}{n}_0 K_s \;(1 + a_1) = - K\theta \tag{4.41}$$

$$\overset{(1)}{S_i} - \overset{(1)}{S_j} = 2\,\overset{(1)}{n}_0\;\mu_1(\varepsilon_i - \varepsilon_j) = 2\mu_p(\varepsilon_i - \varepsilon_j) \tag{4.42}$$

where

K_s = bulk modulus of poreless rock

K = bulk modulus of porous rock

μ_p = shear modulus of porous rock

Equations (4.41) and (4.42) imply that:

$$K = \overset{(1)}{n}_0 \, K_S \, (1 + a_1) \tag{4.43}$$

$$\mu_p = \overset{(1)}{n}_0 \, \mu_1 \tag{4.44}$$

It is shown elsewhere[55] that relationship (4.43) is consistent with the linear theory of elasticity. However, we note here that Eq. (4.44) represents a physically unrealistic result. Most porous rocks exhibit a very small shear modulus at low confining pressures.[56] Furthermore, the measured values of the shear modulus have been found to be path-dependent.[57,58]

The relationship (4.44) is a consequence of the assumed relationship between the effective deformation gradient $\overset{(\alpha)}{\underset{\sim}{F}}{}^{e}$ and partial deformation gradient $\overset{(\alpha)}{\underset{\sim}{F}}$.

$$\overset{(\alpha)}{\underset{\sim}{F}}{}^{e} = \begin{vmatrix} \lambda_1^e & & \\ & \lambda_2^e & \\ & & \lambda_3^e \end{vmatrix} = \left(\frac{\overset{(1)}{n}}{\overset{(1)}{n}_0} \right)^{1/3} \overset{(\alpha)}{\underset{\sim}{F}}$$

$$= \begin{vmatrix} \left(\frac{\overset{(1)}{n}}{\overset{(1)}{n}_0} \right)^{1/3} \lambda_1 & & \\ & \left(\frac{\overset{(1)}{n}}{\overset{(1)}{n}_0} \right)^{1/3} \lambda_2 & \\ & & \left(\frac{\overset{(1)}{n}}{\overset{(1)}{n}_0} \right)^{1/3} \lambda_3 \end{vmatrix} \tag{4.45}$$

and

$$\lambda^{e} = \lambda^{e}_{1} \lambda^{e}_{2} \lambda^{e}_{3} = \left(\frac{\overset{(1)}{n}}{\underset{0}{\overset{(1)}{n}}} \right) \lambda_{1} \lambda_{2} \lambda_{3} = \frac{\overset{(1)}{n}}{\underset{0}{\overset{(1)}{n}}} \lambda \qquad (4.46)$$

Equation (4.46) is identically true. The justification for Eq. (4.45) is not so clear. There is little reason to expect that λ^{e}_{i}'s should be related to λ_{i}'s through an isotropic relation of the form of Eq. (4.45). As an example, let us consider a bar with a spherical cavity subjected to uniaxial loading. The spherical cavity would deform into an ellipsoidal cavity. However, for Eq. (4.45) to apply the spherical cavity must retain its shape. We remark here that Eq. (4.45) is approximately correct for water saturated low strength rocks like tuff. In low strength, high porosity rocks the pore pressure is nearly equal (in confined tests) to the confining pressure and helps to retain the original pore shape. However, for dry rocks and high strength saturated rocks, Eq. (4.45) can lead to gross errors. Instead we introduce the following relationship between $\overset{(\alpha)}{\underset{\sim}{F}}{}^{e}$ and $\overset{(\alpha)}{\underset{\sim}{F}}$:

$$\overset{(\alpha)}{\underset{\sim}{F}}{}^{e} = \begin{vmatrix} \lambda^{e}_{1} & & \\ & \lambda^{e}_{2} & \\ & & \lambda^{e}_{3} \end{vmatrix}$$

$$= \begin{vmatrix} \left(\frac{\overset{(1)}{n}}{\underset{0}{\overset{(1)}{n}}} \right)^{\xi_{1}} \lambda_{2} & & \\ & \left(\frac{\overset{(1)}{n}}{\overset{(1)}{n}} \right)^{\xi_{2}} \lambda_{2} & \\ & & \left(\frac{\overset{(1)}{n}}{\overset{(1)}{n}} \right)^{\xi_{3}} \lambda_{3} \end{vmatrix} \qquad (4.47)$$

where

$$\xi_1 + \xi_2 + \xi_3 = 1 \tag{4.48}$$

The restriction, Eq. (4.48), on the exponents ξ_i is required to satisfy Eq. (4.46). With the decomposition relation in Eq. (4.47), the deviatoric stress strain relationship, replacing Eq. (4.38), becomes:

$$\overset{(1)}{S}_i - \overset{(1)}{S}_j = 2\overset{(1)}{n}\mu_1 \left\{ \left(\frac{\overset{(1)}{n}}{\overset{(1)}{n}_0}\right)^{\xi_i} \lambda_i - \left(\frac{\overset{(1)}{n}}{\overset{(1)}{n}_0}\right)^{\xi_j} \lambda_j \right\} \tag{4.49}$$

where the repeated subscripts i and j <u>do</u> <u>not</u> imply summation.

Substituting from Eqs. (4.39) and (4.40) into Eqs. (4.49), we are led to the following relationship between μ_1 and μ_p:

$$\mu_p = \frac{\overset{(1)}{n}_0 \mu_1}{\varepsilon_i - \varepsilon_j} \left\{ \varepsilon_i - \varepsilon_j + a_1 \theta(\varepsilon_i - \varepsilon_j) \right\} \tag{4.50}$$

Equation (4.50) implies a path-dependent relationship between μ_1 and μ_p. Thus, for example, for uniaxial strain and triaxial tests we have:

<u>Uniaxial Strain:</u>

$$\varepsilon_1 \neq 0, \quad \varepsilon_2 = \varepsilon_3 = 0, \quad \theta = \varepsilon_1,$$

$$\xi_2 = \xi_3 = (1 - \xi_1)/2$$

$$\mu_p = \overset{(1)}{n}_0 \mu_1 \left\{ 1 + \alpha_1(-1/2 + 3\xi_1/2) \right\}$$

Triaxial Loading:

$$\varepsilon_1 \neq 0 , \quad \varepsilon_2 = \varepsilon_3 \neq 0 , \quad \theta = \varepsilon_1 + 2\varepsilon_2$$

$$\xi_2 = \xi_3 = (1 - \varepsilon_1)/2$$

$$\mu_p = \overset{(1)}{n}_0 \, \mu_1 \left\{ 1 + a_1 \frac{\varepsilon_1 + 2\varepsilon_2}{\varepsilon_1 - \varepsilon_2} (-1/2 + 3\xi_1/2) \right\}$$

The factors ξ_i will in general depend upon the deformation path and may be evaluated if appropriate data are available. This could be quite a cumbersome process.

Fortunately, for geologic composites, only the rock matrix can sustain shear stresses, and the partial shear stresses for the rock equal the composite shear stresses. It is, therefore, unnecessary to calculate effective shear stresses. Instead, one can directly postulate a shear law of the form:

$$\overset{(1)}{S}_i - \overset{(1)}{S}_j = 2\mu_p(\lambda_i - \lambda_j) \tag{4.51}$$

As was remarked earlier, μ_p will in general depend upon the deformation path and pore pressure. We shall presume here that such a functional dependence is known from the experimental data. Thus, the mechanical TINC constitutive relations become Eqs. (4.38a), (4.38b), and (4.51). The new formulation retains the major advantage of the previous work, viz. the treatment of porosity as an independent variable. This is quite important in studying the effect of pore pressure. The constitutive law for shear stresses, Eq. (4.51), sidesteps the difficulties inherent in relating the components of the partial deformation gradient to those of the effective deformation gradient. It is also to be noted that Eq. (4.51) utilizes the information which can be readily obtained in the laboratory.

4.4.2 Thermodynamic Constitutive Laws

For a thermodynamic theory, we have to develop constitutive laws for rock partial stresses, $\overset{(1)}{\sigma}_i$, and fluid partial pressure, $\overset{(2)}{p}$. As noted earlier, $\overset{(1)}{\sigma}_i$ may be decomposed into an isotropic part, $-\overset{(1)}{p}$, and a deviatoric stress, $\overset{(1)}{S}_i$, Eq. (4.38). We will assume that Eq. (4.51) for shear holds for the thermal case as well. If necessary, the shear modulus, μ_p, can be made to depend upon $\overset{(1)}{E}$ and $\overset{(2)}{E}$ as well. For plastic flow, we will assume von-Mises' law

$$\overset{(1)}{S}{}_1^2 + \overset{(1)}{S}{}_2^2 + \overset{(1)}{S}{}_3^2 \leq \frac{2}{3} Y_p^2 \tag{4.52}$$

where Y_p denotes the yield stress of the porous rock in simple tension or compression. The yield stress, Y_p, may depend upon the two pressures, $\overset{(1)}{p}$ and $\overset{(2)}{p}$, and the internal energies, $\overset{(1)}{E}$ and $\overset{(2)}{E}$. We will not, however, attempt here to specify any particular functional relationships for μ_p and Y_p, but will assume these to be known from the experimental data.

The pressure, p_α, for $\overset{(\alpha)}{s}$ constituent in isolation is a function of density and internal energy.

$$p_\alpha = P_\alpha(\rho, \rho_0, E) \tag{4.53}$$

Alternately, p_α may be regarded as a function of ρ, ρ_0 and T (temperature). Specific functional forms for NTS tuff and water are discussed elsewhere in this report.

Within, the mixture, the isotropic part of the stress tensor, $-\overset{(\alpha)}{p}$, is, therefore, given by

$$\overset{(\alpha)}{p} = \overset{(\alpha)}{n} P_\alpha \left(\overset{(\alpha)}{\rho}{}^e, \overset{(\alpha)}{\rho}{}_0^e, \overset{(\alpha)}{E} \right)$$

$$= \overset{(\alpha)}{n} P_\alpha \left(\overset{(\alpha)}{\rho} / \overset{(\alpha)}{n}, \overset{(\alpha)}{\rho}_0 / \overset{(\alpha)}{n}_0, \overset{(\alpha)}{E} \right)$$

This completes our discussion of the thermodynamics except insofar as we still need to outline a procedure for determining $\overset{(\alpha)}{n}$. This is considered in the next section.

4.4.3 Crushup Model

In 3SR-648, mechanical crushup relations were presented for dry and partially saturated tuff. During the present contract period, simpler crushup relations have been developed. These are discussed in detail in Section 2.2.3 of this report. However, for the sake of completeness, we will outline the model here in TINC notation.

For the dry porous rock, we have only one unknown, $\overset{(1)}{n}\left(\overset{(2)}{n} \equiv 0,\ \overset{(3)}{n} = 1 - \overset{(1)}{n}\right)$. It is useful to define a new variable, $\overset{(1)}{p}$ such that

$$\alpha\left(\overset{(1)}{p}\right) = \frac{1}{\overset{(1)}{n}} \tag{4.55}$$

A quadratic relationship is assumed for $\alpha\left(\overset{(1)}{p}\right)$:

$$\alpha\left(\overset{(1)}{p}\right) = 1 + (\alpha_0 - 1)\left(1 - \overset{(1)}{p}/p_c\right)^2$$

$$\text{for} \quad \overset{(1)}{p} \leq p_c \quad \text{and} \quad \frac{\partial \overset{(1)}{p}}{\partial t} \geq 0$$

$$\alpha\left(\overset{(1)}{p}\right) = 1 \qquad \text{for} \quad \overset{(1)}{p} > p_c \tag{4.56}$$

On unloading, α is held constant. Here α_0 denotes the initial value of $\alpha\left(= 1/\overset{(1)}{n}_0\right)$ and p_c is the crushup pressure. Thus, the only required inputs for this model are α_0 and p_c.

For the partially saturated rock, one has two unknown volume fractions, $\overset{(1)}{n}$ and $\overset{(2)}{n}$ $\left(\overset{(3)}{n} \equiv 1 - \overset{(1)}{n} - \overset{(2)}{n}\right)$. In 3SR-648, two postulates concerning pore crushup were introduced. The pores may be considered to be <u>connected</u> such that the water can move freely between the pores. For shock wave studied, however, the more appropriate postulate is that of <u>disconnected</u> pores that are either completely water saturated or gas filled with no water. In this model the partially saturated rock may be considered to be a composite in which the components are water and distended rock.

The disconnected-pores hypothesis will be used here to develop the crushup relations (see also 3SR-648). We now define α to be:

$$\alpha = \frac{\overset{(1)}{n} + \overset{(3)}{n}}{\overset{(1)}{n}} = \frac{1 - \overset{(2)}{n}}{\overset{(1)}{n}} \tag{4.57}$$

The crushup relation (4.56) is modified as follows:

$$\alpha = 1 + (\alpha_0 - 1)\,(1 - p/p_c)^2 \tag{4.58}$$

where

$$p = \frac{\overset{(1)}{n}}{1 - \overset{(2)}{n}}\,\overset{(1)}{p}{}^{e} = \overset{(1)}{p} \Big/ \left(1 - \overset{(2)}{n}\right) \tag{4.59}$$

We need an additional relation to complete the algebraic loop. This is obtained by equating the effective pressures in the water and the distended tuff components, i.e.,

$$\frac{\overset{(1)}{n}}{1 - \overset{(2)}{n}}\,\overset{(1)}{p}{}^{e} = \overset{(2)}{p}{}^{e} \tag{4.60}$$

This completes the description of the crushup model.

It is now readily seen that for the disconnected pores postulate, the interaction terms derived in Section 4.3 for the completely saturated rock are directly applicable to the partially saturated case.

4.5 THERMODYNAMIC POROUS CODE

A description of the mechanical POROUS code finite difference scheme has been given in 3SR-648; this formulation did not include thermodynamics, i.e., the effects of internal energy on the equations of state of the constituents. The finite difference scheme used in the non-thermodynamic POROUS code was based on the Lax-Wendroff technique, and furthermore was not written in conservation-law form. The thermodynamic version of POROUS incorporates the effect of internal energy on pressure in the two constituents, uses a finite difference scheme based on the so-called "leap-frog" technique and is written in conservation-law form, so that the masses of the constituents and total energy are exactly conserved (except for roundoff error), and, in planar geometry, momentum is also conserved. It is well known that the Lax-Wendroff scheme often results in "overshoots" of dependent variables, such as pressure and density, at a shock front; the use of the "leap-frog" scheme tends to eliminate these overshoots, which can be particularly troublesome in problems involving shocks at low stress levels (several kbar or below).

4.5.1 Conservation Law Equations in Moving Coordinates

In the POROUS treatment of water-tuff mixtures, only the tuff has material strength; hence, it is convenient to employ the conservation laws for mass, momentum and energy in a coordinate system which moves with the tuff, i.e., coordinates which are Lagrangian with respect to the tuff. In general, there will be transport of water from cell to cell, but the mass of tuff in a cell remains constant. In this coordinate system, the conservation laws of Section 4.2 appear as follows:

4.5 THERMODYNAMIC POROUS CODE

A description of the mechanical POROUS code finite difference scheme has been given in 3SR-648; this formulation did not include thermodynamics, i.e., the effects of internal energy on the equations of state of the constituents. The finite difference scheme used in the non-thermodynamic POROUS code was based on the Lax-Wendroff technique, and furthermore was not written in conservation-law form. The thermodynamic version of POROUS incorporates the effect of internal energy on pressure in the two constituents, uses a finite difference scheme based on the so-called "leap-frog" technique and is written in conservation-law form, so that the masses of the constituents and total energy are exactly conserved (except for roundoff error), and, in planar geometry, momentum is also conserved. It is well known that the Lax-Wendroff scheme often results in "overshoots" of dependent variables, such as pressure and density, at a shock front; the use of the "leap-frog" scheme tends to eliminate these overshoots, which can be particularly troublesome in problems involving shocks at low stress levels (several kbar or below).

4.5.1 Conservation Law Equations in Moving Coordinates

In the POROUS treatment of water-tuff mixtures, only the tuff has material strength; hence, it is convenient to employ the conservation laws for mass, momentum and energy in a coordinate system which moves with the tuff, i.e., coordinates which are Lagrangian with respect to the tuff. In general, there will be transport of water from cell to cell, but the mass of tuff in a cell remains constant. In this coordinate system, the conservation laws of Section 4.2 appear as follows:

Continuity:

$$\frac{d}{dt} \int_V \overset{(1)}{\rho}\, dV = 0 \tag{4.61a}$$

$$\frac{d}{dt} \int_V \overset{(2)}{\rho}\, dV = - \int_S \overset{(2)}{\rho} \left(\overset{(2)}{v}_j - \overset{(1)}{v}_j \right) n_j \, dS \tag{4.61b}$$

Momentum:

$$\frac{d}{dt} \int_V \overset{(1)}{\rho} \overset{(1)}{v}_i \, dV$$

$$= \int_S \overset{(1)}{\sigma}_{ij} n_j \, dS + \int_V \overset{(1)}{\rho \beta_i} \, dV \tag{4.62a}$$

$$\frac{d}{dt} \int_V \overset{(2)}{\rho} \overset{(2)}{v}_i \, dV$$

$$= \int_S \overset{(2)}{\sigma}_{ij} n_j \, dS + \int_V \overset{(2)}{\rho \beta_i} \, dV$$

$$- \int_S \overset{(2)}{\rho} \overset{(2)}{v}_i \left(\overset{(2)}{v}_j - \overset{(1)}{v}_j \right) n_j \, dS \tag{4.62b}$$

Energy:

$$\frac{d}{dt}\int_V \overset{(1)}{\rho}\left(\overset{(1)}{E} + \frac{1}{2}\overset{(1)}{v_j}\overset{(1)}{v_j}\right)dV$$

$$= \int_S \overset{(1)}{\sigma_{ij}}\ \overset{(1)}{v_i}\ n_j\ dS - \int_S \overset{(1)}{q_j}\ n_j\ dS$$

$$+ \int_V \left(\rho\ \overset{(1)}{\beta_j}\ \overset{(1)}{v_j} + \rho\ \overset{(1)}{\psi}\right)dV \qquad (4.63a)$$

$$\frac{d}{dt}\int_V \overset{(2)}{\rho}\left(\overset{(2)}{E} + \frac{1}{2}\overset{(2)}{v_j}\overset{(2)}{v_j}\right)dV$$

$$= \int_S \overset{(2)}{\sigma_{ij}}\ \overset{(2)}{v_i}\ n_j\ dS - \int_S \overset{(2)}{q_j}\ n_j\ dS$$

$$+ \int_V \left(\rho\ \overset{(2)}{\beta_j}\ \overset{(2)}{v_j} + \rho\ \overset{(2)}{\psi}\right) dV$$

$$- \int_S \overset{(2)}{\rho}\left(\overset{(2)}{E} + \frac{1}{2}\overset{(2)}{v_j}\overset{(2)}{v_j}\right)\left(\overset{(2)}{v_i} - \overset{(1)}{v_i}\right) n_i\ dS \qquad (4.63b)$$

The ordinary time derivative, $\frac{d}{dt}$, is used in the above equations because one is evaluating the time rate of change of mass, momentum and energy in a cell of nonzero width; the hydrodynamic derivative, $\frac{D}{Dt}$, is appropriate to locally defined dependent variables, i.e., variables defined at a point.

4.5.2 Finite Difference Equations

In this subsection, the numerical scheme for computing and updating the dependent variables defined in the previous sections is described. The convention used here defines all quantities at integral time steps, t_n; this obscures the centering of some equations, but has the advantage of identifying time t_n with cycle number n. However, the equations are not entirely time-centered; such centering would greatly increase the length and difficulty of numerical procedures, especially the pressure iteration. Since there is only one independent component of the deviatoric stress tensor in plane and spherical geometry (using the appropriate principal axis coordinate system), but two in cylindrical geometry, and since cylindrical geometry is a case of little interest, the equations have been written for only plane (d=1) and spherical (d=3) geometry.

The following is a description of the current scheme used for setting up the computational grid, and advancing the grid through one computational cycle. No attempt is made to justify the centering or the calling sequence of the equations. Due to the complexity of the phenomena treated, the only adequate test of the numerical method is comparison of computations with known solutions. Variables will be defined as they are encountered. The space centering convention used is: cell boundaries and the tuff and water velocities are defined at integral space points x_i; all other quantities are defined at cell centers, $i+1/2$. Note that subscripts in this subsection refer to spatial positions, not vector and tensor components as in the previous subsection.

In the SETUP routine, the grid boundary array x_i is set, together with tuff mass $m^{(1)}_{i+1/2}$, water mass $m^{(2)}_{i+1/2}$, crushup parameter $\alpha_{i+1/2}$, and water volume fraction $n^{(2)}_{i+1/2}$. The values of $\lambda_{1\ i+1/2}$ and $\lambda_{2\ i+1/2}$ are initialized to unity.

The updating of all variables in a computational cycle is currently done in the following sequence, which employs a velocity boundary condition; a scheme for incorporating a stress boundary condition is under development.

First, the time step dt^{n+1} is computed from the criterion

$$dt^{n+1} = \min\left\{ \frac{dx^n_{i+1/2}}{\overset{(1)}{C}{}^n_{i+1/2}} \, , \, \frac{dx^n_{i+1/2}}{\overset{(2)}{C}{}^n_{i+1/2} + \frac{1}{2}\left| \overset{(2)}{v}{}^n_{i+1} + \overset{(2)}{v}{}^n_{i} - \overset{(1)}{v}{}^n_{i+1} - \overset{(1)}{v}{}^n_{i} \right|} \right\} N_c^{n+1}$$

where

$$dx^n_{i+1/2} = x^n_{i+1} - x^n_i \, , \tag{4.64}$$

N_c^{n+1} is the Courant number $\left(N_c^{n+1} < 1 \right)$, and $\overset{(1)}{C}$ and $\overset{(2)}{C}$ are the tuff and water sound speeds. The time step is the minimum value of the indicated quantities over all cells in the active grid (i.e., all cells containing nonzero stresses).

Next, a test is made to determine whether

$$\left| \overset{(1)}{p}{}^n_{I-1/2} \right| \geq f_a \times \max \left\{ \overset{(1)}{p}{}^n_{i+1/2} \right\} \tag{4.65}$$

where I is the active grid counter and f_a is an accuracy factor ($\sim 10^{-6}$); if this condition is satisfied, I is advanced by one.

The left-hand boundary of the grid is defined to be point i=0. Using a velocity boundary condition, one specifies

$$\overset{(1)}{v}{}^{n+1}_0 = \overset{(2)}{v}{}^{n+1}_0 = f(t_{n+1}) \tag{4.66}$$

where $f(t)$ is some function of time. The left-hand grid

boundary is then updated:

$$x_0^{n+1} = x_0^n + \overset{(1)}{v}{}_0^{n+1} \, dt^{n+1} \ . \tag{4.67}$$

It is assumed that this updating corresponds to a physical process in which work is done, so the tuff and water total energies, $\overset{(1)}{W}$ and $\overset{(2)}{W}$, of the first cell are updated according to the prescription

$$\overset{(1)}{W}{}_{1/2}^{n+1} = \overset{(1)}{W}{}_{1/2}^{n} + f_A\left(x_0^{n+1}\right)^{d-1} \overset{(1)}{v}{}_0^{n+1} \, dt^{n+1}\left(\overset{(1)}{p}{}_{1/2}^{n} + \overset{(1)}{q}{}_{1/2}^{n} - \overset{(1)}{S}{}_{1/2}^{n}\right) ,$$

$$\overset{(2)}{W}{}_{1/2}^{n+1} = \overset{(2)}{W}{}_{1/2}^{n} + f_A\left(x_0^{n+1}\right)^{d-1} \overset{(1)}{v}{}_0^{n+1} \, dt^{n+1}\left(\overset{(2)}{p}{}_{1/2}^{n} + \overset{(2)}{q}{}_{1/2}^{n}\right)$$

(4.68)

where the area factor is given by

$$f_A = 1 \quad \text{for} \quad d = 1 \ ,$$

$$f_A = 4\pi \quad \text{for} \quad d = 3 \ , \tag{4.69}$$

and $\overset{(1)}{q}$ and $\overset{(2)}{q}$ are the tuff and water artificial viscosities, defined by

$$\overset{(\alpha)}{q}{}_{i+1/2}^{n} = \overset{(\alpha)}{\rho}{}_{i+1/2}^{n} \, d\overset{(\alpha)}{v}{}_{i+1/2}^{n}\left(f_q d\overset{(\alpha)}{v}{}_{i+1/2}^{n} - f_\ell \overset{(\alpha)}{C}{}_{i+1/2}^{n}\right)$$

$$\text{for} \quad d\overset{(\alpha)}{v}{}_{i+1/2}^{n} < 0 \ , \tag{4.70}$$

$$\overset{(\alpha)}{q}{}_{i+1/2}^{n} = -\overset{(\alpha)}{\rho}{}_{i+1/2}^{n} \, d\overset{(\alpha)}{v}{}_{i+1/2}^{n} \, f_\ell \overset{(\alpha)}{C}{}_{i+1/2}^{n} \quad \text{for} \quad d\overset{(\alpha)}{v}{}_{i+1/2}^{n} \geq 0 \ .$$

$\overset{(1)}{S}$ is the principal deviatoric stress in the tuff.

Here, f_q ($\sim$ 1.6) and f_ℓ($\sim$ 0.25) are the quadratic and linear artificial viscosity coefficients, and

$$d\,{}^{(\alpha)}v^n_{i+1/2} = {}^{(\alpha)}v^n_{i+1} - {}^{(\alpha)}v^n_i \; . \tag{4.71}$$

Thus, linear and quadratic artificial viscosity terms are used when a cell is crushing up, but only the linear term is retained when a cell is unloading.

After the velocity boundary condition is applied, the pressure equilibration conditions are applied:

$$ {}^{(1)}p^{n+1}_{i+1/2},\ {}^{(2)}p^{n+1}_{i+1/2},\ \alpha^{n+1}_{i+1/2},\ {}^{(2)}n^{n+1}_{i+1/2},\ {}^{(1)}C^{n+1}_{i+1/2} \text{ and } {}^{(2)}C^{n+1}_{i+1/2} \tag{4.72}$$

are computed according to the procedures described in the previous subsections. Also, in the pressure equilibration routine, the tuff and water energies are updated by setting

$$\begin{aligned} {}^{(1)}W^{*}_{i+1/2} &= {}^{(1)}W^{n}_{i+1/2} + \Delta W^n_{i+1/2} \\ {}^{(2)}W^{*}_{i+1/2} &= {}^{(2)}W^{n}_{i+1/2} - \Delta W^n_{i+1/2} \end{aligned} \tag{4.73}$$

where

$$\begin{aligned} \Delta W^n_{i+1/2} = \Bigg[& \frac{1}{{}^{(2)}n^{n+1}_{i+1/2}} \left({}^{(2)}p^{n+1}_{i+1/2} + {}^{(2)}q^{n}_{i+1/2} \right) \left({}^{(2)}n^{n+1}_{i+1/2} - {}^{(2)}n^{n}_{i+1/2} \right) \\ & + dt^{n+1} \frac{\mu}{K} \left({}^{(2)}n^{n+1}_{i+1/2} \right)^2 \left({}^{(1)}v^n_{i+1} + {}^{(1)}v^n_{i} \right) \\ & \times \frac{1}{4} \left({}^{(2)}v^n_{i+1} - {}^{(1)}v^n_{j+1} + {}^{(2)}v^n_{i} - {}^{(1)}v^n_{i} \right) \Bigg] V^n_{i+1/2} \end{aligned} \tag{4.74}$$

where

$$V^n_{i+1/2} = f_V\left[\left(x^n_{i+1}\right)^d - \left(x^n_i\right)^d\right] \tag{4.75}$$

and the volume factor is defined by

$$f_V = 1 \quad \text{for} \quad d = 1 ,$$

$$f_V = 4\pi/3 \text{ for} \quad d = 3 . \tag{4.76}$$

Next, intermediate values of the artificial viscosities are calculated as in the formula above, with $\overset{(\alpha)}{C}{}^n_{i+1/2}$ replaced with $\overset{(\alpha)}{C}{}^{n+1}_{i+1/2}$. Values of $\rho\overset{(1)}{\beta}{}^*_i$ are calculated by

$$\rho\overset{(1)}{\beta}{}^*_i = \frac{\mu}{4K}\left(\overset{(2)}{n}{}^{n+1}_{i+1/2} + \overset{(2)}{n}{}^{n+1}_{i-1/2}\right)^2\left(\overset{(2)}{v}{}^n_i - \overset{(1)}{v}{}^n_i\right)$$

$$- \frac{2}{x^n_{i+1} - x^n_{i-1}} \frac{\left(\overset{(2)}{p}{}^{n+1}_{i-1/2} + \overset{(2)}{q}{}^*_{i-1/2} + \overset{(2)}{p}{}^{n+1}_{i+1/2} + \overset{(2)}{q}{}^*_{i+1/2}\right)}{\overset{(2)}{n}{}^{n+1}_{i-1/2} + \overset{(2)}{n}{}^{n+1}_{i+1/2}}$$

$$\times\left(\overset{(2)}{n}{}^{n+1}_{i+1/2} - \overset{(2)}{n}{}^{n+1}_{i-1/2}\right) \tag{4.77}$$

The tuff velocities are calculated by

$$\overset{(1)}{v}{}^{n+1}_i = \overset{(1)}{v}{}^n_i + \frac{2\, dt^{n+1}}{\overset{(1)}{m}_{i-1/2} + \overset{(1)}{m}_{i+1/2}}$$

$$\times\left\{ f_A\left(x^n_i\right)^{d-1}\left[\overset{(1)}{p}{}^{n+1}_{i-1/2} + \overset{(1)}{q}{}^*_{i-1/2} - \overset{(1)}{S}{}^n_{i-1/2} - \overset{(1)}{p}{}^{n+1}_{i+1/2}\right.\right.$$

$$\left. - \overset{(1)}{q}{}^*_{i+1/2} + \overset{(1)}{S}{}^n_{i+1/2} + \frac{3}{2}\delta_d\left(\overset{(1)}{S}{}^n_{i-1/2} + \overset{(1)}{S}{}^n_{i+1/2}\right)\frac{x^n_{i+1} - x^n_{i-1}}{2x^n_i}\right]$$

$$\left. + \frac{1}{2} f_V\left[\left(x^n_{i+1}\right)^d - \left(x^n_{i-1}\right)^d\right]\rho\overset{(1)}{\beta}{}^*_i\right\} \tag{4.78}$$

where

$$\delta_d = 0 \quad \text{for} \quad d = 1 \,,$$
$$\delta_d = 1 \quad \text{for} \quad d = 3 \,. \qquad (4.79)$$

The Eulerian coordinates (cell boundaries) are updated according to

$$x_i^{n+1} = x_i^n + \overset{(1)}{v}{}_i^{n+1}\, dt^n \qquad (4.80)$$

The water velocity $\overset{(2)}{v}$ is updated in three steps, a procedure necessary for momentum conservation. The first step is

$$\overset{(2)}{v}{}_i^{*} = \overset{(2)}{v}{}_i^{n} + \frac{2dt^{n+1}}{\overset{(2)}{m}{}_{i-1/2}^{n} + \overset{(2)}{m}{}_{i+1/2}^{n}} \left\{ f_A \left(x_i^n\right)^{d-1} \left(\overset{(2)}{p}{}_{i-1/2}^{n} + \overset{(2)}{q}{}_{i-1/2}^{*} - \overset{(2)}{p}{}_{i+1/2}^{n} - \overset{(2)}{q}{}_{i+1/2}^{*} \right) - \frac{1}{2} f_V \left[\left(x_{i+1}^n\right)^d - \left(x_{i-1}^n\right)^d \right] \rho\, \overset{(1)}{\beta}{}_i^{*} \right\} \qquad (4.81)$$

The second step sweeps over interfaces between "momentum cells" and uses the so-called "donor cell" method, which is known to yield stable results in hydrodynamic calculations involving advection, i.e., transport of matter between cells. At each interface between momentum cells, corresponding to $x_{i+1/2}$, the difference between water and tuff velocities at time t_n is calculated:

$$dv_{i+1/2}^n = \frac{1}{2} \left(\overset{(2)}{v}{}_{i+1}^{n} + \overset{(2)}{v}{}_{i}^{n} - \overset{(1)}{v}{}_{i+1}^{n} - \overset{(1)}{v}{}_{i}^{n} \right) . \qquad (4.82)$$

If $dv^n_{i+1/2} \geq 0$, momentum cell i is called the donor cell; if $dv^n_{i+1/2} < 0$, the donor cell is momentum cell $i+1$. Then, at each interface $x_{i+1/2}$,

$$\overset{(2)}{v}{}^{**}_{i+1} = \overset{(2)}{v}{}^{*}_{i+1} + \frac{2}{\overset{(2)}{m}{}^{n}_{i+1/2} + \overset{(2)}{m}{}^{n}_{i+3/2}} \, \delta\left(\overset{(2)}{m}\,\overset{(2)}{v}\right)^{*}_{i+1/2},$$

$$\overset{(2)}{v}{}^{**}_{i} = \overset{(2)}{v}{}^{*}_{i} - \frac{2}{\overset{(2)}{m}{}^{n}_{i-1/2} + \overset{(2)}{m}{}^{n}_{i+1/2}} \, \delta\left(\overset{(2)}{m}\,\overset{(2)}{v}\right)^{*}_{i+1/2} \qquad (4.83)$$

where

$$\delta\left(m\overset{(2)}{v}\right)^{*}_{i+1/2} = dt^{n+1}\, f_A \left[\frac{1}{2}\left(x^n_i + x^n_{i+1}\right)\right]^{d-1}$$

$$\times\, \rho^n_D \, \overset{(2)}{v}{}^{n}_{D} \, dv^n_{i+1/2} \qquad (4.84)$$

where $D = i$ or $i+1$, depending on whether momentum cell i or $i+1$ is the donor cell, and

$$\rho^n_D = \frac{\frac{1}{2}\left(\overset{(2)}{m}{}^{n}_{D-1/2} + \overset{(2)}{m}{}^{n}_{D+1/2}\right)}{f_V\left\{\left[\frac{1}{2}\left(x^n_D + x^n_{D+1}\right)\right]^d - \left[\frac{1}{2}\left(x^n_{D-1} + x^n_D\right)\right]^d\right\}} \qquad (4.85)$$

The water mass in each cell is updated using the donor cell method:

$$\overset{(2)}{m}{}^{n+1}_{i+1/2} = \overset{(2)}{m}{}^{n}_{i+1/2} + \delta\left(\overset{(2)}{m}\right)^{*}_{i},$$

$$\overset{(2)}{m}{}^{n+1}_{i-1/2} = \overset{(2)}{m}{}^{n}_{i-1/2} - \delta\left(\overset{(2)}{m}\right)^{*}_{i} \qquad (4.86)$$

where

$$\delta\left(\overset{(2)}{m}\right)_i^* = dt^{n+1}\, f_A\left(x_i^{n+1}\right)^{d-1} \rho_D^n \, dv_i^n \,, \qquad (4.87)$$

$$dv_i^n = \overset{(2)}{v}_i^n - \overset{(1)}{v}_i^n \,, \qquad (4.88)$$

$$\rho_D^n = \frac{\overset{(2)}{m}_D^n}{f_V\left[\left(x_{D+1/2}^n\right)^d - \left(x_{D-1/2}^n\right)\right]^d} \qquad (4.89)$$

Here $D = i-1/2$ if $dv_i^n \geq 0$, and $D = i + 1/2$ if $dv_i^n < 0$.

A final momentum-conserving correction to the water velocity is made using the updated water masses:

$$\overset{(2)}{v}_i^{n+1} = \overset{(2)}{v}_i^{**} \frac{\overset{(2)}{m}_{i-1/2}^n + \overset{(n)}{m}_{i+1/2}}{\overset{(2)}{m}_{i-1/2}^{n+1} + \overset{(2)}{m}_{i+1/2}^n} \qquad (4.90)$$

New intermediate values of the artificial viscosities, $\overset{(\alpha)}{q}_{i+1/2}^{**}$, are calculated using the above formula with the $\overset{(\alpha)}{v}_i^n$ replaced by $\overset{(\alpha)}{v}_i^{n+1}$. Next, the cell total energies are updated by sweeping through cell interfaces x_i:

$$\begin{aligned} \overset{(1)}{W}_{i+1/2}^{**} &= \overset{(1)}{W}_{i+1/2}^{*} + \delta\left(\overset{(1)}{W}\right)_i^{**}, \\ \overset{(1)}{W}_{i-1/2}^{**} &= \overset{(1)}{W}_{i-1/2}^{*} - \delta\left(\overset{(1)}{W}\right)_i^{**} \end{aligned} \qquad (4.91)$$

where

$$\delta\left({}^{(1)}W\right)_i^{**} = A_i^{n+1}\, dt^{n+1}\, {}^{(1)}v_i^{n+1}$$

$$\times \frac{1}{2}\left({}^{(1)}p_{i-1/2}^{n+1} + {}^{(1)}q_{i-1/2}^{**} - {}^{(1)}S_{i-1/2}^{n} + {}^{(1)}p_{i+1/2}^{n+1}\right.$$

$$\left. + {}^{(1)}q_{i+1/2}^{**} - {}^{(1)}S_{i+1/2}^{n}\right) , \qquad (4.92)$$

$$A_i^{n+1} = f_A\left(x_i^{n+1}\right)^{d-1}$$

For the water energies,

$$\begin{aligned} {}^{(2)}W_{i+1/2}^{**} &= {}^{(2)}W_{i+1/2}^{*} + \delta\left({}^{(2)}W\right)_i^{**} , \\ {}^{(2)}W_{i-1/2}^{**} &= {}^{(2)}W_{i-1/2}^{*} - \delta\left({}^{(2)}W\right)_i^{**} \end{aligned} \qquad (4.93)$$

where

$$\delta\left({}^{(2)}W\right)_i^{**} = A_i^{n+1}\, dt^{n+1}\left\{{}^{(2)}v_i^{n+1}\, \frac{1}{2}\left({}^{(2)}p_{i-1/2}^{n+1} + {}^{(2)}q_{i-1/2}^{**}\right.\right.$$

$$\left.\left. + {}^{(2)}p_{i+1/2}^{n+1} + {}^{(2)}q_{i+1/2}^{**}\right) + {}^{(2)}W_D^{*}\, dv_i^{n+1}/V_D^n\right\} ,$$

$$dv_i^{n+1} = {}^{(2)}v_i^{n+1} - {}^{(1)}v_i \qquad (4.94)$$

$$V_D^n = f_V\left[\left(x^n_{D+1/2}\right)^d - \left(x^n_{D-1/2}\right)^d\right]. \tag{4.95}$$

Here $D = i-1/2$ if $dv_i^{n+1} \geq 0$, $D = i+1/2$ if $dv_i^{n+1} < 0$.

Next in the computational sequence, the λ_i are updated and new deviatoric stresses $\overset{(1)}{S}$ calculated.

$$\left.\begin{aligned} \lambda^{n+1}_{1\ i+1/2} &= \frac{\overset{(1)}{\rho}{}_0{}^e}{\overset{(1)}{n}_0\ \overset{(1)}{\rho}{}^{n+1}_{i+1/2}} \\ \lambda^{n+1}_{2\ i+1/2} &= 1 \end{aligned}\right\} \quad (d=1)\ ; \tag{4.96}$$

$$\left.\begin{aligned} \lambda^{n+1}_{1\ i+1/2} &= \lambda^n_{1\ i+1/2}\left(1 + dt^{n+1}\,\frac{\overset{(1)}{v}{}^{n+1}_{i+1} - \overset{(1)}{v}{}^{n+1}_{i}}{x^{n+1}_{i+1} - x^{n+1}_i}\right), \\ \lambda^{n+1}_{2\ i+1/2} &= \left(\frac{\overset{(1)}{\rho}{}_0{}^e}{\overset{(1)}{n}_0\ \overset{(1)}{\rho}{}^{n+1}_{i+1/2}\ \lambda^{n+1}_{1\ i+1/2}}\right)^{1/2} \end{aligned}\right\} \quad (d=3)\ . \tag{4.97}$$

$$\overset{(1)}{S}{}^*_{i+1/2} = \overset{(1)}{S}_{i+1/2} + \frac{4\mu_p}{3}\left(\lambda^{n+1}_{1\ i+1/2} - \lambda^n_{1\ i+1/2} + \lambda^{n+1}_{2\ i+1/2} - \lambda^n_{2\ i+1/2}\right) \tag{4.98}$$

$$\begin{aligned} \overset{(1)}{S}{}^{n+1}_{i+1/2} &= \overset{(1)}{S}{}^*_{i+1/2} \quad \text{if} \quad \left|\overset{(1)}{S}{}^*_{i+1/2}\right| \leq \frac{2}{3}Y\ , \\ \overset{(1)}{S}{}^{n+1}_{i+1/2} &= \frac{2}{3}Y\ \overset{(1)}{S}{}^*_{i+1/2}\Big/\left|\overset{(1)}{S}{}^*_{i+1/2}\right| \quad \text{if} \quad \left|\overset{(1)}{S}{}^*_{i+1/2}\right| > \frac{2}{3}Y \end{aligned} \tag{4.99}$$

Finally, corrections are made to the water and tuff energies due to interaction terms:

$$
\begin{aligned}
{}^{(1)}W^{n+1}_{i+1/2} &= {}^{(1)}W^{**}_{i+1/2} + \delta(W)^{n+1}_{i+1/2} \,, \\
{}^{(2)}W^{n+1}_{i+1/2} &= {}^{(2)}W^{**}_{i+1/2} - \delta(W)^{n+1}_{i+1/2}
\end{aligned}
\tag{4.100}
$$

where

$$
\begin{aligned}
\delta(W)^{n+1}_{i+1/2} = {} & -dt^{n+1}\, f_V\left[\left(x^{n+1}_{i+1}\right)^d - \left(x^{n+1}_i\right)^d\right] \\
& \times \left({}^{(2)}p^{n+1}_{i+1/2} + {}^{(2)}q^{**}_{i+1/2}\right) \frac{\frac{1}{2}\left({}^{(2)}n^{n+1}_{i+3/2} - {}^{(2)}n^{n+1}_{i-1/2}\right)}{\frac{1}{3}\left(x^{n+1}_{i+2} - x^{n+1}_{i-1}\right)} \\
& \times \frac{\frac{1}{2}\left({}^{(1)}v^{n+1}_i + {}^{(1)}v^{n+1}_{i+1}\right)}{{}^{(2)}n^{n+1}_{i+1/2}} \,.
\end{aligned}
\tag{4.101}
$$

4.6 STRESS PULSE PROPAGATION

The thermodynamic POROUS code has been exercised in the planar option. Initially, a calculation was run for the following input parameters:

$$v_0^{(1)} = v_0^{(2)} = 5 \times 10^4 \text{ cm/sec}$$

$$\rho_{10}^e = 2.22 \text{ g/cc}$$

$$\rho_{20}^e = 0.9982 \text{ g/cc}$$

$$dx_0 = 0.02 \text{ cm}$$

$$D = \mu/k = 0.25 \times 10^9/\text{sec}$$

$$\mu_p = 50 \text{ kbar}$$

$$Y_p = 5 \text{ kbar}$$

$$p_c = 15 \text{ kbar}$$

$$n_0^{(1)} = 0.8$$

$$n_0^{(2)} = 0.1$$

$$n_0^{(3)} = 0.1$$

The results of this calculation are shown in Figs. 4.1 through 4.3. Figure 4.1 shows the particle velocities at $t = 3$ μsec. There is roughly a 10% overshoot in water velocity at the shock front. This result is qualitatively similar to the

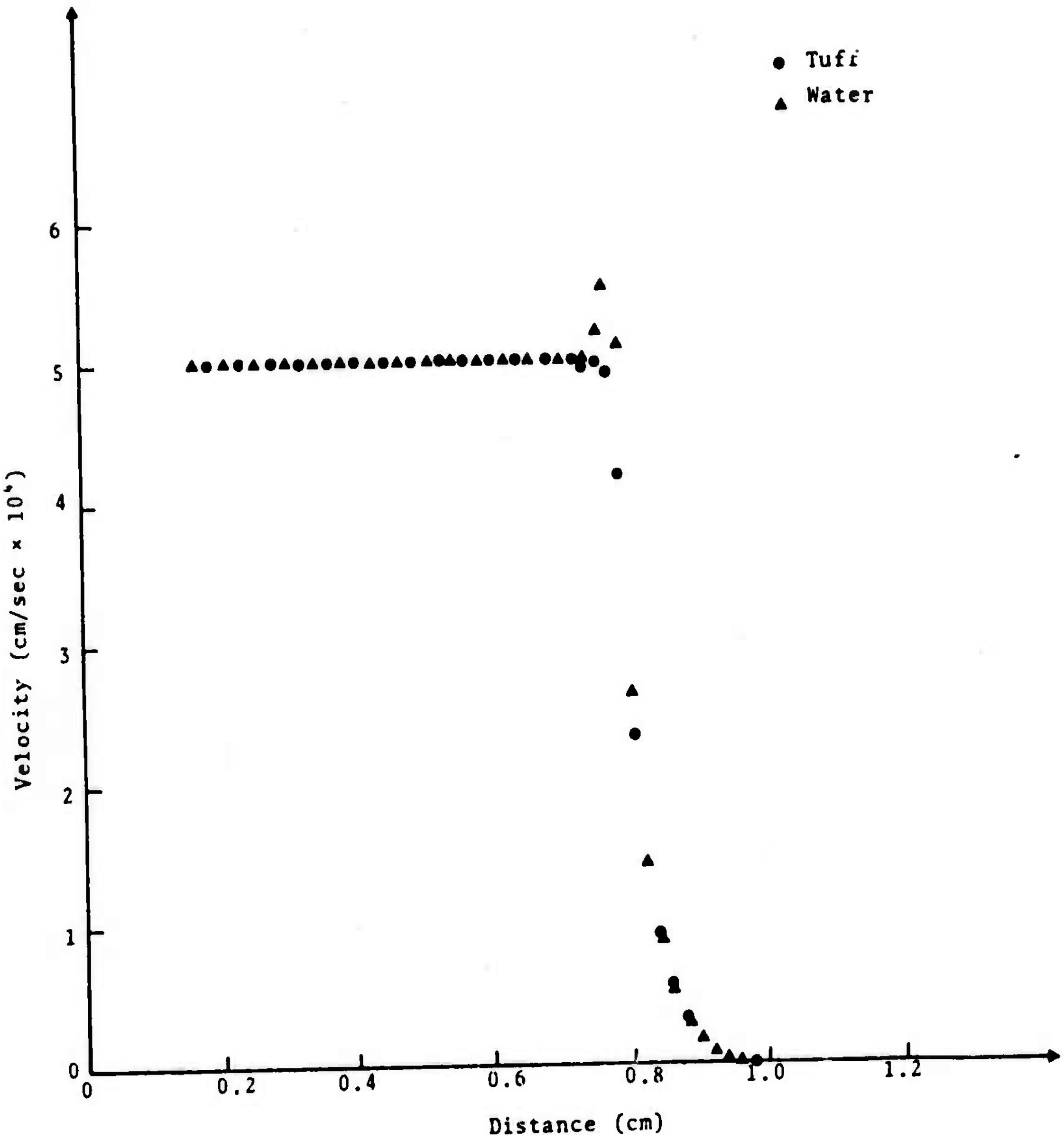

Fig. 4.1--Particle velocity profiles in the tuff and water components at t = 3 μsec.

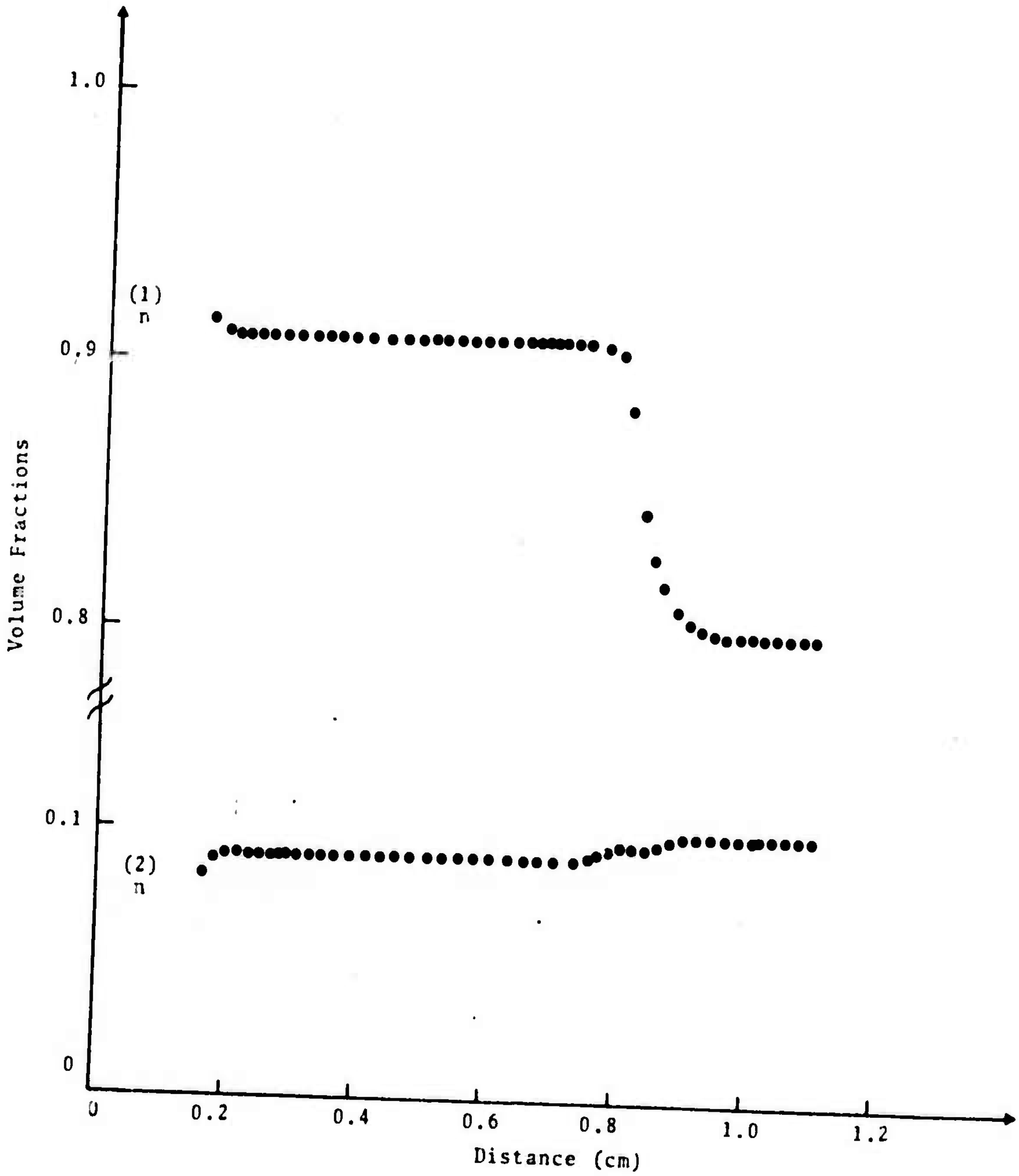

Fig. 4.2--Volume fraction profils for the tuff and water components at t = 3 μsec.

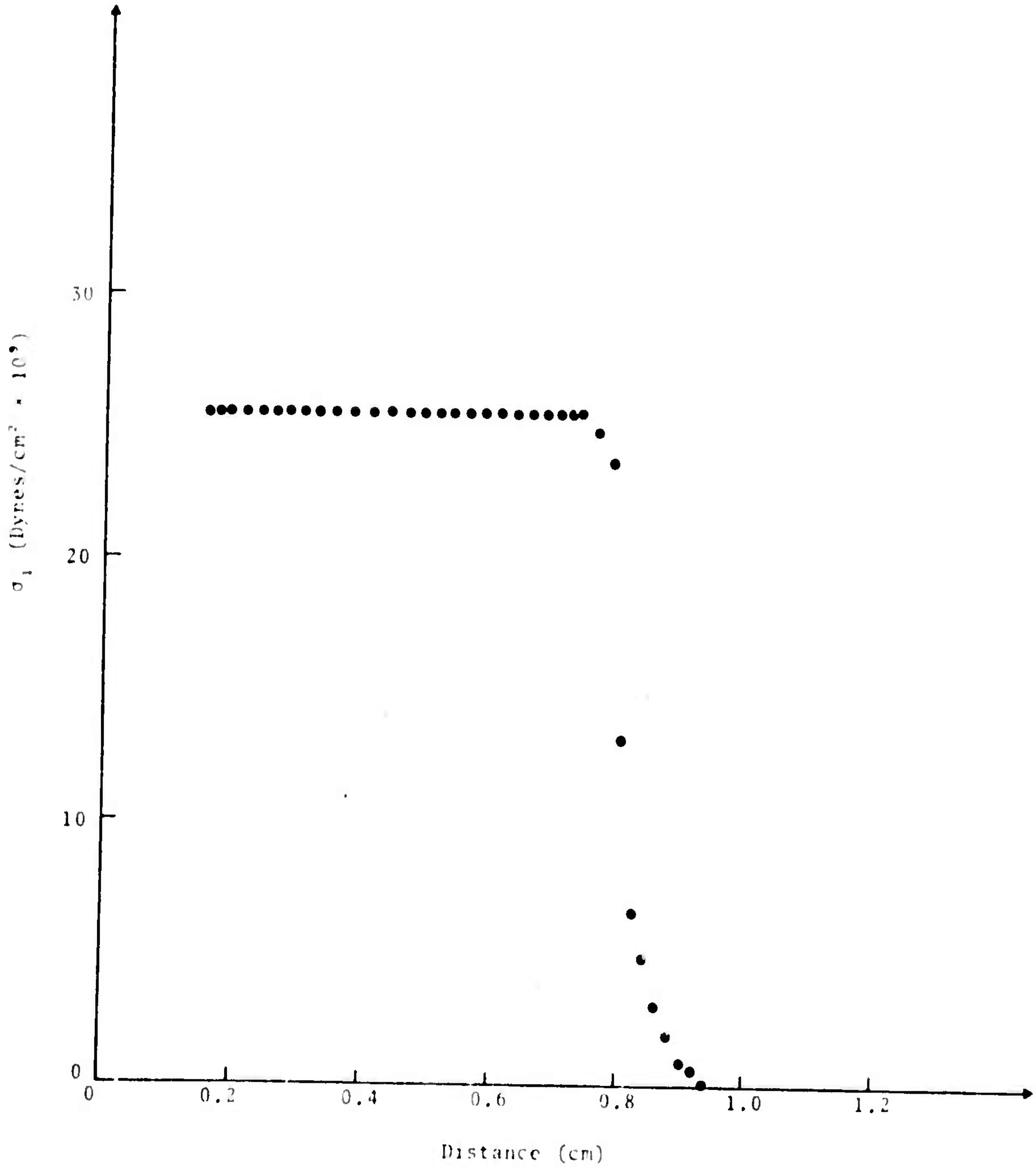

Fig. 4.3--Axial stress profile in the tuff at
t = 3 μsec.

mechanical POROUS code calculations reported in 3SR-648. The volume fractions, $n^{(1)}$ and $n^{(2)}$ are plotted in Fig. 4.2. The tuff volume fraction experiences an increase from 0.8 to approximately 0.908 through the shock front. The water volume fraction changes from 0.1 to 0.092. An interesting phenomenon occurs at the left boundary. Here the water volume fraction drops from 0.092 to roughly 0.083. This results from the advection of water. At high enough stress levels, this can become a serious problem as the water volume fraction in the boundary cells may approach zero. We are still in the process of making the POROUS code general enough to handle this problem as well. In Fig. 4.3, we show the axial stress profile, σ_1, at $t = 3$ μsec. In contra-distinction to the mechanical POROUS code, no overshoots or oscillations are observed at the shock front. This is, of course, the result of using a leap-frog type finite difference scheme instead of the Lax-Wendroff scheme employed in the mechanical POROUS code.

To evaluate the effect of porosity and water content, two additional calculations were run using the following initial volume fractions (all other parameters were kept the same as in the above calculation):

(1) $n_0^{(1)} = 0.9$

$n_0^{(2)} = 0.0$

$n_0^{(3)} = 0.1$

(2) $n_0^{(1)} = 0.9$

$n_0^{(2)} = 0.1$

$n_0^{(3)} = 0.0$

The stress profiles for all three cases at t = 3 μsec are plotted in Fig. 4.4. The dry case (1) results in somewhat higher stress and wave velocity than the partially saturated case $\left(n_0^{(1)} = 0.8,\ n_0^{(2)} = 0.1,\ n_0^{(3)} = 0.1 \right)$. The completely saturated case (2) leads to still higher stress and wave velocity. These calculations demonstrate that the major effect of void porosity is to lower the stress and wave velocity amplitudes.

These calculations are of a preliminary nature. The code is presently being modified to include a pressure boundary condition. Also, an attempt is underway to generalize the boundary treatment to handle high stress levels. During the near future, the new POROUS code will be exercised in spherical geometry as well, and results will be compared with those obtained from homogenized models.

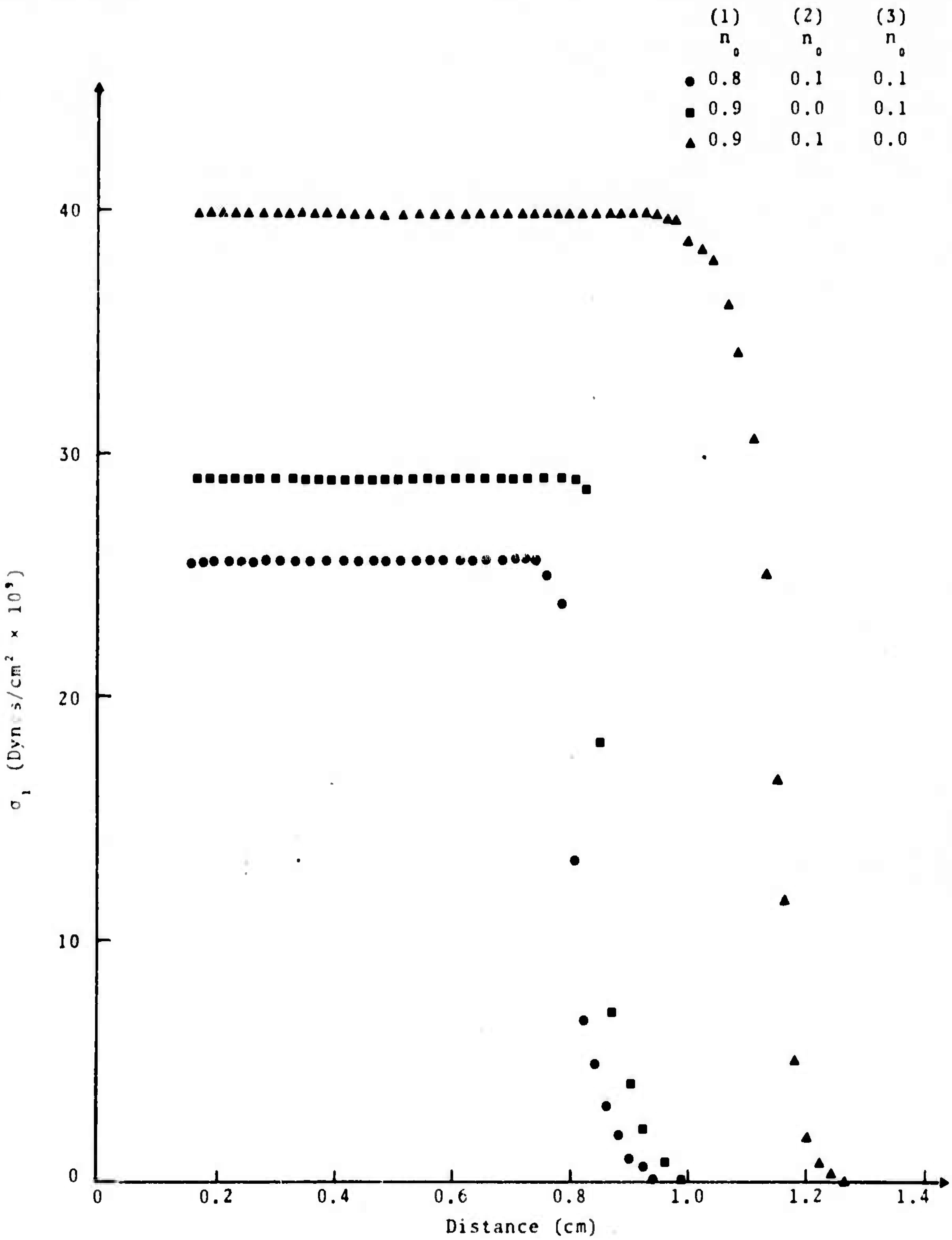

Fig. 4.4--Comparison of stress profiles at t = 3 μsec for a porous tuff matrix whose pore volume is half-saturated, saturated, and void of water.

V. ELASTIC FLUID-ROCK INTERACTION AS A MECHANISM FOR TRIGGERING EARTHQUAKES

5.1 THE POTENTIAL FOR TRIGGERING EARTHQUAKES BY ALTERING THE GROUND WATER CONDITIONS

The crust of the earth is laden with tectonic stresses that heave masses of earth to form mountain ranges and drive continents to move one with respect to another. Earthquakes tend to occur in those regions where the magnitudes of the principal stresses become widely different (high levels of shear stress). This very intense state of stress is generally associated with the earthquake belt which marks the boundary between the crustal plates; however, as evidenced by the occurrence of past earthquakes throughout the world, critically high levels of shear are generated over a much wider region.

In many regions of the United States, tectonic stresses are approaching an unstable condition. This condition exists today just as it has for centuries. In the recent several years, however, the possibility of triggering an earthquake by artificial means has become a problem. For example, earthquake activity has, in some cases, increased in the vicinity of a newly constructed reservoir. Following the construction of Koyna Dam of South India and the subsequent filling of the reservoir, a sequence of small earthquakes were recorded over a period of several years. Then, on December 11, 1967, a magnitude 6.5 earthquake occurred, which resulted in considerable loss of life and a major economic loss.[59] The region was not noted for earthquakes prior to the construction of the reservoir; consequently, it appears likely that the presence of the reservoir somehow served to trigger the catastrophic release of stored strain energy.

The process of injecting fluids into a tectonically stressed region is another means by which earthquake ruptures

can be artificially initiated. Most investigators have concluded that the swarm of hundreds of small earthquakes near Denver, Colorado in the period following 1962 were triggered by the pumping of waste fluids into a 3671-meter disposal well by the Rocky Mountain Arsenal. A conceptual model was presented in 1968 by Healy, Ruby, Griggs, and Rayleigh[60] which accounts for the triggering mechanism of the injected fluid. More recently, the controlled injection of water in the Rangley Field, Western Colorado, by USGS researchers[61,62] clearly demonstrated the potential of this process for triggering earthquakes. In this experimental program water was injected into the western portion of the Rangely Field along a previously mapped fault zone. As the water was driven into the faulted region, the fluid pressure mounted, and small earthquakes began to occur. When the fluid injection was stopped, the occurrence of earthquakes persisted for a period, then, as the fluid pressure began to diminish, the earthquake activity also diminished.

Actually, this description of the earthquake activity associated with the fluid injection process is partially based on conjecture, since the fluid pressure interspersed in the rock was not actually measured at the point of rupture. The sequence of observed activity is consistent with the analytic expressions developed near the end of this section for a simplified spherically symmetric fluid injection system. The theory indicates that there is little possibility of triggering an earthquake at the time that the pumping is first begun; it takes some time for the fluid pressures to spread over the subsurface region of incipient rupture. On the other hand, when the pumping is stopped, the fluid pressures continue to grow for some time before leveling off and diminishing to the background level. Hence, based on our theoretical model, we would expect

the earthquake activity to continue for some time after the fluid injection is stopped. The time lag, of course, depends on the subsurface porosity and the regional extent of the fault zone.

Archambeau and his co-workers at the California Institute of Technology are just beginning a program to monitor earthquake activity associated with the injection of fluid into the Santa Fe Springs Field, Los Angeles. We anticipate a continuous exchange of data with this group in order that we might test our theoretical description of the mechanical interactions between the pore fluid and the rock as it relates to the field experiment.

5.2 ALTERNATE THEORETICAL FORMULATIONS

Various theoretical models have been developed to describe the mechanical interactions between the solid and the fluid constituents of a saturated porous solid material such as soil or rock. Much of this work has been motivated by engineers concerned with the gradual settlement of saturated soils. A simple mechanism to explain this consolidation process was first proposed by Terzaghi.[63]

The next major extension to the theory of consolidation was made by Biot[64] in which the linear consolidation process was modeled in three spatial dimensions. Unfortunately, Biot's formulation does not explicitly show how the various volumetric strains enter the analysis. He states explicitly that the pore water is considered to be incompressible. We assume from this that the small grains of solid material would also be considered to be incompressible. On the other hand, Biot's theory has proven satisfactory for explaining experimental results for the consolidation of a solid sphere of saturated clay,[65,66] and for the consolidation of a two-storied aquifer.[67]

In Biot's formulation, and in essentially all subsequent formulations, we find two physical constants that serve to account for interactions between the two constituents. These constants are operationally defined through explicit laboratory tests. Although it is intuitively obvious that these terms arise from changing dimensions of the fluid-filled pores, no effort is made, at least in Biot's formulation, to develop the physical processes that give rise to the two terms. Details of this type are needed for isolating the rock stress (as opposed to the composite stress) upon which to base fracture criteria.[55]

5.3 QUASISTATIC LINEAR TINC ASSUMPTIONS

In subsurface geologic formations, where stresses are high, the compressibility of the ground water and the rock grains is likely to have a significant effect on the mechanical interactions. For this reason, we use the TINC framework to develop equations for describing the mechanical interactions between porous elastic rock and ground fluid that is permeating through the pores of the rock. The formulation is linear, and as such, it applies to saturated soils or rock where:

1. The strains are small compared to unity.
2. The stresses and strains in the constituents are linearly related by isotropic elastic constants.
3. The velocities are slowly varying so that inertial forces can be neglected.
4. The drag forces between the pore fluid and the rock matrix are linearly related to the relative velocity between the pore fluid and the rock grains (Darcy's law).
5. The rock is saturated. For the case where small gas bubbles are present in the pore liquid, we assume that the gas moves with the liquid influencing only the bulk modulus and density of the gas-liquid mixture. For the case where the rock contains small voids that are not connected (isolated from the permeating fluid), we use the term pore to refer to the connected pores and consider the isolated voids to be homogenized into the rock grains thereby influencing only the bulk modulus and density of the grains.

5.4 CONSERVATION EQUATIONS

The general TINC formulation has been presented in 3SR-267 and 3SR-648, as well as in Section IV of this report. However, in this section we restrict our attention to linear behavior, and as such, much of the redнction of the basic conservation equations to their final form for computer processing is unique to this section. Consequently, we have decided to briefly redevelop the basic TINC equations in their desired form.

The mechanical interactions between porous geologic rock and interspersed ground fluid are governed by the conservation equations:

Conservation of Mass

$$\frac{\partial \overset{(\alpha)}{\rho}}{\partial t} + \frac{\partial}{\partial x_i}\left(\overset{(\alpha)}{\rho}\,\overset{(\alpha)}{v_i}\right) = 0 \tag{5.1}$$

Conservation of Momentum

$$\overset{(\alpha)}{\rho}\left(\frac{\partial \overset{(\alpha)}{v_i}}{\partial t} + \overset{(\alpha)}{v_j}\frac{\partial}{\partial x_j}\overset{(\alpha)}{v_i}\right) = \frac{\partial \overset{(\alpha)}{\sigma_{ij}}}{\partial x_j} + \rho\,\overset{(\alpha)}{f_i} + \rho\,\overset{(\alpha)}{\beta_i} \tag{5.2}$$

Conservation of thermal energy can be disregarded in this development; also, mass transfer due to chemical interactions and phase changes are not being considered. The notation adapted in previous TINC developments is being used with:

(α) = 1 for the solid constituent

= 2 for the fluid constituent (gas-liquid mixture)

$\overset{(\alpha)}{V}{}^{e}$ = volume of constituent (α) excluding the volume occupied by the complementary constituent

$$V = \overset{(1)}{V}{}^{e} + \overset{(2)}{V}{}^{e} \tag{5.3}$$

$$\overset{(\alpha)}{n} = \overset{(\alpha)}{V}{}^{e}/V \tag{5.4}$$

= volume fraction, hence

$$\overset{(1)}{n} + \overset{(2)}{n} = 1 \tag{5.5}$$

$\overset{(\alpha)}{\rho}$ = partial density, i.e., the mass of constituent (α) per unit volume of composite

ρ = composite density

$$= \overset{(1)}{\rho} + \overset{(2)}{\rho} \tag{5.6}$$

$\overset{(\alpha)}{v_i}$ = velocity of a point in constituent (α)

$$= \frac{\partial \overset{(\alpha)}{u_i}}{\partial t} \tag{5.7}$$

$\overset{(\alpha)}{u_i}$ = displacement of a point in constituent (α) from its starting position x_i.

$\overset{(\alpha)}{\sigma_{ij}}$ = partial stress, i.e., the force component in constituent (α) per unit area of composite

σ_{ij} = composite stress

$$= \overset{(1)}{\sigma_{ij}} + \overset{(2)}{\sigma_{ij}} \tag{5.8}$$

$\overset{(\alpha)}{f_i}$ = body force per unit of composite mass due to gravitational forces.

$\overset{(\alpha)}{\beta_i}$ = body force per unit of composite mass that results from drag forces on the complementary constituent.

$$\overset{(1)}{\beta_i} + \overset{(2)}{\beta_i} = 0 \tag{5.9}$$

5.5 CONSTITUTIVE EQUATIONS

In order to complete the description of the fluid-rock composite, we introduce constitutive equations:

1. The drag forces $\overset{(1)}{\beta_i} = - \overset{(2)}{\beta_i}$ are related to the velocity difference between the fluid and the rock $\overset{(2)}{v_i} - \overset{(1)}{v_i}$ through an extended version of Darcy's law

$$\rho \overset{(1)}{\beta_i} = -\rho \overset{(2)}{\beta_i} = \rho_0 d \left(\overset{(2)}{v_i} - \overset{(1)}{v_i} \right) \tag{5.10}$$

in which

$$d = \frac{\overset{(2)}{n}{}^2}{\rho_0} \frac{\mu}{k} \tag{5.11}$$

where μ is the fluid viscosity and k is the permeability of the rock.

2. Changes in porosity are related to volumetric strains in the constituents by a power series expansion. Retaining only the linear terms for the rock constituent we write

$$\overset{(1)}{n} / \overset{(1)}{n_0} = 1 + b_1 \overset{(1)}{\varepsilon} + b_2 \overset{(2)}{\varepsilon} \tag{5.12}$$

in which $\overset{(\alpha)}{\varepsilon}$ is the volumetric component of partial strain defined by

$$\overset{(\alpha)}{\varepsilon} = \delta_{ij} \overset{(\alpha)}{\varepsilon_{ij}} = \frac{1}{2} \delta_{ij} \left(\frac{\partial \overset{(\alpha)}{u_i}}{\partial x_j} + \frac{\partial \overset{(\alpha)}{u_j}}{\partial x_i} \right) \tag{5.13}$$

The volume fraction $\overset{(2)}{n}$ for the fluid constituent is obtained from Eqs. (5.5) and (5.12).

3. In the final constitutive equation we relate stress and strain. First, let us consider the special case when there is no pressure in the pore fluid. Partial stresses in the rock matrix are related to the partial strains in the rock matrix by the conventional isotropic Hooke's law of linear elasticity

$$\overset{(1)}{\sigma}_{ij} = 2\overset{(1)}{\mu}\overset{(1)}{\varepsilon}_{ij} + \overset{(1)}{\lambda}\delta_{ij}\overset{(1)}{\varepsilon} \tag{5.14}$$

where $\overset{(1)}{\mu}$ and $\overset{(1)}{\lambda}$ are Lame's constants. An alternative expression is obtained by decomposing the partial stress into hydrostatic $\overset{(1)}{\sigma}$ and deviatoric $\overset{(1)}{S}_{ij}$ components

$$\overset{(1)}{\sigma}_{ij} = \overset{(1)}{\sigma}\delta_{ij} + \overset{(1)}{S}_{ij} \tag{5.15}$$

such that

$$\overset{(1)}{\sigma} = \frac{1}{3}\delta_{ij}\overset{(1)}{\sigma}_{ij} \tag{5.16}$$

$$= \overset{(1)}{K}\overset{(1)}{\varepsilon} \tag{5.17}$$

and

$$\overset{(1)}{S}_{ij} = \overset{(1)}{\sigma}_{ij} - \delta_{ij}\overset{(1)}{\sigma} \tag{5.18}$$

$$= 2\overset{(1)}{\mu}\left(\overset{(1)}{\varepsilon}_{ij} - \frac{1}{3}\delta_{ij}\overset{(1)}{\varepsilon}\right) \tag{5.19}$$

in which the bulk modulus $\overset{(1)}{K} = \overset{(1)}{\lambda} + \frac{2}{3}\overset{(1)}{\mu}$.

Now we consider the case in which the pore water is acting under pressure. We will assume that introduction of pore pressure does not affect the deviatoric stress-strain relationship for the saturated specimen, Eq. (5.19). In order to develop suitable constitutive equations for the hydrostatic components, we introduce the concept of effective stress—the actual stress in the solid rock grains averaged over several grains. This same concept of average microscopic stresses also applies to the fluid phase so that the effective hydrostatic stress is simply defined

$$\overset{(\alpha)}{\sigma}{}^{e} = \frac{1}{\overset{(\alpha)}{n}} \overset{(\alpha)}{\sigma} \tag{5.20}$$

The corresponding effective volumetric strain—the microscopic volumetric strain in a single constituent averaged over several pore dimensions—is kinematically related to the partial volumetric strain

$$\overset{(\alpha)}{V}{}^{e}/V_0 = \overset{(\alpha)}{n}\left(1 + \overset{(\alpha)}{\varepsilon}\right) = \overset{(\alpha)}{n}_0\left(1 + \overset{(\alpha)}{\varepsilon}{}^{e}\right) \tag{5.21}$$

consequently

$$\overset{(\alpha)}{\varepsilon}{}^{e} = \frac{\overset{(\alpha)}{n}}{\overset{(\alpha)}{n}_0}\left(1 + \overset{(\alpha)}{\varepsilon}\right) - 1 \, . \tag{5.22}$$

Linear hydrostatic stress-strain behavior for the constituents is governed by the bulk modulus of the isolated constituent $\overset{(\alpha)}{K}{}^{e}$,

$$\overset{(\alpha)}{\sigma}{}^{e} = \overset{(\alpha)}{K}{}^{e}\,\overset{(\alpha)}{\varepsilon}{}^{e} \tag{5.23}$$

or by applying Eqs. (5.20) and (5.22), we relate the hydrostatic components of partial stress and partial strain using a variable volume ratio

$$\overset{(\alpha)}{\sigma} = \overset{(\alpha)}{n}\,\overset{(\alpha)}{K}{}^{e}\left[\frac{\overset{(\alpha)}{n}}{\overset{(\alpha)}{n}_{0}}\left(1 + \overset{(\alpha)}{\varepsilon}\right) - 1\right]. \qquad (5.24)$$

Substituting $\overset{(1)}{n}$ from Eq. (5.12) and retaining only the linear terms, we get

$$\overset{(1)}{\sigma} = \overset{(1)}{n}_{0}\,\overset{(1)}{K}{}^{e}\left[(1 + b_{1})\,\overset{(1)}{\varepsilon} + b_{2}\,\overset{(2)}{\varepsilon}\right] \qquad (5.25)$$

and similarly from Eq. (5.5), we get

$$\overset{(2)}{\sigma} = \overset{(2)}{K}{}^{e}\left[-\overset{(1)}{n}_{0}\,b_{1}\,\overset{(1)}{\varepsilon} + \left(1 - \overset{(1)}{n}_{0} - \overset{(1)}{n}_{0}b_{2}\right)\overset{(2)}{\varepsilon}\right] \qquad (5.26)$$

We invert (5.25) and (5.26) to obtain expressions for the hydrostatic components of partial strain

$$\overset{(1)}{\varepsilon} = \frac{\overset{(1)}{\sigma}}{\overset{(1)}{K}} - \frac{\overset{(2)}{\sigma}}{H} \qquad (5.27)$$

and

$$\overset{(2)}{\varepsilon} = -\frac{\overset{(1)}{\sigma}}{H_{1}} + \frac{\overset{(2)}{\sigma}}{R} \qquad (5.28)$$

where

$$\overset{(1)}{K} = \overset{(1)}{n}_0 \overset{(1)}{K}{}^e \frac{\left[1 + b_1 - \overset{(1)}{n}_0 (1 + b_1 + b_2)\right]}{\left[1 - \overset{(1)}{n}_0 (1 + b_2)\right]}$$

$$H = \frac{\overset{(2)}{K}{}^e}{b_2} \left[1 + b_1 - \overset{(1)}{n}_0 (1 + b_1 + b_2)\right]$$

$$H_1 = - \frac{\overset{(1)}{K}{}^e}{b_1} \left[1 + b_1 - \overset{(1)}{n}_0 (1 + b_1 + b_2)\right]$$

$$R = \frac{\overset{(2)}{K}{}^e}{1 + b_1} \left[1 + b_1 - \overset{(1)}{n}_0 (1 + b_1 + b_2)\right] \qquad (5.29)$$

We have succeeded in relating the bulk modulus of the rock matrix, $\overset{(1)}{K} \left(\overset{(2)}{\sigma} = 0 \right)$, with the bulk modulus of the rock grains, $\overset{(1)}{K}{}^e$, by introducing a mechanism to permit variations in the volume fraction, Eq. (5.12). Also, we have arrived at expressions for Biot's[64] interaction constants H, H_1, and R.

In this linear development we require that the final state be independent of loading path. Therefore, the strain energy density

$$U = \frac{1}{2} \overset{(1)}{\varepsilon} \overset{(1)}{\sigma} + \frac{1}{2} \overset{(2)}{\varepsilon} \overset{(2)}{\sigma} \qquad (5.30)$$

can be obtained by applying the load in two stages:

1. The rock matrix is loaded with $\overset{(2)}{\sigma}_1 = 0$, and then
2. the pore pressure is applied with $\overset{(1)}{\sigma}_2 = 0$.

The combined strain energy density then becomes

$$U = \frac{1}{2} \overset{(1)}{\varepsilon}_1 \overset{(1)}{\sigma}_1 + \overset{(1)}{\varepsilon}_2 \overset{(1)}{\sigma}_1 + \frac{1}{2} \overset{(2)}{\varepsilon}_2 \overset{(2)}{\sigma}_2$$

or, if we reverse the order of the loads, we get

$$U = \frac{1}{2} \overset{(1)}{\varepsilon}_1 \overset{(1)}{\sigma}_1 + \frac{1}{2} \overset{(2)}{\varepsilon}_2 \overset{(2)}{\sigma}_2 + \overset{(2)}{\varepsilon}_1 \overset{(2)}{\sigma}_2 .$$

where the subscripts denote the load stage.

We equate the two expressions for strain energy density to obtain a particularized version of Bette's reciprocal theorem

$$\overset{(1)}{\varepsilon}_2 \overset{(1)}{\sigma}_1 = \overset{(2)}{\varepsilon}_1 \overset{(2)}{\sigma}_2 \tag{5.31}$$

or

$$\frac{-\overset{(2)}{\sigma}_2}{H} \overset{(1)}{\sigma}_1 = -\frac{\overset{(1)}{\sigma}_1}{H_1} \overset{(2)}{\sigma}_2$$

using Eqs. (5.27) and (5.28), respectively. From this we conclude

$$H_1 = H \tag{5.32}$$

and consequently

$$\frac{b_1}{\overset{(1)}{K} e} = -\frac{b_2}{\overset{(2)}{K} e} \tag{5.32}$$

Actually b_1 is negative and b_2 is positive

Thus we find the complete stress-strain relationships, effective and partial quantities, involve a total of five independent physical constants: $\overset{(1)}{\mu}$, $\overset{(1)}{K}$ (or alternatively $\overset{(1)}{K}{}^e$ by Eqs. (5.29)), $\overset{(2)}{K}{}^e$, $\overset{(1)}{n}_0$, and b_1 (or alternatively b_2 by Eq. (5.33)). The first four constants are non-interactive in nature, i.e., the stresses and strains in the rock are independent of those in the fluid and conversely the stresses and strains in the fluid are independent of those in the rock for the special case when $b_1 = 0$ (consequently $b_2 = 0$).

Equations (5.25) through (5.28) suggest a number of alternative tests for obtaining the single interactive term b_1. For example, we can use Eq. (5.26) to deduce b_1 from the volume of water $\overset{(2)}{\varepsilon}$ that flows from a drained $\left(\overset{(2)}{\sigma} = 0\right)$ triaxial compression test

$$b_1 = \frac{\left(1 - \overset{(1)}{n}_0\right) / \overset{(1)}{n}_0}{\left(\dfrac{\overset{(1)}{\varepsilon}}{\overset{(2)}{\varepsilon}} - \dfrac{\overset{(2)}{K}{}^e}{\overset{(1)}{K}{}^e}\right)} \qquad (5.34)$$

This expression leads to some interesting bounds for b_1. At one extreme the freely drained specimen is compressed but no fluid seeps out $\left(\overset{(2)}{\varepsilon} = \overset{(1)}{\varepsilon} = \varepsilon\right)$. At the other extreme the volume of fluid that seeps in is equal to the volume that the specimen is compressed so that $\left(\overset{(1)}{\varepsilon} = \varepsilon,\ \overset{(2)}{\varepsilon} = -\varepsilon\right)$. From these extreme modes of behavior we arrive at the bounds

$$\frac{-\left(1 - \overset{(1)}{n}_0\right) / \overset{(1)}{n}_0}{1 + \overset{(2)}{K}{}^e / \overset{(1)}{K}{}^e} < b_1 < \frac{\left(1 - \overset{(1)}{n}_0\right) / \overset{(1)}{n}_0}{\left(1 - \overset{(2)}{K}{}^e / \overset{(1)}{K}{}^e\right)}$$

and by use of Eq. (5.33), we get

$$\frac{\left(1 - {}^{(1)}n_0\right)/{}^{(1)}n_0}{1 - {}^{(1)}K^e/{}^{(2)}K^e} < b_2 < \frac{\left(1 - {}^{(1)}n_0\right)/{}^{(1)}n_0}{1 + {}^{(1)}K^e/{}^{(2)}K^e} \tag{5.36}$$

In general we might expect the b_1 (b_2) for saturated clay soils to lie near to the lower (upper) bound.

A critical test of the suitability of the non-diffusive constitutive equations developed above has been provided through a series of experimental measurements recently reported by Nur and Byerlee.[68] They derived an "effective stress" law for eliminating the influence of pore pressures from their test data of the form

$$\langle\sigma_{ij}\rangle_{NB} = \sigma_{ij} + \left(1 - {}^{(1)}K/{}^{(1)}K^e\right){}^{(2)}\sigma^e\delta_{ij} \tag{5.37}$$

using TINC notation where $\langle\sigma_{ij}\rangle_{NB}$ is their effective stress term intended to correspond to the equivalent stress in a dry specimen. They presented experimental evidence that their effective stress law accounts for the influence of the pressurized pore fluid considerably better than the conventional effective stress law which simply subtracts the fluid pressure directly, i.e., Eq. (5.37) with ${}^{(1)}K^e = \infty$. The same data was processed using the TINC framework in which the effective stress in the rock is taken to be the microscopic stress in the rock grains averaged over several grains. The rather small bias in the wet data that remained after the attempt to remove the influence of the pore fluid by Eq. (5.37) was essentially eliminated using the TINC concept of effective stress. This rather impressive demonstration of the use of the TINC model to fit stress-strain data is presented in detail in Appendix D.

5.6 FLUID SEEPAGE

We now have the basic equations with which to describe the elastic behavior of the fluid-rock composite. Using the constitutive laws developed above, we shall proceed to express the conservation equations, Eqs. (5.1) and (5.2), in terms of the fluid pressure

$$p = -\overset{(2)}{\sigma}{}^{e} = \frac{-1}{\left(1 - \overset{(1)}{n}\right)}\overset{(2)}{\sigma} \tag{5.38}$$

and components of displacement $\overset{(1)}{u}_i$ $\left(\text{and } \overset{(1)}{\varepsilon} = \frac{\partial \overset{(1)}{u}_i}{\partial x_i}\right)$ for the rock.

First we will investigate the conservation of mass equations. From the kinematics of the deforming composite, we equate the ratio of density to initial density with the inverse ratio of volume to initial volume and write

$$\frac{\overset{(\alpha)}{\rho}}{\overset{(\alpha)}{\rho}_0} = \left(1 + \overset{(\alpha)}{\varepsilon}\right)^{-1} \tag{5.39}$$

Consequently

$$\frac{1}{\overset{(\alpha)}{\rho}_0}\frac{\partial \overset{(\alpha)}{\rho}}{\partial t} = -\frac{\partial \overset{(\alpha)}{\varepsilon}}{\partial t} \tag{5.40}$$

and

$$\frac{1}{\overset{(\alpha)}{\rho}_0}\frac{\partial \overset{(\alpha)}{\rho}}{\partial x_i} = -\frac{\partial \overset{(\alpha)}{\varepsilon}}{\partial x_i} \tag{5.41}$$

when we disregard components of strain compared to unity after performing the indicated derivatives. These expressions are substitutived into Eq. (5.1) to give the alternative form for the conservation equation

$$- \frac{\partial \overset{(\alpha)}{\varepsilon}}{\partial t} + \frac{\overset{(\alpha)}{\rho}}{\overset{(\alpha)}{\rho_0}} \frac{\partial \overset{(\alpha)}{\varepsilon}}{\partial t} - \overset{(\alpha)}{v_i} \frac{\partial \overset{(\alpha)}{\varepsilon}}{\partial x_i} = 0 \tag{5.42}$$

since $\dfrac{\partial \overset{(\alpha)}{v_i}}{\partial x_i} = \dfrac{\partial \overset{(\alpha)}{\varepsilon}}{\partial t}$. Clearly the first two terms cancel to first order accuracy, from which we are led to conclude that the third term $\overset{(\alpha)}{v_i}\left(\partial \overset{(\alpha)}{\varepsilon} / \partial x_i \right)$ is higher order than the term $\partial \overset{(\alpha)}{\varepsilon} / \partial t$. [The fact that the mass conservation equations are automatically satisfied is a consequence of the manner in which we related partial density to partial strain in Eq. (5.39)]

Momentum is conserved quasistatically, i.e., we eliminate the inertial forces from Eq. (5.2) to obtain the equilibrium expression for the fluid phase ($\alpha = 2$).

$$\frac{\partial \overset{(2)}{\sigma}}{\partial x_i} + \overset{(2)}{\rho} f_i - \rho_0 d \left(\overset{(2)}{v_i} - \overset{(1)}{v_i} \right) = 0 \tag{5.43}$$

The expression, in the absence of inertial forces, remains time varying because of the drag forces between the fluid and the rock, which have been related to the relative velocities between the two constituents by Eq. (5.10). Equation (5.43) is reduced to a single nonsubscripted equation by differentiating with respect to x_i and summing on i

$$\nabla^2 \overset{(2)}{\sigma} + \nabla \cdot \left(\overset{(2)}{\rho} \underset{\rightarrow}{f} \right) = \rho_0 d \left(\frac{\partial \overset{(2)}{\varepsilon}}{\partial t} - \frac{\partial \overset{(1)}{\varepsilon}}{\partial t} \right) \tag{5.44}$$

The strain component $\overset{(2)}{\varepsilon}$ is expressed in terms of $\overset{(2)}{\sigma}$ and $\overset{(1)}{\varepsilon}$ by Eq. (5.26), and $\overset{(2)}{\sigma}$ is in term related to the fluid pressure by Eq. (5.38).

In carrying out these substitutions we reason that $p\,\partial \overset{(1)}{n}/\partial t$ is of order $p\,\partial \overset{(\alpha)}{\varepsilon}/\partial t$ by Eq. (5.12), and $p\left(\partial \overset{(\alpha)}{\varepsilon}/\partial t\right)$ is of order $\left(p/\overset{(2)}{K}e\right)\left(\partial p/\partial t\right)$ by Eqs. (5.26) and (5.38), and $\left(p/\overset{(2)}{K}e\right)\left(\partial p/\partial t\right)$ is of order $\overset{(\alpha)}{\varepsilon}\left(\partial p/\partial t\right)$ by Eqs. (5.26) and (5.38); consequently, the product differentiation

$$\frac{\partial}{\partial t}\left(\overset{(1)}{n}p\right) = \overset{(1)}{n}\frac{\partial p}{\partial t} + p\frac{\partial \overset{(1)}{n}}{\partial t} ,$$

to first order, reduces to the form

$$\frac{\partial}{\partial t}\left(\overset{(1)}{n}p\right) = \overset{(1)}{n}\frac{\partial p}{\partial t} . \tag{5.45}$$

Similarly we reduce

$$\frac{\partial}{\partial x_i}\left(\overset{(1)}{n}p\right) = \overset{(1)}{n}\frac{\partial p}{\partial x_i} + p\frac{\partial \overset{(1)}{n}}{\partial x_i}$$

to the form

$$\frac{\partial}{\partial x_i}\left(\overset{(1)}{n}p\right) = \overset{(1)}{n}\frac{\partial p}{\partial x_i} \tag{5.46}$$

Following these substitutions, Eq. (5.44) becomes

$$\frac{\left(1-\overset{(1)}{n}_0\right)}{\rho_0 d}\nabla^2 p = \frac{1}{\rho_0 d}\nabla\cdot(\rho \underset{\rightarrow}{f}) + \left(1+\frac{\overset{(1)}{K}}{H}\right)\frac{\partial \overset{(1)}{\varepsilon}}{\partial t} + \frac{\left(1-\overset{(1)}{n}_0\right)}{Q}\frac{\partial p}{\partial t} \tag{5.47}$$

where

$$Q = \overset{(2)}{K} e \left[1 - \overset{(1)}{n}_0 (1 + b_2)\right]$$

The elastic compliance of the rock matrix influences this "seepage" equation through the term $\partial \overset{(1)}{\varepsilon} / \partial t$, which originates not only from volumetric fluxuations in the porosity (nonzero b_1 and b_2) but also from the fact that the drag forces depend on the relative velocity between the rock and the fluid rather than the fluid velocity alone, Eq. (5.10). It was discovered through actual computer applications that presence of the interactive term $\partial \overset{(1)}{\varepsilon} / \partial t$ <u>strongly</u> influences the seepage process to the point where rather severe stability problems arise in some cases. This troublesome phenomenon can be eliminated if we rearrange Eq. (5.47) to obtain a modified interaction term as some combination of $\partial \overset{(1)}{\varepsilon} / \partial t$ and $\partial p / \partial t$. The modified interaction term should have little influence on the seepage process for optimum computer processing. The total hydrostatic stress $\sigma = \overset{(1)}{\sigma} + \overset{(2)}{\sigma}$ has the desired character. As ground water is driven through the subsurface rock formations, increases in the pore fluid pressure reduce compressive loads on the rock matrix so that the total hydrostatic stress tends to remain invariant. In fact, we find that the total hydrostatic stress remains totally invariant when fluid is injected into a spherically symmetric environment, Section 5.9.

Substituting from Eqs. (5.27), and (5.38) with $\overset{(1)}{\sigma} = \sigma - \overset{(2)}{\sigma}$, we get

$$\overset{(1)}{\varepsilon} = \frac{\sigma}{\overset{(1)}{K}} + \left(1 - \overset{(1)}{n}_0\right)\left(\frac{1}{\overset{(1)}{K}} + \frac{1}{H}\right) p \tag{5.48}$$

which we use to eliminate $\partial \varepsilon^{(1)}/\partial t$ from Eq. (5.47) and arrive at

$$\frac{\left(1 - n_0^{(1)}\right)}{\rho_0 d} \nabla^2 p = \frac{1}{\rho_0 d} \nabla \cdot (\rho \vec{f}) + \left(\frac{1}{K^{(1)}} + \frac{1}{\Pi}\right)\frac{\partial \sigma}{\partial t}$$

$$\left(1 - n_0^{(1)}\right)\left(\frac{1}{\bar{K}} + \frac{1}{K^{(1)}} + \frac{2}{\Pi}\right)\frac{\partial p}{\partial t} \qquad (5.49)$$

5.7 ELASTIC DEFORMATIONS IN THE ROCK MATRIX

Equilibrium conditions in the elastic rock matrix are expressed most conveniently by combining the momentum equations for the fluid and the rock, Eq. (5.2) with $\alpha = 1$ and $\alpha = 2$, thereby eliminating the drag forces, Eq. (5.10). We again disregard inertial forces and write

$$\frac{\partial \overset{(1)}{\sigma}_{ij}}{\partial x_j} + \frac{\partial \overset{(2)}{\sigma}}{\partial x_i} + \rho f_i = 0 . \tag{5.52}$$

in which $f_i = \overset{(1)}{f}_i + \overset{(2)}{f}_i$. We use Eqs. (5.15), (5.19), and (5.27) to reduce $\overset{(1)}{\sigma}_{ij}$ into components of $\overset{(1)}{\varepsilon}_{ij}$ and $\overset{(2)}{\sigma}$. The partial stress in the fluid, $\overset{(2)}{\sigma}$, is then expressed as pore pressure using Eq. (5.38), and the equilibrium equation for the composite becomes

$$2 \frac{\partial}{\partial x_j}\left(\overset{(1)}{\mu}\,\overset{(1)}{\varepsilon}_{ij}\right) + \frac{\partial}{\partial x_i}\left[\left(\overset{(1)}{K} - \frac{2}{3}\overset{(1)}{\mu}\right)\overset{(1)}{\varepsilon}\right] + \rho f_i$$

$$= \left(1 - \overset{(1)}{n}_0\right)\frac{\partial}{\partial x_i}\left[\left(1 + \frac{\overset{(1)}{K}}{H}\right)p\right] \tag{5.53}$$

or by Eq. (5.13)

$$\frac{\partial}{\partial x_j}\left[\overset{(1)}{\mu}\left(\frac{\partial \overset{(1)}{u}_i}{\partial x_j} + \frac{\partial \overset{(1)}{u}_j}{\partial x_i}\right)\right] + \frac{\partial}{\partial x_i}\left[\left(\overset{(1)}{K} - \frac{2}{3}\overset{(1)}{\mu}\right)\frac{\partial \overset{(1)}{u}_j}{\partial x_j}\right] + \rho f_i$$

$$= \left(1 - \overset{(1)}{n}_0\right)\frac{\partial}{\partial x_i}\left[\left(1 + \frac{\overset{(1)}{K}}{H}\right)p\right] \tag{5.54}$$

For the special case of homogeneous material, Eq. (5.54) assumes the form

$$\overset{(1)}{\mu}\,\nabla^2 \overset{(1)}{\underset{\to}{u}} + \left(\overset{(1)}{K} + \frac{1}{3}\overset{(1)}{\mu}\right)\nabla\left(\nabla \cdot \overset{(1)}{\underset{\to}{u}}\right) + \rho \underset{\to}{f} = \left(1 - \overset{(1)}{n}_0\right)\left(1 + \frac{\overset{(1)}{K}}{H}\right)\nabla p \tag{5.55}$$

or alternatively

$$\left(\overset{(1)}{K} + \frac{4}{3}\overset{(1)}{\mu}\right)\nabla\left(\nabla \cdot \overset{(1)}{\underset{\to}{u}}\right) - \overset{(1)}{\mu}\,\nabla \times \left(\nabla \times \overset{(1)}{\underset{\to}{u}}\right) + \rho \underset{\to}{f} = \left(1 - \overset{(1)}{n}_0\right)\left(1 + \frac{\overset{(1)}{K}}{H}\right)\nabla p \tag{5.56}$$

5.8 FRI CODE

The mechanical interaction between ground fluids and porous subsurface formations have been mathematically modeled using a linearized version of TINC. The penetration of elastically compressible fluid through the pores of a subsurface geologic mass is modeled by Eq. (5.47) or, in a form more suited for computer processing, by Eq. (5.49). The elastic compliance of the porous material to the pressure of interspersed fluid is represented by the presence of an interactive term related to the volumetric strain rate in the rock matrix. The interactive seepage equation has the form of a diffusion equation, which can be treated by one of several existing numerical codes. A 2-D finite element code, originally programmed by Wilson,[69] was selected to treat the seepage process with the term that contains the elastic compliance of rock matrix appearing as a source term.

The elastic deformations in the rock matrix, expressed by Eq. (5.54), were also treated by a 2-D finite element code in which the pore pressure enters as a body force. The two finite element codes were merged into a single 2-D code (FRI). Figure 5.1 illustrates the sequence of operations that are performed to simulate the interactive seepage process. The diffusion equation is solved to give the fluid pressure field at an advanced time step with the interactive term extrapolated from the previous time step. The updated fluid pressure field then feeds into the elasticity portion of the FRI code to generate an updated displacement field from which rock dilatation and total hydrostatic stress are computed. The solution to the diffusion equation is repeated to give a corrected pressure field at the advanced time step base on an updated interactive term. The complete cycle is repeated two to five times for a single time step in order to avoid any lag in the interactions between the fluid and the rock.

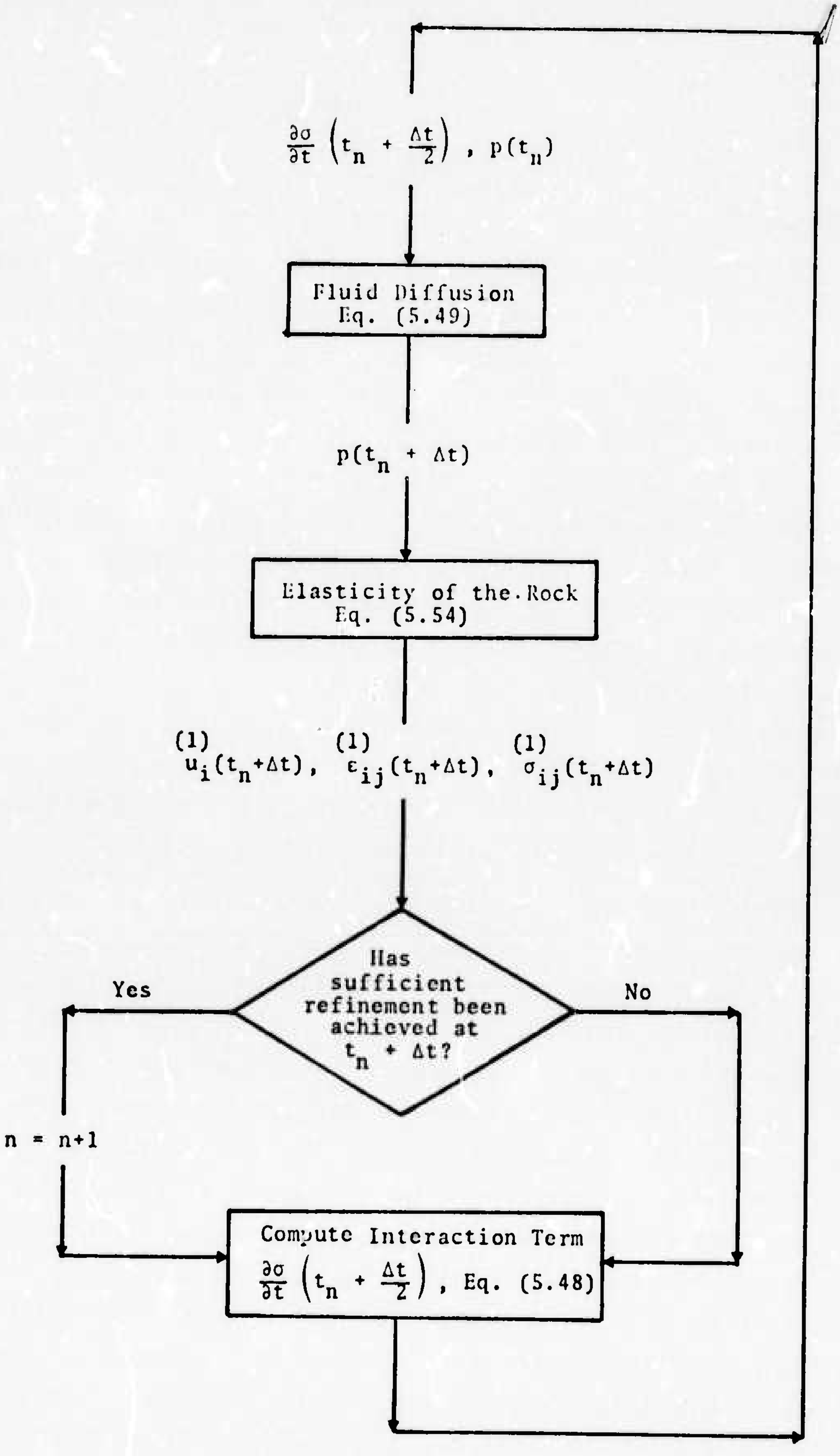

Fig. 5.1--Computational sequence for FRI.

The newly formed FRI code was first tested on non-interactive systems. The rock elasticity mode was suppressed to produce purely diffusive seepage which was compared with analytic solutions. The converse situation, in which the diffusion mode was suppressed, was also run to test elastic deformations in the rock matrix against closed form results.

The first interactive test was performed on a 2-D simulation of a 1-D compaction process. A closed form solution was obtained for the response of a single layer of fluid saturated material to a uniform surface load, Fig. 5.2. Elastic deformations in both the rock and the fluid are treated using the linear version of TINC to yield the series solution

$$p(y) = \frac{4p_0}{\pi} \sum_{i=0}^{\infty} \frac{(-1)^i}{(2i+1)} e^{-(2i+1)^2 \pi^2 \tau/4} \sin\left[(2i+1) \frac{\pi}{2y_0} y\right] \qquad (5.57)$$

$$\tau = \frac{t}{\rho d\, y_0^2 \left[\frac{1}{nK} + \frac{1}{(1-n)(\lambda+2\mu)}\right]}$$

(dimensionless time)

d = fluid diffusion coefficient
(large d makes seepage slow)

ρ = mass density of the saturated composite

n = porosity of the solid material (the ratio of the pore volume to the total volume)

λ, μ = Lame's constants for the solid material

K = bulk modulus of the fluid

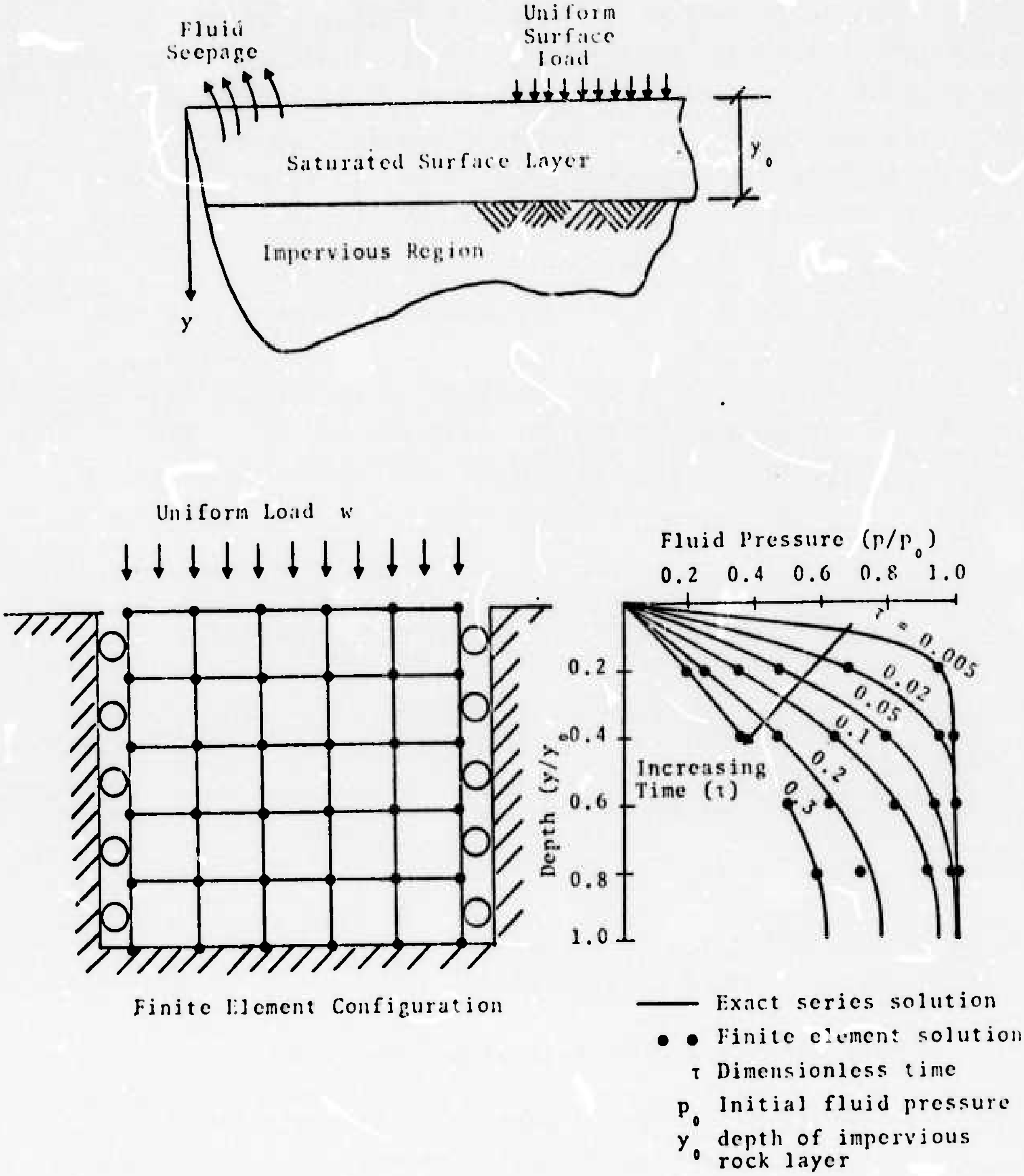

Fig. 5.2--Comparison of FRI code solution with exact solution for a test fluid/rock interaction problem.

$$p_2 = \frac{2}{n + \frac{(1-n)(\lambda+2\mu)}{K}}$$

w = uniform surface load density

As seen in Fig. 5.2, the numerical finite element solution follows the exact series solution well even up to late times when much of the seepage has taken place. A variable time step was used to achieve the finite element results with $\Delta\tau = 0.0025$ initially and $\Delta\tau$ gradually increasing to $\Delta\tau = 0.05$ for the late time calculation $\tau \geq 0.10$.

The elastic compliance of the solid material as the fluid seeps to the surface follows the equation

$$\overset{(1)}{\varepsilon} = \overset{(1)}{\varepsilon_\infty} + \frac{np}{(1-n)(\lambda+2\mu)} \tag{5.58}$$

where

$\overset{(1)}{\varepsilon}$ = dilatation of the elastic rock matrix,

$$\overset{(1)}{\varepsilon_\infty} = \frac{-w}{(1-n)(\lambda+2\mu)}$$

(final dilatation state when $p = 0$)

The finite element calculations follow this relationship precisely for the initial test problem.

5.9 INJECTION WELL

More recently the FRI code has been exercised to examine the interactive seepage process associated with an injection well. Simultaneously an effort has been made to obtain a closed form solution for the injection of fluid into a homogeneous formation with which to compare computer generated results. Obviously an analytic expression describing this process would have far reaching implications for providing guidance in future injection projects. This effort has met with considerable success.

We consider the problem of a cased well (which we will ignore in our analysis) pumping fluid into a spherical cavity of radius r_0 which is located in a homogeneous saturated region, Fig. 5.3. For simplicity we assume no initial stress in the rock and no initial pressure in the fluid. The injection process is then accomplished by stepping the pressure in the cavity instantly from zero to p_0 where it remains throughout the injection process. Pressures develop in the region outside the cavity at the instant the cavity pressure is applied (t = 0). These stresses can be calculated from Eqs. (5.47) and (5.54) with $d = \infty$ to prevent seepage at this initial loading. From Eq. (5.47) we get

$$\frac{\partial p}{\partial t} = \frac{Q}{1 - n_0^{(1)}} \left(1 + \frac{K^{(1)}}{H}\right) \frac{\partial \varepsilon^{(1)}}{\partial t}$$

or

$$p = \frac{Q}{1 - n_0^{(1)}} \left(1 + \frac{K^{(1)}}{H}\right) \varepsilon^{(1)} \tag{5.59}$$

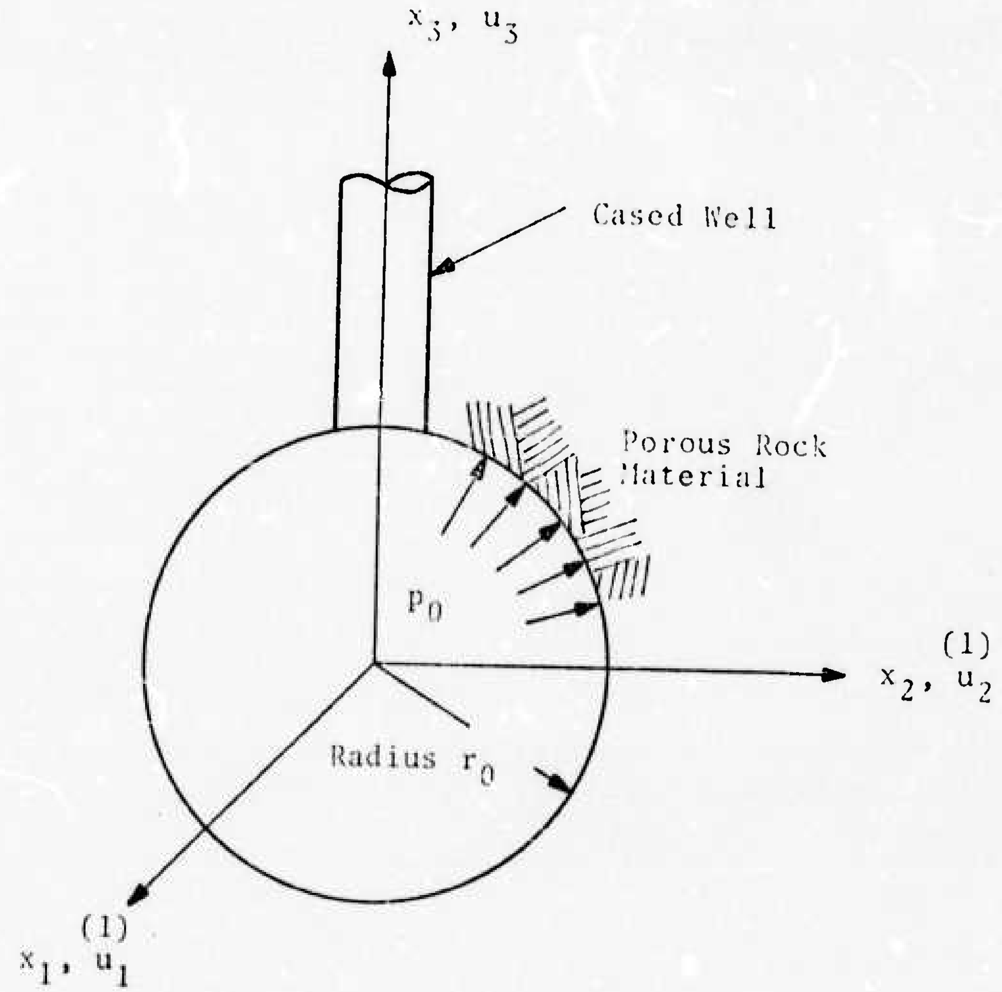

Fig. 5.3--Spherically symmetric fluid injection system. The pressure p_0 is introduced in the cavity at the initial time and then held at this level with the pore fluid in the rock formation assigned zero initial pressure.

where $\overset{(1)}{K}$ and H are defined by Eq. (5.29) and Q is given following Eq. (5.47).

We substitute this expression for the initial pressure p into the elasticity equation, Eq. (5.56) to get

$$\left[\overset{(1)}{K} + Q\left(1 + \frac{\overset{(1)}{K}}{H}\right)\right]\nabla\left(\nabla \cdot \overset{(1)}{\underset{\to}{u}}\right) = 0 \qquad (5.60)$$

using the fact that

$$\nabla \cdot \overset{(1)}{\underset{\to}{u}} = \overset{(1)}{\varepsilon}$$

and

$$\nabla x \overset{(1)}{\underset{\to}{u}} = 0 \qquad (5.61)$$

for the homogeneous spherically symmetric injection environment where only radial displacements occur. The behavior of the rock is constrained to satisfy the boundary condition at the well injection cavity

$$\sigma_{rr} = -p_0 \text{ at } r = r_0 \qquad (5.62)$$

i.e.,

$$\overset{(1)}{\sigma}_{rr} = -\overset{(1)}{n}_0 p_0 \text{ at } r = r_0 \qquad (5.63)$$

and the condition of no displacement at large distances from the well. The solution to Eq. (5.60) that satisfies these conditions is found to be

$$\overset{(1)}{u}_i \,(\underset{\sim}{x}, t = 0) = \frac{\overset{(1)}{n}_0 p_0}{4 \overset{(1)}{\mu}} \left(\frac{r_0}{r}\right)^3 x_i \qquad (5.64)$$

which leads to

$$\overset{(1)}{\sigma}_{ij}(\underset{\sim}{x}, t = 0) = - \frac{n_0 \overset{(1)}{p}_0}{2} \left(\frac{r_0}{r}\right)^3 \left(\frac{3x_i x_j}{r^2} - \delta_{ij}\right) \tag{5.65}$$

Somewhat surprisingly, we find that the initial pressure in the cavity generates no hydrostatic stress in the surrounding rock formation, i e.,

$$\overset{(1)}{\sigma} = \frac{1}{3} \delta_{ij} \overset{(1)}{\sigma}_{ij} = 0 \tag{5.66}$$

and consequently there is no pressure generated in the pore fluid outside the cavity at the initiation of the injection process.

The results presented above apply in the initial injection process, before fluid seepage begins. Throughout the life of the injection well, the composite stress $\sigma_{ij} = \overset{(1)}{\sigma}_{ij} + \overset{(2)}{\sigma}_{ij}$ must satisfy the equilibrium equation

$$\frac{\partial \sigma_{ij}}{\partial x_j} = 0 \tag{5.67}$$

outside of the injection well and Eq. (5.62) at the cavity boundary which yields

$$\sigma_{ij} = - \frac{p_0}{2} \left(\frac{r_0}{r}\right)^3 \left(\frac{3x_i x_j}{r^2} - \delta_{ij}\right) \tag{5.68}$$

and consequently

$$\sigma = \frac{1}{3} \delta_{ij} \sigma_{ij} = 0 \tag{5.69}$$

for all time. This simply indicates that the hydrostatic stress in the combined fluid-rock composite permits us to decouple the seepage equation, Eq. (5.49), from the elasticity equations for the rock, since $\frac{\partial \sigma}{\partial t} = 0$ for all time. Thus, our "interactive" seepage process is described by

$$C \nabla^2 p = \frac{\partial p}{\partial t} \tag{5.70}$$

where

$$C = \frac{1}{\rho_0 d \left(\frac{1}{R} + \frac{1}{K^{(1)}} + \frac{2}{\Pi} \right)} \tag{5.71}$$

The constitutive terms R, $K^{(1)}$, and H are given by Eq. (5.29). At the initial time there is no fluid pressure outside the injection cavity as deduced above. At the cavity boundary the pressure is held at p_0. From these conditions we are able to uniquely express the complete fluid pressure time history

$$p(r,\tau) = \left(\frac{r_0}{r}\right) p_0 \left[1 - \mathrm{erf}\left(\frac{(r/r_0) - 1}{2\sqrt{\tau}}\right)\right] \tag{5.72}$$

where the dimensionless time τ is given by

$$\tau = \frac{Ct}{r_0^2} \tag{5.73}$$

We substitute this result back into the elasticity equations for the rock to determine the stresses and deformations that are occurring there, and we find

$$\overset{(1)}{\sigma}_{ij}(\underset{\sim}{x},\tau) = -\frac{p_0}{2}\left(\frac{r_0}{r}\right)^3\left(\frac{3x_ix_j}{r^2} - \delta_{ij}\right)$$

$$\left(1 - \overset{(1)}{n}_0\right)\left(\frac{r_0}{r}\right) p_0 \left[1 - \operatorname{erf}\left(\frac{(r/r_0) - 1}{2\sqrt{\tau}}\right)\right]\delta_{ij} \tag{5.74}$$

$$\overset{(1)}{\varepsilon}_{ij}(\underset{\sim}{x},\tau) = -\overset{(1)}{\mu}\, p_0\left(\frac{r_0}{r}\right)^3\left(\frac{3x_ix_j}{r^2} - \delta_{ij}\right)$$

$$+\frac{\left(1 - \overset{(1)}{n}_0\right) C p_0}{\left(\overset{(1)}{K} + \frac{4}{3}\overset{(1)}{\mu}\right)}\left(\frac{r_0}{r}\right)\left[1 - \operatorname{erf}\left(\frac{(r/r_0) - 1}{2\sqrt{\tau}}\right)\right]\delta_{ij} \tag{5.75}$$

and

$$\overset{(1)}{u}_r(r,\tau) = \frac{\overset{(1)}{n}\, p_0}{4\overset{(1)}{\mu}}\left(\frac{r_0}{r}\right)^2 r_0 + \frac{\left(1 - \overset{(1)}{n}_0 C\right)}{r^2\left(\overset{(1)}{K} + \frac{4}{3}\overset{(1)}{\mu}\right) r_0}$$

$$\times \int_{r_0}^{r} \xi^2 p(\xi,\tau)\, d\xi \tag{5.76}$$

$$\overset{(1)}{u}_\theta = \overset{(1)}{u}_\phi = 0 .$$

We have not carried out the indicated integration to determine the radial displacement field; however, we have obtained the early and the late time limiting values

$$\overset{(1)}{u}_r(r,\tau) \simeq \frac{\overset{(1)}{n}\, p_0}{4\overset{(1)}{\mu}}\left(\frac{r_0}{r}\right)^2 r_0 \quad \text{for} \left(\frac{(r/r_0) - 1}{2\sqrt{\tau}}\right) > 2 \tag{5.77}$$

$$u_r^{(1)}(r,\tau) \cong \frac{n^{(1)} p_0}{4\,\mu^{(1)}} \left(\frac{r_0}{r}\right)^2 r_0 + \frac{\left(1 - n_0^{(1)}\right) c\, p_0\, r_0}{\left(K^{(1)} + \frac{4}{3}\,\mu^{(1)}\right)}$$

$$\text{for} \quad \left(\frac{(r/r_0) - 1}{2\sqrt{\tau}}\right) < 0.01 \; . \tag{5.78}$$

It appears that there is much to be learned from examining the results developed above about the potential for triggering an earthquake by pumping fluid into the earth. We note, for example, that shear stresses are due entirely to the presence of pressure in the cavity; there are no shear stresses generated by fluid seeping through the rock. The greatest potential for triggering an earthquake, therefore, lies in the tensile stresses (relative to the pre-injection state) that are generated in the rock matrix as pore fluid is pressurized at points away from the cavity. Figure 5.4 illustrates the spread of the fluid pressure through the pores of the rock. Both the time rate of loading in the rock matrix and the pore fluid are depicted.

The spherically symmetric injection system was also treated using the numerical FRI code. Fluid pressure, rock stress, and rock deformation are generated with the FRI code operating in the completely interactive mode, i.e., with no assumptions as to the nature of the interactions. The numerical simulation results in hydrostatic stresses in the fluid-rock composite which are two orders of magnitude less than the radial and hoop stresses in the rock matrix. Ideally the hydrostatic composite stress should be zero for the spherically symmetric environment, Eq. (5.69). The fluid pressures from the numerical simulation are presented in Fig. 5.4. We see very good agreement with the analytic solution even at early times where the pressure front is quite steep.

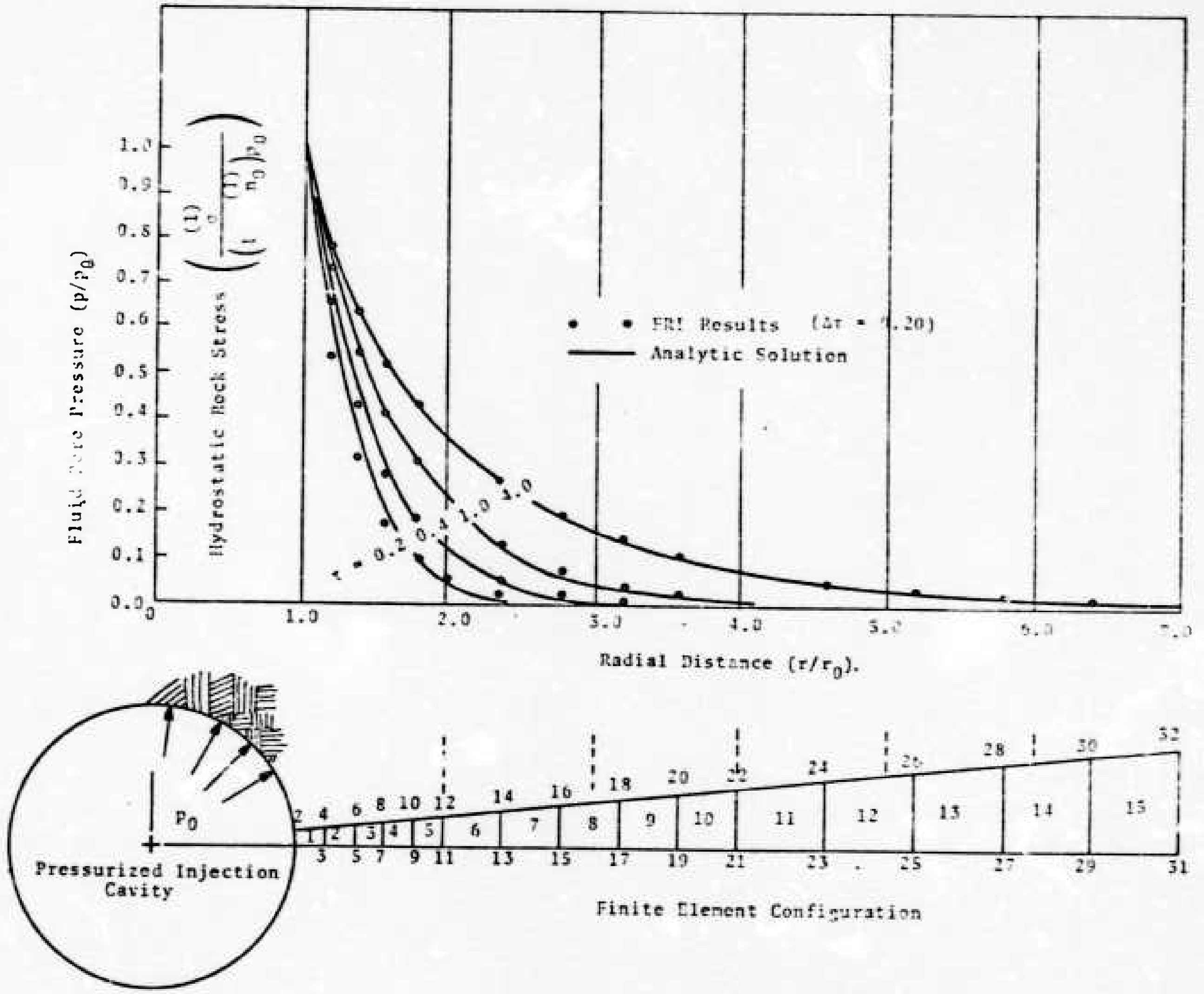

Fig. 5.4--Ground water pressure and hydrostatic rock stress generated by a spherically symmetric fluid injection system.

We will now investigate what happens when the injection process is terminated. At time t_1 (dimensionless time τ_1), the pressure in the injection cavity is dropped from p_0 to zero. This can be accomplished analytically by simply introducing an additional injection solution with a negative cavity pressure $-p_0$ at the retarded time τ_1. Then, after pumping is stopped, we get

$$\sigma_{ij} = 0 \tag{5.79}$$

$$p(r,\tau) = \left(\frac{r_0}{r}\right) p_0 \left[\operatorname{erf}\left(\frac{\frac{r}{r_0} - 1}{2\sqrt{\tau-\tau_1}}\right) - \operatorname{erf}\left(\frac{\frac{r}{r_0} - 1}{2\sqrt{\tau}}\right)\right] \tag{5.80}$$

$$\overset{(1)}{\sigma}_{ij}(r,\tau) = \left(1 - \overset{(1)}{n}_0\right)\left(\frac{r_0}{r}\right) p_0 \left[\operatorname{erf}\left(\frac{\frac{r}{r_0} - 1}{2\sqrt{\tau-\tau_1}}\right) - \operatorname{erf}\left(\frac{\frac{r}{r_0} - 1}{2\sqrt{\tau}}\right)\right]\delta_{ij} \tag{5.81}$$

$$\overset{(1)}{\varepsilon}_{ij}(r,\tau) = \frac{\left(1 - \overset{(1)}{n}_0\right) C\, p_0}{\left(\overset{(1)}{K} + \frac{4}{3}\overset{(1)}{\mu}\right)}\left(\frac{r_0}{r}\right)\left[\operatorname{erf}\left(\frac{\frac{r}{r_0} - 1}{2\sqrt{\tau-\tau_1}}\right) - \operatorname{erf}\left(\frac{\frac{r}{r_0} - 1}{2\sqrt{\tau}}\right)\right]\delta_{ij} \tag{5.82}$$

from Eqs. (5.68), (5.72), (5.74), and (5.75), respectively. We find from Eq. (5.80) that the fluid pressure will continue to increase away from the injection cavity for some time after the injection pressure has dropped to zero. Hence the potential for triggering an earthquake is not eliminated when the pumping is stopped. Actually the most critical conditions (maximum $\overset{(1)}{\sigma}_{ij}$) will generally occur after the pumping has stopped.

5.10 SUMMARY AND CONCLUSIONS

The processes by which alterations in the ground water state can trigger a major rupture in the earth should be carefully examined in order to guard against the possibility of accidently initiating a catastrophic earthquake. The possibility of controlling the natural process should also be considered. It might be that earthquakes can be produced for the purpose of relieving stress in the earth that might otherwise accumulate and result in major damage.

The theoretical formulation of the mechanical interactions between the fluid and the rock is somewhat involved. Actually, the resulting equations are quite similar to those developed previously by Biot.[64] The major points where the linearized TINC formulation differs from Biot's, and essentially all subsequent, formulations are noted below.

1. A mechanism for fluid-rock interaction is provided in the linearized TINC formulation by dealing with variable pore dimensions. Using this approach the interaction terms take on a new meaning.

2. The linearized TINC formulation includes the elastic deformations in the rock particles and in the pore fluid.

3. The rock velocity as well as the fluid velocity is considered when expressing the drag forces between the fluid and the rock (Darcy's law).

A finite element code (FRI) has been developed to treat the TINC seepage equations in two spatial dimensions (plane strain or axisymmetric). While the FRI code is suited for complex geologic formations, we have concentrated on elementary cases in order to examine the accuracy of the numerical simulation. We find that the FRI code is well

suited for interaction calculations, at least for the cases that were run. Good accuracy is obtained even one time step into the calculations, Fig. 5.4. The FRI code has not been critically tested for simulating late time solutions.

Analytic solutions were obtained for an injection well in a spherically symmetric environment. The injection well analysis points out the potential for triggering an earthquake by pumping fluid into the ground. Whereas the stresses that result from an artificially applied load (e.g., a surface load or a pressurized cavity) diminish as $1/r^3$ away from the point of application, the stresses that are generated in the rock matrix by fluid injection diminish as $1/r$ at late times (steady state). Furthermore, the rock stresses generated by fluid injection are not relieved by stopping the pumping, in fact, the stresses continue to mount for a period of time after the pumping has stopped before the fluid pressure begins to diminish. This phenomena should be carefully considered in order to avoid triggering a major earthquake unintentionally.

VI. DISCUSSION

The successful implementation of the TAMEOS equation of state for homogenized rock-water-void mixes as a subroutine in the SKIPPER code is an important milestone. This subroutine can be readily incorporated into other standard ground motion finite difference codes, whether 1D, 2D, or 3D. The table look-up routine used with the PEQ model can also be used in conjunction with tables generated with the P*EQ and PTEQ models. This capability is currently being added to TAMEOS.

At present the PEQ, P*EQ and PTEQ models are limited to hydrodynamic pressures less than 1 mbar, with primary emphasis on pressures less than 200 kbars. Additional work is needed to extend the range of the tables to be used in TAMEOS up to tens of megabars. Shock metamorphisms[70,71] in the rock component (e.g., poreless tuff or granite) should be considered to determine adequate treatments of these phase changes. Previous work in rock-water mixes by Butkovich[44] treated only the high pressure states for saturated rock under the PEQ model. Cratering calculations are believed to be very sensitive to the model used for energy partition between the components upon release after shock processing.

The irreversible pore collapse model used in TAMEOS is based on the disconnected pores postulate. Because of the sensitivity of the stress wave propagation calculations to the crushup constitutive model at these low pressures, a study should be made to determine the conditions under which the postulate is appropriate. The connected pore model and such phenomena as partial void recovery upon release should be considered in conjunction with the available experimental data.

The inclusion of four generalized plasticity models into SKIPPER provide the code with options that possess both sophistication and considerable flexibility to match available laboratory test data. The cap model and three Mohr-Coulomb models are included, one without work hardening, one with isotropic work hardening and one with kinematic work hardening. Comparison of calculations with field measurements in granite show the Mohr-Coulomb model with kinematic work hardening to give better agreement than is possible with the cap model. It appears at this time that the four models in the SKIPPER code are a sufficient base for treatments in which the medium is considered as a single material. Modifications are required, however, to adequately account for pore pressure effects and relative motion between blocks of jointed rock masses. These phenomena are believed to be the basic reason for the reduction in the laboratory flow stress value (by a factor of six) that is required to bring calculations for granite into agreement with field data. Such discrepancies do not appear to be severe for competent sedimentary materials.

In formulating the generalized plasticity models for the SKIPPER code a logrithmic definition of strain was employed. This is a preferred definition for one-dimensional codes but its interpretation in 2D codes is not apparent. Work is needed to permit these plasticity models to be also used in other codes, e.g., CRAM.

The TINC model for treating relative motion between the rock and water components in ground shock calculations has been significantly advanced with the development of the new POROUS code. The ground motion predictions for a partially saturated wet tuff using this new thermodynamic version of the code should be modified to treat a spherical high explosive charge as energy source so that the comparison can be made with an instrumented

high explosive field test. Consideration should also be given to modifying the TINC plasticity treatment in POROUS to include a generalized cap model for the rock component.

The 2D quasistatic FRI code represents a new tool for evaluating the interaction between a pore fluid and a stressed rock matrix as the fluid is driven through the rock mass. The code should be applied in a series of calculations for a region around an injection well in an effort to explain the mechanisms associated with hydrofracture. The intent would be to perform the quasistatic analysis at various stages of rupture in an effort to follow the redistribution of tectonic stresses and alterations in the permeability as the rock is fractured. Calculations should be devised for comparison with field data on the Rangley field, Colorado, and/or the Santa Fe Springs field, Los Angeles.

Consideration should be given to the development of a 2-D dynamic FRI computer code with a mechanism for spontaneous rupture. Such a code would provide a more adequate treatment than currently exists for evaluating the possibility of triggering earthquakes at NTS by the passage of a shock wave over a pre-existing fault zone.

REFERENCES

1. Riney, T. D., S. K. Garg, J. W. Kirsch, L. W. Morland, and C. R. Hastings, "Stress Wave Effects in Inhomogeneous and Porous Earth Materials," Systems, Science and Software Report 3SR-267, Defense Atomic Support Agency Report DASA-2498, March 31, 1970.

2. Riney, T. D., S. K. Garg, J. W. Kirsch, C. R. Hastings and K. G. Hamilton, "Wave Propagation in Geologic Composites," Systems, Science and Software Report 3SR-648, Defense Nuclear Agency Report DNA-2725I, July 1, 1971.

3. S^3 Presentation at MIDDLE GUST Meeting at Air Force Weapons Laboratory, July 8, 1971.

4. Sandler, I., and F. L. DiMaggio, "Material Model for Rocks," Paul Weidlinger, Consulting Engineer, Defense Atomic Support Agency Report DASA-2595, October 1970.

5. Gurtman, G. A., J. W. Kirsch, and C. R. Hastings, "Analytical Equations of State for Water Compressed to 300 Kbar," J. Appl. Phys., Vol. 42, no. 2, February 1971.

6. Morland, L. W., "A Simple Constitutive Theory for a Fluid-Saturated Porous Solid," J. Geophys. Res., Vol. 77, no. 5, February 10, 1972.

7. Garg, S. K., "Wave Propagation Effects in a Fluid Saturated Porous Solid," J. Geophys. Res., Vol. 76, no. 32, November 10, 1971.

8. Garg, S. K., and J. W. Kirsch, "Hugoniot Analysis of Composite Materials," J. Comp. Materials, Vol. 5, October 1971.

9. Morland, L. W., "Finite Deformation Plasticity Theory with Applications to Geologic Materials," J. Geophys. Res., Vol. 76, no. 29, October 10, 1971

10. Mogenstern, N. R., and A. L. Tamuly Dhukan, "Non-Linear Stress-Strain Relations for a Homogeneous Sandstone," Int. J. Rock Mech. and Min. Sci., Vol. 6, pp. 127-142, 1969.

11. Stephens, D. R., H. Louis, and E. M. Lilley, "Loading-Unloading PV Curves for Tuffs from the Nevada Test Site," UCRL-50554, February 20, 1969

Preceding page blank

12. Stephens, D. R., and E. M. Lilley, "Static PV Curves of Cracked Consolidated Earth Materials to 40 kbars," UCRL-14711, March 1966.

13. Froula, N. H., E. L. Suenaga, and R. L. Bryson, "Shock Compression and Release Behavior of Two Nevada Test Site Tuffs," S³ Report for Defense Nuclear Agency, Contract DNA 01-71-C-0080, 3SR-973, February 1972.

14. Herrmann, W., "Constitutive Equation for the Dynamic Compaction of Ductile Porous Materials," J. Appl. Phys., Vol. 40, no. 6, pp. 2490-2499, 1969.

15. Carroll, M., and A. C. Holt, "Suggested Modification of the P-α Model for Porous Materials," J. Appl. Phys., Vol. 43, no. 2, pp. 759-761, 1972.

16. Bjork, R. L., and M. L. Gittings, "Wave Generation by Underwater Explosions," Systems, Science and Software Report 3SR-1008 (draft), prepared for Defense Nuclear Agency under Contract DASA 01-71-C-0097, February 1972.

17. Shipman, F. H., W. M. Isbell, and A. H. Jones, "High Pressure Hugoniot Measurements for Several Nevada Test Site Rocks," DASA 2214, Materials and Structures Laboratory, General Motors Corporation Report MSL-68-15, March 1969.

18. Prieto, F. E., and C. Renero, "Equation for the Shock Adiabat," J. Appl. Phys., Vol. 41 p. 3876, 1970.

19. Prieto, F. E., and C. Renero, "Reduced Hugoniots," J. Appl. Phys. Vol. 42, p. 296, 1971.

20. Butkovich, T. R., "Influence of Water in Rocks on Effects of Underground Nuclear Explosions," J. Geophys. Res., Vol. 76, p. 1993, 1971.

21. Bjork, R. L., "Computed Response of the Hudson Moon H.E. Experiment," Topical Report prepared for Defense Nuclear Agency, Contract DASA 01-69-C-0146, S³ Report 3SIR-976, February 1972.

22. Anderson, G. D., "Determination of Test Needs for the VELA UNIFORM Program," Final Report prepared for Defense Nuclear Agency, Contract DASA 01-70-C-0122, Report DASA 2665, S³ Report 3SR-513, December 1970.

23. Anderson, G. D., "Near Field Seismic Predictions," Final Report prepared for Defense Nuclear Agency, Contract DASA 01-71-C-0129, S³ Report 3SR-741, July 1971.

24. Dienes, J. K., "Hardening Models for Granite at High Pressure," Topical Report prepared for Defense Nuclear Agency, Contract DASA 01-69-C-0159(P00003), S[3] Report 3SR-881, January 1972.

25. Truesdell, C., "The Mechanical Foundations of Elasticity and Fluid Dynamics," J. Rat. Mech. and Anal., Vol. 1, pp. 125-300, April 1952.

26. Truesdell, C., The Elements of Continuum Mechanics, Springer-Verlag, 1966.

27. Clifton, R. J., "On the Analysis of Elastic/Visco-Plastic Waves of Finite Uniaxial Strain," in Shock Waves and the Mechanical Properties of Solids, Syracuse University Press, 1971.

28. Wilkins, M. L., "Calculation of Elastic-Plastic Flow," in Methods of Computational Physics, Vol. 3, 1964, Academic Press.

29. Allen, R. T., "Equation of State of Rocks and Minerals," General Atomic Report GAMD-7834, March 1967.

30. Sandler, I., and F. L. DiMaggio, "Material Models for Rocks," Defense Nuclear Agency Report DASA 2595, October 1970.

31. Cherry, J. T., and F. L. Peterson, "Numerical Simulation of Stress Wave Propagation from Underground Nuclear Explosions," in the Proceedings of the Symposium on Engineering with Nuclear Explosives, Jan. 14-16, 1970, Las Vegas, Nevada.

32. Freudenthal, A. M., and P. F. Gore, "Second Order Effects in the Theory of Plasticity, Acta Mechanica, Vol. 8, pp. 34-52, 1969.

33. Drucker, D. C., and W. Prager, "Soil Mechanics and Plastic Analysis on Limit Design," Quarterly of Applied Mathematics, Vol. X, no. 2, July 1952.

34. Drucker, D. C., R. E. Gibson and D. J. Henkel," Soil Mechanics and Work-Hardening Theories of Plasticity," Proc. of the Am. Soc. of Civil Engineers, Vol. 81, September 1955.

35. Swanson, S. R., "Development of Constitutive Equations for Rocks," Ph.D. dissertation, Univ. of Utah, 1969.

36. Hill, R., "The Mathematical Theory of Plasticity," Oxford, 1950.

37. Prager, W., "The Theory of Plasticity: A Survey of Recent Achievements," Proc. Inst. Mech. Engrs. 169, no. 41, 1955.

38. Handin, John, "Strength and Ductility," Section 11 of Handbook of Physical Constants, Geologic Society of America, 1966.

39. Serdengecti, S., and G. D. Boozer, "The Effects of Strain Rate and Temperature on the Behavior of Rocks Subjected to Triaxial Compression," Symposium on Rock Mechanics, Proc. 4th (1961).

40. Zhurkov, S. N., and T. P. Sanfirova, "A Study of the Time and Temperature Dependences of Mechanical Strength," Soviet Phys. Solid State (English Transl.), Vol. 2, no. 6, p. 933 (1960).

41. Samanta, S. K., "Dynamic Deformation of Aluminum and Copper at Elevated Temperatures," J. Mech. Phys. Solids, Vol. 19, 1971.

42. Allen, R. T., and R. E. Duff, "Effect of Material Properties on Cavity Size from an Underground Nuclear Explosion," Nuclear Applications, Vol. 6, June 1969.

43. Wagner, M. H., and N. A. Louie, "Hard Hat/Piledriver Ground Motion Calculations," Space and Missile Systems Organization Report No. SAMSO-TR-69-47, March 1969.

44. Butkovitch, T. R., "The Gas Equation of State for Natural Materials," Lawrence Radiation Laboratory Report UCRL-14729, January 1967.

45. Fisher, R. H., R. A. Cecil, and G. A. Lane, "RIP, A One-Dimensional Material Response Code," Systems, Science and Software Report 3SR-751-II.

46. Boardman, C. R., D. R. Rabb, and R. D. McArthur, "Response of Four Rock Mediums to Contained Nuclear Explosions," J. Geophys. Res., Vol. 69, no. 16, August 1964.

47. Perret, William R., "Free Field Ground Motion in Granite, Operation Flint Lock, Shot Pile Driver," Defense Nuclear Agency Report POR-4001, September 1968.

48. Werth, G. C., and R. F. Herbst, "Comparison of Amplitudes of Seismic Waves from Nuclear Explosions in Four Mediums," J. Geophys. Res., Vol. 68, no. 5, March 1963.

49. Borg, I. Y., "Survey of Pile Driver Results and Preliminary Interpretation of Three Postshot Cores in and Near the Cavity," Lawrence Radiation Laboratory Report UCRL-50865, April 1970.

50. Allen, R. T., T. R. Blake and G. P. Schneyer, "Calculations of Pile Driver Event," Systems, Science and Software Report 3SR-854, November 1971.

51. Morland, L. W., "Finite Deformation Plasticity Theory with Application to Geologic Materials," J. Geophys. Res., Vol. 76, no. 29, October 1971.

52. Maxwell, D. E., J. E. Reaugh, and T. F. Stubbs, "Recent Physics International Computations of Pile Driver," Physics International Report TCAM Technical Memorandum 71-6, October 1971.

53. McKay, M. W., and C. S. Godfrey, "Study of Spherically Diverging Shock Waves in Earth Media," Physics International Report PIFR-064, March 1969.

54. Marble, F., "Dynamics of Dusty Gases," Annual Reviews of Fluid Mechanics, Vol. II, pp. 397-446, 1970.

55. Garg, S. K., and A. Nur, "Effective Stress Laws for Deformation and Fracture of Fluid-Saturated Porous Rocks," Submitted for Publication.

56. Nur, A., and G. Simmons, "The Effect of Saturation on Velocity in Low Porosity Rocks," Earth and Planetary Sci. Letters, Vol. 7, pp. 183-193, 1960.

57. Walsh, J. B., "The Effect of Cracks in Uniaxial Elastic Compression of Rocks," J. Geophys. Res., Vol. 70, no. 2, pp. 399-411, 1965.

58. Walsh, J. B., "The Effect of Cracks in Rocks on Poisson's Ratio," J. Geophys. Res., Vol. 70, no. 20, pp. 5249-5257, 1965.

59. Earthquake Engineering Research, a report to the N.S.F. by the Committee on Earthquake Engineering Research, National Academy of Sciences, Washington, D. C. 1969.

60. Healy, J. H., W. W. Rubey, D. T. Griggs, and C. B. Raleigh, "The Denver Earthquakes," Science, Vol. 161, pp. 1301-1310, 1968.

61. Raleigh, C. B., "Rangley, Colorado," Presentation at the Penrose Conference, Snowmass at Aspen, Colorado, September 1971.

62. Healy, J. H.,"Rangley Microearthquakes," Presentation at the Penrose Conference, Snowmass at Aspen, Colorado, September 1971.

63. Terzaghi, K., "Principle of Soil Mechanics," Eng. News Record, 1925, a series of articles.

64. Biot, M. A., "General Theory of Three-Dimensional Consolidation," J. Appl. Phys., Vol. 12, pp. 155-164, 1941.

65. Gibson, R. E., K. Knight, and P. W. Taylor, "A Critical Experiment to Examine Theories of Three-Dimensional Consolidation," Proc. European Conf. Soil Mech. and Found. Eng., Wiesbaden, Vol. 1, pp. 69-76, 1963.

66. Verruijt, A., Discussion, Proc. 6th Intern. Conf. Soil Mech. and Found Eng., Montreal, Vol. 3, pp. 401-402, 1965.

67. Verruijt, A., "Elastic Storage in Aquifers (Chapter 8)," Flow Through Porous Media, R.J.M. DeWiest (Ed.), Academic Press, 1969.

69. Wilson, E. L., and R. E. Nickell, "Application of the Finite Element Method to Heat Conduction Analysis," Nuclear Engrg. and Design, Vol. 4, pp. 276-286, 1966.

70. Ahrens, T. J., and J. T. Rosenberg, "Shock Metamorphism: Experiments on Quartz and Plagioclase," in Shock Metamorphism of Natural Materials, Mono Book Co., Baltimore, Md., 1968.

71. Ahrens, T. J., C. F. Petersen, and J. T. Rosenberg, "Shock Compressions of Feldspars," J. Geophys. Res., Vol. 74, pp. 2727-2746, 1969.

72. Green, S. J., R. M. Griffin, A. D. Black, S. W. Butters, S. W. Duncan and K. B. Watson, "High Pressure Properties of Several Nevada Test Site Tuffs," Terra Tek, Inc. Report TR 71-30, submitted to Test Command, DNA, August 1971.

73. Lee, E. L., H. C. Hornig, and J. W. Kury, "Adiabatic Expansion of High Explosive Detonation Products," Lawrence Radiation Laboratory Report UCRL-50422, May 1968.

74. Coleburn, N. L., and T. P. Liddiard, "Hugoniot Equations of State of Several Unreacted Explosives, J. Chem. Phys., Vol. 44, p. 1929, March 1966.

75. Hubbert, M. K., and W. W. Rubey, "Role of Fluid Pressure in Mechanics of Overthrust Faulting, Bull. Geo. Soc. Am., Vol. 70, p. 115, 1959.

76. Hubbert, M. K., and W. W. Rubey, "Role of Fluid Pressure in Mechanics of Overthrust Faulting: A reply, Bull. Geo. Soc. Am., Vol. 71, p. 611, 1960.

77. Robinson, L. H., Jr., "The Effect of Pore and Confining Pressure on the Failure Process in Sedimentary Rock," Colorado School of Mines Quarterly, Vol. 54, no. 3, p. 177, 1959.

78. Handin, J., R. V. Hager, Jr., M. Friedman, J. N. Feather, "Experimental Deformation of Sedimentary Rocks under Confining Pressure: Pore Pressure Tests," Bull. Am. Pet. Geo., Vol. 47, p. 717, 1963,

79. Murrell, S.A.F., "A Criterion for Brittle Fracture of Rocks and Concrete under Triaxial Stress, and the Effect of Pore Pressure on the Criterion," Rock Mechanics (Proc. 5th Sympo. on Rock Mech.) Ed. by C. Fairhurst, p. 563, Pergammon Press, 1963.

80. Brace, W. F., R. J. Martin, III, "A Test of the Law of Ineffective Stress for Crystalline Rocks of Low Porosity," Int. J. Rock Mech. Min. Sci., Vol. 5, pp. 415-426, 1968.

81. Geertsma, J., "The Effect of Fluid Pressure Decline on Volumetric Changes of Porous Rocks," Trans. AIME, p. 310-331, 1957.

82. Skempton, A. W., "Effective Stress in Soils, Concrete and Rock," in Pore Pressure and Suction in Soils, Butterworth, London, 1960.

83. Skulje, L., Rheological Aspects of Soil Mechanics, p. 123, Interscience Publishing Co., 1969.

APPENDIX A
SOUND SPEED IN A POROUS MATERIAL

The model of a porous material introduced in 3SR-648 specifies that the bulk hydrodynamic pressure in the porous material is given by

$$p = \frac{\underline{P}\left(\frac{V}{\alpha}, E\right)}{\alpha} \tag{A.1}$$

where

V = bulk specific volume

E = specific internal energy

α = distension ratio

$$\equiv \frac{n^{(S)} + n^{(V)}}{n^{(S)}}, \quad n^{(S)} = \text{volume fraction of solid}$$

$$n^{(V)} = \text{volume fraction of voids}$$

$\underline{P}(V^e, E)$ is the hydrodynamic equation of state of the solid material where V^e is the effective specific volume of the poreless solid, i.e.,

$$V^e = \frac{V}{\alpha} \tag{A.2}$$

In the present formulation, we recognize that the bulk pressure is averaged over the total surface area, so that the effective stress is reduced by a factor of $1/\alpha$. This differs from Herrmann's[14] model wherein bulk pressure is set to

$$(p)_{Herrmann} = \underline{P}\left(\frac{V}{\alpha}, E\right) = \underline{P}(V^e, E) \tag{A.3}$$

Preceding page blank

Carroll and Holt[15] have discussed these two formulations and recommended that Eq. (A.1) be adopted for strengthless porous matrices. They did not rederive the expression for the sound speed of the bulk material in their analysis. This relationship is presented below and compared to the original expression proposed by Herrmann.

Let us retain Herrmann's form for the distension ratio, i.e.,

$$\alpha = \alpha(p) \tag{A.4}$$

The sound speed, c, may be obtained as follows;

$$\frac{c^2}{V^2} = -\left(\frac{\partial p}{\partial V}\right)_E + p\left(\frac{\partial p}{\partial E}\right)_V \tag{A.5}$$

Differentiating Eq. (A.1) leads to

$$\left(\frac{\partial p}{\partial V}\right)_E = \frac{\frac{1}{\alpha^2}\left(\frac{\partial P}{\partial V^e}\right)_E}{1 + \left(V^e \frac{\partial P}{\partial V^e} + \underline{P}\right)\frac{\alpha'(p)}{\alpha^2}} \tag{A.6}$$

and

$$\left(\frac{\partial p}{\partial E}\right)_V = \frac{\frac{1}{\alpha}\left(\frac{\partial P}{\partial E}\right)_{V^e}}{1 + \left(V^e \frac{\partial P}{\partial V^e} + \underline{P}\right)\frac{\alpha'(p)}{\alpha^2}} \tag{A.7}$$

Since the sound speed in the solid material is defined by

$$c_S^2 \equiv -(V^e)^2 \frac{\partial P}{\partial V^e} + V_e^2\, \underline{P}\, \frac{\partial P}{\partial E}, \tag{A.8}$$

we arrive at the following expression for bulk sound speed

$$c^2 = \frac{c_S^2}{1 + \left(V^e \dfrac{\partial \underline{P}}{\partial V^e} + \underline{P}\right) \dfrac{\alpha'(p)}{\alpha^2}} \tag{A.9}$$

In the limit of $P \to 0$, this reduces to

$$c^2 = \frac{c_{S_0}^2}{1 - \left(\dfrac{\alpha'(0)}{\alpha_0^2} K_0\right)} \tag{A.10}$$

where

$K_0 \equiv$ normal bulk modulus

$$= \lim_{\underline{P} \to 0} \left(-V^e \frac{\partial \underline{P}}{\partial V^e}\right)$$

c_{S_0} = sound speed in solid material at zero pressure

Herrmann's expression is

$$(c^2)_{\text{Herrmann}} = \frac{\alpha_0 \, c_{S_0}^2}{\left(1 - \dfrac{\alpha'(0) K_0}{\alpha_0}\right)} \tag{A.11}$$

It is apparent that both results indicate that major reductions in the sound speed of porous materials can be achieved only if the matrix deforms under infinitesimal compressions ($\alpha'(0) < 0$). The major difference between the two models is the factor of α_0 which appears in the numerator of Herrmann's expression. This term is troublesome from a physical viewpoint since it implies that in the limit of a perfectly rigid

matrice structure ($\alpha'(0) \rightarrow 0$), the sound speed is increased by adding to the void volume fraction. In the present formulation, the α_0 factor no longer appears. Hence in the same limit we are left with sound speeds that are identical to those in the matrix material. Although not cited by Carroll and Holt, this last result lends more weight to the arguments in favor of utilization of the effective stress model (Eq. (A.1)).

APPENDIX B
H.E. TEST PARAMETER CALCULATIONS

In response to a request by the contract monitor, C. B. McFarland of Hdq., DNA, calculations were made to investigate the relevance of material properties to the ground motion and stress pulse generated by high explosive tests in NTS tuff. The material models employed were based on fits to laboratory data on tuff samples obtained from specific locations at the Nevada Underground Test site. The calculations also examined the sensitivity of the results to the representation of the high explosive energy source in the calculations.

Tuff properties from two locations near the (U12e-12) underground nuclear test site were considered in the calculations. Samples of the tuff at distances from the working point of 30 ft (Slifer Hole #1) and 1330 ft (Drill Back 7) were selected from those tested under quasi-static loading by Green, et al.[72] These two locations represent the extremes in the measured gas-filled porosities measured at the site. At the Drill Back 7 (DB-7) location the tuff is almost completely saturated with only 1.6 percent of the volume gas-filled. At Slifer Hole #1 (SH-1) fully 7.6 percent of the volume is gas-filled, representing 22% of the total pore volume in the tuff. The solid-water-void volume fractions for the two tuffs are listed in Table B.1.

A fit to the quasi-static data from the DB-7 location was used by Bjork[21] in a predictive calculation for a 1000-lb nitromethane sphere detonated at that site. The ground motion measurements subsequently made in thetest were

TABLE B.1

DESCRIPTION OF TEST SPECIMENS

	SH-1	DB-7
In-Situ Density (g/cc)	1.86 ± 0.03	1.88 ± 0.02
Tuff Grain Density (g/cc)	2.35 +	2.37 +
Grain Volume Fraction, $n_0^{(1)}$	0.655	0.634
Water Volume Fraction, $n_0^{(2)}$	0.269	0.350
Air Volume Fraction, $n_0^{(3)}$	0.076	0.016
$n_0^{(3)} / \left(n_0^{(2)} + n_0^{(3)} \right)$	22%	4.4%

in good agreement with the calculations. It was decided to use the same tuff model in the parameter calculations reported here except a treatment of the irreversible crushup states was added in order to permit the calculations to follow the stress pulse propagation to greater distances from the source while using the SKIPPER code.

The constitutive relations for tuff used in the computations therefore consisted of three parts. First, the energy-pressure-volume equation of state for the completely crushed material is specified by the equation

$$p = G\rho E + A\mu + B\mu^2, \quad \mu = \frac{\rho}{\rho_0} - 1 \tag{B.1}$$

where the reference density ρ_0 here refers to the completely crushed tuff/water mix (only water filled pores remaining) at ambient conditions. Second, the partially crushed material is characterized by a porosity parameter $\alpha(p) = \rho_s(p)/\rho_p(p)$. Here ρ_s and ρ_p are the densities of the completely crushed and partially crushed materials respectively at the same pressure. A simple form for $\alpha(p)$ was used since the limited data available did not justify a more elaborate fit,

$$\alpha = 1 + (\alpha_0 - 1)(1 - p/p_c)^2 \qquad \text{(B.2)}$$

Here α_0 is the value of α at ambient conditions and p_c is the pressure at which all gas-filled pores are crushed out of the tuff. The p_c value was estimated from uniaxial strain test data.[72] Third, the deviatoric stress was computed with an elastic-perfectly plastic model, using a constant rigidity modulus G and a simple von Mises yield condition,

$$S_1^2 + S_2^2 + S_3^2 \leq \frac{2}{3} Y^2 , \qquad \text{(B.3)}$$

where the S_i are the principal deviatoric stresses.

The values of the constants used in the constitutive relations for the two partially saturated wet tuffs are listed in Table B.2. The higher volume of gas-filled porosity at the SH-1 location may be expected to enhance the displacement at given pressure, but its higher shear strength should counteract this to some extent. It was of interest to evaluate these competing effects, to assist in the selection of the site for a planned high explosive test in the U16a tunnel complex at the Nevada Test Site.

TABLE B.2

CONSTITUTIVE MODEL CONSTANTS FOR TWO LOCATIONS

	SH-1	DB-7
A (kbar)	83.3	83.3
B (kbar)	83.3	83.3
G	1.8	1.8
ρ_0 (g/cc)	2.012	1.911
α_0	1.082	1.0165
p_c (kbar)	1.0	0.5
μ (kbar)	10.5	10.5
Y (kbar)	0.55	0.346

The source was taken to be a 1000-lb sphere of Composition B high explosive with a density of ρ_0 = 1.7 g/cc prior to detonation. The initial radius of the charge is therefore R_0 = 39.5 cm. Four tuff comparison calculations were made for two representations of the source. Two calculations treated the burning process and employed a pressure-volume-energy equation of state to compute the detailed behavior of the detonation products. Two additional calculations were made in which the source was approximated by a γ-law gas in the expanding spherical cavity of initial radius R_0.

In the calculations which included the burning process in the source representation, the empirical Jones-Wilkins-Lee equation of state[73] was used to describe the

Composition B detonation products. This equation is prescribed by the pVE relation

$$p = A\left(1 - \frac{\omega}{C_1 V}\right)e^{-C_1 V} + B\left(1 - \frac{\omega}{C_2 V}\right)e^{-C_2 V} + \frac{\omega E}{V} \qquad (B.4)$$

The constants for Composition B are listed in Table B3. In the computations the detonation front propagates from the center of the sphere at wave speed $D_{CJ} = 7.98 \times 10^5$ cm/sec and the chemical energy released on detonation is $E_0 = 4.95 \times 10^{10}$ ergs/g. The corresponding Chapman-Jouguet pressure and density are $p_{CJ} = 295$ kbar and $\rho_{CJ} = 2.35$ g/cc, respectively.

In the two calculations in which the source was approximated by a cavity containing a γ-law gas, the pressure in the expanding cavity was computed from

$$p = p_{CJ}\left(\frac{\rho}{\rho_{CJ}}\right)^{\gamma} \qquad (B.5)$$

where the value $\gamma = 2.77$ and the associated parameters listed in Table B.3 were estimated from work by Coleburn and Liddiard.[74] The density and pressure are assumed to be uniform within the cavity at any time. The initial cavity pressure in the computations is given by

$$p_0 = 283\left(\frac{1.7}{2.35}\right)^{2.77} = 116 \text{ kbar} \qquad (B.6)$$

In Fig. B.1 the profound effect of air-filled porosity on shock wave attenuation is illustrated. The less saturated SH-1 material requires only about half the distance to attenuate the shock to a given pressure as does the DB-7 material. The γ-law gas approximation is seen to produce results very close to those obtained using the detailed treatment of the burning process in the source

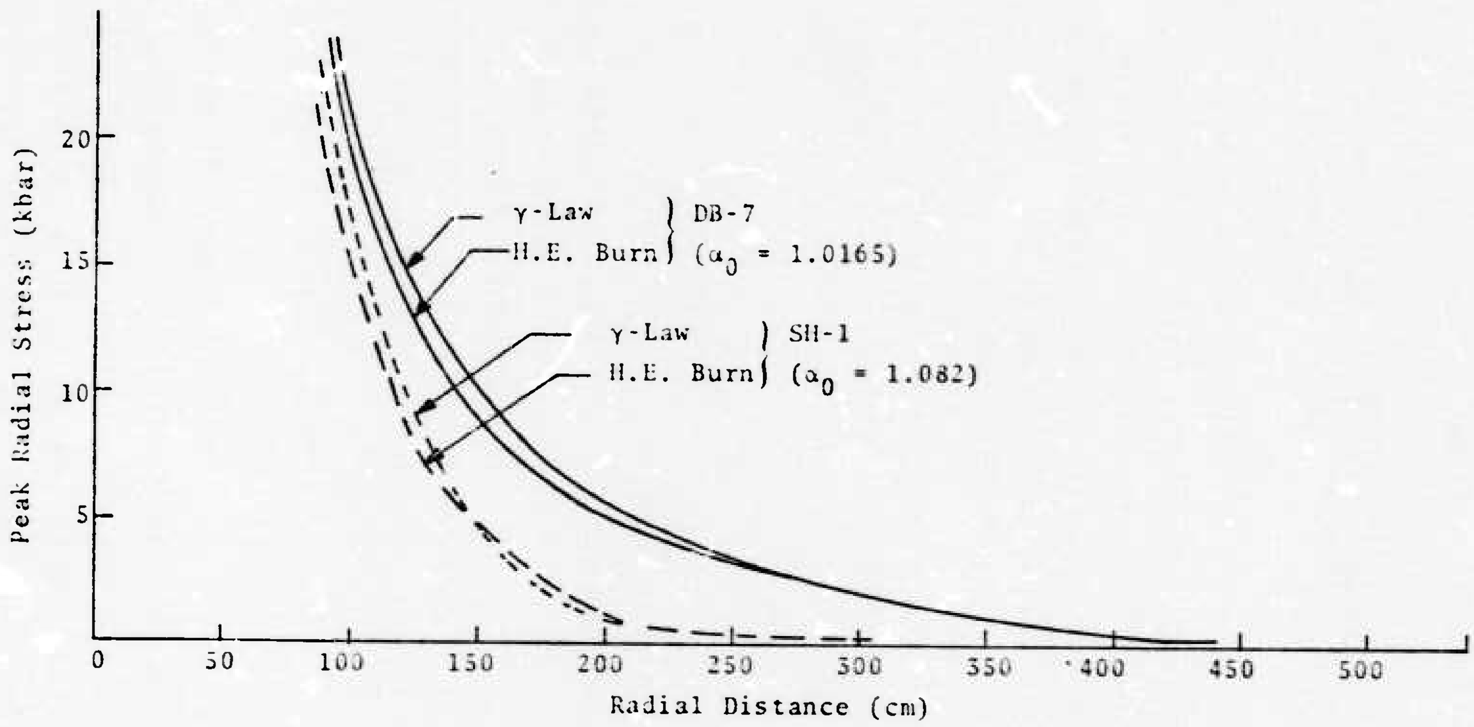

Fig. B1--Peak radial stress vs distance from 1000 lb Composition B energy source.

TABLE B.3

EQUATION OF STATE PARAMETERS FOR COMPOSITION B HIGH EXPLOSIVE

	JWL	γ-Law
A (dynes/cm^2)	5.24×10^{12}	-
B (dynes/cm^2)	7.678×10^{10}	-
C_1 (g/cc)	7.21	-
C_2 (g/cc)	1.89	-
ω	0.34	-
ρ_0 (g/cc)	1.717	1.7
E_0 (ergs/g)	4.95×10^{10}	-
p_{CJ} (dynes/cm^2)	2.95×10^{11}	2.83×10^{11}
ρ_{CJ} (g/cc)	2.35	2.35
D_{CJ} (cm/sec)	7.98×10^5	7.95×10^5

representation. At early times the γ-law approximation overestimates the driving pressure and at late times it underestimates it. This is illustrated by the results shown in Fig. B.2.

The stress-time history at radial distances from the source of R_0 = 123.7 cm and 203.6 cm, respectively, are shown in Figs. B.3 and B.4. The hump in the profiles for the calculations which treated the detonation processes result from a wave which is reflected at the center of the cavity and eventually catches up with the shock front.

In Fig. B.5 the radial displacement-time history is shown at a distance of R_0 = 203.6 cm from the source (R_0 = 207 cm for SH-1). Although the calculations have not

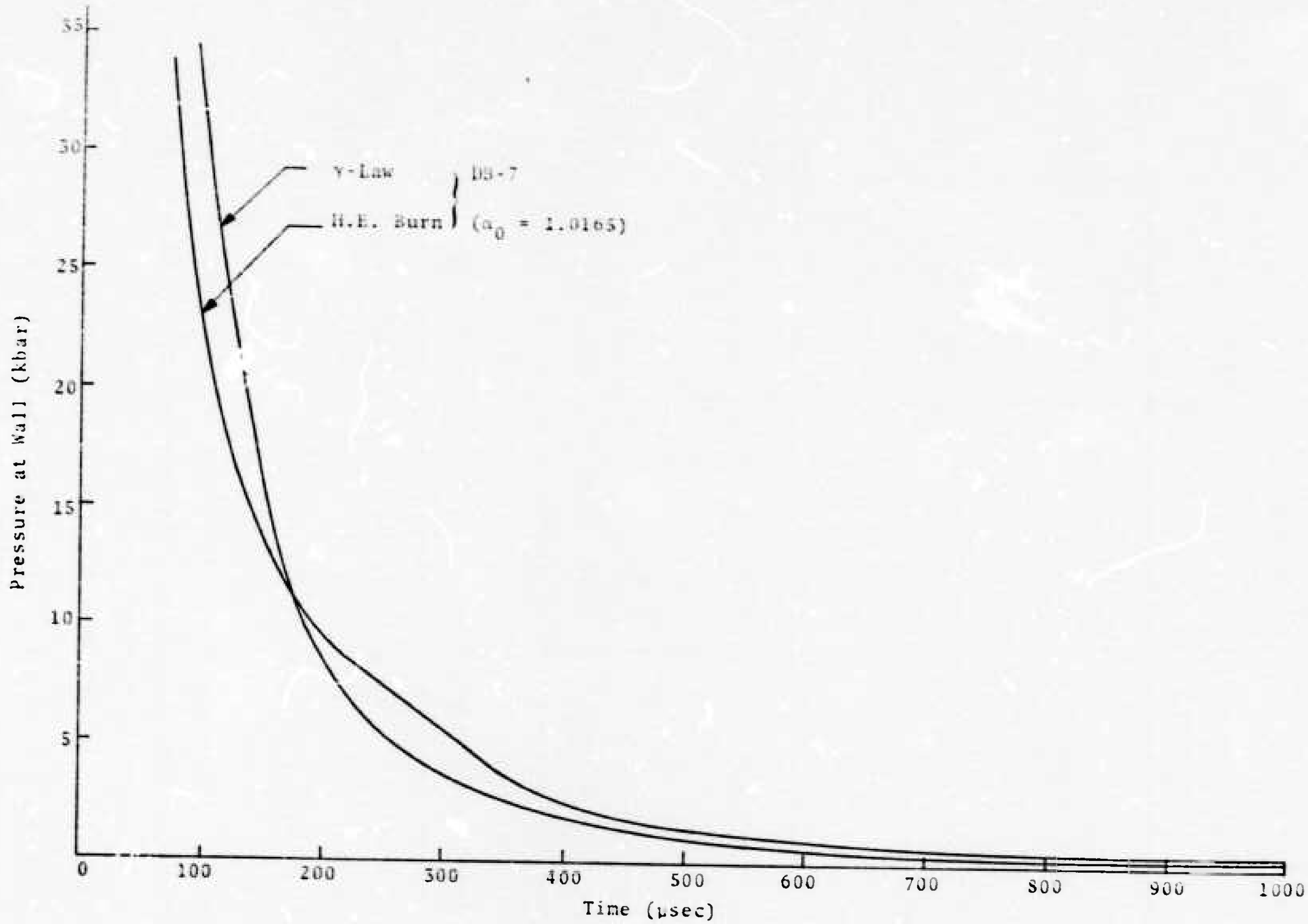

Fig. B2--Pressure at the cavity wall for γ-Law gas and H.E. burn representations of energy source.

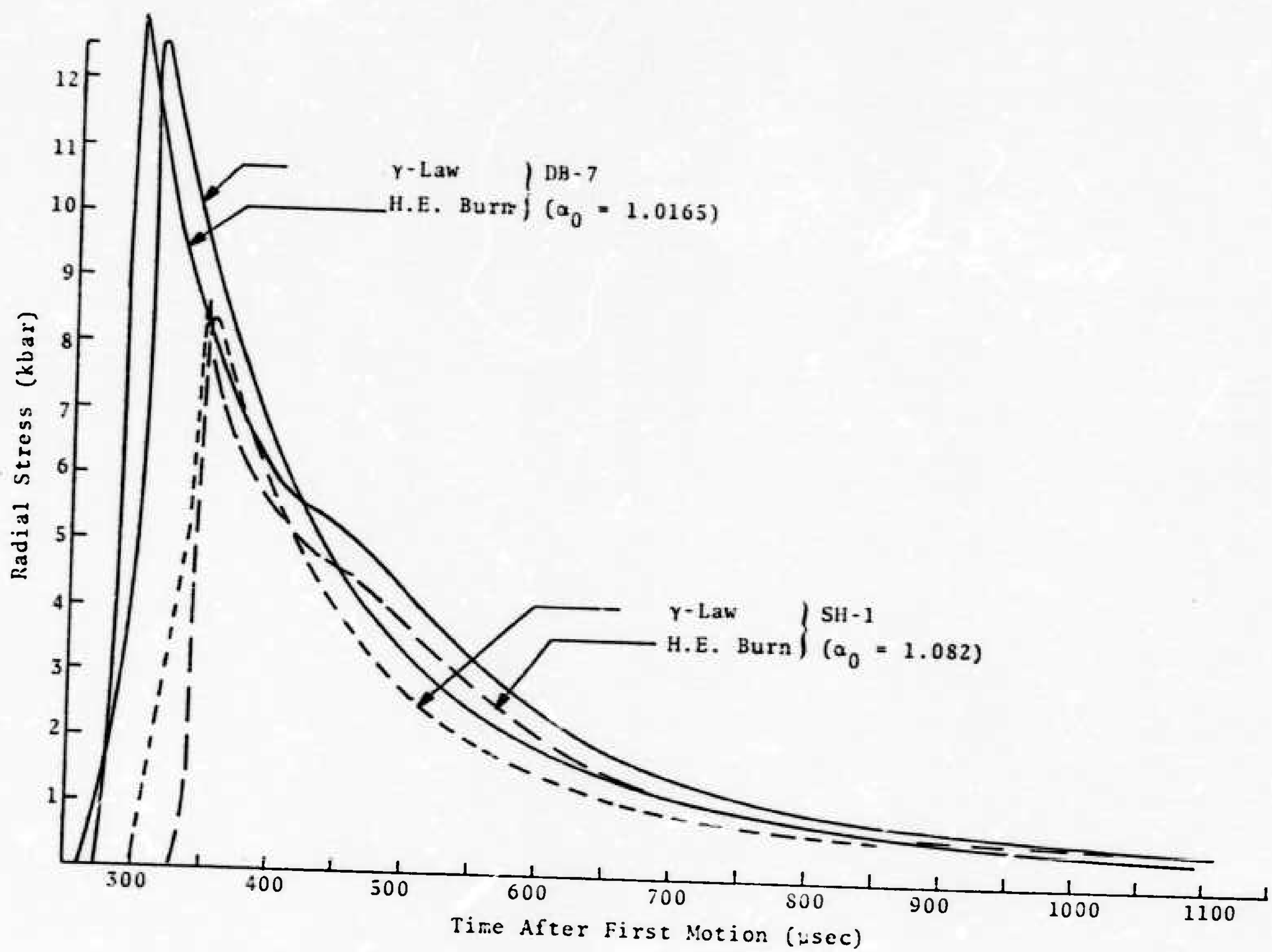

Fig. B3--Radial stress-time history at a radial distance of R_0 = 123.7 cm from the 1000 lb Composition B high explosive source

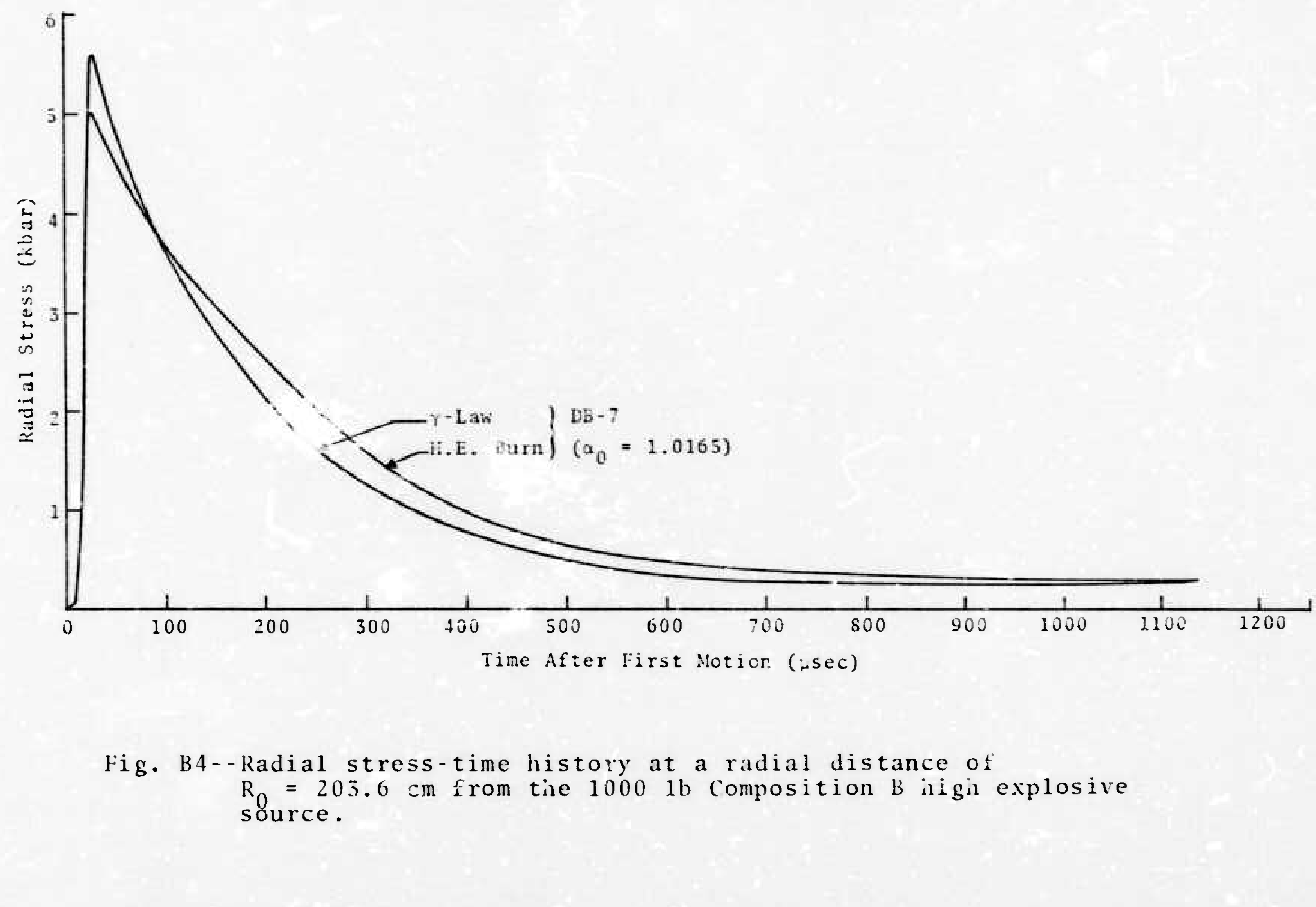

Fig. B4--Radial stress-time history at a radial distance of R_0 = 203.6 cm from the 1000 lb Composition B high explosive source.

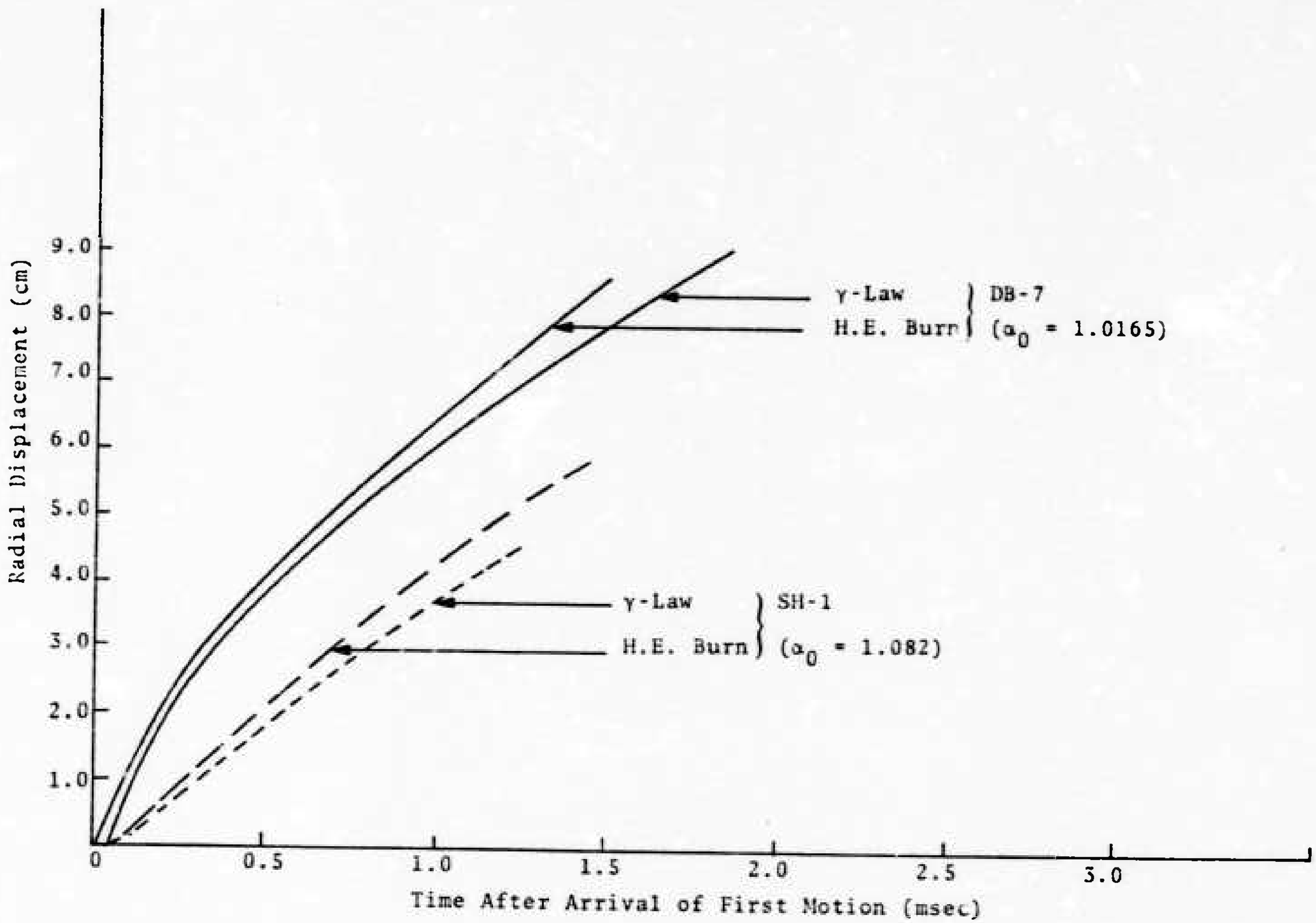

Fig. B5--Radial displacement-time history at a radial distance of R_0 = 203.6 cm from the 1000 lb Composition B high explosive source.

been carried to late enough times to determine final displacements, it is clear that much greater displacements occur in the more saturated DB-[illegible] tuff. At this distance it experiences a peak stress of 5 kbar whereas the SH-1 tuff is subjected to a peak stress of only $\sim$ 1 kbar. Finally, the time of arrival of the shock front at a given radial distance is shown in Fig. B.6 for each of the two tuffs.

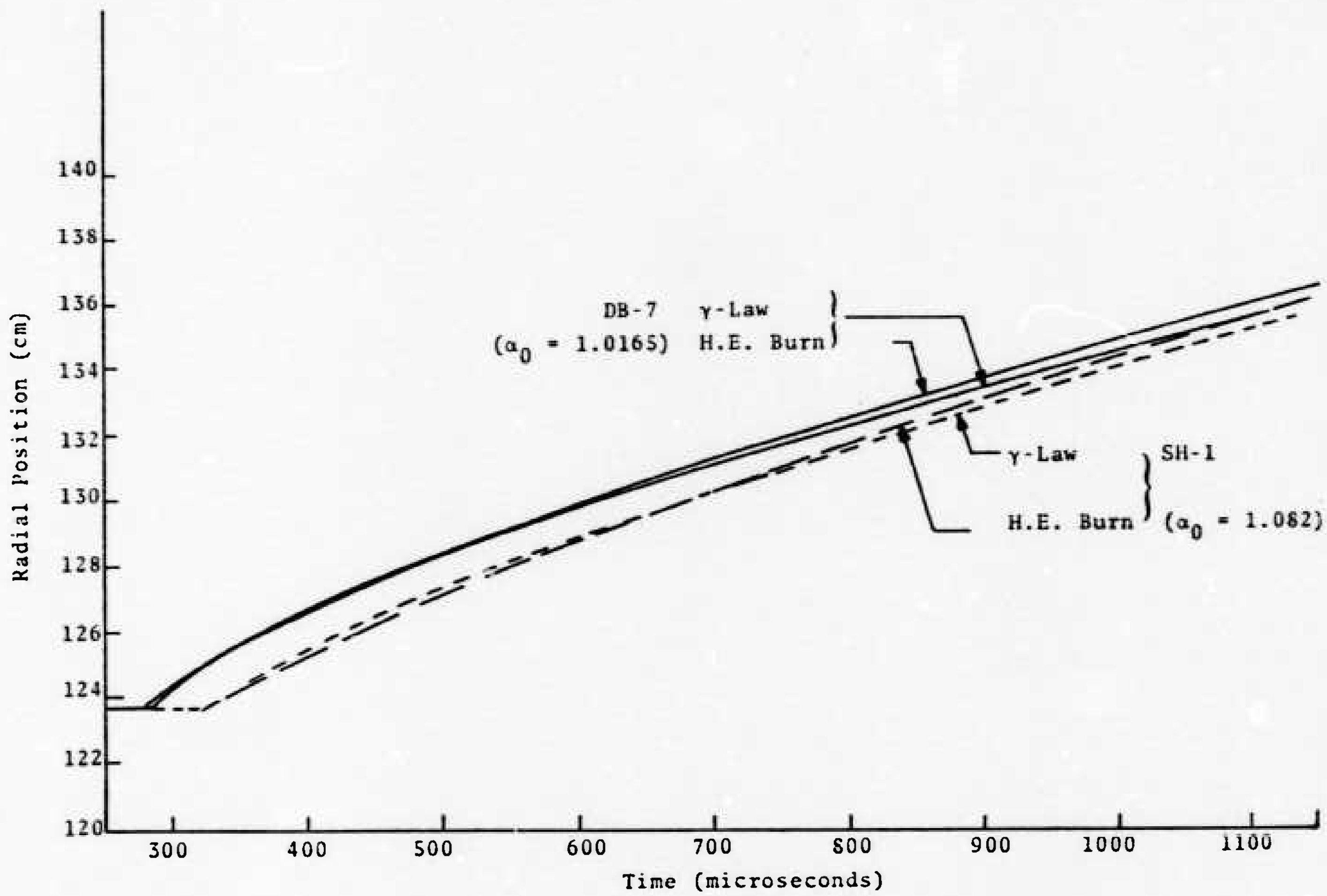

Fig. B6--Time of arrival of shock front at indicated radial distance from the 1000 lb Composition B high explosive source.

APPENDIX C

INTERACTION TERMS

In the Theory of Interacting Continua (TINC), each $\overset{(\alpha)}{s}$ has a velocity field $\overset{(\alpha)}{\underline{v}}(x,t)$, stress field $\overset{(\alpha)}{\sigma}_{ij}(x,t)$ and a density field $\overset{(\alpha)}{\rho}(x,t)$. Associated with these mixture quantities, we postulate the existence of $\overset{(\alpha)}{\underline{v}}{}^e(x,t)$, $\overset{(\alpha)}{\sigma}{}^e_{ij}(x,t)$ and $\overset{(\alpha)}{\rho}{}^e(x,t)$ in the physical configuration. It is to be noted that neither of the two sets of quantities corresponds to the actual distribution in the body. The quantities in the physical configuration $\left(\overset{(\alpha)}{\underline{v}}{}^e, \overset{(\alpha)}{\sigma}{}^e_{ij}, \overset{(\alpha)}{\rho}{}^e\right)$ represent the averages of the actual variables taken over several grains. Thus, purely local effects (e.g., stress concentrations along a pore boundary) are ignored. The relationships between $\overset{(\alpha)}{\sigma}_{ij}$ and $\overset{(\alpha)}{\sigma}{}^e_{ij}$, and $\overset{(\alpha)}{\rho}$ and $\overset{(\alpha)}{\rho}{}^e$ were given in Section IV. The velocity distributions $\overset{(\alpha)}{\underline{v}}(x,t)$ and $\overset{(\alpha)}{\underline{v}}{}^e(x,t)$ will not be in general identical. In the following discussion, it will be, however, presumed that

$$\frac{\overset{(\alpha)}{D}}{Dt} \equiv \frac{\overset{(\alpha)}{D}{}^e}{Dt}$$

where

$$\frac{\overset{(\alpha)}{D}}{Dt} = \frac{\partial}{\partial t} + \overset{(\alpha)}{\underline{v}} \cdot \text{grad}; \quad \frac{\overset{(\alpha)}{D}{}^e}{Dt} = \frac{\partial}{\partial t} + \overset{(\alpha)}{\underline{v}}{}^e \cdot \text{grad} \qquad \text{(C.1)}$$

This follows from the fact that one is trying to follow the same particle in both the mixture and the physical configuration.

The following discussion will be restricted to a two-component mixture. Superscripts (1) and (2) are used to denote $\overset{(1)}{s}$ (rock) and $\overset{(2)}{s}$ (fluid), respectively. The rock is regarded to be an elastic-plastic solid. The fluid is

Preceding page blank

taken to be inviscid, but due account is taken of the viscous effects by postulating the existence of a diffusive force, $-\rho_0 \underline{n}$. It represents the drag force experienced by the fluid as it passes through the porous rock.

The mass conservation relations for $\overset{(\alpha)}{s}$ are:

<u>Mixture:</u>

$$\frac{\overset{(\alpha)}{D}\,\overset{(\alpha)}{\rho}}{Dt} + \overset{(\alpha)}{\rho}\operatorname{div}\overset{(\alpha)}{\underline{v}} = 0$$

$$\alpha = 1,\ 2 \qquad (C.2)$$

<u>Physical Configuration:</u>

$$\frac{\overset{(\alpha)}{D}{}^{e}\,\overset{(\alpha)}{\rho}{}^{e}}{Dt} + \overset{(\alpha)}{\rho}{}^{e}\operatorname{div}\overset{(\alpha)}{\underline{v}}{}^{e} = 0$$

$$\alpha = 1,\ 2 \qquad (C.3)$$

Combining Eqs. (1) through (3) and noting the

$$\overset{(\alpha)}{\rho} = \overset{(\alpha)}{n}\,\overset{(\alpha)}{\rho}{}^{e} \qquad (C.4)$$

there follows:

$$\operatorname{div}\overset{(\alpha)}{\underline{v}}{}^{e} = \operatorname{div}\overset{(\alpha)}{\underline{v}} + \frac{1}{\overset{(\alpha)}{n}}\left[\frac{\partial \overset{(\alpha)}{n}}{\partial t} + \overset{(\alpha)}{\underline{v}}\cdot\operatorname{grad}\overset{(\alpha)}{n}\right]$$

$$\alpha = 1,\ 2. \qquad (C.5)$$

The momentum balance relation for $\overset{(\alpha)}{s}$ in the mixture is given by:

$$\overset{(\alpha)}{\rho}\,\frac{\overset{(\alpha)}{D}\,\overset{(\alpha)}{v}_i}{Dt} = \frac{\partial\,\overset{(\alpha)}{\sigma}_{ij}}{\partial x_j} + \rho\,\overset{(\alpha)}{\beta}_i$$

$$\alpha = 1,\ 2 \qquad \text{(C.6)}$$

For a two-component mixture, we have

$$\rho\,\overset{(1)}{\underline{\beta}} = -\rho\,\overset{(2)}{\underline{\beta}} = \rho\underline{\beta} \qquad \text{(C.7)}$$

For $\overset{(2)}{s}$, the stress tensor $\overset{(\alpha)}{\sigma}_{ij}$ $\left(\text{or } \overset{(\alpha)}{\sigma}{}^{e}_{ij}\right)$ is isotropic, i.e.,

$$\overset{(2)}{\sigma}_{ij} = -\overset{(2)}{p}\,\delta_{ij} = -\overset{(2)}{n}\,\overset{(2)}{p}{}^{e}\,\delta_{ij} = \overset{(2)}{n}\,\overset{(2)}{\sigma}{}^{e}_{ij} \qquad \text{(C.8)}$$

Noting that the fluid is subjected a drag force $-\rho_0\eta$ as it passes through the rock, the momentum balance relation for the fluid in the physical configuration may be written as:

$$\frac{\overset{(2)}{D}{}^{e}\,\overset{(2)}{v}{}^{e}_i}{Dt} = -\frac{\partial\,\overset{(2)}{p}{}^{e}}{\partial x_i} - \rho_0\eta_i \qquad \text{(C.9)}$$

We now require that

$$\frac{\overset{(2)}{D}{}^{e}\,\overset{(2)}{v}{}^{e}_i}{Dt} = \frac{\overset{(2)}{D}\,\overset{(2)}{v}_i}{Dt} \qquad \text{(C.10)}$$

Relation (C.10) follows from the fact that the change of momentum in the physical configuration must equal to the change in the mixture configuration. Therefore, combining Eqs. (C.6)

through (10), we obtain

$$\rho\underline{\beta} = -\overset{(2)}{p}^{e}\,\mathrm{grad}\,\overset{(2)}{n} + \rho_0\underline{n} \qquad (C.11)$$

Thus the momentum interaction term, $\rho\underline{\beta}$, consists of two parts, i.e., dilatation $\left(-\overset{(2)}{p}^{e}\,\mathrm{grad}\,\overset{(2)}{n}\right)$ and shear $(\rho_0\underline{n})$ contributions.

Let us now examine the momentum balance relations for the rock matrix, $\overset{(1)}{s}$. In contradistinction to the fluid $\left(\overset{(2)}{s}\right)$, the relationship between the mixture and the physical configurations is not readily obvious. The interaction force, $\rho\underline{\beta}$, may induce a complex state of stress in the solid. As an example, let us consider the mixture to be in a state of uni-axial strain. In this equation, the momentum balance for $\overset{(1)}{s}$ in the mixture is

$$\overset{(1)}{\rho}\,\frac{\overset{(1)}{D}\,\overset{(1)}{v}_1}{Dt} = \frac{\partial\,\overset{(1)}{\sigma}_{11}}{\partial x_1} + \rho\,\overset{(1)}{\beta}_1 \qquad (C.12)$$

In the physical configuration, the momentum balance relation (using (C.10)) is:

$$\overset{(1)}{\rho}^{e}\,\frac{\overset{(1)}{D}\,\overset{(1)}{v}_1}{Dt} = \frac{\partial\,\overset{(1)}{\sigma}^{e}_{11}}{\partial x_1} + \frac{\partial\,\overset{(1)}{\sigma}^{e}_{12}}{\partial x_2} + \frac{\partial\,\overset{(1)}{\sigma}^{e}_{13}}{\partial x_3} \qquad (C.13)$$

The stress components $\overset{(1)}{\sigma}^{e}_{12}$ and $\overset{(1)}{\sigma}^{e}_{13}$ will in general be non-zero. Although the mixture is undergoing uni-axial motion, the individual constituents may be in a more complex stress state. In this particular case, $\overset{(1)}{\sigma}^{e}_{12}$ and $\overset{(1)}{\sigma}^{e}_{13}$ are the result of the interactive force, $\rho\,\overset{(1)}{\beta}_1$. Combining equations (C.12) and (C.13) and noting that

$$\overset{(\alpha)}{\sigma}_{ij} = \overset{(\alpha)}{n}\,\overset{(\alpha)}{\sigma}^{e}_{ij}\,, \qquad (C.14)$$

there follows:

$$\overset{(1)}{\rho}\,\beta_1 = \rho\beta_1 = -\overset{(1)}{\sigma}{}^{e}_{11}\frac{\partial \overset{(1)}{n}}{\partial x_1} + \frac{\partial \overset{(1)}{\sigma}{}^{e}_{12}}{\partial x_2} + \frac{\partial \overset{(1)}{\sigma}{}^{e}}{\partial x_3} \tag{C.15}$$

From Eqs. (C.11) and (C.15), we have also:

$$\rho\beta_1 = -\overset{(2)}{p}{}^{e}\frac{\partial \overset{(2)}{n}}{\partial x_1} + \rho_0 n_1 = -\overset{(1)}{\sigma}{}^{e}_{11}\frac{\partial \overset{(1)}{n}}{\partial x_1}$$

$$+ \frac{\partial \overset{(1)}{\sigma}{}^{e}_{12}}{\partial x_2} + \frac{\partial \overset{(1)}{\sigma}{}^{e}_{13}}{\partial x_3} \tag{C.16}$$

Thus, in trying to relate the mixture configuration to the physical configuration for $\overset{(1)}{s}$, it is necessary to separate out the stresses induced by the interaction with $\overset{(2)}{s}$. Such an identification may be impossible except in very simple cases such as uni-axial motion.

The internal energy balance relation for $\overset{(\alpha)}{s}$ in the mixture is

$$\overset{(\alpha)}{\rho}\,\frac{\overset{(\alpha)}{D}\,\overset{(\alpha)}{E}}{Dt} = \overset{(\alpha)}{\sigma}_{ij}\,\frac{\partial \overset{(\alpha)}{v}_i}{\partial x_j} + \rho\,\overset{(\alpha)}{\psi} \tag{C.17}$$

$$\alpha = 1,\ 2.$$

We will now assert that:

$$\overset{(\alpha)}{E}{}^{e} \equiv \overset{(\alpha)}{E} \qquad \alpha = 1,\ 2 \tag{C.18}$$

In other words, the internal energy $\overset{(\alpha)}{E}$ is the same in both the mixture and the physical configurations.

For the fluid, we will assume that $\rho \overset{(2)}{\psi}$ consists of two parts, $\rho \overset{(2)}{\psi}_d$ and $\rho \overset{(2)}{\psi}_s$,

$$\rho \overset{(2)}{\psi} = \rho \overset{(2)}{\psi}_d + \rho \overset{(2)}{\psi}_s \qquad (C.19)$$

where $\rho \overset{(2)}{\psi}_d$ denotes the dilatation contribution and $\rho \overset{(2)}{\psi}_s$, the diffusive contribution.

We now consider the energy balance equation for the fluid in the physical configuration

$$\overset{(2)}{\rho}{}^{e} \frac{\overset{(2)}{D}\,\overset{(2)}{E}}{Dt} = - \overset{(2)}{p}{}^{e} \operatorname{div} \overset{(2)}{\underline{v}}{}^{e} + \rho \overset{(2)}{\psi}_s \qquad (C.20)$$

Combining Eqs. (C.4), (C.5), (C.8) and (C.17) through (C.20) we obtain:

$$\rho \overset{(2)}{\psi}_d = - \overset{(2)}{p}{}^{e} \left[\frac{\partial \overset{(2)}{n}}{\partial t} + \overset{(2)}{\underline{v}} \cdot \operatorname{grad} \overset{(2)}{n} \right] \qquad (C.21)$$

Thus

$$\rho \overset{(2)}{\beta} \cdot \overset{(2)}{v} + \rho \overset{(2)}{\psi} = - \overset{(2)}{p}{}^{e} \frac{\partial \overset{(2)}{n}}{\partial t} - \rho_0 \underline{n} \cdot \overset{(2)}{\underline{v}} + \rho \overset{(2)}{\psi}_s \qquad (C.22)$$

For the solid, $\overset{(1)}{s}$, the energy balance considerations are much more complex. Even for the uni-axial case considered in connection with the momentum balance, the situation is quite difficult. In the physical configuration, $\overset{(1)}{v}{}^{e}_{2}$ and $\overset{(1)}{v}{}^{e}_{3}$ need not be zero and indeed may depend upon all the three space dimensions. One, therefore, needs to introduce some additional assumptions for the solid energy balance.

The requirement that the energy contribution of the internal material interaction forces be zero may be written

as

$$\rho\underline{\beta}\cdot\left(\overset{(1)}{\underline{v}}-\overset{(2)}{\underline{v}}\right)+\rho\overset{(1)}{\psi}+\rho\overset{(2)}{\psi}=0 \tag{C.23}$$

Substituting from Eqs. (C.11), (C.19) and (C.22) into Eq. (C.23), there follows:

$$\left[-\overset{(2)}{p}{}^{e}\,\mathrm{grad}\,\overset{(2)}{n}+\rho_0\underline{n}\right]\cdot\overset{(1)}{\underline{v}}+\rho\overset{(1)}{\psi}-\overset{(2)}{p}{}^{e}\,\frac{\partial\overset{(2)}{n}}{\partial t}-\rho_0\eta\cdot\overset{(2)}{\underline{v}}$$
$$+\rho\overset{(2)}{\psi}_s=0$$

or

$$\left[-\overset{(2)}{p}{}^{e}\,\frac{\partial\overset{(2)}{n}}{\partial t}+\overset{(2)}{p}{}^{e}\cdot\mathrm{grad}\,\overset{(2)}{n}\cdot\overset{(1)}{\underline{v}}\right]+\rho\overset{(1)}{\psi}+\rho_0\underline{n}\cdot\left(\overset{(1)}{\underline{v}}-\overset{(2)}{\underline{v}}\right)$$
$$+\rho\overset{(2)}{\psi}_s=0 \tag{C.24}$$

The internal energy contribution $\rho\overset{(1)}{\psi}$ can be split up into two parts, $\rho\overset{(1)}{\psi}_d$ and $\rho\overset{(1)}{\psi}_s$.

$$\rho\overset{(1)}{\psi}=\rho\overset{(1)}{\psi}_d+\rho\overset{(1)}{\psi}_s \tag{C.25}$$

This yields

$$-\left[\overset{(2)}{p}{}^{e}\,\frac{\partial\overset{(2)}{n}}{\partial t}+\overset{(2)}{p}{}^{e}\,\mathrm{grad}\,\overset{(2)}{n}\cdot\overset{(1)}{\underline{v}}\right]+\rho\overset{(1)}{\psi}_d+\rho\overset{(1)}{\psi}_s+\rho\overset{(2)}{\psi}_s$$
$$+\rho_0\underline{n}\cdot\left(\overset{(1)}{v}-\overset{(2)}{v}\right)=0 \tag{C.26}$$

We have thus one equation for three unknowns, $\overset{(1)}{\psi}_d$, $\overset{(1)}{\psi}_s$, $\overset{(2)}{\psi}_s$. We will now assume that the dilatation and shear contributions must be separately equal to zero, i.e.,

$$\rho \overset{(1)}{\psi}_d = \overset{(2)}{p}e \left[\frac{\partial \overset{(2)}{n}}{\partial t} + \text{grad}\, \overset{(2)}{n} \cdot \overset{(1)}{\underline{v}} \right] \tag{C.27a}$$

$$\rho \overset{(1)}{\psi}_s + \rho \overset{(2)}{\psi}_s = \rho_0 \underline{n} \cdot \left(\overset{(2)}{v} - \overset{(1)}{v} \right) \tag{C.27b}$$

This procedure is exact for inviscid $\left(\rho \overset{(1)}{\psi}_s \equiv \rho \overset{(2)}{\psi}_s \equiv \rho_0 \underline{n} \equiv 0 \right)$ or incompressible materials $\left(\overset{(2)}{n} \equiv \text{constant} \right)$. However, in the general case, it has to be regarded as a constitutive assumption.

The next question that arises is as to how we should split the diffusive contribution. Since diffusion is a dissipative process, it is reasonable to require that

$$\rho \overset{(1)}{\psi}_s \geq 0 \qquad \rho \overset{(2)}{\psi}_s \geq 0 \tag{C.28}$$

One further assumption is now necessary regarding the partition of the diffusive energy contribution. The simplest hypothesis is to assume $\rho \overset{(1)}{\psi}_s$ to be zero. This yields:

$$\rho \overset{(2)}{\psi}_s = \rho_0 \underline{n} \cdot \left(\overset{(2)}{\underline{v}} - \overset{(1)}{\underline{v}} \right) \geq 0 \tag{C.29}$$

The last assumption merely states that the fluid receives all the diffusive energy contribution.

In our previous work (3SR-648), it was assumed that

$$\rho \overset{(1)}{\psi}_s = -\rho_0 \underline{n} \cdot \overset{(1)}{\underline{v}}$$

$$\rho \overset{(2)}{\psi}_s = \rho_0 \underline{n} \cdot \overset{(2)}{\underline{v}} \tag{C.30}$$

It is now seen that such an assumption cannot possibly satisfy Eqs. (C.28), and hence is erroneous. This last conclusion of course does not apply if $\rho_0 \underline{n}$ is regarded as a shear (non-dissipative) force. It may also be verified that for the steady case, present expressions for $\rho \psi_d^{(1)}$ and $\rho \psi_d^{(2)}$ reduce to those derived in 3SR-648.

APPENDIX D
EFFECTIVE STRESS LAWS

The effect of fluid pressure on the deformation and strength of saturated rocks has been studied by a number of investigators. This role of fluid pressure is usually considered by defining an "effective stress" $\langle\sigma_{ij}\rangle$

$$\langle\sigma_{ij}\rangle = \sigma_{ij} - \alpha p_p \delta_{ij} \tag{D.1}$$

where

σ_{ij} = applied stress on the rock/fluid composite

α = constant

p_p = pore pressure

The "effective stress law" simply implies that the stress-strain (and strength) response of the saturated rock is identical with that of the dry rock if one utilizes the effective stress $\langle\sigma_{ij}\rangle$ instead of the composite stress σ_{ij}.

There is considerable disagreement as to the value of the parameter α. Terzaghi[63] argued that α should equal the porosity, 1-n, so that the effect of pore pressure is eliminated when the porosity is zero. Hubbert and Rubey[75,76] attempted to prove theoretically that α should be 1. Although the validity of their proof is somewhat controversial,[68] experimental measurements on strength have generally revealed a fair agreement with Eq. (D.1) with $\alpha = 1$.[77-80] One exception to this good agreement appears to be in the area of strength measurements on low porosity rocks.[78] However, Brace and Martin[80] present

quite plausible arguments to the effect that this apparent disagreement is due to fluid pressure in not being fully effective. Prior to gross fracture, the rocks begin to dilate under compressive stresses. Above a certain critical strain rate, fluid pressure inside the pores is considerably less than the applied pore pressure.

Even though $\alpha = 1$ gives good agreement with strength tests, its application to stress-strain measurements is questionable.[81-83,68] Skempton[82] and Geertsma[81] have suggested that

$$\alpha = 1 - K/K_s \tag{D.2}$$

where K = bulk modulus of porous rock

K_s = bulk modulus of rock grain.

Skulje[83] proposed the form

$$\alpha = 1 - n\ K/K_s\ , \tag{D.3}$$

where n denotes the volume fraction of the rock matrix. Because of lack of good theoretical basis or sufficient data, expressions like (D.2) and (D.3) have not been generally employed. Recently, Nur and Byerlee[68] have derived Eq. (D.2) from certain linear elasticity considerations and tried to correlate it with stress-strain data.

Nur and Byerlee[68,84] have tested Weber sandstone under hydrostatic pressure both with no pore fluid and when the pores are saturated. Choice of Weber sandstone minimizes weakening of the rock matrix by chemico-physical interaction with the pore fluid. They measured the confining pressure p_c, pore pressure p_p, and the partial volumetric strain for the rock, $\theta^{(1)}$. In Fig. D.1 we show the stress-strain points obtained by using the conventional

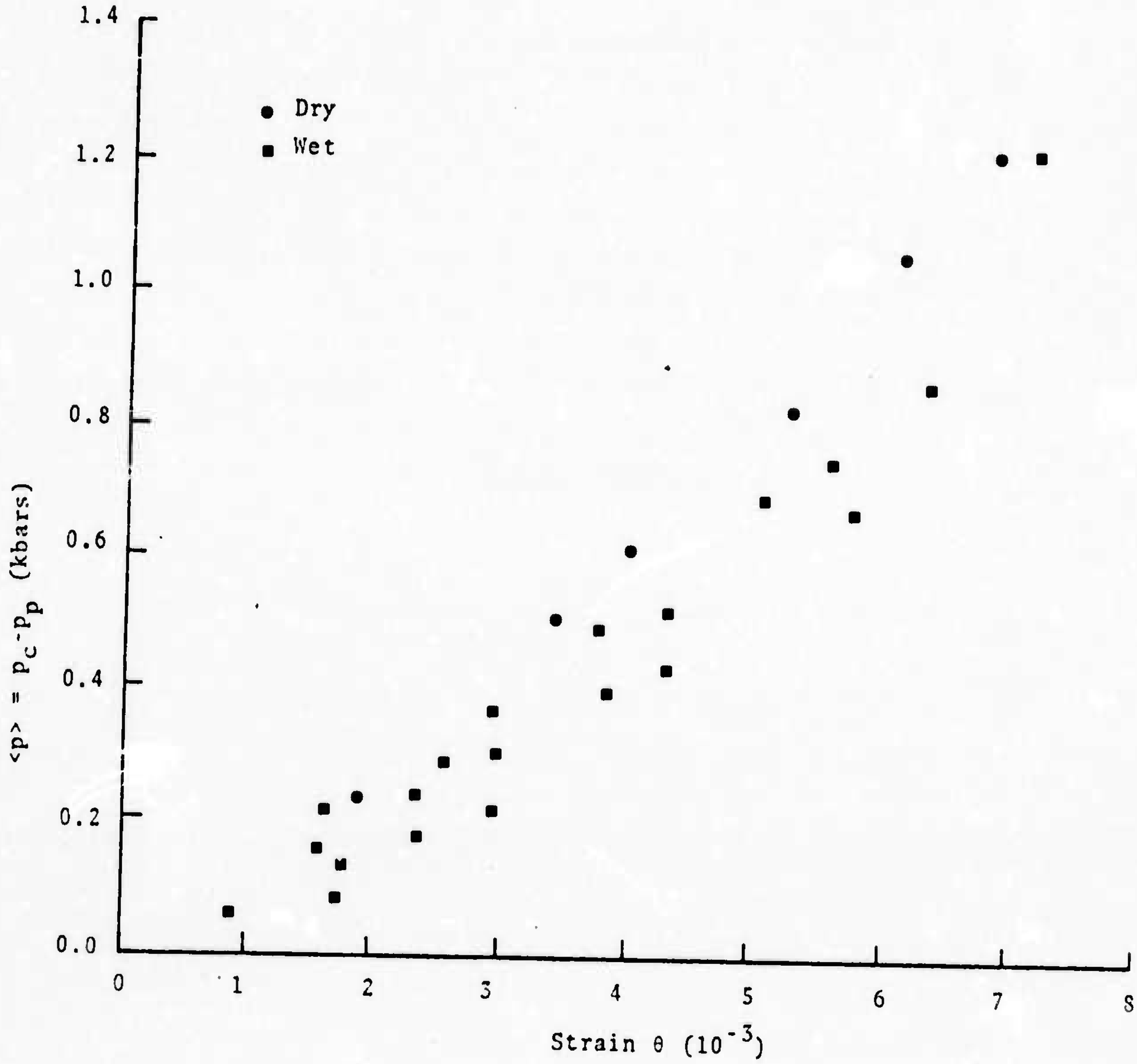

Fig. D.1--Conventional effective stress law.

effective stress law. It is seen that all the saturated data lies on one side of the dry data. Had the conventional effective stress law been applicable, all the saturated data should have fallen on the dry curve. The conventional effective stress law overcorrects for the pore pressure effect and is evidently inadequate. In Fig. D.2 we plot the stress-strain data obtained from the Nur-Byerlee effective stress law. The dry stress-strain data was numerically differentiated (linear) to yield K as a discrete function of p_c. Least square technique was then employed to express K as a second degree polynomial in p_c. Following Nur and Byerlee[68], K_s was taken to be 0.36 mbar. For the wet case, K was evaluated from the polynomial function by replacing p_c by $p_c - p_p$. Comparing Figs. D.1 and D.2, it is readily seen that use of the Nur-Byerlee effective stress law considerably reduces the data scatter. However, even in this case all the wet data lie on one side of the dry data. Clearly, the Nur-Byerlee effective stress law undercorrects for the pore pressure effect.

In Fig. D.3, we plot the TINC effective stress $\overset{(1)}{p}{}^e$ versus effective strain $\overset{(1)}{\theta}{}^e$ and n. The interaction function n was then expressed as a second degree polynomial function in p_c. For the wet rock, n was evaluated from this functional relationship with p_c replaced by $p_c - 1.31\ p_p$. Effective pressure $\overset{(1)}{p}{}^e$ and effective strain $\overset{(1)}{\theta}{}^e$ were then determined from Eqs. (8) and (23). In this case, the scatter of wet data around the dry data is considerably reduced. Also, the wet data lies evenly on both sides of the dry data. Thus the TINC model provides a good model for data fitting. This, however, does not constitute a proof of the model. To provide a proof of the model, one would also need to measure the porosity (1-n) during the test and compare it with theoretically calculated values. It is, however, comforting to observe that the dependence of n_{wet} on p_c and p_p is in accord with the physical intuition.

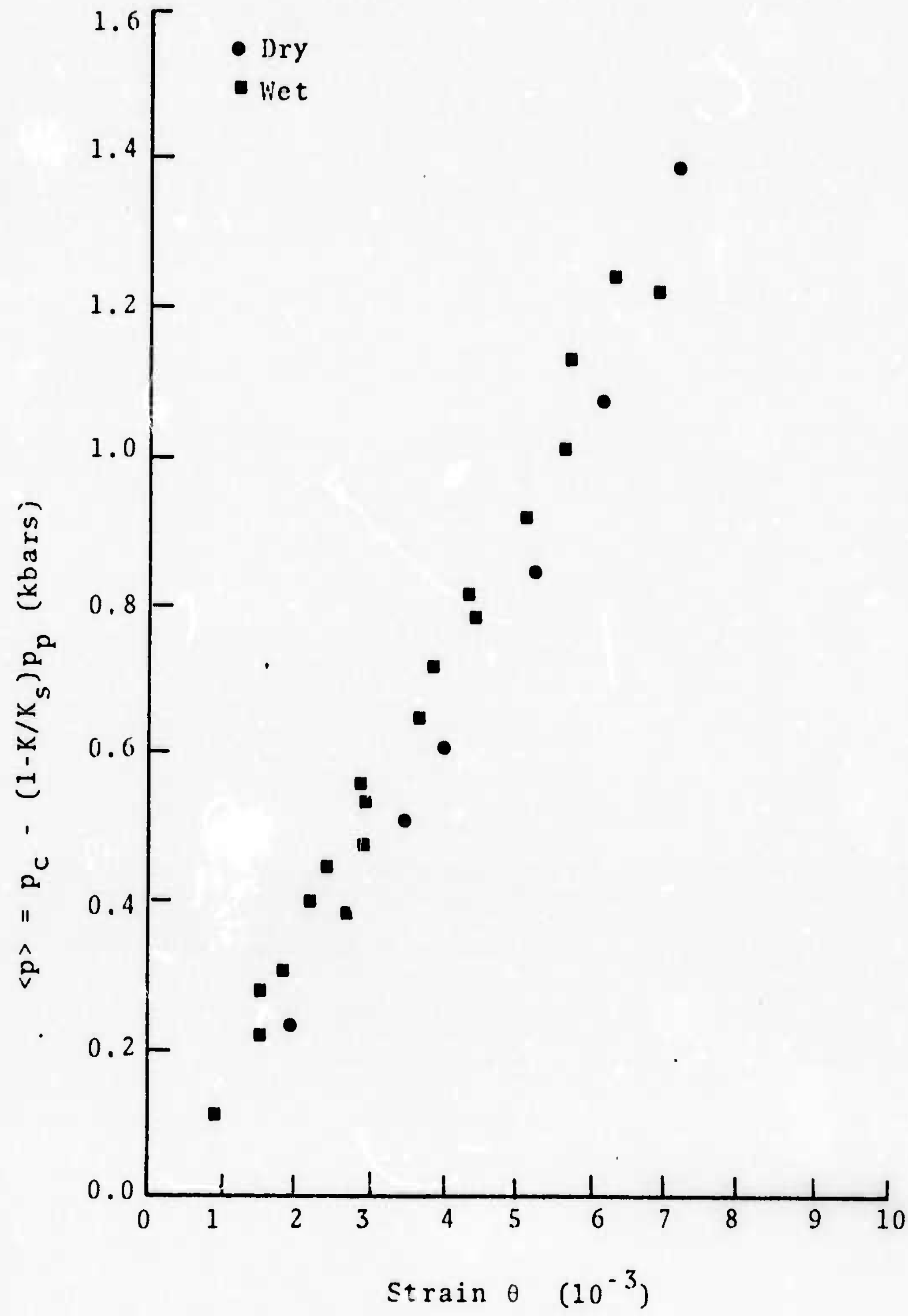

Fig. D.2--Nur-Byerlee effective stress law.

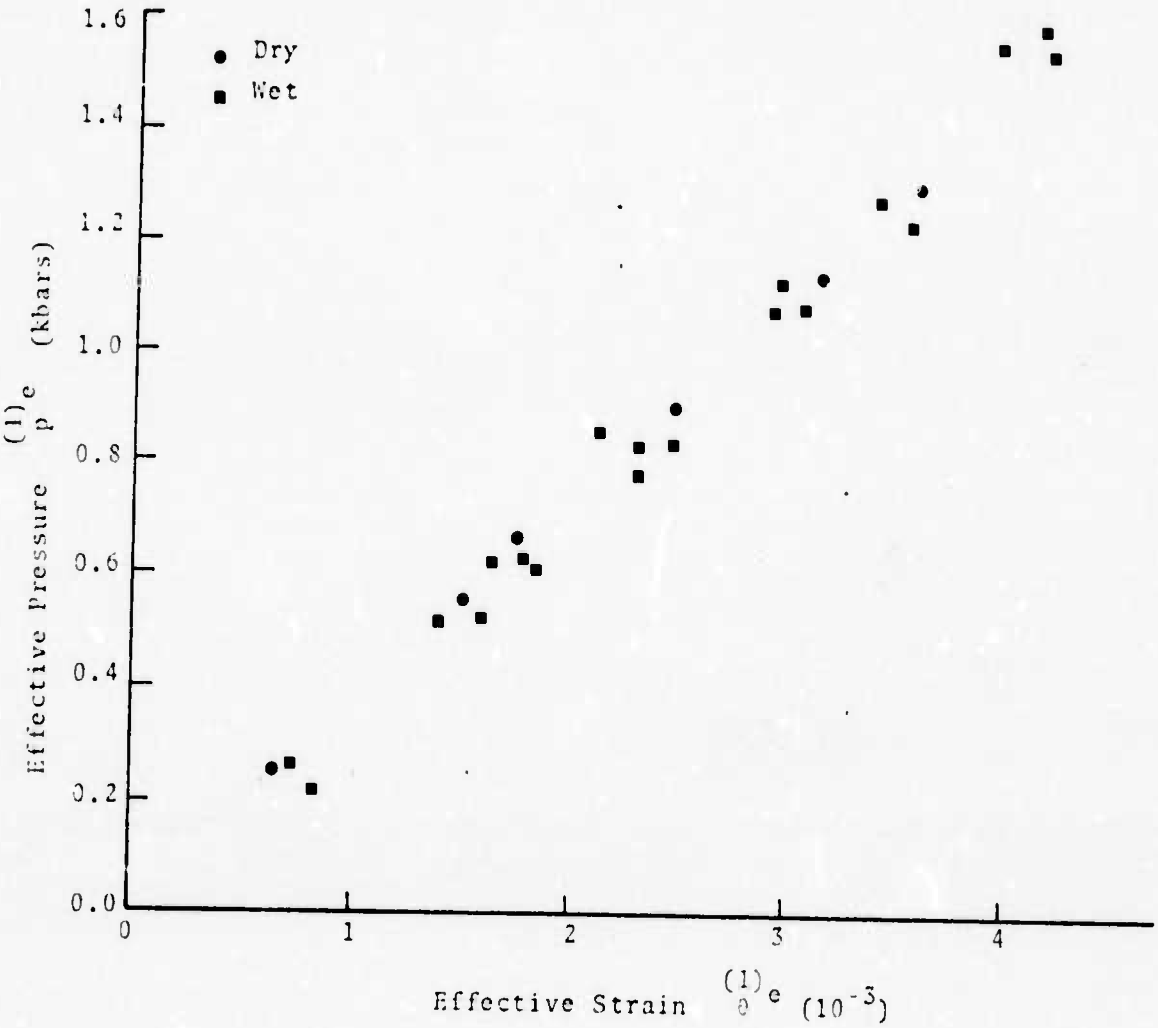

Fig. D.3--TINC effective stress law with
$n_{wet} = n_{dry} (p_c - 1.31\ p_p)$.

UNCLASSIFIED

Security Classification

DOCUMENT CONTROL DATA - R & D

(Security classification of title, body of abstract and indexing annotation must be entered when the overall report is classified)

1. ORIGINATING ACTIVITY (Corporate author)

Systems, Science and Software
P. O. Box 1620
La Jolla, California

2a. REPORT SECURITY CLASSIFICATION

UNCLASSIFIED

2b. GROUP

3. REPORT TITLE

GROUND MOTION MODELS AND COMPUTER TECHNIQUES

4. DESCRIPTIVE NOTES (Type of report and inclusive dates)

Formal Report

5. AUTHOR(S) (First name, middle initial, last name)

T. D. Riney, J. K. Dienes, G. A. Frazier, S. K. Garg, J. W. Kirsch, D. H. Brownell, A. J. Good

6. REPORT DATE	7a. TOTAL NO. OF PAGES	7b. NO. OF REFS
April 10, 1972	273	83

8a. CONTRACT OR GRANT NO.

DASA 01-69-C-0159 (P00003)

b. PROJECT NO. NWER XAXZ

c. Task & Subtask L438

d. Work Unit 01

9a. ORIGINATOR'S REPORT NUMBER(S)

3SR-1071

9b. OTHER REPORT NO(S) (Any other numbers that may be assigned this report)

DNA 2915Z

10. DISTRIBUTION STATEMENT

Approved for Public Release; Distribution Unlimited

11. SUPPLEMENTARY NOTES

12. SPONSORING MILITARY ACTIVITY

Director
Advanced Research Projects Agency
Washington, D. C. 20301

13. ABSTRACT

The work reported consists of three task areas: (a) development of constitutive models and computer methods for calculating stress wave effects in geologic media in the vicinity of a buried energy source, (b) verification of the computer models and their application to examine the sensitivity of ground motion predictions to the material parameters assumed in the constitutive models, and (c) development of methods for calculating the perturbation of residual tectonic stress-strain distributions induced by changing the pore water pressure. A general computer subroutine (TAMEOS) is described which generates thermodynamic equations of state of porous wet media for use with a table look-up procedure in standard ground motion codes. TAMEOS has been applied to NTS tuff and is used in the SKIPPER code for a series of spherical calculations in which the crushup strength and volume fractions of the rock-water-void mixture were varied. Four constitutive models and associated subroutines have been incorporated into SKIPPER for improved ground motion calculations for rocks with high shear strength. The cap model is generalized to treat the full range of pressure and strain encountered in underground tests. Generalized Mohr-Coulomb models include one without work hardening, one with isotropic work hardening, and one with kinematic work hardening. Model sensitivity calculations for granite are presented for the four SKIPPER options. Detailed comparison of calculations with field measurements are presented for the kinematic work hardening and cap models. A thermodynamic formulation of the Theory of Interacting Continua (TINC) is presented as well as the numerical procedure used in the new POROUS code for treating spherical ground motion problems in the TINC framework. Limited calculations using the new code are presented for partially saturated tuff. Linearized TINC equations are developed for describing the interaction of a pore fluid with a rock matrix as the fluid is driven through the geologic mass under a hydraulic gradient. The 2-D finite element computer code (FRI) for treating these geohydrological processes is described. Test calculations for the rock-fluid interactions in the vicinity of a fluid injection well are presented.

DD FORM 1 NOV 65 1473

UNCLASSIFIED

Security Classification

14 KEY WORDS	LINK A		LINK B		LINK C	
	ROLE	WT	ROLE	WT	ROLE	WT
Ground Motion Calculation						
Composite Materials						
Stress Waves in Geologic Media						
Porous Wet Media						
Decoupling						
Nevada Tuff						
Granite						
Rock and Soil Models						